GEOPHYSICAL AND HYDROGEOLOGIC INVESTIGATIONS OF TWO PRIMARY ALLUVIAL AQUIFERS EMBEDDED IN THE SOUTHERN SAN ANDREAS FAULT SYSTEM: SAN BERNARDINO BASIN AND UPPER COACHELLA VALLEY

by

BETH ANN WISELY

A DISSERTATION

Presented to the Department of Geological Sciences
and the Graduate School of the University of Oregon
in partial fulfillment of the requirements
for the degree of
Doctor of Philosophy

June 2012

DISSERTATION APPROVAL PAGE

Student: Beth Ann Wisely

Title: Geophysical and Hydrogeologic Investigations of Two Primary Alluvial Aquifers Embedded in the Southern San Andreas Fault System: San Bernardino Basin and Upper Coachella Valley

This dissertation has been accepted and approved in partial fulfillment of the requirements for the Doctor of Philosophy degree in the Department of Geological Sciences by

David Schmidt	Chairperson
Rebecca Dorsey	Member
Ray Weldon	Member
Pat Bartlein	Outside Member

and

Kimberly Andrews Espy	Vice President for Research & Innovation/Dean of the The Graduate School

Original approval signatures are on file with the University of Oregon Graduate School.

Degree awarded June 2012

DISSERTATION ABSTRACT

Beth Ann Wisely

Doctor of Philosophy

Department of Geological Sciences

June 2012

Title: Geophysical and Hydrogeologic Investigations of Two Primary Alluvial Aquifers Embedded in the Southern San Andreas Fault System: San Bernardino Basin and Upper Coachella Valley

This study of alluvial aquifer basins in southern California is centered on observations of differential surface displacement and the search for the mechanisms of deformation. The San Bernardino basin and the Upper Coachella Valley aquifers are bound by range fronts and fault segments of the southern San Andreas fault system. I have worked to quantify long-term compaction in these groundwater dependent population centers with a unique synthesis of data and methodologies using Interferometric Synthetic Aperture Radar (InSAR) and groundwater data. My dissertation contributes to the understanding of alluvial aquifer heterogeneity and partitioning. I model hydrogeologic and tectonic interpretations of deformation where decades of overdraft conditions and ongoing aquifer development contribute to extreme rapid subsidence.

I develop the Hydrogeologic InSAR Integration (HII) method for the characterization of surface deformation in aquifer basins. The method allows for the separation of superimposed hydraulic and/or tectonic processes in operation. This formalization of InSAR and groundwater level integration provides opportunities for

application in other aquifer basins where overdraft conditions may be causing permanent loss of aquifer storage capacity through compaction.

Sixteen years of SAR data for the Upper Coachella Valley exhibit rapid vertical surface displacement (≤ 48mm/a) in sharply bound areas of the western basin margin. Using well driller logs, I categorize a generalized facies analysis of the western basin margin, describing heterogeneity of the aquifer. This allowed for assessment of the relationships between observed surface deformation and sub-surface material properties.

Providing the setting and context for the hydrogeologic evolution of California's primary aquifers, the mature San Andreas transform fault is studied extensively by a broad range of geoscientists. I present a compilation of observations of creep, line integrals across the Pacific-North America Plate Boundary, and strain tensor volumes for comparison to the Working Group 2007 (UCERF 2) seismicity-based deformation model. I find that the moment accumulation across the plate boundary is consistent with the deformation model, suggesting fault displacement observations within the plate boundary zone accurately capture the strain across the plate boundary.

This dissertation includes co-authored materials previously published, and also includes unpublished work currently under revisions for submission to a technical journal.

CURRICULUM VITAE

NAME OF AUTHOR: Beth Ann Wisely

GRADUATE AND UNDERGRADUATE SCHOOLS ATTENDED:

University of Oregon, Eugene
Sonoma State University, Rohnert Park, California
College of Marin, Kentfield, California

DEGREES AWARDED:

Doctor of Philosophy, Geophysics, 2012, University of Oregon

Bachelor of Science, Geology, Minor in Mathematics, 2003, Sonoma State University, *cum laude*

AREAS OF SPECIAL INTEREST:

Hydrogeology
InSAR
Southern San Andreas fault system
Aquifer Basins
Applied Mathematics

GRANTS, AWARDS, AND HONORS:

Undergraduate Grant, Marin Education Fund, San Rafael, California, 2001-2003

Outstanding Student in Earth Science, College of Marin, 2001

American Association of University Women, Annual Scholarship, Marin County Chapter, 2001

California Federation of Mineralogical Societies, Annual Scholarship, Placer County, 2002

Undergraduate Research Grant, Sonoma State University, California, 2003

Thayer Scholarship in Geophysics, University of Oregon, 2005 and 2008
Richard Chamber's Memorial Scholarship, Northern California Geological Society, 2008

PUBLICATIONS:

Wisely, B.A., and D. Schmidt, 2010, Deciphering vertical deformation and poroelastic parameters in a tectonically active fault-bound aquifer using InSAR and well level data, San Bernardino basin, California, *Geophys. J. Int.*, doi: 10.1111/j.1365-246X.2010.04568.x.

Wisely, B.A., D.A. Schmidt, 2009, Aquifer system compaction rates estimated for the Coachella Valley, California, using InSAR, groundwater level data, and drillers' logs. *Abstracts With Programs – Geol. Soc. Am., 41(7)*, p 175.

Philibosian, B., T. Fumal, R.J. Weldon, K. Kendrick, K. Scharer, S. Bemis, R. Burgette, and B.A. Wisely, 2009, Photomosaics and logs of trenches on the San Andreas fault near Coachella, California, *USGS Open-file Rep. 2009-1039*.

Wisely, B.A., D.A. Schmidt, and R.J. Weldon, 2007, Compilation of surface creep on California faults and comparison of WG-07 deformation model to Pacific-North American plate motion: Appendix P in the Uniform California Earthquake Rupture Forecast, version 2 (UCERF 2), *USGS Open-file Rep. 2007-1437*, and *CGS Spec. Rep. 203P*, 43 p., [http://pubs.usgs.gov/of/2007/1437/p/].

Wisely, B.A., D. Schmidt, 2007, The characterization of aquifer deformation in regions of active tectonics using InSAR and well level data; a case study for San Bernardino Basin, California. *Abstracts With Programs – Geol. Soc. Am., 39(6)*, 269.

Emerson, L.F., A. Soule, I. Belien, N. Deardorff, E. Gottesfeld, E. Johnson, and B.A. Wisely, 2007, Implementation of ground-based LiDAR, total station, and GPS in an advanced geophysical study of basaltic cinder cone morphology, Four Craters volcanic field, Oregon. *Abstracts With Programs – Geol. Soc. Am., 39(6)*, 123.

Wisely, B. A., D. Schmidt, 2005, Subsidence and differential surface movement in the Upper Coachella Valley, California, as indicated by InSAR, *Eos Trans. AGU 86(52) Fall Meet. Suppl.* Abstract G51C-0843.

Burgette, R., R.J. Weldon, D. Livelybrooks, D. Schmidt, S. Alba, B.A. Wisely, 2005, Constraints on the extent of subduction zone locking along the central Oregon coast from leveling and sea level observations, *Eos Trans. AGU 86(52) Fall Meet. Suppl.* Abstract S51C-1017.

Anderson, T.B., B.A. Wisely, 2004, Inner fan channel deposits in the German Rancho Formation near Salt Point State Park, Sonoma County, California." *Abstracts With Programs – Geol. Soc. Am.,* 36(4), p 78.

ACKNOWLEDGEMENTS

Family and friends have been an invaluable resource during the challenges of research and scientific writing. I thank my grandparents who moved to the Coachella Valley in the late 1970's and told me about the "underground lake beneath the city". My love of Earth Science is rooted in my early exposure to camping and boating, for which I thank my parents. I thank my son for providing the ultimate motivation to earn a doctoral degree, and thank our dog Maggie for making me smile everyday.

I am grateful to the University of Oregon for the wide array of opportunities and funding offered. The UO Libraries and Library Staff have provided an extraordinary breadth and depth of academic resources, and the Administrative Staff in the Department of Geological Sciences does a fine job looking out for those of us with our noses in articles and deadlines faintly scratched on calendars.

Thanks to David Schmidt for teaching me a wide variety of technical skills, and for encouraging the development of my scientific interests. I am grateful to Ray Weldon for the opportunities to do paleoseismic fieldwork in the Coachella Valley, seismic hazard fieldwork in Kyrgyzstan, and for the opportunity to participate in a joint USGS-CGS project. Thanks to Becky Dorsey for always sharing her true passion for science and providing a positive spin on difficult tasks.

My work would not be complete without the data provided by Michelle Malahoff and Steven Bigley at the Coachella Valley Water District, and by Dick Peterson (retired) at the San Bernardino Valley Municipal Water District. Thanks to Vicki Langenheim and Megan Anderson for sharing their geophysical digital data files. This research was partially funded by a grant form the Southern California Earthquake Center.

For my Grandparents Myna and Gilbert Seidel, and Virginia and F. E. Wisely.

TABLE OF CONTENTS

Chapter Page

Chapter Page

LIST OF FIGURES

Figure Page

Figure Page

LIST OF TABLES

Table Page

CHAPTER I

INTRODUCTION

In the arid southwestern United States a major societal concern is what happens to alluvial aquifers when groundwater is mined to excess. Alluvial aquifer basins in southern California rely heavily on imported water to artificially recharge groundwater aquifers in efforts to avoid the costly effects of prolonged overdraft. Aquifer overdraft can cause loss of groundwater storage capacity, land subsidence, and the need for deeper wells that require more energy to access and pump the groundwater resource to the surface. Groundwater pumping can cause deformation of the fine-grained aquifer skeleton, and under extreme pore pressure changes can cause non-recoverable loss of storage capacity. I document land subsidence, a problematic result of overdraft conditions, in localized regions of the San Bernardino basin (1993-2000) and the Upper Coachella Valley (1993-2009), on the order of 0.5-4.8 cm/a. Land subsidence may cause damage to structural foundations and municipal systems like roadways and sewers. Some portion of the observed subsidence is related to decades of sustained overdraft conditions in these basins and the permanent loss of aquifer storage through fine-grained compaction.

The southern San Andreas fault system is known in many locations to bound alluvial aquifer basins and/or act as a semi-permeable barrier to groundwater flow. Another major question addressed in this dissertation is whether it is possible to differentiate the deformation caused by hydraulic processes from the deformation caused by tectonic processes. I image differential surface displacement across known

groundwater flow barriers, as well as hypothesized groundwater flow barriers using Interferometric Synthetic Aperture Radar (InSAR). Differential surface displacement can be used in the numerical modeling of deformation in the subsurface, and efforts are made to constrain both elastic and inelastic deformation components in San Bernardino Basin and the Upper Coachella Valley. The folding and faulting of the regional San Andreas system formed the structural troughs in which the alluvial deposits and connate water accumulated, forming the present day hydrogeology of the California Coastal Basin aquifers. The interplay between ground water hydraulics and fault-related aquifer structure complicates both efforts towards seismic hazard analysis and groundwater management.

Chapter II and Chapter III are investigations into the characterization of aquifer deformation using extensive InSAR data and groundwater levels in the San Bernardino basin and Upper Coachella Valley. InSAR is used in many geoscientific applications, and has provided surface deformation data for the hydrogeologic community as well as the crustal deformation community. InSAR data is a major source of data used in this dissertation. The raw data was downloaded from online archives hosted by geophysical consortiums and processed with community software. The satellite wavelengths (5-20 cm) are well suited for the magnitude of deformation observed in the San Bernardino and Coachella Valley study areas. Groundwater data provide insight into pore pressure conditions in the aquifer and are compared to the observed surface displacement in both Chapter II and III.

The surface displacement and groundwater level data are the basis for the development of the HII method for characterization of aquifer deformation in Chapter II,

which calculates model estimates for poroelasticity and inelastic deformation rates for the San Bernardino Basin alluvial aquifer. The HII method is applied again in Chapter III to the Coachella Valley aquifer, where I also perform a sensitivity analysis on the method constraining minimal data requirements and uncertainties associated with the method. For both aquifer basins, I interpret the observed subsidence as being caused by compaction of clay-rich layers or lenses, and in Chapter III I explore whether the surface deformation can be explained by compacting lenses at depth using a series of forward models.

As both aquifer basins are within the San Andreas fault zone, an important aspect of this work was to investigate the possibility of fault related surface displacement contributing to the InSAR measurements. Chapter IV is a co-authored compilation of the tectonic setting, specifically fault displacement and fault orientations gathered for California, and ultimately serves as an appendix in a larger publication analyzing the hazard potential used to set earthquake insurance rates. Chapter V is a summary recap of the previous chapters.

Along with the case study of the San Bernardino basin aquifer and the formalization of the HII method for alluvial aquifer characterization, Chapter II also includes interseismic models of surface displacement using the RefGF fault database to determine the possible vertical contribution from interseismic deformation below the locking depth of the fault plane. (The RefGF database also serves as the fault database for strain tensor analysis in Chapter IV.) I estimate residual subsidence (i.e. subsidence not attributed to seasonal groundwater pumping and recharge patterns) on the order of 2mm/a, most likely representing fine-grain sediment compaction near the San Jacinto

fault rather than interseismic tectonic deformation. The San Jacinto fault in this location is a well-known groundwater flow barrier, which has contributed to the concentration of fine-grained lakebed deposition in this setting. Poroelastic parameter estimates from the HII method application are consistent with the known material properties of the subsurface and with those of other studies in alluvial aquifer basins.

The Coachella Valley aquifer is undergoing more extreme and sharply defined surface displacement patterns, described in detail in Chapter III. The study also includes a novel hydrostratigraphic analysis of well driller logs in which depositional facies of the upper ~300m of the aquifer column are interpreted in order to relate observed deformation to variations in subsurface hydrogeology. Using Coulomb 3.3 elastic modeling software, I am able to make predictions of surface displacement in response to closing on a plane(s) at depth in the aquifer. The closure is used to represent compaction of fine-grained layers and lenses at depth in the aquifer, a key hypothesis considered in explanation of observed subsidence in the Coachella Valley.

The aquifers of the San Bernardino basin and the Coachella Valley are embedded in the southern San Andreas fault system, a mature transform plate boundary studied extensively by a broad range of geoscientists. Chapter IV is a co-authored work, containing a compilation of published observations of surface creep on California faults. Aseismic fault slip must be incorporated into earthquake rupture models because moment release on a fault is reduced from what would be inferred directly from the fault's slip rate. Chapter IV also constructs line integrals across California to test the WG-07 deformation model plate boundary rate, finding the deformation model accurate within reasonable uncertainties. Lastly, in Chapter IV I construct strain tensors of volumes

across the WG-07 deformation model to compare the seismic moment budget to that of the expected motion across the plate boundary. Strain tensor analysis strongly suggests that the WG-07 deformation model accurately captures strain across the plate boundary.

I am first author on Chapters II, III, and IV in this dissertation, responsible for the data analysis, methodology development, and interpretations of results in Chapters II and III, and responsible for the strain tensor analysis in Chapter IV. Chapter II has been published in *Geophysical Journal International* in April 2010 and was co-authored and co-edited by my advisor Dr. David Schmidt. Chapter III is in preparation for publication and will also be co-authored by Dr. David Schmidt. Chapter IV has been published in 2007 as Appendix P in a joint USGS and CGS report, Uniform California Earthquake Rupture Forecast, version 2 (UCERF 2), and was co-authored by Dr. David Schmidt and Dr. Ray Weldon. This project is currently being updated and revised as an appendix for UCERF 3. Chapter V is a synthesis of the work discussed in the previous chapters.

CHAPTER II

DECIPHERING VERTICAL DEFORMATION AND POROELASTIC PARAMETERS IN A TECTONICALLY ACTIVE FAULT-BOUND AQUIFER USING INSAR AND WELL LEVEL DATA, SAN BERNARDINO BASIN, CALIFORNIA

This work was published in the Geophysical Journal International in April 2010. I performed the data collection, research and analysis, and was first author. My coauthor David Schmidt aided in the development of methodology and editorial processes.

1. INTRODUCTION

1.1. Project Summary

Using InSAR and hydrogeologic time series spanning 1995 to 2000, we characterize the elastic storage and surface deformation in the vicinity of the San Bernardino basin, California. The region encompasses a complex major aquifer located at the junction of the San Andreas and San Jacinto faults that supplies groundwater to over 600,000 people. We remove the elastic vertical surface displacement associated with changes in groundwater levels from the InSAR time series by a least squares inversion. Our method estimates a poroelastic ratio at 60 well sites, which we normalize by basin depth, allowing for comparison of the elastic response of the aquifer skeleton from site to site. Our method also estimates residual vertical displacement rates at each well site, surface displacement not explained by observed trends in groundwater levels. Residual vertical displacement rates reveal patterns of subsidence and uplift across the basin over the five-year period from 1995 to 2000. In a narrow zone of observed residual

subsidence near the San Jacinto fault, where many normalized poroelastic ratios trend higher than expected, we find permanent compaction of clay-rich strata to be the most likely explanation for 0.5-2.0 mm/yr of residual subsidence. This permanent compaction is likely a result of delayed compaction due to previous overdraft conditions and/or a result of the installation of deep production wells during the span of the InSAR time series. Observations of localized subsidence within stepovers of the San Jacinto fault zone and relative uplift at the range fronts are consistent with current basin development models; however, interseismic strain modeling of the regional faults does not reproduce the surface displacement pattern or magnitude of these observations.

1.2. Project Background

California Coastal Basin aquifers provided over 4% of the total public-supply groundwater withdrawals for the United States in 2000, more than any other single-state principal aquifer (Planert & Williams 1995; Maupin & Barber 2005). The preservation of these resources requires careful management in order to assure fresh groundwater quality and aquifer sustainability. An understanding of the lateral and depth dependent structure of an aquifer system, including mapping of permeable units and the identification of groundwater barriers, is required for proper management. For example, variation in grain size, both laterally and vertically within an aquifer system, affects the local storage and transmissivity of groundwater. Most of the California Coastal Basin aquifers are structural troughs formed by folding and faulting (Planert & Williams 1995). Such structures often act as groundwater barriers, affecting groundwater flow patterns and pore pressures. Additional insight into the state of an aquifer is provided by the

active deformation that results from changes in pore pressure levels. First proposed by Terzaghi (1925), the concepts of effective stress, aquitard drainage and aquifer-system compaction describe the relationship of groundwater levels and deformation of an aquifer system. After prolonged groundwater pumping, even with stabilization of groundwater levels from aquifer recharge, land subsidence may continue due to the long-term residual compaction of fine-grained aquitard layers (e.g. Galloway *et al*. 1998). The extraction of groundwater from aquitards represents a non-recoverable reduction in pore volume, and therefore a reduction in storage capacity.

As an important groundwater resource in a moderately populated and seismically active region, the eastern Santa Ana Watershed (Fig. 2.1) has been the focus of over a century's worth of scientific investigation. The first published hydrogeologic study of the region was in 1888 (Hall 1888). Work continued through the 20th century and Dutcher & Garrett (1963) published a comprehensive hydrogeologic review of the watershed basin. The discovery of groundwater contamination from volatile organic compounds near the city of San Bernardino (Fig. 2.1) in 1980 instigated intensive chemical and isotopic analyses of the region's groundwater (Izbicki *et al*. 1998; Hamlin *et al*. 2002). Another primary topic of interest for this region has been the constraining of basement rock topography beneath the alluvial fill, largely because of the effect of basin geometry on ground motion predictions (Stephenson *et al*. 2002). In an integrated geophysical study using seismic, aeromagnetic and gravimetric data, Anderson *et al*. (2004) presented a basin depth model, estimating depth to basement rock beneath the alluvial deposits, and a structural interpretation of the upper crust. Most recently, Danskin *et al*. (2006) reported on an integrated analysis of the surface and groundwater

systems, describing current computer models of the aquifer system, and suggesting water management plans for different usage forecasts and contamination plume remediation options.

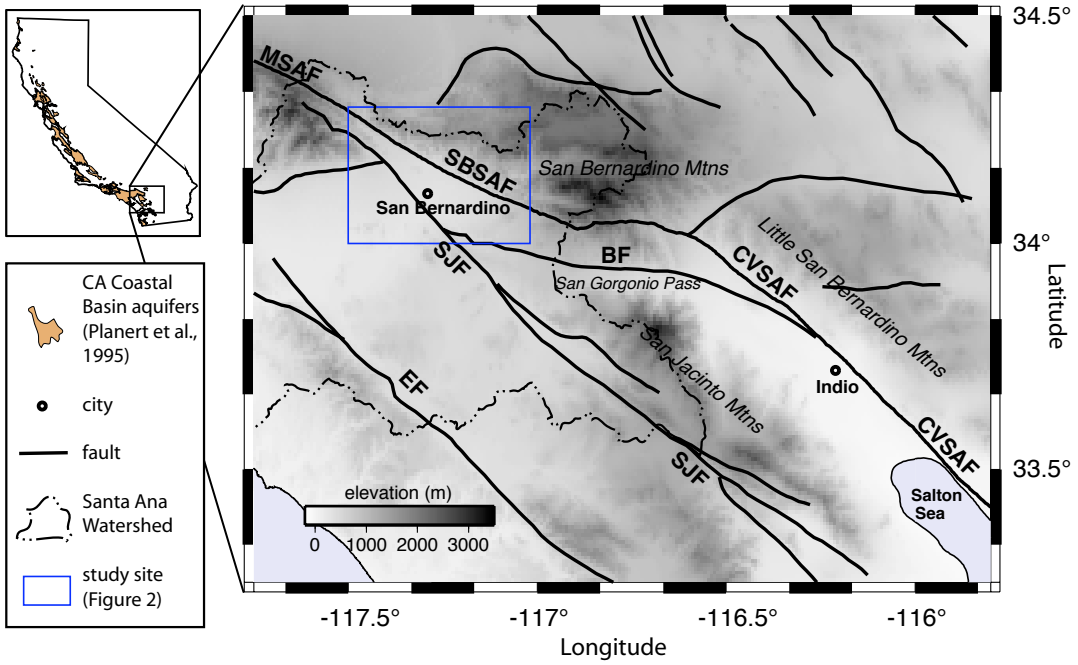

Figure 2.1. Regional fault map of the southern San Andreas fault system located in California (modified from Bennett, 2004), also showing topographic elevation, and boundaries of the Santa Ana Watershed and the San Bernardino study site. Fault abbreviations are: MSAF, Mojave section San Andreas fault; SBSAF, San Bernardino section San Andreas fault; CVSAF, Coachella section San Andreas fault; SJF, San Jacinto fault; EF, Elsinore fault. The blue rectangle corresponds to the boundary of the study area and interferometry figures.

One of the more recent developments in the monitoring of aquifer basins has been the use of Interferometric Synthetic Aperture Radar (InSAR) for measuring relative surface displacement (e.g. Amelung *et al*. 1999; Galloway *et al*. 2000; Bawden *et al*. 2001). Lu & Danskin (2001) published an InSAR study of the San Bernardino basin from 1992 to 1995 identifying areas prone to runoff and recharge induced surface deformation, specifically noting varying poroelastic response ratios in the Santa Ana

River Drainage area from the rest of the basin (Fig. 2.2). Their study also identifies locations where faults act as restrictive barriers to groundwater flow, and suggest an aerial distribution of fine-grained aquifer material. Lu & Danskin (2001) suggest that combining stream runoff and aquifer recharge data with InSAR surface deformation data can aid in defining basin structure and hydrogeology, and is useful in circumventing the need for traditional, time consuming and expensive field data collection. This study extends the record of InSAR for the San Bernardino basin (Lu & Danskin 2001) and provides a time-dependent look at aquifer surface deformation for the five-year study period of 1995 to 2000. Following the methods of Schmidt & Bürgmann (2003), we construct an InSAR time series of surface displacement for the period following that of the Lu & Danskin (2001) study.

Many of the California Coastal Basin alluvial aquifers are bounded by active faults such that the deformation signals from hydrologic and tectonic processes are superimposed. This is particularly an issue along many plate boundaries where the resolution of interseismic fault slip rates in basins is complicated by groundwater-induced deformation. For example, Bawden *et al*. (2001) and Watson *et al*. (2002) revealed how groundwater pumping has affected GPS observations of interseismic strain in the Los Angeles basin. More recently, Argus *et al*. (2005) attempted to resolve this issue by using the seasonal fluctuations in GPS and InSAR data to calibrate estimates of interseismic velocities in the San Gabriel valley. In the San Bernardino study area, interseismic deformation is caused by the active San Jacinto and San Andreas faults, which bound the basin to the west and the east, respectively. The expected pattern of interseismic deformation is sensitive to the fault geometry and mode of slip transfer

across the basin, the details of which are poorly resolved and opinions vary greatly among authors (e.g. Weldon & Sieh 1985; Stephenson *et al*. 2002; Anderson *et al*. 2004; UCERF2 2008). Based on fault geometries and the location of this basin within a major stepover of the San Andreas fault system, one might expect to see vertical evidence of on-going slip transfer across the basin study area (Crowell 1974; Bilham & King 1989; McClay & Bonora 2001).

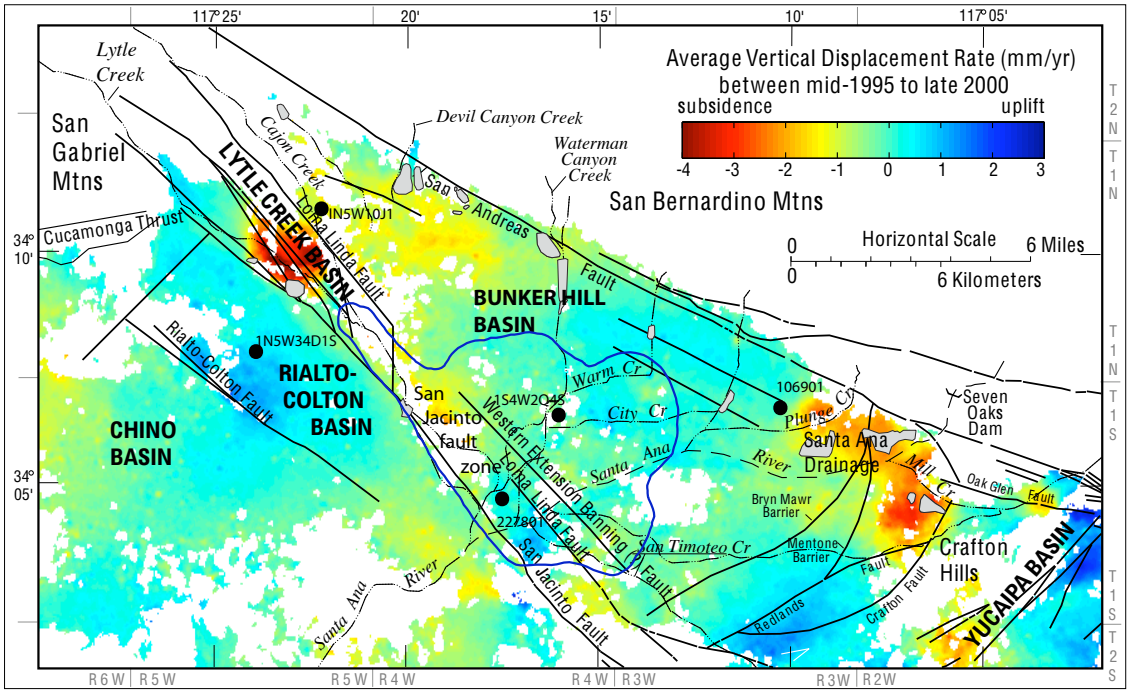

Figure 2.2. Detailed fault and groundwater barrier map modified from Danskin *et al*. (2006) with artificial recharge facility locations shown in gray. An InSAR stack showing average rate of vertical surface displacement between mid-1995 and late 2000 is overlain on the map. Negative rates are red and represent relative subsidence. Positive rates are blue and represent relative uplift. Municipal sub-basins and areas of interest are labeled. Black lines are faults and groundwater barriers. Black circles are well sites correlating to Fig. 2.4. The dark blue solid line surrounding the western Bunker Hill basin is the boundary of the former artesian area.

In order to characterize the surface deformation observed with InSAR in this tectonically active aquifer basin, we developed the Hydrogeologic InSAR Integration

(HII) method. The HII method uses a least squares inversion to separate vertical deformation due to groundwater extraction and recharge from the residual vertical displacement trends caused by geologic processes such as interseismic faulting and/or permanent sediment compaction. By incorporating groundwater level data with the surface elevation changes measured with InSAR, we are able to remotely assess the poroelasticity of the aquifer, and estimate the vertical displacement associated with short-term (e.g. seasonal) changes in groundwater level for 60 well sites. Our method also estimates the residual rate of surface displacement over 5 years at each well site thereby identifying locations of relative net subsidence and uplift. We find that the modeled poroelastic parameters and residual deformation reveal suggestive patterns and interpret these patterns in both a tectonic and hydrologic context.

1.3. Basin Hydrogeology

A number of fault splays and minor faults are present in the San Bernardino basin (Fig. 2.2), many of which act as groundwater flow barriers (Dutcher & Garrett 1963; Woolfenden & Kadhim 1997; Anderson *et al*. 2004; Danskin *et al*. 2006). The study area spans all or part of four different municipal sub-basins, the Bunker Hill basin, the Rialto-Colton basin, the Chino basin and the Yucaipa basin (Fig. 2.2), divided essentially based upon the major fault boundaries. The basins are bounded to the north and northeast by the San Gabriel and San Bernardino Mountains and to the south by the San Timoteo Badlands. The Bunker Hill basin is a down-faulted wedge entirely between the oblique right-lateral San Jacinto and San Andreas faults, and for purposes of this study includes the narrow Lytle Creek basin. The Rialto-Colton basin lies between the San Jacinto fault

on the east and the Rialto-Colton fault on the west. West of the Rialto-Colton fault is the Chino basin. Separated from the Bunker Hill basin by the uplifted bedrock and structures of the Crafton Hills fault zone is the gently sloping Yucaipa basin. In this section, we review the pertinent hydrogeologic characteristics of these fault-bound municipal sub-basins.

The geology of the eastern Santa Ana Watershed is composed of inter-fingering water bearing alluvial and river channel deposits overlying a bedrock basin. Basement rock is pre-Tertiary igneous and metamorphic rock and indurated sediments (Dutcher & Garrett 1963). Relative to the alluvial basin fill, basement rock is nearly impermeable (Danskin & Freckleton 1992; Hamlin *et al*. 2002), and has been uplifted and exposed in several places, most notably at the Crafton Hills.

Depth to groundwater in this major alluvial aquifer is typically tens of meters below the surface around the basin margins to very near the surface near the San Jacinto fault zone (Hamlin *et al*. 2002). Recharge to the aquifer occurs naturally and artificially through the coarse-grained deposits largely near the base of the San Gabriel and San Bernardino Mountains (Hamlin *et al*. 2002; Danskin *et al*. 2006). Natural storm runoff is diverted into short-term detention basins, which also operate as recharge facilities (Fig. 2.2). The principal area of natural recharge for the Bunker Hill aquifer is the Santa Ana Spreading Grounds at the confluence of the Santa Ana River channel and Plunge Creek in the southeastern study area. This location has been an artificial recharge site since 1911 (Schaefer & Warner 1975). Water from the Colorado River and northern California are also used for aquifer recharge (Hamlin *et al*. 2002). Most of the recharge from the Santa Ana River occurs in the stream channel itself, but the artificial recharge basins are

important for recharging imported water and containment during high-runoff years (Danskin *et al*. 2006).

The Quaternary alluvium of the Bunker Hill, Rialto-Colton, and Chino basins is poorly sorted gravel, sand, silt, clay, and boulders derived from the surrounding mountains, moderately permeable and readily yields groundwater where saturated (Dutcher & Garrett 1963; Danskin & Freckleton 1992; Anderson *et al*. 2004). In general, the alluvial deposits are coarser and more poorly sorted nearest the mountains, fining, sorting and thickening towards the San Jacinto fault zone (Danskin & Freckleton 1992). There are at least three areally extensive fine-grained deposits of silt, sandy silt, and clay (≥ 20m thickness) that act as aquitards, and smaller local lenses (≤ 5m thickness) that are not vertically or aerially extensive (Dutcher & Garrett 1963; Danskin *et al*. 2006). The thickest section of alluvial sediments (~ 2km) in the basin lies between the Loma Linda fault and western extension of the Banning fault of the San Jacinto fault zone (Fig. 2.2), and is interpreted to be a down-dropped sliver of the basin (Stephenson *et al*. 2002; Anderson *et al*. 2004; Danskin *et al*. 2006). Groundwater flow moves from the basin margins towards the deeper basin center. As the main trace of the San Jacinto fault is a restrictive barrier to the natural western flow of groundwater, upward flow develops east of the fault. Clay-rich surface layers near the fault act as confining layers, and diminish vertical conductivity, increasing hydraulic head (Danskin & Freckleton 1992). The aerial extent of this clay-rich unit represents the presence of a former marshland, and prior to extensive groundwater extraction, was under artesian conditions (Fig. 2.2).

Extensive groundwater extraction began in the mid 1900's, and by the 1970's, artificial recharge became necessary to maintain acceptable groundwater levels

throughout the basin. Since the inception of artificial recharge the former artesian area has endured problems associated with high groundwater pressure and shallow groundwater table. Although clay-rich units are effective aquitards to vertical flow, Holocene stream channel deposits provide vertical connectivity in the layered aquifer, as do the improper abandonment of wells throughout the last century of aquifer development (Danskin *et al*. 2006). Conditions can be described as semi-confined. Downtown San Bernardino is located in this zone of high pressure, where historically the slow upward seep of groundwater through the clay layers increased the potential for buckled foundations, severed utility lines, and liquefaction in an earthquake (Danskin & Freckleton 1992). The need to extract water constantly from this high-pressure area to keep liquefaction at a lower risk must be balanced against the need to not over-extract from the same area due to land subsidence concerns (Danskin *et al*. 2006). Municipal water management works to maintain a pressure that supports a tilted groundwater table, thereby maintaining adequately low groundwater levels in the areas susceptible to flooding and liquefaction while maintaining high enough groundwater levels at the basin margins for energy-efficient and cost-effective pumping (Danskin & Freckleton 1992).

Permanent land subsidence in the former artesian area has been assumed, but a lack of quantitative estimates exists in the literature. In the late 1960's land subsidence up to 30 cm associated with a 60 m groundwater level decline over two decades was observed, but presumed to be dominantly recoverable deformation (Miller & Singer 1971). According to Danskin *et al*. (2006), there has been a significant decrease in groundwater storage in the San Bernardino basin through the 20th century as a result of lowering groundwater levels. Some component of water released from the aquifer is

likely inelastic, but this quantity is unknown (Danskin *et al*. 2006, table 11). Our study investigates potential inelastic hydraulic deformation and attempts to constrain modern anthropogenic compaction rates for this part of the San Bernardino basin.

Southeast of the Bunker Hill basin and the uplifted rocks of the Crafton Hills, the deposits of the Yucaipa basin are largely unconsolidated, composed of boulders, gravel, sand, silt, and clay, with deeply incised Holocene river channel deposits (Hamlin *et al*. 2002). There are numerous faults in the Yucaipa basin trending both sub-parallel and nearly perpendicular to the local trend of the San Andreas fault. As a result of active tectonics, alluvial deposits have been uplifted, dissected, and folded in places (Mendez *et al*. 2001; Hamlin *et al*. 2002). Most groundwater in the Yucaipa aquifer occurs in moderately consolidated middle to late Pleistocene alluvium at 60-200 m below the surface, and artesian conditions existed historically in the western part of the Yucaipa Plain (Moreland 1970; CDWR Bulletin 118 2004). Steps in head level across local faults indicate the faults act as restrictive barriers to groundwater flow (CDWR Bulletin 118 2004). Since the 1970's and particularly in the 1990's, previously undeveloped and agricultural land with sparse human population has been transformed into housing tracts. This has resulted in an increased demand for groundwater and a decline in groundwater levels in the Yucaipa basin. Recharge to the groundwater system is dominantly from percolation of precipitation and infiltration through stream channel deposits, underflow from surrounding fractured bedrock, and artificial recharge.

1.4. Aquifer Elasticity

Recoverable elastic deformation occurs in all aquifers with the removal and replenishment of groundwater and can be measured as a change in surface elevation (Terzaghi 1925). For water level changes on the order of tens-of-meters, the resulting vertical surface displacement is in the millimeter-to-centimeter range (Helm 1978). The granular structure of the aquifer, known as the skeleton, contracts with the removal of groundwater, as support of the overlying material shifts from the pressurized pore fluid to the granular skeleton. Conversely, as groundwater is recharged, support for the overburden is shifted back to the pressurized pore fluid. This type of elastic deformation occurs within a particular range of pore pressure changes as a result of the cycles of groundwater pumping and recharge, and is observed in both confined and unconfined aquifers (e.g. Terzaghi 1925; Galloway *et al*. 1999). With the exception of the very edges of aquifer basins, most hydrologically induced surface displacement is in the vertical direction (Bawden *et al*. 2001; Hoffmann & Zebker 2003).

As multiple disciplines have developed and applied poroelastic theory, poroelastic parameters have been neither uniformly defined nor consistently represented by the same symbols in the literature (Kümpel 1991). For this study we chose to discuss the poroelastic material properties after the classic works of Riley (1969) and Poland (1984). The component of the aquifer system storage coefficient, S, that is attributable to elastic recovery of the aquifer system skeleton, S_{ke}, is

$$S_{ke} = \Delta b / \Delta h, \qquad (1)$$

where Δb is the change in the aquifer thickness, and Δh is the change in applied stress inferred from a change in head level (Riley 1969; Poland 1984). For this study, vertical displacement observations with InSAR represent the change in aquifer thickness, and the groundwater level time series are a proxy for change in head level. We refer to S_{ke} as the poroelastic ratio.

The component of average specific storage due to elastic deformation S_{Ske} (Riley 1969; Poland 1984), is

$$S_{Ske} = S_{ke} / b, \qquad (2)$$

where b is the effective thickness of the aquifer. We refer to S_{Ske} as the normalized poroelastic ratio.

Both S_{ke} and S_{Ske} are attributes that describe the elastic component of aquifer system deformation and represent recoverable compressibility that occurs within a certain range of pressure changes. However, S_{Ske} values are normalized by basin depth and can be directly compared across a study area or to other aquifer research sites. Both parameters represent the usable storage capacity of an aquifer system, the volume that can be released and recharged through elastic deformation of the aquifer system (Poland 1981). Accurate representation of these poroelastic parameters is essential to aquifer management and the maintaining of storage capacity (Sneed 2001).

Determination of both aquifer storage and compressibility is possible using measured changes in the thickness of the aquifer and the corresponding changes in water level (Riley 1969; Poland 1984). The change in aquifer thickness is classically measured

with observations from borehole extensometer arrays (e.g. Ireland 1986). Other methods for estimating poroelastic parameters of aquifer and aquitard material include aquifer pump tests, stress-strain analyses, laboratory tests on borehole samples, and model simulations (Sneed 2001). Using the satellite based InSAR data to measure the change in aquifer thickness, we can construct a more detailed, basin-wide assessment the aquifer system poroelastic properties. Where the stratigraphy is known, certain poroelastic responses can be expected and locations where observations deviate from expectations can be ideal sites for further investigation and assessment of the possibility of ongoing inelastic aquifer deformation. To assess the poroelasticity across the San Bernardino basin study site, we incorporate depth to groundwater sampling data with surface displacement observations from InSAR.

2. DATA

2.1. Well Data

Groundwater level data for the well sites used in this analysis were primarily acquired from the San Bernardino Valley Municipal Water District, and in part from the California Department of Water Resources: Water Data Library and the USGS National Water Information System: Web Interface. A small number of well sites used in this study have readily accessible generalized lithologic logs, available through the USGS California Water Science Center – San Bernardino Valley Optimal Basin Management. This information is used to infer an effective aquifer thickness, by scaling the geophysical basin depth model (Anderson *et al*. 2004) according to elevations of indurated bedrock-like material indicated by drillers. The groundwater level data is assumed to represent

the head level changes in the local saturated aquifer column. Sampling of water levels occurred irregularly during 1995 to 2000 at the 224 well sites amassed for this study, ranging from continuous monitoring through the entire study period to gaps of up to two years in sampling. From this initial set of well sites, 60 sites meet the criteria for use in our analysis. The systematic culling of well sites is discussed later in the Methodology section.

2.2. InSAR Data

Interferometric Synthetic Aperture Radar (InSAR) is an effective tool for monitoring surface deformation due to groundwater extraction (e.g. Galloway *et al*. 1998; Amelung *et al*. 1999; Bawden *et al*. 2001; Lu & Danskin 2001; Schmidt & Bürgmann 2003; Bell *et al*. 2008). Data used in processing differential interferograms for this study area are from the ERS1/2 satellite of the European Space Agency and processed with the ROI_PAC software package (Rosen *et al*. 2004). InSAR from the ERS1/2 satellite works best in areas with very little vegetative cover and in urban areas, and therefore is well suited to the semi-arid, developed San Bernardino basin. Differential interferograms can be constructed to span months, even years, depending upon the suitability of SAR pairs for interferometry and coherence of each scene. The interferometric phase is flattened to remove any gradient caused by orbital errors. In the flattening process, the horizontal displacement signal associated with plate boundary deformation is also effectively removed. Because the perpendicular baseline between the orbital passes is greater than zero, there is a topographic contribution to the phase difference (Bürgmann *et al*. 2000). This is removed using a 30 m digital elevation model from the SRTM shuttle mission.

The phase difference is then unwrapped for estimating range change in the satellite line-of-sight or look direction. InSAR does not determine the full 3-D displacement vector. Assuming the dominant mode of deformation during the study period for this aquifer basin was in the vertical direction (Bawden *et al*. 2001; Hoffmann & Zebker 2003), we calculate the vertical component of the surface displacement required to explain the line-of-sight observations.

We use several techniques to scrutinize over 100 differential interferograms of the study area between 1992 and 2000. The set of differential interferograms were initially culled through the visual identification of atmospheric patterns. Scenes contaminated by significant cloud or fog layers can cause a delay in wave travel time, thereby falsely increasing or decreasing the range change observed in an interferogram (Zebker *et al*. 1997). Through careful scrutiny, these scenes were eliminated from the analysis set, thereby minimizing the atmospheric source of noise from the data set. We stack the 24 best interferograms (processed from 17 independent SAR scenes) by summing the vertical displacement for a given pixel and dividing by the cumulative time spanned by all of the interferograms (Table 2.1). Stacking interferograms estimates an average rate of deformation for each pixel and will dampen the effect of any remaining atmospheric noise.

All differential interferograms used in the analysis are within mid-1995 through 2000 and have a perpendicular baseline of ≤150m, averaging ~80m. These short distances in satellite positioning from acquisition to acquisition maximize coherence and minimize topographic errors. We choose to not use the available SAR data from 1992

and 1993 due to a change in satellite mission in 1994, resulting in a significant break in the time series.

Table 2.1. Interferograms used for stacking and time series are from ERS, Track 399, Frame 2925: acquisition dates and perpendicular baselines for interferometric pairs

Scene 1	Scene 2	b-perp (m)
19950611	19951204	106
19950611	19960108	118
19950611	19990621	103
19950611	20001127	150
19950925	19970127	83
19951204	19960909	95
19951204	19971208	73
19951204	19970616	97
19960108	19960318	52
19960108	19980323	6
19960318	19970127	87
19960318	19980323	58
19960909	19990201	44
19970127	19980427	92
19970127	19990517	27
19970616	19971208	24
19970616	19990201	148
19971208	19990621	136
19980323	19990621	9
19980427	19990517	65
19980427	19991213	17
19990201	20000501	134
19990517	20001127	134
19990621	20001127	47

The patterns of time dependent surface displacement can be assessed with a time series construction. We produce a pixel-by-pixel time series of vertical displacement using an inversion method developed by Schmidt & Bürgmann (2003). The method solves for the incremental range change between SAR scene acquisitions by a linear

inversion, translating the set of interferograms into a range change time series. The same interferograms used in stacking were used in the time series construction (Table 2.1). Scenes used in multiple interferograms are down weighted in the time series inversion process, so that artifacts in repeated scenes do not dominate the time series of deformation. The result of the time series is a pixel-by-pixel deformation map sequence from 1995 through 2000, showing line-of-sight deformation accumulating from scene acquisition date to acquisition date. The final frame of the time series plots the cumulative deformation through the five-year period.

3. INSAR RESULTS

The spatial and temporal pattern of displacement observed with InSAR in the San Bernardino study area illustrates a dynamically deforming complex aquifer basin (Fig. 2.2). Since InSAR measures relative displacement, we have attempted to identify areas that appear to be vertically stable through time, essentially defining a reference frame for the observed relative displacement. One continuous GPS station located in the Crafton Hills (Fig. 2.2) was operative during the InSAR time series and showed no long-term trend of vertical displacement. The zero on our displacement scales is tied to the location of this GPS station, fixing the displacement scale.

Average vertical displacement, from 1995 through 2000, is estimated with a stacked differential interferogram (Fig. 2.2). Much of the study area exhibits a near zero average displacement rate. The Lytle basin and the Santa Ana River drainage show some of the highest average deformation rates, for this time period appearing to subside at a maximum rate of 4 mm/yr. In the years following the abundant aquifer recharge of 1998,

groundwater levels and surface elevation decreased in these locales, which is reflected in the high subsidence rates. The stacked differential interferogram (Fig. 2.2) also highlights sharp color contrasts that coincide with many mapped faults (Morton & Miller 2003; Anderson *et al*. 2004; Danskin *et al*. 2006). Groundwater barriers enclosing the Rialto-Colton basin appear to border a slightly uplifting region. The vertical displacement rates of a few millimeters per year seen in small areas of the stacked interferogram are contrasted by broader regions of several centimeters of displacement observed in some short-term single-pair interferograms (Fig. 2.3a). In general, differential interferograms for the San Bernardino study area spanning 2-9 months show a greater magnitude of relative displacement than those composed of scenes separated by a year or more. Seasonal trends in land surface elevation are illustrated in Fig. 2.3(a). Land surface rebound is observed in the western Bunker Hill basin as a result of decreased pumping after summer, while land surface subsidence is observed in the eastern basin resulting from the decline in groundwater level prior to the arrival of significant rain and aquifer recharge (Danskin *et al*. 2006).

A correlation of topography to InSAR measurements is observed in Fig. 2.3(b), particularly along the northern basin edge. The broad red swath across the study area may seem suggestive of regional subsidence, but when observed to follow the canyons into the mountains, we can assume the topographic correlation is due the presence of a fog layer blanketing the basin and filling the canyons at low elevations. In fact, when paired with other scenes, the August 1993 scene continually biases the interferograms this way. So although this image is adequate for finding groundwater barriers or regions of relatively high deformation, such as Lytle Creek or the Santa Ana River drainage (Fig.

2.2), it is the type of image excluded from the InSAR stacking and from the time series constructions discussed below.

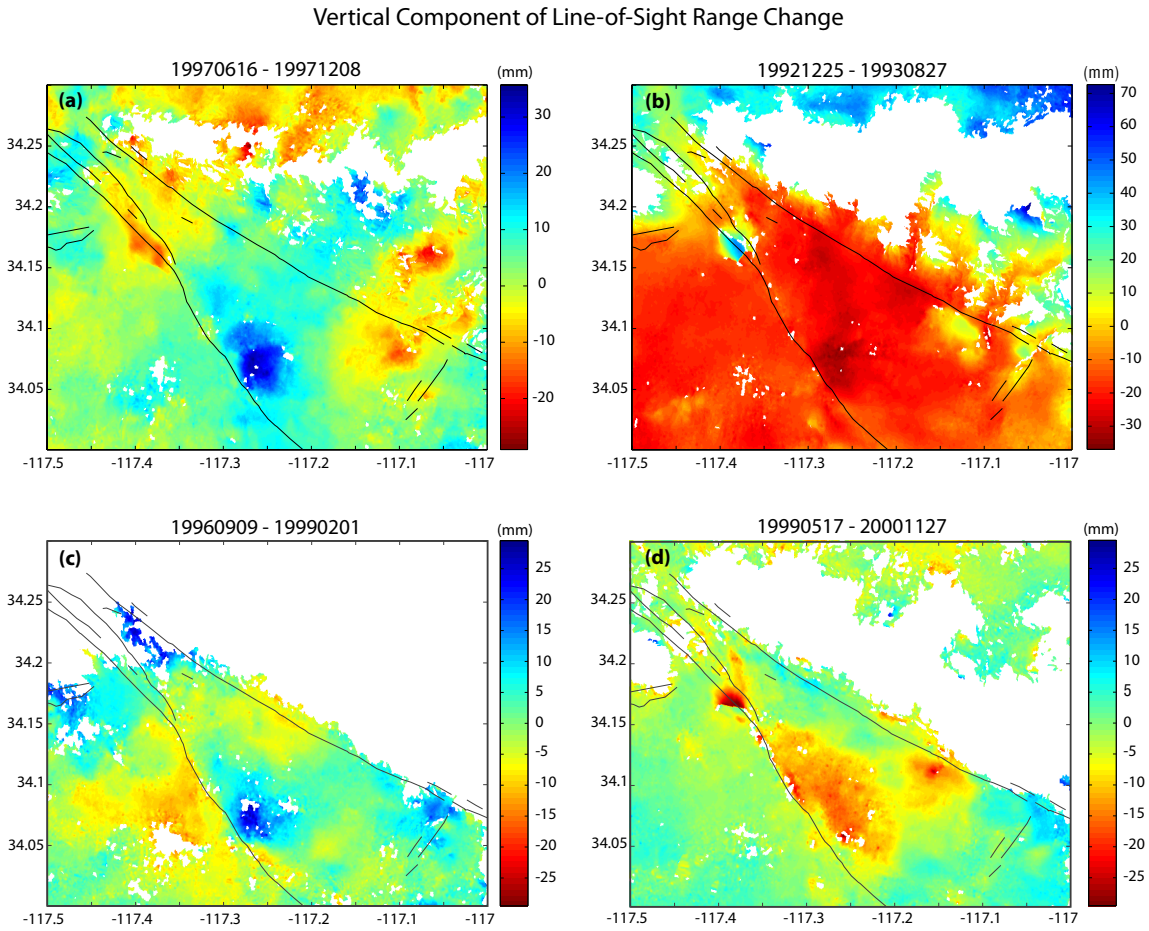

Figure 2.3. Images (a-d) are single-pair differential interferograms measuring relative vertical surface displacement (mm) over 4 distinct intervals. Black lines represent the known active regional faults.

A wide range of surface displacement in the Bunker Hill basin is illustrated in Figs 2.3(c) and 2.3(d). Each interferogram uses independent pairs of SAR scenes, thereby assuring the deformation pattern is not an artifact of a particular scene. These

two interferograms represent subsequent 1.5-year periods of deformation and show nearly opposite patterns of displacement with magnitudes on the order of several centimeters each. As the Santa Ana River acts as a confluence of the minor streams in the study area (Fig. 2.2), groundwater flow follows a similar pattern (Schaefer & Warner, 1975). The subsurface ponding of groundwater against the eastern side of the San Jacinto fault is evidenced in Fig. 2.3(c) with the uplift occurring in an elliptical shape, elongated parallel to the fault (Dutcher & Garrett 1963; Woolfenden & Kadhim 1997; Anderson *et al*. 2004; Danskin *et al*. 2006). The subsequent interferogram (Fig. 2.3d) shows the same region subsiding, a response to the lowering of groundwater levels.

The longer the time interval represented by the interferogram, the more likely the total range of deformation is to be underestimated. Both stacking and single-pair interferometry can manifest the same problematic issue in that the short-term deformation may not be adequately represented by average rates or the longer single-pair interferograms. Therefore, the optimal method of analysis for this locale is the time series (Schmidt & Bürgmann 2003), as it estimates time dependent deformation over the shortest possible time intervals, between SAR acquisitions.

The InSAR time series allows for the comparison of vertical surface displacement to groundwater levels at well locations in the study area (Fig. 2.4), demonstrating several points. Most importantly, this comparison emphasizes the concomitant relationship of the surface displacement to transient changes in groundwater level. Other observations are that groundwater levels in the study area vary up to tens-of-meters over a horizontal distance of just a few kilometers, and that groundwater levels may rise and fall significantly in a short period of time (Well 227801, Fig. 2.4). The direction and

magnitude of vertical surface displacement observed with InSAR also varies laterally within the basin.

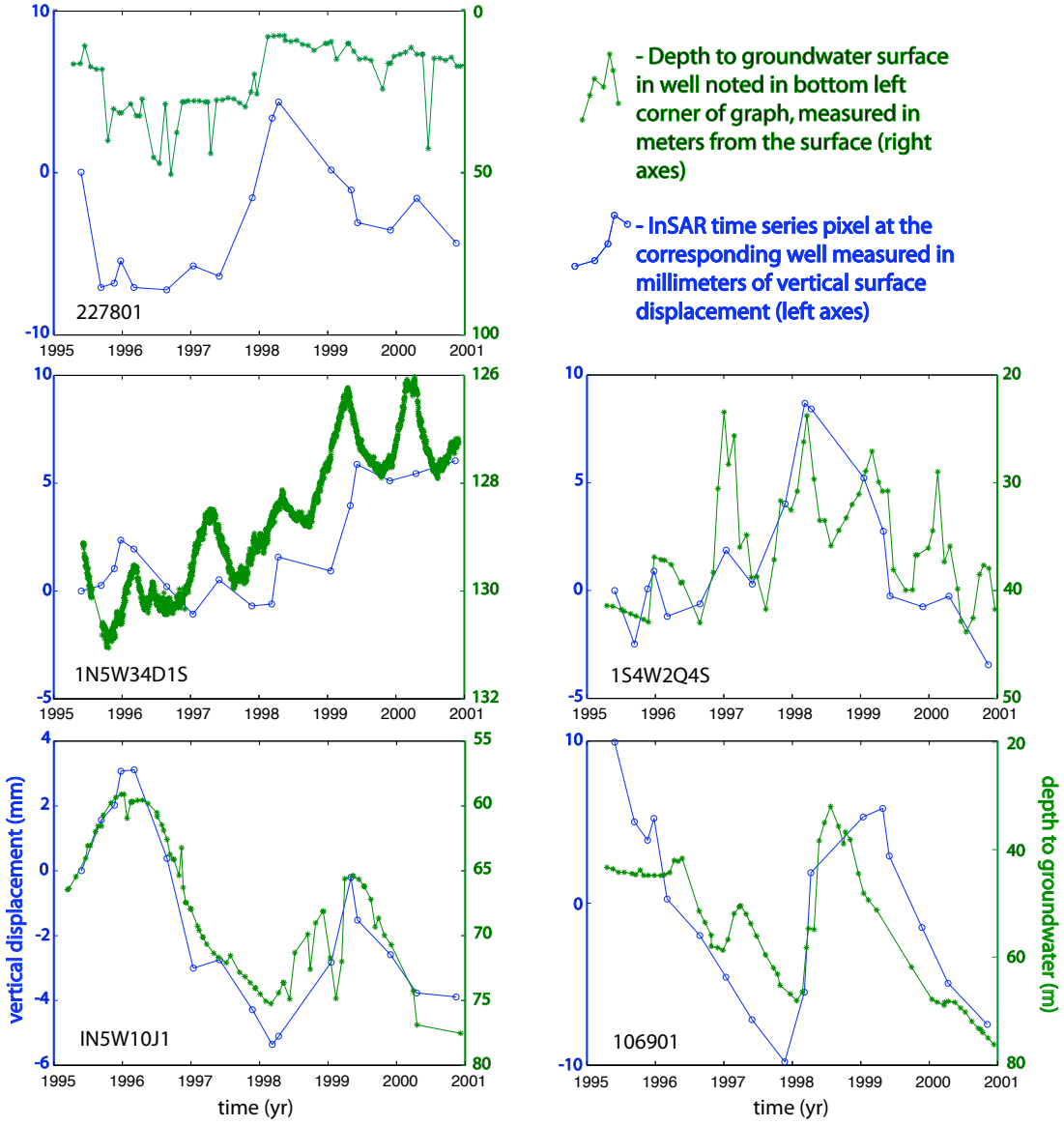

Figure 2.4. Graphs plot the InSAR time series of vertical displacement with groundwater level time series at 5 select well sites (see Fig. 2.2 for well locations). The blue curves correspond to the left axes and show the InSAR time series at the coherent pixel nearest each well site. The green curves correspond to the right axes and show coeval groundwater levels at each well site. Vertical surface displacement is measured in millimeters; groundwater levels are measured in meters from the surface.

Other notable features of the time series comparisons include varying intervals for groundwater level sampling both temporally and spatially. At times data sampling is sparse and irregular, like that of well site 106901. Daily groundwater sampling is clearly a useful data set when assessing the elastic deformation of an aquifer, as seen at well 1N5W34D1S, Fig. 2.4. Monthly sampling such as that of wells 1N5W10J1 and 1S4W2Q4S also adequately demonstrates the varying trends of groundwater level across the study area. This study uses the unique patterns of surface deformation and well level data to estimate the predicted surface displacement due to short term changes in groundwater levels, while attempting to identify regions deforming due to more subtle and long-term causes such as interseismic strain or sediment compaction.

4. HYDROGEOLOGIC INSAR INTEGRATION (HII) METHOD

Using InSAR to quantify vertical surface displacement and groundwater levels as a proxy for head level changes in the aquifer, we relate the data sets through the Hydrogeologic InSAR Integration (HII) method for the characterization of surface deformation in groundwater aquifer basins. The HII method is a least squares inversion, estimating two parameters: 1) the poroelastic ratio of the aquifer column and 2) the residual vertical displacement rate at every well site. We normalize each poroelastic ratio by depth of the saturated aquifer column at the well location, making these parameters comparable to each other and to those of other alluvial aquifer studies. The integration of surface deformation and aquifer head levels is not a new concept (e.g. Riley 1969; Poland 1984) and several recent studies have directly compared InSAR data with well data (e.g. Lu & Danskin 2001; Hoffmann *et al*. 2003; Bell *et al*. 2008). This study aims to

formalize the integration of InSAR and groundwater level time series. The residual vertical displacement rate is mapped, and we assess whether this five-year displacement rate is tectonic in nature, a result of fine-grained sediment compaction, and/or reflective of other processes.

We assume the InSAR and well data are related as follows,

$$I(\vec{x},t) = S_{ke}(\vec{x})w(\vec{x},t) + u(\vec{x})t + c \qquad (3)$$

where $\vec{x}$ is a position vector, $I(\vec{x},t)$ is the vertical displacement observed from the InSAR time series at a well location, $S_{ke}(\vec{x})$ is the poroelastic ratio related to the elastic compressibility of the sediments (Riley 1969), $w(\vec{x},t)$ is the well level as a function of time, $u(\vec{x})$ is the residual vertical displacement rate observed at the well location, and c is a fitting parameter that allows for the direct comparison of water level changes and the InSAR time series. This model assumes that a well level time series reflects effective pore pressure change through the aquifer column. We formulate this problem as a least squares inversion, $Gm=d$, and estimate the model parameters S_{ke} and u at each well site where,

$$m = \text{model parameters} = \left[S_{ke}(\vec{x}) \quad u(\vec{x}) \quad c\right]^{\mathrm{T}}$$

$$d = \text{data} = \left[I(\vec{x},t)\right]$$

$$G = \text{design matrix} = \left[w(\vec{x},t) \quad t \quad 1\right].$$

Since the InSAR data and well level data are sampled at different times, the well data are linearly interpolated at the times of the SAR scene acquisitions. An assumption of the HII method inversion is that an aquifer is deforming in an elastic regime. However, some deformation may be inelastic, in which case, normalized poroelastic ratios will trend high.

The set of 224 wells amassed for this project contains 156 sites in the San Bernardino study area that have a minimum sampling rate of 4 times per year between 1995 to 2000. Of the 156 well sites, we eliminate 45 wells with negative poroelastic ratios from the analysis set. This anti-correlation of changing groundwater levels and surface displacement is likely due to a misrepresentation of total pore pressure changes at depth from the well accessing only a portion of the aquifer column. In order for the HII method to be applicable, we require that well level and surface deformation be temporally correlated. To select those wells that are best suited for interpretation, we first visually inspect the time series at the remaining 111 well sites, looking for the graphical appearance of a good match of surface displacement to changing groundwater levels. Next, using the estimated model parameters and groundwater level data, we predict surface displacement for each well site, and then compare the predicted displacement time series to the displacement time series observed with InSAR, calculating a correlation coefficient between the two curves. Independent of the calculation of the correlation coefficient, we visually assess good matches between the predicted and observed time series. We find the average correlation coefficient of 0.67 to be a value consistent with the visual determination of a good match between the predicted and observed time series. We eliminate well sites below this value, leaving 60 wells that best represent the

relationship of surface displacement to local changes in groundwater levels, and are suitable for analysis using the HII method. Well sites where surface deformation and groundwater level changes do not appear temporally correlated consistently have correlation coefficients less than the average value.

5. HII METHOD RESULTS

5.1. Residual Vertical Displacement Rates

Residual vertical displacement rates estimated by the HII method show a distinct variation in net surface displacement from 1995 to 2000 (Fig. 2.5a) with some localities subsiding and some uplifting. These rates are hypothesized to be an indicator of inelastic hydraulic deformation, tectonic deformation, or a combination of both. Maximum subsidence rates are observed within the San Jacinto fault zone (up to 1.9 mm/yr), and at the single well site in the Yucaipa basin (2.0 mm/yr). Sites in the southeastern Chino basin and the Santa Ana River drainage also exhibit residual subsidence, on the order of 0.5 to 1.0 mm/yr. The most rapid uplift rates in the study area reach 1.5-2.0 mm/yr in three locations: 1) the Rialto-Colton basin, 2) the Santa Ana River drainage where Plunge Creek intersects the San Andreas fault, and 3) in the southwest of the former artesian area where the Santa Ana River intersects the San Jacinto fault. In the following sections we discuss various hypotheses and tests used to determine the source(s) of spatially varying patterns of residual vertical displacement.

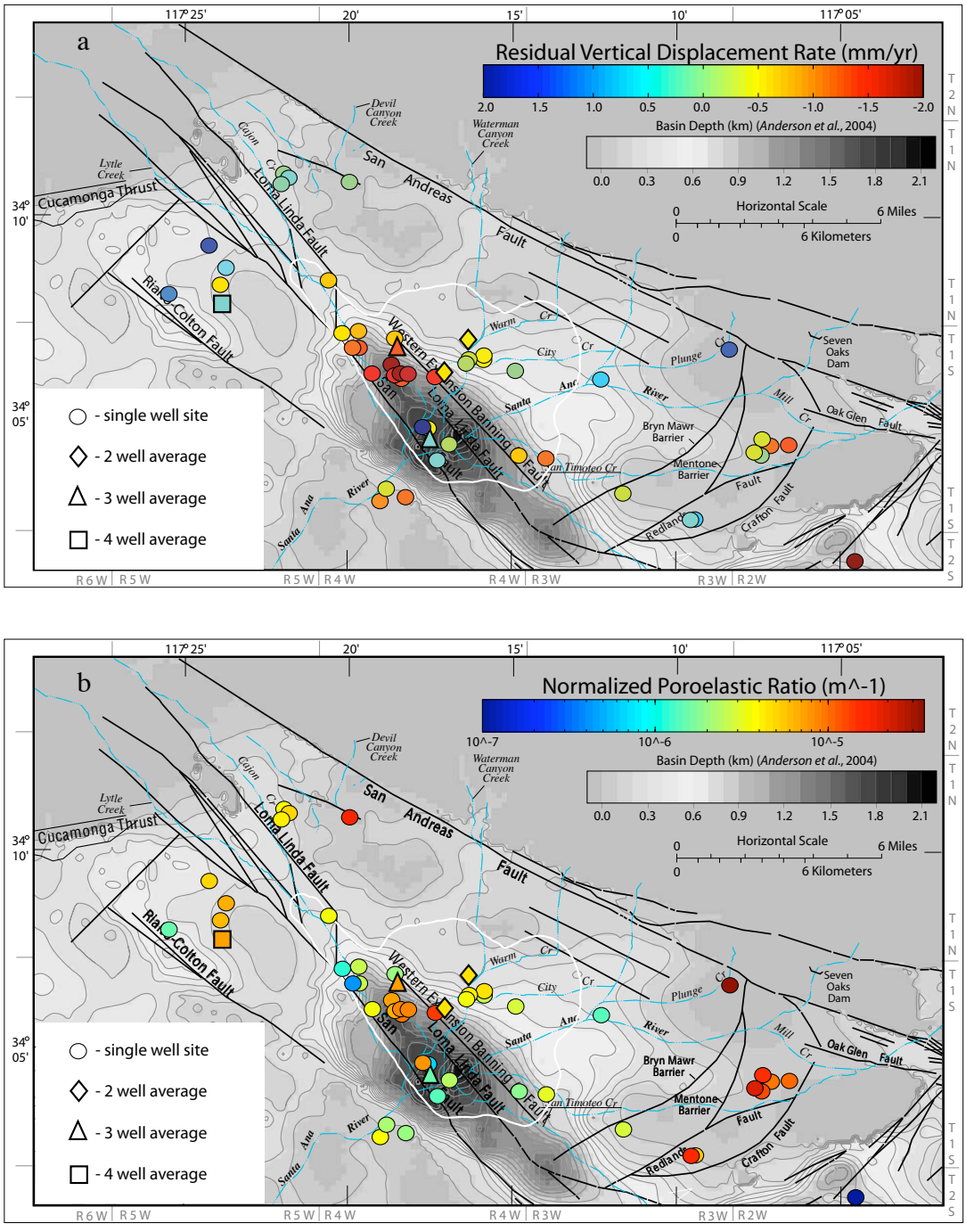

Figure 2.5. HII method results for each well site used in this analysis. (a) Residual vertical displacement rate estimates, and (b) Normalized poroelastic ratio estimates are plotted on the fault and groundwater barrier map modified from Danskin *et al*. (2006), along with surface water, and a geophysical basin depth model (Anderson *et al*. 2004). A solid white line denotes the boundary of the former artesian area. Circles denote a single well site; diamonds represent a 2 well average; triangles represent a 3 well average; squares represent a 4 well average.

5.2. Normalized Poroelastic Ratios

Using a geophysical basin depth model by Anderson *et al*. (2004), we normalize poroelastic ratios estimated with the HII method (Fig. 2.5b). The basin depth model, derived from gravity, seismic, and aeromagnetic data, provides an upper limit on the thickness of water-bearing units. According to Dutcher & Garrett (1963), geologic evidence from well logs suggests the maximum depth of significant water-bearing aquifer material for this region is ~430m. To estimate what percentage of the basin depth column would best represent the effective thickness of the aquifer column, we use the few drillers' logs on public record to scale the Anderson *et al*. (2004) basin depth model. We divide the elevation at which drillers indicate contact with basement-like indurated rock by the basin depth, determining effective aquifer thickness to approximate 40% of the basin depth model as estimated by Anderson *et al*. (2004). For the well near the northern basin margin where Plunge Creek intersects the San Andreas fault, the basin depth model estimates ~0 km thickness of alluvial material, for this site we use stratigraphic cross-sections from Dutcher & Garrett (1963) to estimate effective aquifer thickness.

Normalized poroelastic ratios are plotted in Fig. 2.5(b), with the highest estimates clustered in the Santa Ana River drainage ($\sim 10^{-5}$ m^{-1}), with some relatively high estimates also appearing in the northernmost basin margins and the San Jacinto fault zone. The lowest normalized poroelastic ratios are observed also within the San Jacinto fault zone and in the Yucaipa basin ($\sim 10^{-7}$ m^{-1}). There is a great deal of variability in these values across the San Jacinto fault zone within the former artesian area (4.2×10^{-7} m^{-1} to 1.4×10^{-5} m^{-1}).

5.3. Uncertainties for Estimated Model Parameters

Uncertainties in both displacement rate and poroelastic ratio (S_{ke}) estimates are calculated at each well site using a standard least squares formulation and errors of the InSAR time series (Schmidt & Bürgmann 2003). The average uncertainty of the residual vertical displacement rate for the analysis set is ±0.4 mm/yr. The average uncertainty of the poroelastic ratios for the analysis set is 3.0 x 10^{-4}. Given the uncertainties of the Anderson *et al*. (2004) basin depth model are ~100 m for depths less than 1 km and ~ 100-300 m for depths greater than 1 km, propagated model uncertainties in the normalized poroelastic ratios are quite large (average uncertainty for analysis set is 7.6 x 10^{-6} m^{-1}). This is also the case in previous studies that estimated similar parameters (Helm 1978; Sneed 2001). (A list of uncertainties at each well site is provided in the Appendix A Table A.1, Fig. A.1.)

6. DISCUSSION

6.1. Vertical Displacement Related to Interseismic Deformation

The transtensional structures of the San Bernardino basin are suggestive of a fractured and segmented arrangement of fault blocks and slivers particularly in the northwest study area. Approaching the juncture of the San Andreas and San Jacinto faults, the San Jacinto slip rate decreases from ~20 mm/yr to 6 mm/yr (Weldon & Sieh 1985; Feigl *et al*. 1993; Bennett *et al*. 2004; Meade & Hager 2005; van der Woerd *et al*. 2006, UCERF2 2008). Although it is postulated that there is not one single through-going structure (Weldon & Sieh 1985; Stephenson *et al*. *2002*; Anderson *et al*. 2004), the San Jacinto fault zone is considered the primary active structure bisecting the region with

geologic interpretations of ~25 km of through-going right lateral slip and up to 1 km of normal displacement over the last 1.5-2.0 Ma (Kendrick *et al*. 2002; Anderson *et al*. 2004). The Rialto-Colton fault to the west of the San Bernardino Valley (Fig. 2.2) is thought to be an abandoned trace of the San Jacinto fault and also exhibits vertical offset (Woolfenden & Kadhim 1997). We therefore must assess tectonic strain as a potential source of residual vertical displacement estimated with the HII method (Fig. 2.5a).

In the majority of geodetic studies, the vertical component of displacement is often ignored because of large measurement error in the GPS data and the potential for bias from non-tectonic signals (Bawden *et al*. 2001). The use of only the horizontal components is a generally accepted practice given that the San Andreas fault system is a transpressive plate boundary dominated by strike-slip motion. However, using InSAR gives us an opportunity to incorporate the vertical component of strain. Furthermore, vertical deformation is expected during the interseismic period at fault bends, fault junctions, and locations where the interseismic slip rate changes (e.g. Crowell 1974; Bilham & King 1989; McClay & Bonora 2001). Evidence for vertical structural complexity within the San Bernardino study area includes exposures of exhumed basement rock in the valley floor and models of basin depth from seismic and other geophysical data (Stephenson *et al*. 2002; Anderson *et al*. 2004; Langenheim *et al*. 2005). The San Bernardino Mountains also have a complex vertical deformation history with distinct patterns of exhumation. Blythe *et al*. (2002) estimate an exhumation rate for the Yucaipa Ridge Block in the mountains northeast of the Yucaipa basin of 1.6 mm/yr, ca. 1.5 Ma to present, the highest exhumation rate in southern California.

As there were no earthquakes greater than M4.5 in the study area during 1995 to 2000, any tectonic strain would necessarily represent interseismic deformation. Using deformation and stress change software Coulomb 3.0 (Lin & Stein 2004; Toda *et al*. 2005), we model the vertical interseismic deformation related to right-lateral slip at depth on the San Andreas, San Jacinto, and other small faults. The sensitivity of vertical surface displacement related to variations in fault geometry and slip rate was tested using elastic models based on the California Reference Geologic Fault Database (RefGF) established for the Working Group on Earthquake Probabilities (WGCEP). Parameters used to define an interseismic fault map at depth include fault trace, dip and rake. The fault parameter values were determined by expert consensus inferred from paleoseismic trenches and other site-specific studies (UCERF2 2008). A Poisson's Ratio of 0.25 and a shear modulus 32 GPa were prescribed for all models. For modeling interseismic strain at the basin surface, slip rates were assigned to the deep fault planes, and the seismogenic zone was kept locked. We focus only on the vertical component from the model because the horizontal deformation produces a near linear gradient across the San Bernardino basin, a smoother deformation field than the vertical. Projected onto the InSAR line-of-sight vector, this horizontal surface displacement prediction is not expected to bias the results of the HII method or impose significantly on the measured range change.

Using a 3D fault map based on the RefGF database we estimate the vertical surface displacement related to deep fault slip (Fig. 2.6a). This model of interseismic strain illustrates slip distribution across the basin study area with a maximum subsidence rate of ~0.3 mm/yr. There are obvious discrepancies between the HII method results of Fig. 2.5(a) and the pattern of displacement from the elastic model shown in Fig. 2.6(a).

Residual subsidence observed with the HII method is primarily observed in a narrow region within the San Jacinto fault zone, and is an order of magnitude larger than the RefGF-based interseismic elastic model. Other recent geophysical studies (e.g. Anderson *et al*. 2004) also indicate a narrow pull-apart basin, restricted to strands of the San Jacinto fault zone, indicating very little to no slip transfer across the broader basin. We therefore run a systematic survey of interseismic fault slip rate combinations, while maintaining total slip across the transform boundary. These alternate slip models all produce broadly varying patterns that more poorly fit the HII method results.

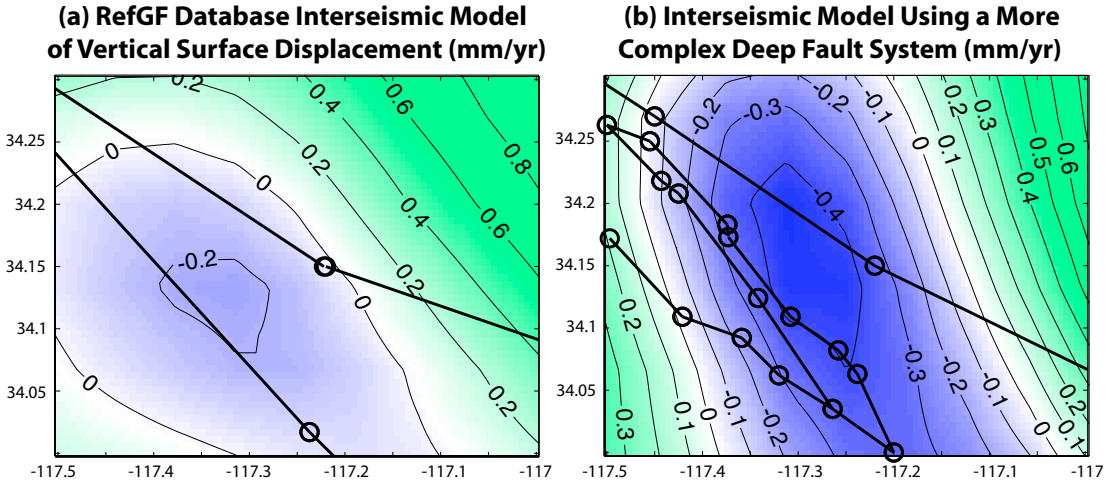

Figure 2.6. Interseismic vertical deformation predicted by elastic models related to right-lateral slip at depth on the San Andreas, San Jacinto, and other small faults. Black lines are surface projections of deep faults, and circles dividing fault segments are locations of fault slip rate changes. Models were constructed to test the sensitivity of surface displacement to deep fault slip, by assigning slip rates to deep fault planes, and keeping the seismogenic zone locked. We use deformation and stress change software Coulomb 3.0 (Lin & Stein 2004; Toda *et al*. 2005) and input fault parameters for the southern San Andreas fault system, based on the RefGF database (UCERF2 2008). (a) Contours of interseismic uplift (mm) predicted for the portion of the basic RefGF model representing the San Bernardino basin. (b) An example of a more complex and detailed interpretation of the local fault system. Adding complexity to the deep fault system alters the pattern of modeled interseismic vertical surface displacement, but continues to produce a broad, basin-wide pattern of vertical displacement, unlike the pattern of displacement estimated with the HII method, and an order of magnitude less that the maximum rates estimated.

A comprehensive literature review of the San Andreas and San Jacinto fault juncture reveals a wide variety of regional fault interpretations. Many studies have utilized elastic modeling, though not all during the interseismic period, to assess regional-scale plate boundary deformation of the San Bernardino basin (e.g. Bennett et al. 1996; Meade & Hager 2005), deep fault configurations through the restraining bends of the San Gorgonio Pass (Dair & Cooke 2009), and along the San Jacinto fault (Kendrick *et al*. 2002) in the southern study area. To thoroughly test deep-seated interseismic deformation as a potential cause for the observed deformation patterns, we increased complexity in the deep fault zone, adding inferred regional faults that are not included in the RefGF database, and adding normal slip components along faults know to have vertical geologic offsets across them (Fig. 2.6b). For example, the Banning fault is continually discussed in the literature. Its illusive fault trace, discontinuous surface exposure, and distinctly active deep-seated seismicity have invited many varying interpretations, particularly along the westernmost extension where it is postulated to intersect the San Jacinto fault (e.g. Stephenson *et al*. 2002; Anderson *et al*. 2004; Langenheim *et al*. 2005).

We are unable to reproduce through modeling of interseismic deformation the focus or magnitude of the observed pattern of uplift and subsidence. Increasing the complexity of the deep fault system, as in Fig. 2.6(b), does not create a better match to residual vertical trends of the HII method. It is possible that the modeling software does not adequately represent the material properties of the uppermost crust, such as up to 2 km of alluvial fill in the deepest basin. Discrepancies may also be due to the oversimplification of the material properties and fault structure of the uppercrust. The

elastic modeling results do support the consensus UCERF2 (2008) model of southward slip transfer from the San Andreas to the San Jacinto with slip rate changes along faults within the study area, ruling out models where all slip is focused on only one fault or the other.

Elastic models of interseismic strain imply that processes other than interseismic deformation are the cause of up to 1.9 mm/yr of focused subsidence within the San Jacinto fault zone. Elastic modeling can account for up to 0.5 mm/yr of regional subsidence, but cannot account for the near 4mm/yr range of vertical displacement rates observed in the inversion results within the study area.

6.2. Parameter Correlation

Given the variation in both residual vertical displacement and normalized poroelastic ratios, particularly within the San Jacinto fault zone, we test for correlations between the model parameter estimates and site-specific characteristics; such as average depth to groundwater, magnitude of groundwater level changes during the study period, and basin depth (Appendix A). Correlation between the estimated model parameters themselves is not observed. We do, however, observe a correlation between increasing basin depth (alluvial thickness) and increasing subsidence rates within the former artesian area (Fig. 2.7). The increasing alluvial thicknesses away from the range fronts contains greater content of fine grained deposits making well sites in these areas more susceptible to delayed compaction. This correlation stands with the exception of the uplifting sites (blue oval in Fig. 2.7) in the southwest artesian basin. We suspect these uplifting

locations do not follow the trend of increasing subsidence with increasing basin depth due to upwelling groundwater flow.

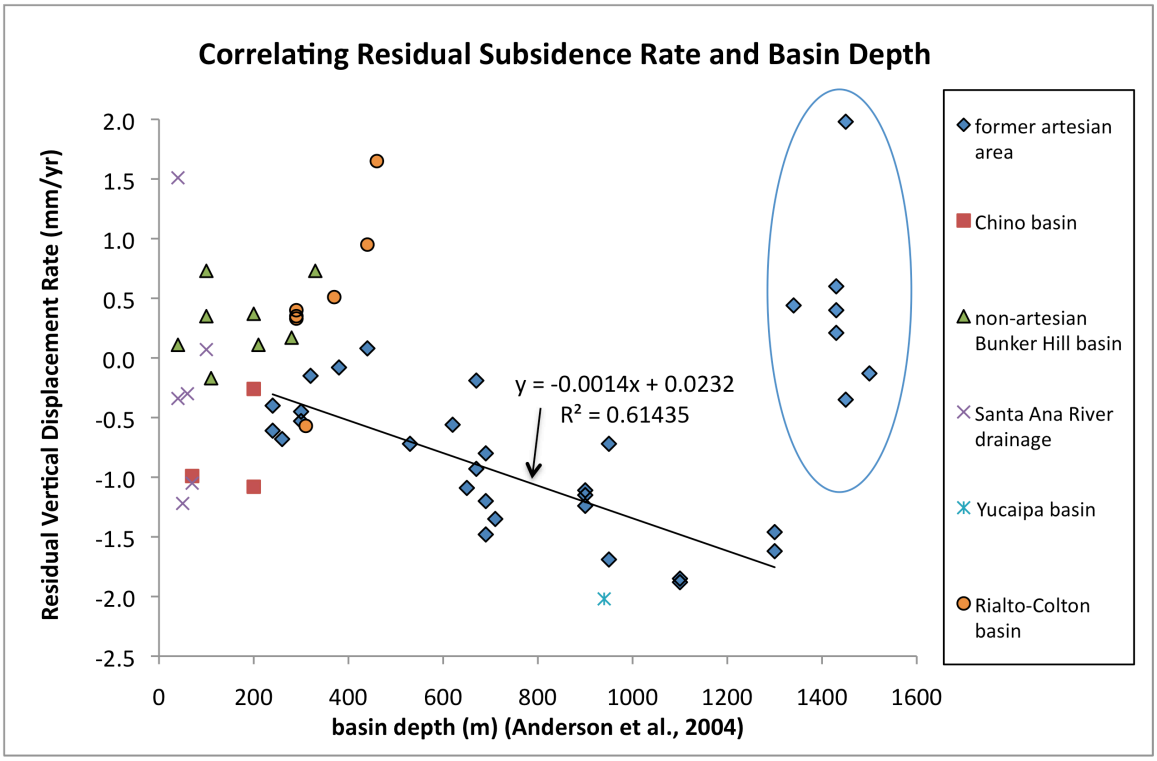

Figure 2.7. The correlation plot between residual subsidence rates and basin depth illustrates that in the former artesian area, as sediment thickness and fine-grained concentrations increase, residual subsidence becomes more pronounced. The oval in the upper right corner of the plot encompasses the uplifting and near zero displacement locations overlying the deepest basin, where the Santa Ana River crosses the San Jacinto fault, that do not follow the aforementioned correlation. This is likely due to vertical hydraulic gradients and upwelling.

6.3. Vertical Displacement Related to Hydraulic Aquifer Deformation

A long history of groundwater pumping in the San Bernardino basin suggests that compaction of near-surface, fine-grained layers may be a factor in the residual vertical subsidence rates observed with the HII method, particularly in the former artesian area (Fig. 2.5a). The deepest alluvial basin associated with the San Jacinto fault zone, and

formed by long-term geologic deformation of the basement, contains clay-rich aquitards, thick and extensive enough to retard vertical groundwater flow. An aquitard layer estimated to be 30 m thick is exposed at the surface in this vicinity; clayey strata are also observed at deeper intervals in this locale (Dutcher & Garrett, 1963; Danskin & Freckleton, 1992). Danskin *et al*. (2006) state that there has been some inelastic release of water from storage; however, this quantity is unknown. The Yucaipa aquifer is also known to have significant clay-rich layers, and the HII method estimates the highest subsidence rate and the lowest normalized poroelastic ratios for the study area at this location (Fig. 2.5). However, with only one site meeting criteria for analysis, we forgo conclusive statements regarding deformation and poroelasticity for the Yucaipa basin.

Inelastic aquifer deformation and storage loss tend to occur in low permeability aquitard layers as a result of continued overdraft to an aquifer system, where groundwater pumping is consistently greater than the groundwater recharge (Poland 1984; Galloway *et al*. 1999). Compaction of aquifer material, referring to both the process and result, reflects the rearrangement of the pore structure under stresses greater than the maximum preconsolidation stress. Production wells typically access sand and gravel layers, as these coarser deposits have higher transmissivities. Draining water from coarse-grained aquifer layers decreases pore pressure. Adjacent clay-rich aquitards drain more slowly and a pressure gradient can develop between the coarse and fine-grained deposits. The slower draining aquitards may continue to dewater and compact, even after the recovery of groundwater levels. Concomitant compaction can require decades or centuries to complete (Terzaghi, 1926; Helm, 1978; Galloway *et al*. 1999).

For equal changes in water level, inelastic aquifer deformation is 10-100 times greater than elastic deformation (Poland 1984), indicating that once the threshold from an elastic to an inelastic stress regime has been crossed, rapid and extreme compaction is likely to occur. Thin clay-rich layers will dewater and compact more quickly than thick layers of the same composition, as the path to escaping higher pressure is short in a thin layer. Thicker clay-rich layers do not allow fluids to escape as readily, and varying lateral thickness of a dewatering clay-rich layer can result in differential land surface displacement (Riley 1969; Carver 1971).

In an elastic stress regime, normalized poroelastic ratios numbers estimated with the HII method should be relatively higher for coarse-grained deposits than for finer grained deposits, signifying greater elasticity to the aquifer skeleton in coarse-grained material. If the San Bernardino basin were deforming solely within an elastic regime, normalized poroelastic ratios should be relatively high in the coarse-grained shallower basin margins compared to the clay and silt-rich strata of the deeper central basin, yet significant variation is observed, particularly in the former artesian basin (Fig. 2.5b). This study proposes that the poroelastic parameters estimated with the HII method can identify sites that may be undergoing inelastic compaction, and we develop this concept below. Miller & Singer (1971) identified the location of maximum subsidence (30 cm) and maximum groundwater level decline (30 m) for the Bunker Hill basin near the southern edge of the former artesian boundary in the late 1960's. At the time of their study, lag effects related to dewatering of aquitards were considered negligible, small enough to be considered insignificant, and measurable only with the installation of an

extensometer. Currently, such measurements need not be considered negligible and may be estimated using the spatially continuous, millimeter-scale sensitivity of InSAR.

Delayed compaction of clay-rich strata due to historic episodes of extreme groundwater depletion is a likely cause of the observed 0.5-1.9 mm/yr of residual subsidence in the western Bunker Hill basin during 1995 to 2000. 1950-1970 was a period of extreme groundwater extraction (Fig. 2.8), with levels declining up to 30 m in the central basin and up to 60 m near the base of the San Bernardino Mountains. A drought in the late 1980's and early 1990's caused another episode of groundwater depletion although not as severe as the late 1960's (Fig. 2.8). These periods of groundwater depletion may have triggered dewatering of clay-rich aquitards in the western Bunker Hill basin, for which we are observing the tail end of compaction or consolidation processes.

Previous work regarding compaction rates of clay-rich aquifer layers in other locations is consistent with the above interpretation of subsidence rate estimates. A classic site for the study of aquifer compaction using extensometers is near Pixley, California. Based on laboratory test data from Pixley sample cores, 60% of permanent compaction will occur within a few weeks of dewatering. However, roughly 40 years is required for 90% of ultimate compaction to occur (Lofgren 1968; Helm 1978; Poland 1984). Other studies of permanent compaction include Bell *et al*. (2008) in which the authors observe residual compaction related to aquitard drainage in Las Vegas, Nevada. Despite over a decade of recovering groundwater levels, the authors predict continued subsidence for another 5 to 10 years, although at decelerating velocities. Recent studies by Teatini *et al*. (2005, 2006) in the Emilia-Romagna coastland aquifer highlight land

settlement due to the delayed compaction of clayey aquitards following historic levels of groundwater pumping and lowering of groundwater levels. Like the San Bernardino study, the Italian aquifer is of similar size and depth, and both localities bear a paucity of historical groundwater data. Although wells are not scarce, wells are irregularly sampled and often it is unclear which hydrogeologic unit the well is accessing. Using InSAR and other modern geophysical data to monitor surface elevation changes, Teatini *et al*. (2006) estimate on-going anthropogenic rates of subsidence of 0.1 to 1.7 mm/yr, comparable to subsidence rates observed for the San Bernardino study area using the HII method (0.5-1.9 mm/yr). This delayed consolidation of aquitards is observed decades after general head level recovery in the Italian aquifer.

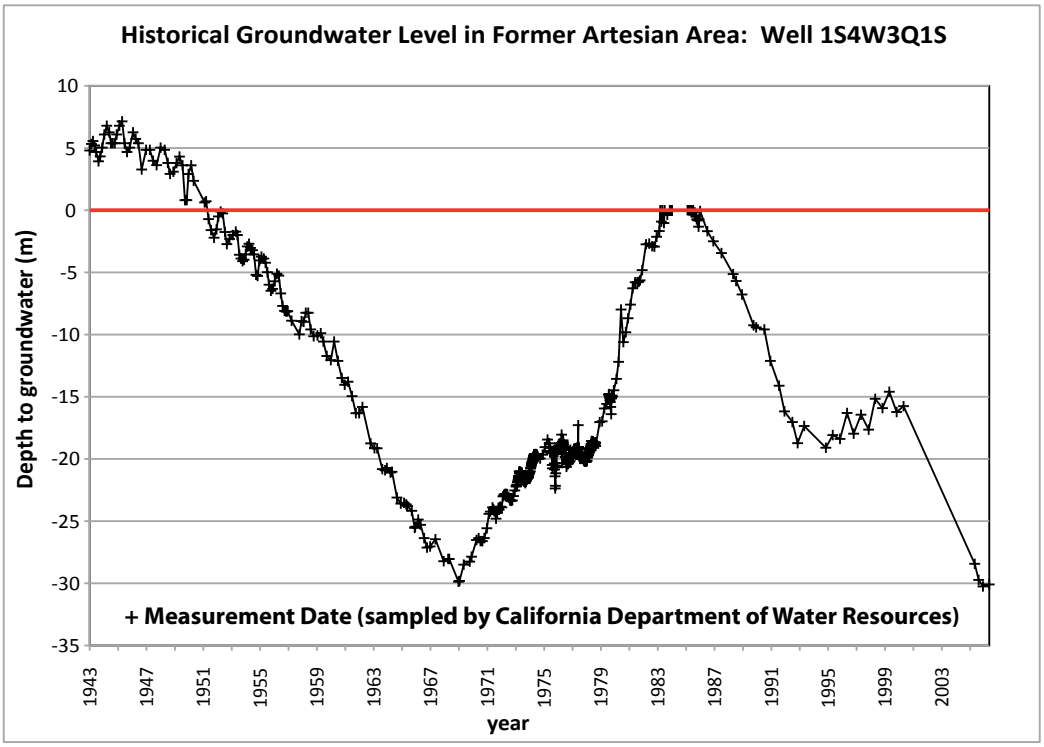

Figure 2.8. Historical groundwater levels at a well site in the former artesian area of the Bunker Hill basin. Note groundwater levels above the surface (red line) prior to 1950, and recent levels comparable to those of historic low levels in the late 1960's.

Another potential cause of inelastic compaction and land subsidence in the western Bunker Hill basin is the installation of new large production wells. As of 1998, many new large production wells are perforated below ~60-90 m, deeper than the majority of previous production wells, and Danskin *et al*. (2006) point out that the additional deeper extractions may also induce land subsidence and the compaction of deeper aquitards. The subsiding well sites at the juncture of the Loma Linda fault and the San Jacinto fault (Fig. 2.5a) are in close proximity to the location predicted by Danskin *et al*. (2006) to be at risk of subsidence if pumpage were to be increased without sufficient recharge. We are unable to definitively state at which depth(s) in the aquifer column compaction is occurring. Groundwater levels through 2007, past the span of the InSAR time series used in analysis, are plotted in Fig. 2.8. It is apparent from well measurements in 2005 and 206 that groundwater levels recently reached the historic low levels of the late 1960's. Thus we predict that permanent compaction of fine grained layers continues, most likely at more rapid rates than estimated by our analysis which ends in 2000.

In the southwestern former artesian area, where both the Santa Ana River and general flow of groundwater intersect the San Jacinto fault, residual uplift is estimated by the HII method (Fig. 2.5a). This region of the former marshland may experience significant groundwater upwelling, and is actively managed to maintain stable groundwater levels below the surface (e.g. Danskin *et al*. 2006). Upward, vertical hydraulic gradients in this area have been previously observed (Danskin & Freckleton 1992). We suspect the residual uplift estimated for this area may be related to transient vertical hydraulic gradients. As well, the winter of 1997/1998 was an El Nino year with

greater than average storm run-off and natural groundwater recharge. This can be seen as a rise in groundwater levels for wells in the semi-confined former artesian area (wells 227801, and 1S4W2Q4S; Figs 2.2, 2.4) and may have contributed to localized surface uplift during 1995 to 2000.

The Santa Ana River drainage (Fig. 2.2) has a relatively wide range of residual vertical displacement rate estimates, from 1.2 mm/yr of subsidence to 1.5 mm/yr of uplift (Fig. 2.5a), yet normalized poroelastic ratios for this area are some of the most consistent (Fig. 2.5b). As this part of the aquifer basin contains several artificial recharge basins (Fig. 2.2), the filling, storage, and percolation related to aquifer resource management may be contributing to the variation in residual vertical displacement rates. Definitively testing this relationship between artificial recharge and the observed variation in surface displacement is beyond the scope of this study. In contrast to the range of displacement rate estimates, poroelastic estimates for the Santa Ana River drainage (Fig. 2.5b) are similar in magnitude, some of the highest in the study area, and consistent with the coarse grained stratigraphy of these range front deposits. The deposits of the shallow basin margins readily transmit percolating groundwater, making adequate sites for groundwater recharge (CDWR Bulletin 118 2004). Surface elevation changes would be correlated with the flooding of recharge spreading grounds and the downward percolation of imported groundwater and storm runoff (Lu & Danskin 2001). It is this rapid transmission of groundwater and the coarseness of the local deposits that are represented by the higher normalized poroelastic ratios.

Alternately, poroelastic results within the former artesian boundaries vary widely. As the coarse and poorly sorted sediments nearest the mountains fine and thicken towards

the San Jacinto fault zone (Danskin & Freckleton 1992), the stratigraphy becomes more layered and vertically complex with silt and clay-rich layers that pinch in and out of the sequence, and deeply incised coarse-grained stream deposits that create some level of vertical connectivity in the aquifer column (Dutcher & Garrett 1963; Danskin *et al*. 2006). As skeletal compressibility of fine-grained aquifer materials can be several orders of magnitude less than that of coarser aquifer material (Sneed 2001), we expect less elastic deformation for equal changes in water level in fine-grained material than in coarse. The observation of scattered relatively high poroelastic values in the former artesian area suggests larger surface displacements with changes in groundwater level than expected to occur in an elastic regime. We infer that the local aquifer column may be actively compacting under effective pore pressure stress surpassing preconsolidation stress conditions. Such sites exhibiting residual subsidence not associated with short-term changes in groundwater level, and relatively high normalized poroelastic ratios, could be targeted for further investigation, perhaps by installing compaction sensitive extensometers.

We currently find the HII method to be a viable way to remotely assess aquifer storage parameters and elasticity. We suggest normalized poroelastic ratios can be used not only to remotely assess the elasticity of the aquifer, but also to identify locations that may be experiencing inelastic and/or delayed compaction of fine-grained material. Typically assessment of inelastic deformation is calculated using at least a decade of stress and strain data (Riley 1969; Poland 1984). The HII method can be applied over a period of no less than 5 years, significantly decreasing both ground-based field data collection and length of required study period from traditional hydrogeologic methods.

The installation of extensometers into well sites targeted as experiencing on-going compaction may definitively test the suggested use of the normalized poroelastic ratios estimated with the HII method.

7. CONCLUSIONS

With an extensive set of interferometric data, we observe time-dependent changes in the surface elevation of the San Bernardino aquifer basin from 1995 to 2000. Combined with groundwater level data for the study area, we remotely estimate poroelastic material properties and observe a 4 mm/yr range in residual vertical surface displacement rates that is not related to coeval changes in groundwater levels. The western Bunker Hill basin exhibits residual subsidence rates approaching 2 mm/yr, that appears to represent sediment compaction, values consistent with anthropogenic compaction rates estimated in other locations. Earlier studies in permanent land subsidence were limited by the ground-based approach of extensometer arrays and leveling lines. With InSAR we can observe spatial heterogeneity in the aquifer response to pumping and recharge. The HII method allows for the separation of superimposed processes that operate in dynamically deforming locations like the San Bernardino basin, and this formalization of InSAR and groundwater level integration provides opportunities for application in other aquifer basins.

The application of the HII method is greatly assisted by continuous monitoring of groundwater levels, frequent SAR scene acquisitions, and minimal atmospheric interference. Lithologic descriptions from drillers' logs provide insight into what layer(s) a well is accessing in the aquifer, and what portion of the aquifer column is expected to

respond to groundwater level changes. Geophysical data can also provide information about vertical flow in the aquifer column as well as material characterization. Ideally wells used for this type of analysis in the future will have consistent standards of monitoring, recording, and retrieval for hydrogeologic data. Future work for the San Bernardino study area should also include the expansion of the InSAR time series with the processing of SAR data after 2000.

Previous work in the San Bernardino basin documents permanent land subsidence and infers storage loss. This study identifies specific locations within the basin where recent and possibly on-going compaction is likely occurring, and estimates compaction rates of 0.5-1.9 mm/yr where clay-rich layers formerly subjected to artesian conditions continue to dewater. We discount interseismic strain contributing to the localized patterns of vertical displacement observed with the HII method, and instead interpret residual vertical displacement rates to be related to long-term hydraulic conditions in the aquifer.

CHAPTER III

HYDROGEOLOGIC BASIN STRUCTURE OF THE WESTERN COACHELLA VALLEY, SOUTHERN CALIFORNIA

This work will be submitted for publication post-graduation following further committee review. I completed all data processing, research, analysis, and elastic modeling for this study. My advisor David Schmidt has aided in review and editing, as have Ray Weldon and Rebecca Dorsey.

1. INTRODUCTION

1.1. Project Summary

InSAR observations between 2006-2009 reveal steep gradients in vertical surface displacement in the western Upper Coachella Valley. I map the steep gradients by stacking 48 differential interferograms, and analyze their locations using geologic maps, surface hydrology, topography, and geophysical data. Water well drillers' logs assist in the interpretation of these features through a generalized facies analysis of the upper ~300m of the western basin aquifer based on grain size and sorting of recorded sediment with depth. The steep gradients in vertical displacement are bound by very linear lineaments near the western basin margin, suggestive of intense, localized groundwater pumping in areas of the aquifer bounded by low permeability subsurface structures, such as buried faults or abrupt changes in lithology at depth. Unfortunately, production wells in the Coachella Valley were not identified by local water management agencies, and I cannot definitively rule out or support that concentrated pumping of the groundwater in

these areas are a direct cause of localized rapid subsidence. These subsiding features may represent isolated portions of the aquifer, partitioned by a combination of offset transmissive lithologies and the presence of clay-rich layers and lenses retarding and limiting the subsurface horizontal flow of groundwater recharge. The presence of an inactive fault at the base of the Santa Rosa Mountains has long been suspected, however, no active fault trace is visible at the basin surface. I synthesize the broad variety of observations and model surface displacement to suggest plausible hydrogeologic structures and stratigraphic evolution.

1.2. Geologic and Hydrogeologic Background

The Coachella Valley is a tectonic basin embedded in the southern San Andreas fault system (Fig. 3.1a), and is the northernmost extension of the Salton Trough. The Salton Trough includes the Imperial and Mexicali Valleys to the south separated from the northern basin by the Colorado River delta. The Upper Coachella Valley is bound to the north and southwest by some of the steepest slopes in the United States and terminates to the northwest at the San Gorgonio Pass restraining bend in which the right lateral San Andreas fault steps 15km to the left over in a complex zone where faulting has migrated in time and space over the last 5Ma (e.g. Matti & Morton 1993; Seeber & Armbruster 1995; Yule & Sieh 2003).

The Coachella Valley is a topographically higher part of the basin that contains evidence of active Holocene strike-slip faulting and transpressional deformation (e.g. Allen 1957; Keller *et al*. 1982; Matti *et al*. 1992; Rymer 2000; Philibosian *et al*. 2011). The thick Cenozoic sedimentary section of the Salton Trough is offset by both exposed

and buried Quaternary faults (e.g. Fuis & Mooney 1990; Matti *et al*. 1992). The most permeable basin-fill materials of the Salton Trough are Pliocene and Holocene age alluvial fan, or fluvial deposits (Planert & Williams 1995). Intermittent strike-slip faulting within the alluvial basin has altered the continuity of original depositional environments, resulting in the lateral displacement of alluvial units (e.g. Biehler *et al*. 1964; Matti *et al*. 1992; Van der Woerd *et al*. 2006).

Deep canyons and spurs of basement rock jutting into the alluvial basin characterize the irregular base of the San Jacinto and Santa Rosa mountain ranges at the western basin margin (Fig. 3.1b) Lacking the wineglass canyons, narrow canyon mouths, and linear range fronts of fault-controlled basin boundaries, the western basin margin does not appear tectonically active and erosion has become the dominant process. The inversion of isostatic residual gravity data for the Upper Coachella Valley (Langenheim *et al*. 2005) reveals a basement rock/sediment interface that is a complex zone of localized fault blocks, and abrupt lithologic changes. Earlier gravity surveys, seismic refraction data, and magnetic measurements (e.g. Biehler *et al*. 1964; Biehler *et al*. 1992; Ponce & Langenheim 1992) are in agreement with this interpretation of the basement

---

Figure 3.1. (next page) The Upper Coachella Valley hydrologic basin (blue line) in context of the Southern San Andreas fault system (3.1a), from the San Gorgonio Pass (SGP) to the Salton Sea, plotted on SRTM surface elevation. Fault map modified from Bennett *et al*. (2004). Boundary for Figure 1b is outlined in red. The satellite image of the Upper Coachella Valley (3.1b) is overlain by surface hydrology and the hydrologic basin boundary, the contact between basin alluvium and crystalline non-water bearing rock. Other hydrologic features include the Whitewater Recharge Facility, and the modeled Area of Benefit (CVWD 2005), as well as the broad modern wash of the Whitewater River in the northwest study area. Fault abbreviations are: MSAF, Mojave segment San Andreas fault; SBSAF, San Bernardino segment San Andreas fault; CVSAF, Coachella Valley segment San Andreas fault); BF (Banning fault); SJF (San Jacinto fault); EF, (Elsinore fault). Lines of cross-section correspond to Figures 3.17-3.21.

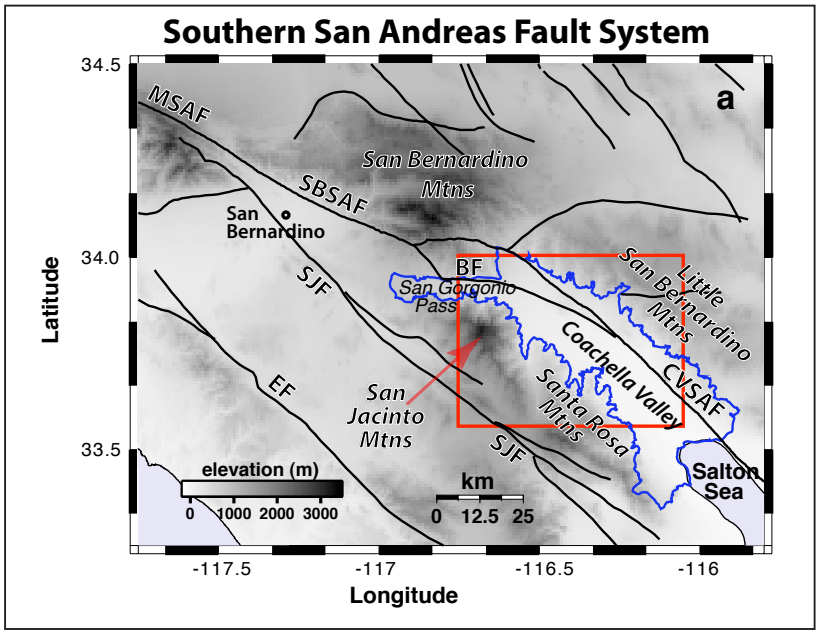

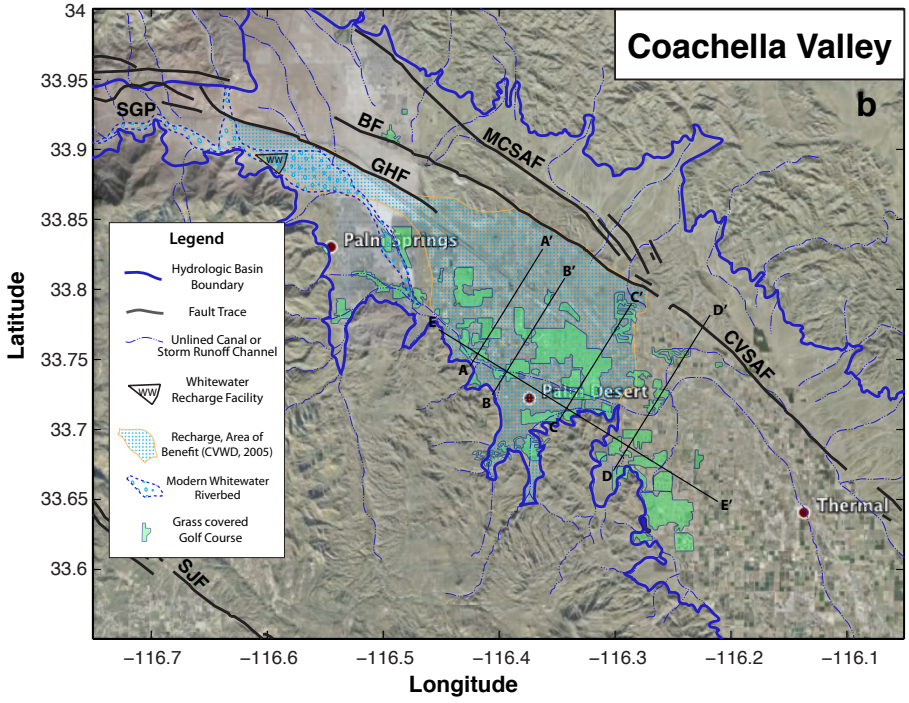

topography, specifically discussing the NW trending axis of an uplifted block south of the Banning fault. Large basins along irregularly shaped strike slip faults exhibit intricate composites of basins within basins (Crowell & Sylvester 1980; Aydin & Nur 1982), and

provide clues to the migration of a fault system and basin formation through time, as well as potential localized earthquake hazards (e.g. Aydin & Nur 1982; Yule & Sieh 2003).

Biehler *et al*. (1964) discuss a steep gravity gradient along the eastern front of the Santa Rosa Mountains (~5 mGals), which the author suggested represents a fault concealed by Quaternary alluvium. Furthermore, discontinuities in the trend of the gradient were posited to be minor cross faults (Biehler *et al*. 1964). However this suspected buried fault system is not directly addressed in the later gravimetric studies.

Groundwater management is a crucial component for this populated arid region of southern California. The Coachella Valley Water District (CVWD) receives the 3rd largest entitlement of imported Colorado River Water in the state, and the region is granted advanced amounts of water in wet years. This imported allotment has benefitted the overall stability of the Coachella Valley aquifer, thus far, as recharge surplus over the actual State Water Project entitlement has been received. The Whitewater Recharge Facility is located the northernmost extension of the Salton trough (Fig. 3.1b) and began artificial recharge to the aquifer in the early 1970's. Recharge facilities in the Upper Coachella Valley are intended to help remedy problems associated with at least four decades of prolonged overdraft conditions (e.g. land subsidence, surface fissures, aquifer compaction and storage loss).

Recharge at the Whitewater Facility has been effective in raising water levels in the immediate recharge area and in slowing the decline of water levels in some wells in the northwestern basin (CVWD 2005). However, replenishment of groundwater resources is not sufficient for full recovery of the aquifer system, and the groundwater resources are effectively being mined (CVWD 2005). The CVWD has outlined an area

of benefit for the Whitewater artificial replenishment (Fig. 3.1b), however, the analyses in this study will reveal that the replenishment area of benefit may be overestimated and that recharge may not be reaching parts of western basin margin aquifer. Fault zones in this area can act as efficient barriers to groundwater flow and create horizontal pressure differentials in the aquifer (Reichard & Meadows 1992). Active fault traces often coincide with differential surface displacement observed with InSAR (e.g. Lu & Danskin 2001; Bell *et al*. 2008; Wisely & Schmidt 2010). Some aspects of this study may directly relate to the reach of the recharged groundwater in the Upper Coachella Valley and I examine the possibility of the presence of fault related groundwater flow barriers buried in the western basin margin.

Decades of declining water levels in the Coachella Valley are causing subsidence of the land surface, some portion of which may be permanent. The USGS has a series of open file reports documenting episodes of subsidence using InSAR, GPS and leveling data (e.g. Sneed and Brandt 2007). To better understand the subsurface structures of the Coachella Valley, at the time of the drafting of this report, the USGS is conducting a seismic survey in the Salton Trough (pers. comm., Gary Fuis, January 2011), and updating a basin thickness geophysical model (pers. comm., Victoria Langenheim, May 2011). Overdraft related land subsidence in the Coachella Valley has been studied since the 1930's (Table 3.1), including geodetic observations (e.g. Ikehara *et al*. 1997; Sneed *et al*. 2001, 2002; Sneed & Brandt 2007), as well as observations of surface fissures (Ikehara *et al*. 1997). Ikehara *et al*. (1997) state that a significant portion of the land subsidence has occurred since the 1990's, when groundwater levels began declining below previously recorded lows. GPS data indicate that some years experience

subsidence when other years remain fairly stable in net surface elevation (Sneed *et al*. 2001, 2002). Using InSAR to characterize subsidence near Palm Desert and Indian Wells between 1996-2005, Sneed & Brandt (2007) identify short lineaments that appear in some data, suggestive of sharp lithologic contrast in the aquifer. They also note that localization of subsidence may be related to the tectonic setting of the aquifer. My study investigates the implications of the tectonic setting on the regional hydrogeology through synthesis of varied observations and data sets, including more recent InSAR.

Table 3.1. Comparison of measured surface subsidence in the Coachella Valley.

Location of Extreme Subsidence	Period of Observed Subsidence	Estimated Average Subsidence Rate	Study: † Leveling @ GPS * INSAR
Lower Coachella Valley	1930-1996	2.3 mm/yr (~0.2 mm/month)	†@ Ikehara *et al*. 1997
Rancho Mirage/ Palm Desert	1996-2000	3 mm/month	@* Sneed *et al*. 2002
	2003-2005	6 mm/month	@* Sneed & Brandt 2007
	2006-2009	45 mm/yr (~4 mm/month)	* this study
Indian Wells	1996-2000	1.6 mm/month	@* Sneed *et al*. 2002
	2003-2005	3-4 mm/month	@* Sneed Brandt 2007
	2006-2009	36 mm/yr (~3 mm/month)	* this study
La Quinta	1996-2000	1-3 mm/month	@* Sneed *et al*. 2002
	2003-2005	4-6 mm/month	@* Sneed & Brandt 2007
	2006-2009	48 mm/yr (~4 mm/month)	* this study

Using L-band SAR data, I extend the InSAR coverage for the Upper Coachella Valley, and am able to map sharply defined boundaries of extreme subsidence using 48 differential interferograms between 2006-2009. Through stacking differential interferograms, I observe a systematic array of steep subsidence gradients in elongated northwest trending parallel and subparallel lineaments. The features are consistent with

the trend of the local tectonic structures, but no fault traces have been observed at the surface. This study investigates the nature of sharp subsidence gradients observed with InSAR, and related partitioning of the aquifer.

2. INSAR DATA AND RESULTS

InSAR is an effective tool for monitoring surface deformation related to groundwater withdrawal and recharge. SAR data used in processing differential interferograms for this study area primarily include the L-band ALOS satellite data of the Japanese Aerospace Exploration Agency, between 2006-2009. I also present InSAR data using the earlier C-band ERS1/2 and ENVISAT satellite platforms for examining time dependent deformation from different periods between 1993-2009, but remain focused on the ALOS platform, as the L-band data provides superior spatial continuity of data in the regions of rapid and extreme subsidence. L-band satellites have a lower frequency range than C-band and therefore L-band interferometry can capture larger magnitudes of surface displacement and maintain data coherence. The longer satellite bandwidth is more appropriate for the magnitude and range of on-going aquifer surface displacement. All SAR data are processed with the ROI_PAC software package (Rosen *et al*. 2004). Differential interferograms processed for the Upper Coachella Valley span 36 days to nearly 6 years (Tables 3.2, 3.3, and 3.4). The interferometric phase is flattened to remove any gradient caused by orbital errors. This step in processing effectively removes any displacement signal that may be associated with plate boundary deformation. The topographic contribution to the phase (Bürgmann *et al*. 2000) is removed using a 30 m digital elevation model from the SRTM shuttle mission. The interferogram is then

unwrapped to estimate the range change in the satellite look direction. Assuming the dominant mode of deformation is in the vertical direction, I back project the line-of-sight range change onto a vertical displacement vector.

SAR scenes processed from the ALOS L-band satellite span late 2006 through late 2009. Out of 69 SAR pairs I found 48 interferograms to be relatively free of visual atmospheric patterns. Scenes contaminated by significant cloud or fog layers can cause a delay in wave travel time, falsely increasing or decreasing the range change observed in an interferogram (Zebker *et al*. 1997). Through careful scrutiny, these scenes were eliminated from the analysis set, thereby minimizing the atmospheric source of noise from the data set. The 48 ALOS differential interferograms used in this study have an average perpendicular baseline of 370m (Table 3.2). I find excellent spatial coherence in ALOS SAR pairs with perpendicular baselines up to 1700m. Stacking the 48 interferograms provides estimates of the average rate of deformation for each pixel (Fig. 3.2), which dampens the effect of any remaining atmospheric noise. I find that stacking interferograms is an effective method for enhancing common signals and locating steep differential displacement gradients that may in effect vary through time due to changes in pumping and recharge activity.

Table 3.2. Acquisition dates and perpendicular baselines for interferometric pairs, ALOS, Ascending Track 213, Frame 0660.

Scene 1	Scene 2	b-perp (m)
20060925	20061110	718
20060925	20061226	-932
20060925	20070210	300
20060925	20070628	801
20060925	20070813	1038
20060925	20080630	176
20060925	20080930	-1507
20060925	20081115	-989
20060925	20081231	-1089
20060925	20090215	-389
20061110	20070628	83
20061110	20080630	-541
20061110	20090818	-685
20061226	20080630	1108
20061226	20090215	542
20061226	20090703	942
20070628	20070813	237
20070628	20070928	425
20070628	20080330	1798
20070628	20090215	-1191
20070628	20090703	-791
20070628	20090818	-768
20070628	20091003	-231
20070813	20070928	188
20070813	20080330	1561
20070813	20080515	1932
20070813	20090703	-1028
20070813	20090818	-1005
20070813	20091003	-468
20070928	20071113	650
20070928	20080213	1293
20070928	20080330	1372
20070928	20080515	1744
20070928	20090703	-1216
20070928	20090818	-1193
20070928	20091003	-656
20071113	20080213	642
20071113	20080330	722
20071113	20080515	1093
20071113	20080630	-1701
20080213	20080515	451
20080330	20080515	372
20080630	20081231	-1265
20080815	20080930	1031
20080930	20090703	1517
20080930	20090818	1540
20081231	20090215	700
20090703	20090818	23

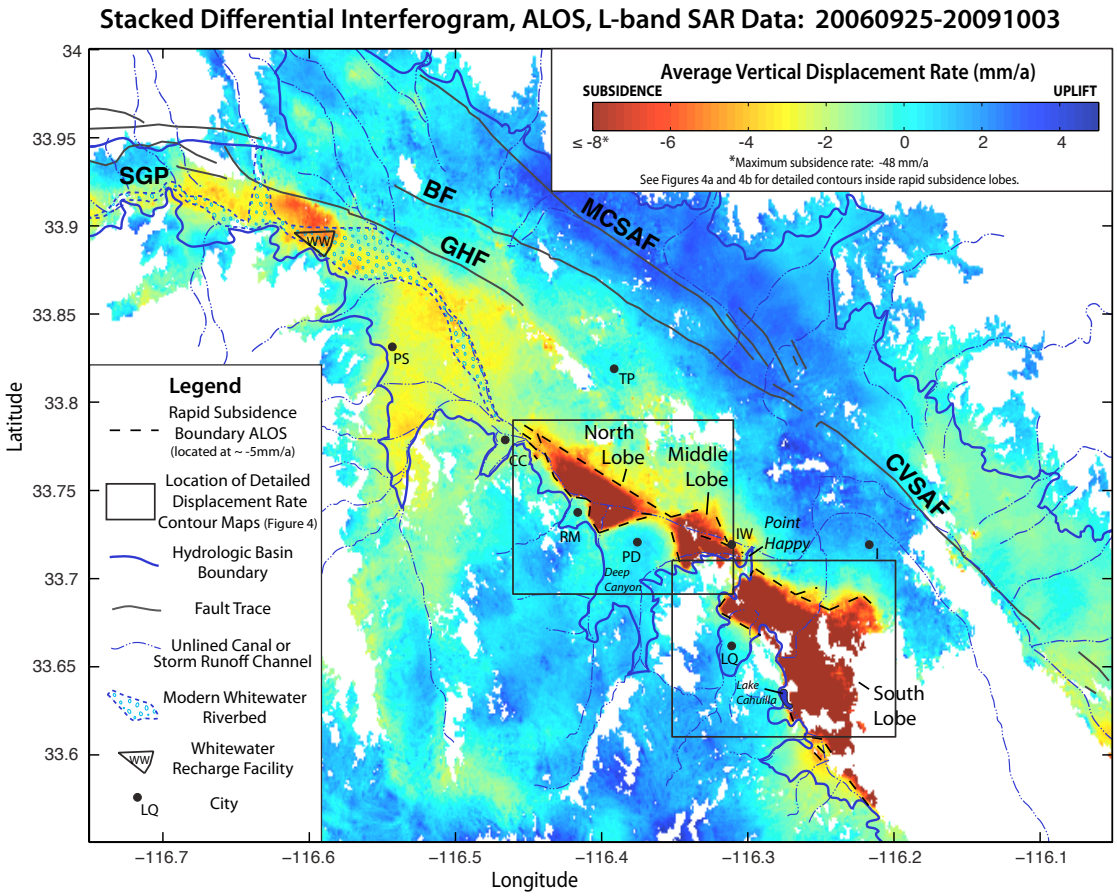

Figure 3.2. Average vertical displacement rate estimated with a stacked differential interferogram, spanning late-2006 through late-2009. Red represents relative subsidence and blue represents relative uplift. The color scale is saturated in red (8-48 mm/yr) to highlight the locations of steep displacement gradients bounding areas of rapid subsidence, and to avoid obscuring the more subtle differential displacement occurring in the central and northwestern basin. Contours of surface displacement within the subsiding lobes are mapped in Figures 3.4a and 3.4b. Dashed lineaments are located at ~5 mm/yr, and will be mapped within later figures.

The C-band satellites (ERS1/2 and ENVISAT) require shorter perpendicular baselines to effectively maximize coherence. The 34 ERS1/2 differential interferograms stacked in Figure 3.3a have an average perpendicular baseline of 105m (Table 3.3). The 29 ENVISAT differential interferograms stacked in Figure 3.3b have an average perpendicular baseline of 109m (Table 3.4). ERS1/2 interferograms span mid-1993

through late 2006, with two significant gaps in acquisition dates, between late 1993 and mid-1995, and again between late 2001 and late 2005. ENVISAT differential interferograms span late 2003 through late 2009 (Fig. 3.3b).

Table 3.3. Acquisition dates and perpendicular baselines for interferometric pairs, ERS1/2, Descending Track 127, Frame 2925. Red text indicates pairs that crossover into the time span of ENVISAT data, allowing for the continuous 16-year vertical displacement time series and for confirmation that the observed surface displacement is dominated by the vertical signal.

Scene 1	Scene 2	b-perp (m)
19930425	19931121	106
19930425	19960507	12
19931121	19951010	68
19950801	19951010	270
19950801	19991229	191
19950801	20000412	111
19951010	19980617	95
19951010	19991229	78
19951114	19951220	292
19951114	19960123	4
19951114	19971224	42
19951114	20000308	40
19951220	20000412	41
19960123	19971224	38
19960123	20000308	44
19960402	19970319	20
19960402	19980128	1
19960402	20000308	192
19960507	19980617	90
19961030	19990217	76
19961204	19980408	120
19970319	19980128	21
19970319	20000308	212
19970319	20000726	25
19971224	19980128	272
19971224	20000308	81
19980128	20000308	191
19980408	19990915	130
19990217	19990811	37
19991124	20010815	45
20000412	20001108	79
20000726	20010815	160
20001108	20060809	173
20051207	20061227	193

Table 3.4. Acquisition dates and perpendicular baselines for interferometric pairs, ENVISAT, Ascending Track 77, Frame 675.

Scene 1	Scene 2	b-perp (m)
20031130	20040523	157
20040523	20050123	51
20040801	20050403	14
20050123	20050717	43
20050227	20050612	211
20050612	20050821	100
20050612	20060212	54
20050717	20060423	106
20050821	20060212	46
20060212	20061224	34
20060319	20061119	116
20061015	20070128	52
20061015	20070930	175
20070128	20080914	37
20070930	20080217	158
20070930	20080914	194
20071104	20080323	161
20071104	20080427	21
20071104	20090517	63
20080217	20080914	36
20080217	20090517	189
20080323	20080427	135
20080323	20090517	221
20080427	20090517	86
20080427	20090830	118
20080914	20090517	225
20090517	20090830	204
20090517	20091108	44

The most striking feature observed with InSAR is a northwest trending swath of rapid subsidence (5-48 mm/yr) that persists in the western basin margin of the Upper Coachella Valley (Fig. 3.2), extending southeast from Cathedral City. This feature may be observed with all three SAR satellite platforms as early as the mid-1990's (Figs. 3.3a, 3.3b), but is most clearly observed using the ALOS satellite data (Fig. 3.2). Subsidence rates are relative to a location in the central study area, midway between the San Andreas fault trace and the abrupt subsidence boundaries, a point selected in the interferometric data processing. I map the boundaries of rapid subsidence at approximately 5 mm/yr, as beyond this rate subsidence rate gradients tend to steepen dramatically, and there is a

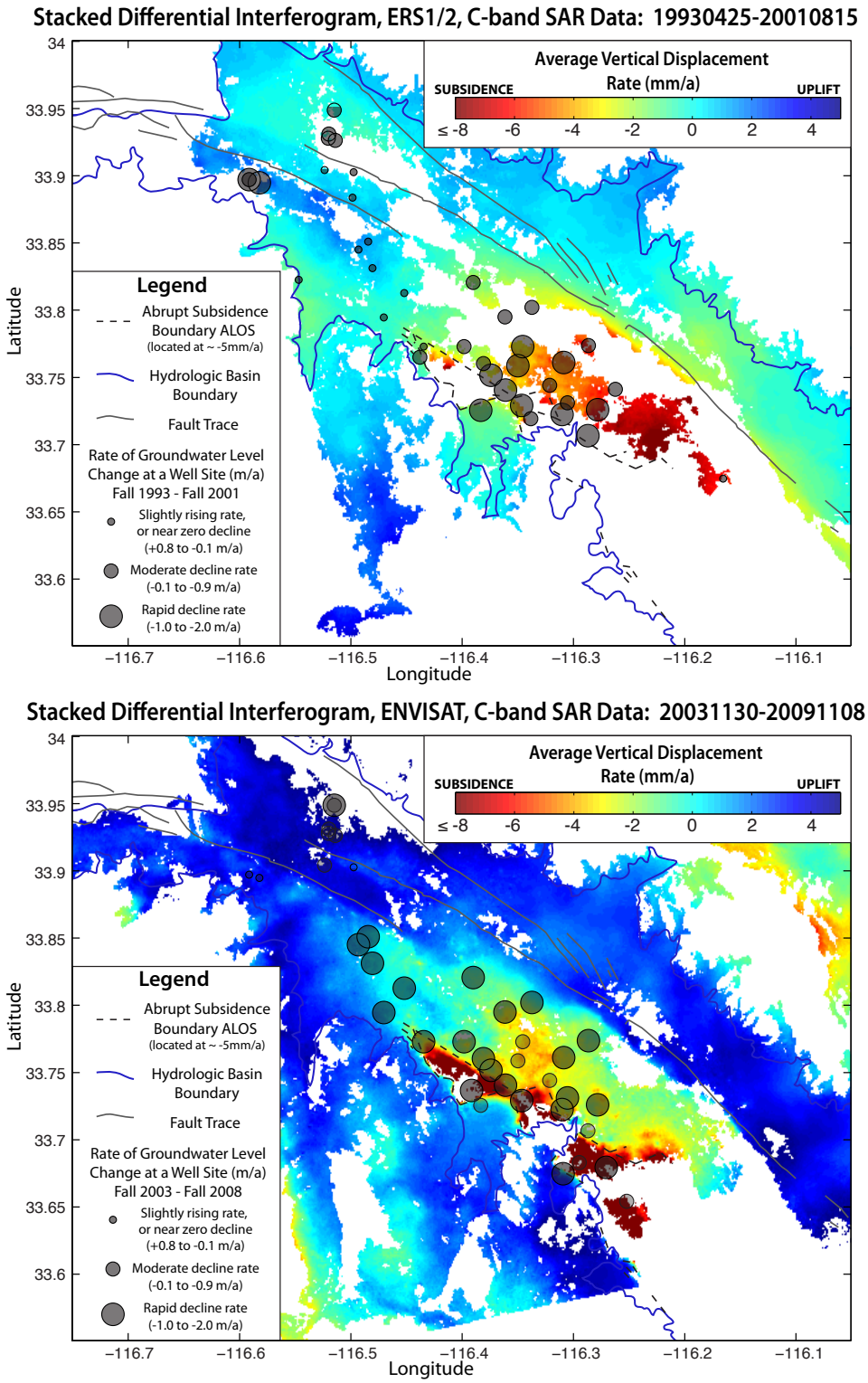

Figure 3.3. Average vertical displacement rate estimated with stacked differential interferograms, spanning 1993-2001 (3.3a), and 2003-2009 (3.3b). The same red-saturated color scale is used as in Figure 3.2. Along with interferometry, the rate of change in groundwater level at various well sites is also plotted for each time period.

marked linear characteristic to this contour, particularly in the northern subsidence lobes (Fig. 3.4a). I saturate the color scale of the stacked interferograms of Figures 3.2 and 3.3 to best highlight the linear characteristic of the 5-mm/yr contours in map view, and in Figure 3.4 illustrate the range and the asymmetry of rapid subsidence.

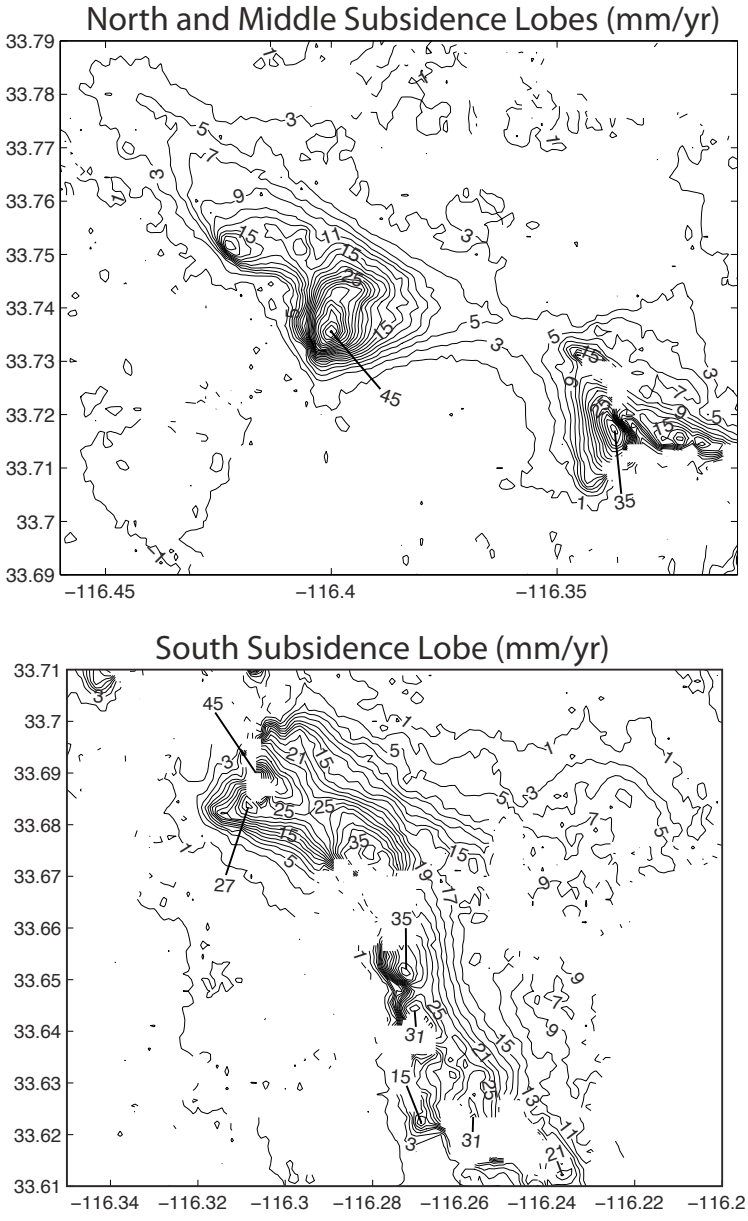

Figure 3.4. Contoured average vertical displacement rate within rapid subsidence lobes, estimated with ALOS interferometry spanning late-2006 through late-2009. See insets of Figure 3.2 for location of subsidence lobes.

The three separate lobes of rapid subsidence are bound by borders that are distinctly abrupt, hinge-like in cross section and often linear in map view (Fig. 3.2, 3.4). The northern subsidence lobe near Rancho Mirage has a notched triangular shape and a maximum subsidence rate of 45 mm/yr between 2006-2009 (Fig. 3.4a). The middle subsidence lobe, near Indian Wells, exhibits a maximum subsidence rate of 36 mm/yr and is subsiding most rapidly in the southern portion (Fig. 3.4a). A lineament parallel to the basin-ward boundary of the northern subsidence lobe separates the rapidly subsiding portion of the middle lobe from the more gently subsiding northern portion. This lineation continues towards the southeast, bounding part of the largest of the three subsidence lobes. The southern subsidence lobe widens to the southeast and the gradient of subsidence rate becomes gentler at the edge of the InSAR data (Fig. 3.4b). The middle subsidence lobe abuts the base of a crystalline bedrock spur jutting into the valley floor, the tip of which is known as Point Happy. On the south side of Point Happy, rapid subsidence abuts the bedrock spur, exhibiting a maximum rate of 48 mm/yr. The south subsidence lobe also abuts bedrock east of Lake Cahuilla (Fig. 3.2) and again in the southernmost study area.

The primary NW trending basin-ward lineament of the three lobes is most defined along the northern subsidence lobe and becomes slightly less steep and a more diffuse gradient along the subsidence lobes to the south. Lineaments parallel to the primary lineament border the western side of the southern subsidence lobe, and several crosscutting lineaments intersect this generally NW trending system (Figs. 3.2 and 3.3). Near zero displacement rates are observed in the more urbanized notch canyons of the western Coachella Valley, with abrupt changes between the subsiding lobes and the

canyon alluvial surfaces. Differential surface displacement is also observed across known faults and groundwater barriers in the northwestern basin, and appears to vary in sign and magnitude through the span of InSAR data (Figs. 3.2 and 3.3).

Extending as far north as Cathedral City, as far west as Palm Desert, and southeast towards Indio is an elongated bowl of subsidence with a maximum subsidence rate of 7.1 mm/yr between 1993-2001 (Fig. 3.3a). The 2003-2009 ENVISAT data (Fig. 3.3b) confirms that subsidence was lessening in this area by 2003. Between 2006-2009 (Fig. 3.2) subsidence is no longer observed in the central basin most likely due to long-term recharge efforts of the Whitewater Recharge Facility.

3. INSAR INTERPRETATION

This study primarily focuses on the distinct pattern of rapid subsidence in the western basin margin, however, other subsiding regions of the basin are also of interest due to observable changes in deformation style over the span of InSAR coverage. Differential surface displacement across the Garnet Hill and Banning faults can be observed with all satellite platforms in the northwest study area. These faults are known groundwater flow barriers (CVWD 2005; Appana & Saar 2007) just north of the Whitewater Recharge Facility. Between the faults, the ground surface aspect of displacement is reversed from the period of earliest interferograms (Fig. 3.3a) to the period of the most recent (Fig. 3.2). As both data sets are from ascending track satellite acquisitions, I can assume the observed reversal in displacement trends across the faults are dominated by vertical displacement with little or no component of horizontal motion affecting the signal. Between 1992-2001 I observe differential surface displacement on

the order of 1.5 mm/yr across each fault, with the region north of the Banning fault undergoing slight subsidence, the region between faults near stable elevation, while south of the Garnet Hill fault near the recharge facility the ground surface is uplifting slightly. Alternately, between 2006-2009 south of the Garnet Hill fault, I observe between 3-6 mm/yr of subsidence, and the Banning fault lineament is not readily visible. I attribute the decline in subsidence to the installation of a local groundwater recharge facility north of the Banning fault, in the Mission Creek sub-basin of the aquifer as it was discovered recharge from the Whitewater facility was not reaching north of the Banning fault (CVWD, 2010). The ENVISAT data spanning 2003-2009 (Fig. 3.3b) shows relatively less differential surface displacement, from which I infer the majority of subsidence near the Whitewater facility has occurred during the later half of the period, as illustrated with the ALOS data (Fig. 3.2).

Between the northern and the middle subsidence lobes near the city of Palm Desert is the Deep Canyon alluvial fan, a very thick gravel rich deposit, where rates of surface displacement are near zero (Figs. 3.2, 3.3). Other notched canyons of the western Coachella Valley also exhibit near zero subsidence rates, and similarly contain the relatively more urbanized city centers (Cathedral City, Rancho Mirage, and La Quinta). These relatively coarse-grained alluvial accumulations are not experiencing significant on-going subsidence, and the character of the abrupt subsidence boundaries towards the fan toes suggests an interplay between the subsidence boundaries and the deposition of coarse alluvial fan material.

The central basin of the Upper Coachella Valley is another region of changing trends in surface displacement through the span of InSAR coverage. The central

elongated bowl of rapid subsidence observed in the 1990's appears to have stabilized in elevation during more recent years. This in part may be due to the installation of groundwater reclamation sites in the central basin used to irrigate agriculture and golf courses without overly taxing the groundwater (CVWD, 2010).

The most notable deformation in the Upper Coachella Valley is certainly the distinct pattern of steep gradients in surface displacement in the western basin margin. Sneed & Brandt (2007) identify short lineaments that appear in some data between 1996-2005 in the middle subsidence lobe, and suggest the lineaments may be related to tectonics or sharp lithologic changes. Sneed & Brandt (2007) also identify elongated regions of subsidence in the basin margins, but without the stacking of tens of interferograms as I did in this study, the broader system of lineaments in map view was not readily observable. The NW trending system of lineaments and crosscutting set of sub-parallel lineaments is distinctly suggestive subsurface aquifer partitioning. Surface displacement in Figure 3.3b (ENVISAT) also shows a distinct en echelon pattern in the east side of the Coachella Valley, mirroring the pattern on the western side. This pattern is not seen in the stacks from the other satellites. Geologic literature does not indicate any observed fault traces or major scarps at the surface of the western basin, even before major urbanization of the last century. I assume if the differential surface displacement is controlled by subsurface en echelon faults that those faults are buried and inactive. In the following sections I explore what structures may be controlling the unique pattern of surface displacement in the western basin margin.

4. INSAR AND GROUNDWATER LEVELS

To begin to understand the causes of the distinct patterns of differential surface displacement in the Coachella Valley aquifer, groundwater level data was amassed courtesy of the CVWD, spanning all or some portion of 1992-2008, at 50 well sites from the San Gorgonio Pass southeast to Thermal (Figs. 3.3a, 3.3b). The well levels are typically sampled 3× yearly and groundwater levels are assumed to represent the head level changes in the saturated aquifer column due to pumping and recharge. Groundwater level data from the Coachella well array are dominated by declining levels, although some stable and some rising levels are also observed (Figs. 3.3a, 3.3b). A subset of 27 well sites in the study area have well drillers' logs, which document intervals of grain size and sorting variation and other features of the upper ~300m of the aquifer, such as groundwater levels at the time of well installation/completion and perforation intervals. I systematically incorporate these drillers' records into my analyses in order to look for evidence of a relationship between material characteristics and surface displacement and identify potential causes for the sharply bound subsidence lobes in the western basin margin.

As can be observed in Figure 3.5a, the amount of imported water delivered to the Whitewater Recharge Facility varies greatly from year to year, and the recharge is reflected in the water levels at wells closest to the facility (Figs. 3.5b, 3.5c). Patterns of time dependent surface displacement related to groundwater level changes can be assessed with an InSAR time series (Fig. 3.5d), a pixel-by-pixel linear inversion that solves for the incremental range change between SAR scene acquisitions (Schmidt & Bürgmann 2003). I assume that our InSAR observations reflect only vertical surface

deformation, given the majority of hydrologically induced aquifer deformation occurs in the vertical direction (Bawden *et al*. 2001; Hoffmann & Zebker 2003). I also use only the ERS and ENVISAT satellites in time series construction (Figs. 3.3a, 3.3b), as the span of the ALOS SAR data has at most a 2-year overlap in data with groundwater level data, whereas the earlier satellites overlap almost entirely with groundwater level data. The InSAR time series are composed of the same set of interferograms used in stacking (Tables 3.3, 3.4). Two interferograms from the earliest ERS satellite platform crossover in time into the era of the ENVISAT platform, and therefore I am able to combine data sets in the inversion and produce one continuous time series for most of the 16-year period.

Some portion of subsidence observed with InSAR in the Coachella Valley is an elastic response to shifting pore pressures due to coeval changes in groundwater level (e.g. Riley 1969; Poland 1984; Lu & Danskin 2001). Using the HII method developed by Wisely & Schmidt (2010), I investigate the possibility that some portion of subsidence may be a permanent and delayed response of slowly draining clay-rich aquitard layers resulting from 40+ years of overdraft conditions. The HII method uses InSAR to quantify vertical displacement, and ground water levels as a proxy for head level changes in the aquifer (Fig. 3.5), in order to characterize the surface deformation in groundwater aquifer basins. The HII method is a least squares inversion that estimates 1) the poroelastic ratio (S_{ke}), related to compressibility of the aquifer sediments (Riley 1969) and 2) the residual vertical displacement rate, permanent deformation that is not attributable to on-going changes in groundwater levels.

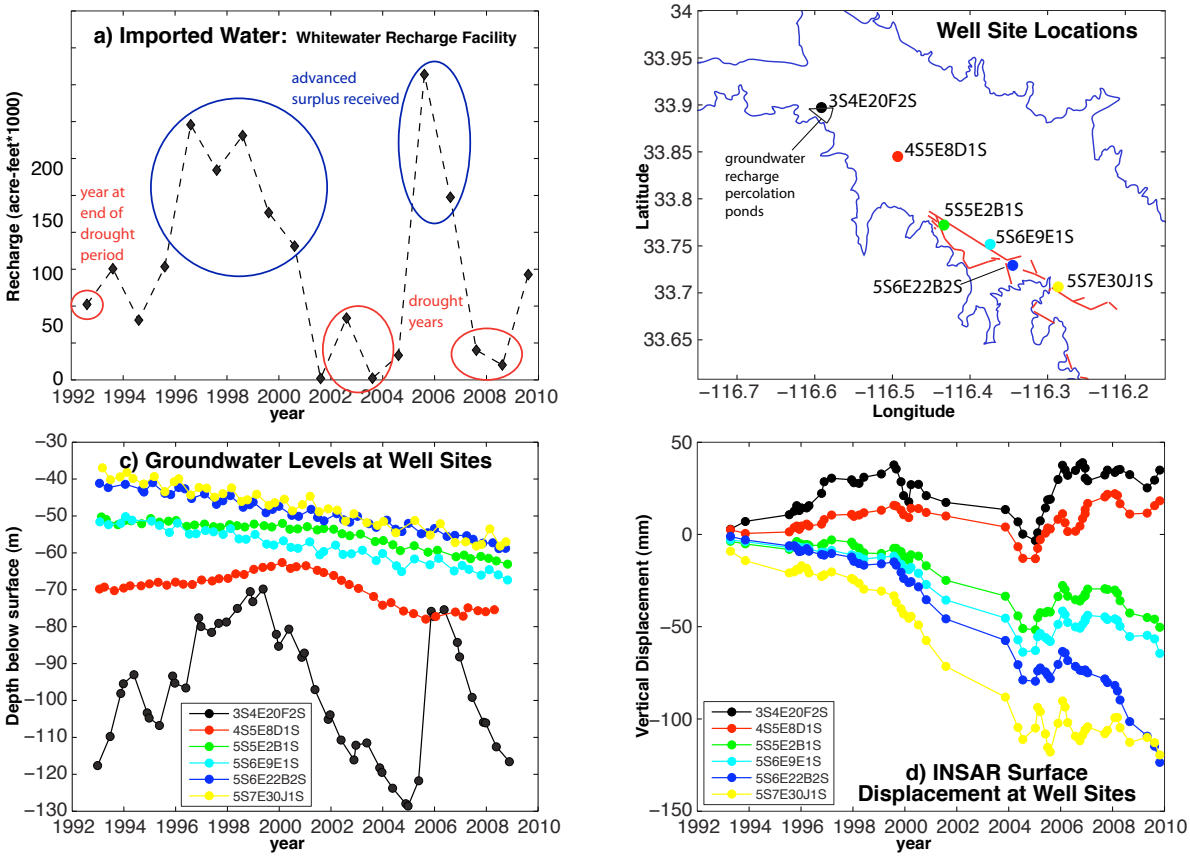

Figure 3.5. The graphs and maps relate groundwater recharge, groundwater levels and surface deformation at several well sites in the study area. Figure 3.5a plots yearly deliverance quantities of artificial recharge to the Whitewater Recharge Facility, in acre-feet. The representative well locations are plotted in Figure 3.5b. Figure 3.5c plots depth to groundwater at each well (m below surface) and 3.5d plots the time dependent surface displacement (mm) measured with the ERS1/2 and ENVISAT satellite platforms, 1993-2009. Well sites are color coordinated to easily identify the groundwater levels and surface displacement at each well site.

5. SENSITIVITY TESTING OF THE HII METHOD

The HII method was originally developed in another aquifer basin, San Bernardino, and significant differences in study locations and data sampling dictate some adjustments to the HII method for the Coachella Valley. The primary difference is the groundwater sampling frequency. The sampling frequency for the Coachella Valley does not exceed 3 times per year, a sampling frequency deemed too low during the

development of the HII method. The San Bernardino basin is also significantly smaller and less deep than the Coachella Valley, and is bound by known faults that correlate well with InSAR observations. In this section I test the significance of these adjustments and assess the utility of the HII method analysis for the Coachella Valley with the available data in order to utilize the HII method in its capacity to aid in the characterization of this uniquely deforming aquifer.

Groundwater sampling frequency in the Coachella Valley has been identified as too low to make meaningful interpretations of surface displacement in response to groundwater level changes (Sneed & Brandt 2007). To test the sensitivity of the HII method to sampling frequency of groundwater levels I generate synthetic continuous groundwater and vertical surface displacement data, constructed to simulate physical scenarios of an idealized alluvial aquifer. By varying sampling frequencies and repeatedly sampling the continuous time series, I create synthetic data sets for processing through the HII method, and assess uncertainties related to groundwater level sampling frequency.

Synthetic data sets incorporate varying combinations of both short-term and long-term changes in groundwater levels and related vertical surface displacement, using sinusoidal and linear components to create continuous time series. Seasonal fluctuations associated with "pumping" and "recharge" and the related elastic vertical surface displacement are incorporated into each of the simulated scenarios with sine curves. Long-term changes are represented linearly. Although transient aquifer deformation, like delayed compaction due to overdraft, may be more accurately portrayed with non-linear

decay functions (Gonzalez & Fernandez 2011), the use of linear equations is adequate for representing decadal aquifer compaction rates, to a first order (Wisely & Schmidt 2010).

I address the HII method sensitivity to groundwater sampling frequency as it relates to the accuracy of model parameter estimates under the following simulated hydrogeologic conditions (Fig. 3.6): 1) a stable situation in which there is no long-term change in groundwater levels or surface elevation, 2) a situation where although groundwater levels are over years declining, surface displacement is entirely recoverable and no permanent compaction is occurring, 3) a situation where groundwater levels are stable, but delayed compaction related to previous overdraft conditions is causing subsidence, and 4) a situation where groundwater levels are declining over years, while delayed compaction is also occurring due to continued long-term overdraft.

In the formulation of continuous surface displacement and groundwater level time series, I assign model parameters, specifically a S_{ke} of 1.0e-3 (Helm 1978; Poland 1984), and a residual vertical displacement rate, representing permanent compaction/subsidence or lack thereof, depending upon the simulated hydrogeologic conditions. The simulated surface displacement time series are randomly sampled 3× yearly, a frequency comparable to the InSAR time series of Wisely & Schmidt (2010) and comparable to the InSAR time series for the Upper Coachella Valley. The simulated groundwater level curves are sampled with frequencies from 2-10× yearly, varied to assess the effects of groundwater level sampling frequency on HII method model parameter estimates. I use fifty sets of synthetic groundwater level and surface elevation data for each combination of groundwater level sampling frequency and hydrogeologic simulation as input for the HII method. I then compare the resulting model estimates to the assigned parameters and

am able to comment on the reliability of the HII method to estimate model parameters at different groundwater level sampling frequencies, under varying simulated hydraulic aquifer conditions. Examples of synthetic data sets, representing varying hydrogeologic simulations, and corresponding HII method inversion results are shown in (Fig. 3.6).

In application of the HII method, groundwater level data with a sampling frequency of 4× yearly most accurately estimates the model parameter S_{ke} (Fig. 3.7). Lower sampling frequency than 4× yearly tends to slightly underestimate S_{ke}, while greater sampling frequency tends to slightly overestimate the poroelasticity. Estimated S_{ke} values remain within an order of magnitude of the assigned parameter (1.0e-3), and as sampling frequency increases, the estimates stabilize at 1.1e-3.

Another aspect of groundwater sampling that affects the accuracy of S_{ke} values estimated with the HII method is the regularity of sampling, how evenly through each year sampling is spread. Synthetic groundwater data spread evenly through each year produces more accurate estimates for S_{ke} than the synthetic data that misses large periods of a given year and where samplings are clustered in time (Fig. 3.8). Although the best estimate for S_{ke} is attained with a groundwater level sampling frequency of 4× yearly, synthetic data testing reveals that a sampling frequency of 3× yearly may also accurately predict S_{ke}, particularly where sampling is regularly spaced in time (Fig. 3.8).

Figure 3.6. (next page) Examples of synthetic data sets: varying hydrogeologic simulations, and corresponding HII method inversion results. Graphs on left side of page (a, c, e, g) represent data input for HII method, and correspond to graphs directly to the right (b, d, f, h). Figures 3.6a, c, e, g plot synthetic surface displacement data (blue line, left axis) and groundwater level data (green line, right axis). Figures 3.6b, d, f, h compare synthetic surface displacement data (blue line) and forward model predicted surface displacement (red line) using model parameter estimates from HII method inversion. Each pair of graphs share simulated hydrogeologic conditions, described in Figures 3.6a, c, e, g, and corresponding model parameter estimates shown in 3.6b, d, f, h.

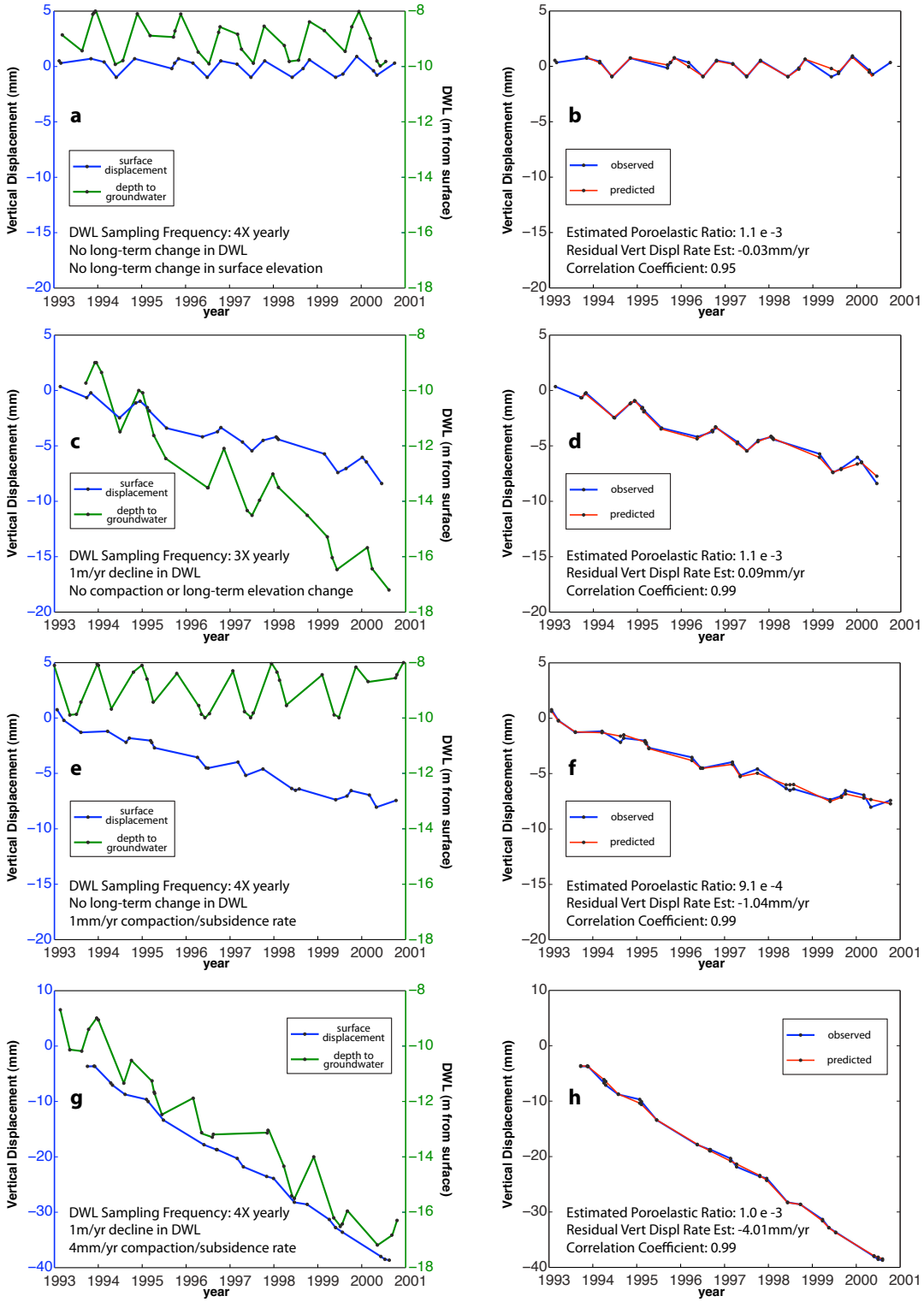
a
surface displacement
depth to groundwater
DWL Sampling Frequency: 4X yearly
No long-term change in DWL
No long-term change in surface elevation
b
observed
predicted
Estimated Poroelastic Ratio: 1.1 e -3
Residual Vert Displ Rate Est: -0.03mm/yr
Correlation Coefficient: 0.95
c
surface displacement
depth to groundwater
DWL Sampling Frequency: 3X yearly
1m/yr decline in DWL
No compaction or long-term elevation change
d
observed
predicted
Estimated Poroelastic Ratio: 1.1 e -3
Residual Vert Displ Rate Est: 0.09mm/yr
Correlation Coefficient: 0.99
e
surface displacement
depth to groundwater
DWL Sampling Frequency: 4X yearly
No long-term change in DWL
1mm/yr compaction/subsidence rate
f
observed
predicted
Estimated Poroelastic Ratio: 9.1 e -4
Residual Vert Displ Rate Est: -1.04mm/yr
Correlation Coefficient: 0.99
g
surface displacement
depth to groundwater
DWL Sampling Frequency: 4X yearly
1m/yr decline in DWL
4mm/yr compaction/subsidence rate
h
observed
predicted
Estimated Poroelastic Ratio: 1.0 e -3
Residual Vert Displ Rate Est: -4.01mm/yr
Correlation Coefficient: 0.99
Vertical Displacement (mm)
DWL (m from surface)
year

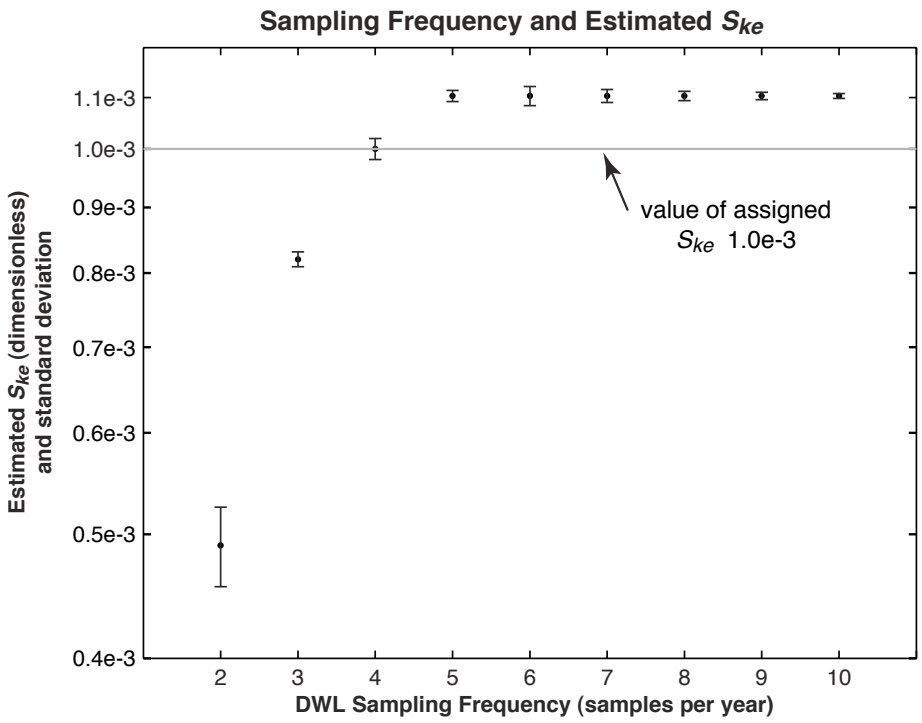

Figure 3.7. Estimated S_{ke} and standard deviation dependence upon depth to groundwater sampling frequency.

In application of the HII method some negative S_{ke} estimates may be produced indicating an anti-correlation between groundwater levels and surface elevation changes. This implies the opposite of what is mechanically and hydraulically reasonable, such as surface uplift where groundwater levels are declining. I find in the synthetic data tests that negative S_{ke} values are eliminated where groundwater levels are sampled 5× yearly. At 4× yearly sampling frequency, occasional negative S_{ke} values are produced. At 3× yearly sampling frequency, negative poroelastic results are produced with greater frequency, and most often appear where assigned residual vertical displacement is between -1 and 1 mm/yr. I conclude that the maximum 3× yearly sampling frequency of groundwater levels in the Coachella Valley will produce negative poroelastic results as a

consequence, and for more precise estimates poroelasticity of the Coachella Valley aquifer an increased sampling frequency of 4-5× per year would be ideal.

The synthetic data tests reveal a minimum model parameter uncertainty of ±0.5 mm/yr associated with the residual vertical displacement rates estimated with the HII method. This uncertainty is introduced in the inversion because the groundwater level and surface elevation data sets are not sampled on the same days, or at the same intervals. This offset in temporal sampling is handled in the HII method inversion by linearly interpolating the well data at the times of the SAR scene acquisitions. The inversion then solves for a fitting parameter *c* that allows for the direct comparison of water level changes and the InSAR time series. The standard deviation for model parameter *c* in the synthetic data testing decreases with increased sampling frequency (Fig. 3.9), simply reflecting that coincident data sampling between groundwater level and surface elevation measurements allows for a more direct comparison between these data sets. It is within the above linear interpolation of the groundwater level data and the estimation of the best-fit fitting parameter *c* that ±0.5 mm/yr minimum uncertainty is accumulated in the analysis. This uncertainty is separate and in addition to observational errors associated with the InSAR data and groundwater measurements.

Another insight revealed by the synthetic data testing of the HII method is that residual vertical displacement rates may be accurately estimated with as few groundwater level samplings as twice per year in a stable hydrogeologic setting. So although S_{ke} values are consistently underestimated with such a low sampling frequency, estimates of residual vertical displacement may still be accurate. In fact, a sampling frequency of

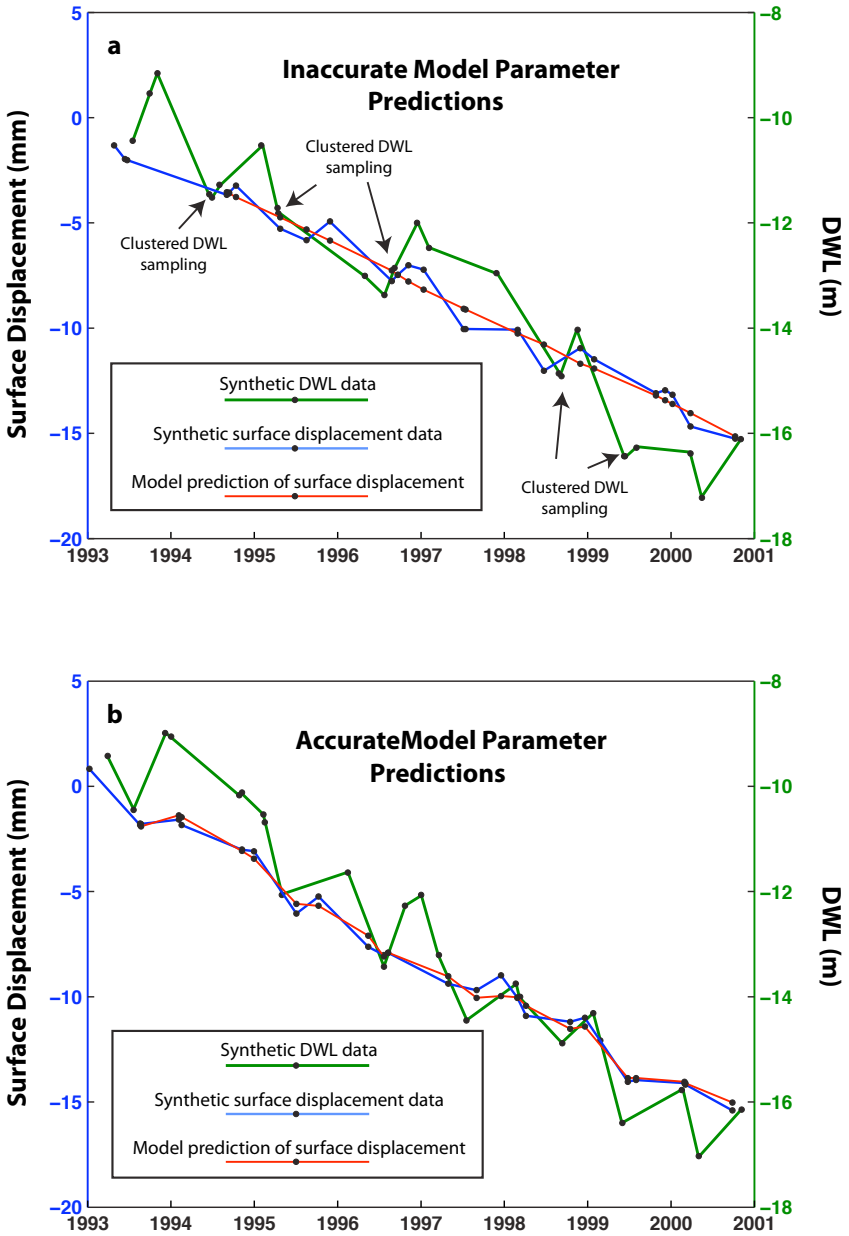

Figure 3.8. Each graph plots pairs of synthetic data (sampled 3 times per year) and model predictions under the same simulated hydrogeologic conditions of 1m/a decline in groundwater level and 1 mm/yr residual vertical displacement rate, with an assigned poroelastic ratio of 1.0e-3. Total yearly displacement rate therefore is 2 mm/yr, with half representing elastic changes related to on-going groundwater withdrawal and half related to fine grained aquifer compaction related to previously existing overdraft conditions. Figure 3.8a is an example of synthetic data producing inaccurate estimates of assigned model parameters, specifically underestimating S_{ke} and overestimating subsidence related to permanent processes (-1.5e-4 and 2.0 mm/yr of subsidence, respectively). Figure 3.8b is an example of synthetic data producing relatively accurate estimates of assigned model parameters (1.1e-3 and 0.9 mm/yr of subsidence). The graphs illustrate the effect of clustered groundwater level sampling in application of the HII method.

twice yearly can produce accurate estimates for residual vertical displacement rates as well as a sampling frequency of 10× yearly. However, as expected, the standard deviation of the estimates decreases as sampling frequency of groundwater level increases. The exception to this comes when significant long-term changes in groundwater level are prescribed, greater groundwater level sampling frequency is necessary to improve residual vertical displacement rate estimates, since subsidence rates are overestimated with low sampling frequency.

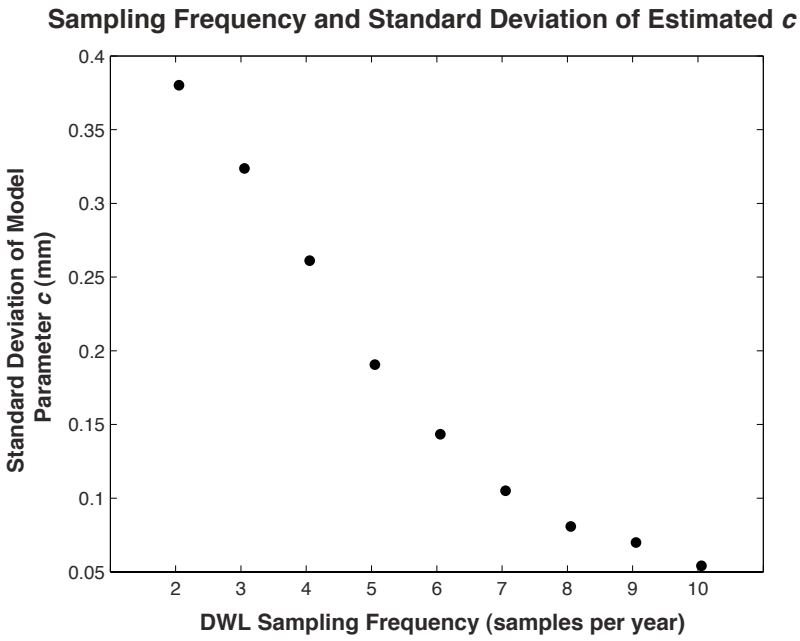

Figure 3.9. Relationship of groundwater level sampling frequency on the standard deviation of fitting parameter c, a model estimate of the HII method that allows for direct comparison of groundwater levels and surface displacement data that are not sampled coevally or at the same temporal intervals.

Correlation coefficients between the synthetic surface displacement and the forward model prediction of surface displacement are calculated for each synthetic data pair (e.g. Fig. 3.6b, d, f, h). Wisely & Schmidt (2010) indicate that an average correlation coefficient of 0.67 was the minimum value for the visual determination of a good match

between the predicted and observed time series. Groundwater level sampling frequency of 3× yearly in the synthetic data testing produces average correlation coefficients of 0.64, and a sampling frequency of 4× yearly averages 0.77. This suggests 3× yearly sampling of groundwater levels may be adequate for meaningful model predictions, while 4× yearly sampling is significantly more reliable. All Coachella Valley results obtained from the application of the HII method and used in analysis (plotted in Figs. 3.11a and 3.11b) have correlation coefficients of 0.67 or higher, averaging 0.91.

I have confirmed the utility of the HII method for aquifer characterization and assessed its limitations in regard to data sampling frequency. The most accurate model parameter estimates from the HII method analysis occur where there is a low misfit between observed and predicted surface displacement time series, and where groundwater levels are sampled seasonally and at regular intervals. A direct way to further maximize the accuracy of aquifer characterization using the HII method would be coincident sampling of groundwater levels on or near satellite acquisition dates. For the Coachella Valley, the synthetic data testing reveals that the 3× yearly sampling frequency may overestimate residual displacement rates where rapid subsidence is occurring and/or underestimating S_{ke}. Counteracting these systematic biases is the regularity and consistency of groundwater sampling dates from year to year. To further minimize the effects of less than optimal sampling frequency, I use for analysis only the well sites in the Coachella Valley with the highest correlation coefficients (≥ 0.67) calculated in the HII method.

6. HII METHOD: APPLICATION AND ANALYSIS

Groundwater recharge quantities (Fig. 3.5a) are reflected in the groundwater levels (Fig. 3.5c) and in the vertical surface displacement patterns (Fig. 3.5d) of the wells in the northwest basin. Further southeast, the recharge patterns are not readily observable in the groundwater level data, but still are observed to affect surface displacement. I infer this is due to a transition from unconfined aquifer conditions in the northwest to semi-confined conditions towards the south central basin. Aquifer partitioning becomes significant enough to impede vertical hydraulic conductivity towards the southeast, creating distinct upper and lower aquifer layers. Artificial recharge from the Whitewater Facility primarily reaches the lower aquifer (CVWD 2005) and is therefore not as distinctly reflected in the upper water table measurements.

An assumption of the HII method is that aquifer deformation is occurring in an elastic regime. In reality, some deformation may be inelastic, on the temporal scale of InSAR coverage, in which case S_{ke} values will trend high (Wisely & Schmidt 2010). Where negative S_{ke} values are estimated by the HII method, these wells are assumed to misrepresent the total changes in pore pressure at depth and the sites are not used in analysis, nor are sites where groundwater levels are not temporally correlated to surface deformation. The last determining factor of a well site's usability in the HII method analysis is whether the forward model prediction, using estimated model parameters, exhibits a correlation coefficient of 0.67 or higher when compared to the observed time dependent displacement at that location. Representative plots of surface displacement, groundwater levels and forward model predictions illustrate 2 examples of site-specific data sets and suitability for use in the HII method application (Fig. 3.10). Out of 50 well

sites in the western Coachella Valley, 31 meet the above criteria. As previously mentioned, well levels towards the south central basin may not be reflective of changes in hydraulic head through the entire aquifer column. In this case, residual vertical displacement rates may be overestimated and poroelasticity may be underestimated.

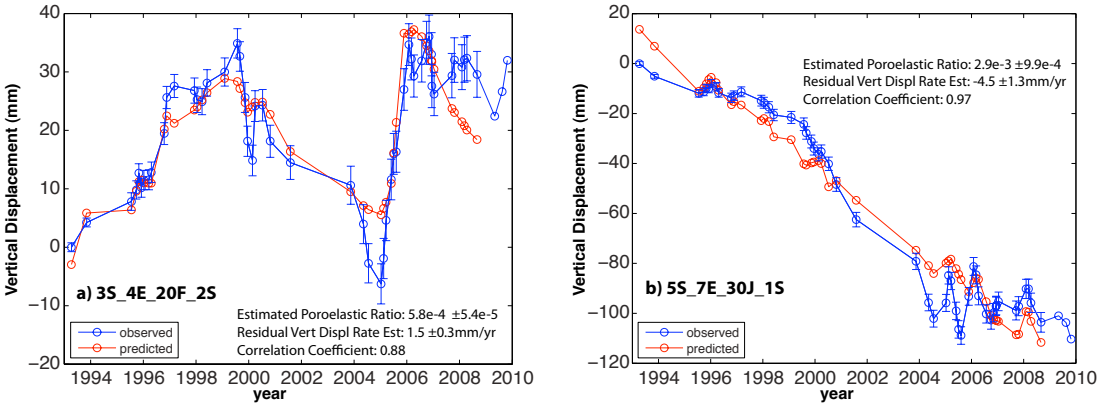

Figure 3.10. Representative plots displaying surface displacement comparison with forward model prediction. Both sites are suitable for use in the HII method aquifer characterization analysis, as the curves have high correlation coefficients and meet the other requirements stated in text.

Residual vertical displacement rates estimated with the HII method (Fig. 3.11a) illustrate that a significant component of deformation may not be readily explained by coeval changes in groundwater levels. A linear regression of average displacement rates and residual displacement rates indicates that ~89% of observed displacement may be related to other processes, possibly aquifer compaction or interseismic deformation. Maximum residual displacement is estimated at 35 mm/yr near La Quinta. Rapid residual subsidence is also estimated in the central basin on the order of 3-7 mm/yr. Well sites centered in the alluvial fans of the deeply incised canyons of the western basin show little to no residual subsidence, even some residual uplift. The wells in close proximity to

the Whitewater Recharge Facility appear stable as well. Average model uncertainty for residual vertical displacement rates is ±1.1 mm/yr (Fig. 3.11a).

Poroelastic estimates from the application of the HII Method average 2.3E-3 with an average model uncertainty of 1.2E-3. This implies that for a meter of groundwater level decline, the surface elevation would subside (recoverably) 2.3 ±1.2 mm. To compare S_{ke} values on a site-by-site basis and to other poroelasticity studies, I normalize the model estimates over the recorded well depth (Fig. 3.11b). Of the 31 wells suitable for analysis in the HII method, 23 have known well depths and therefore estimated normalized poroelastic ratios (S_{Ske}). As previously mentioned, if some deformation not related to ongoing changes in groundwater levels is occurring at a well site, the S_{ke} value will trend high, as will the S_{Ske} value. Typical S_{Ske} values for alluvial aquifer basins are on the order of 10^{-7}-10^{-5}m^{-1} (e.g. Riley 1969; Helm 1978; Poland 1984; Wisely and Schmidt 2010) and are largely dependent upon grain size. Estimated S_{Ske} values for the western Coachella basin, plotted in Figure 3.11b, are consistent with other aquifer studies. The lowest values ($<10^{-7}$m^{-1}) are towards the central basin and are located over deep and thick sections of basin fill. This is consistent with an increase of fine-grained materials towards the lower elevation central basin that have a smaller elastic response to changing water levels and slower transmissivities than coarse deposits. The highest values ($\sim10^{-5}$m^{-1}) are observed at a variety of locations. Sites centered in the incised canyons, and estimated to be uplifting slightly (near Palm Desert and La Quinta) show high S_{Ske} values, consistent with the relatively coarse-grained deposits of the proximal alluvial fan environment. Rapidly subsiding locations, near and within the abrupt subsidence

boundaries, show some of the highest poroelastic ratios, implying that some inelastic changes in surface elevation may be occurring.

The HII method originally used a specified percentage of geophysical basin depth estimates (Anderson *et al*. 2004) to normalize poroelastic ratios for San Bernardino (Wisely & Schmidt 2010). I find the use of well depth more appropriate for its application in the Coachella Valley for a couple reasons. First, the Coachella basin is larger and contains a much deeper alluvial deposits, placing well sites over basin thicknesses ranging from ~100m at the basin margin to 3.5km towards the central basin. Although basin thickness varies greatly in the Coachella Valley (Fig. 3.11), significant water-bearing deposits remain in the upper ~450m, with well depths averaging 270m. Secondly, well depths recorded in drillers' logs have a significantly smaller uncertainty (~1m) than the geophysical model estimates of basin depth, which are on the order of ±100-300m. The risk of using well depths for normalization would be in the systematic overestimation of normalized poroelasticity.

As the HII method reveals a complex interplay of simultaneous elastic and inelastic aquifer deformation and groundwater mining, I further investigate the possible underlying causes for the distinct and abrupt gradients in surface displacement. I begin with the sedimentological information recorded in water well drillers' logs in search of unique stratigraphic signatures, both within and outside of the rapid subsidence lobes.

Figure 3.11. (next page) Residual vertical displacement rates (3.11a) and poroelastic results (3.11b) from the HII method plotted onto model of depth to crystalline basement (Langenheim et al., 2005). Filled circles have well data spanning 1993-2008, whereas filled semi-circles have well data spanning only a portion of the InSAR coverage.

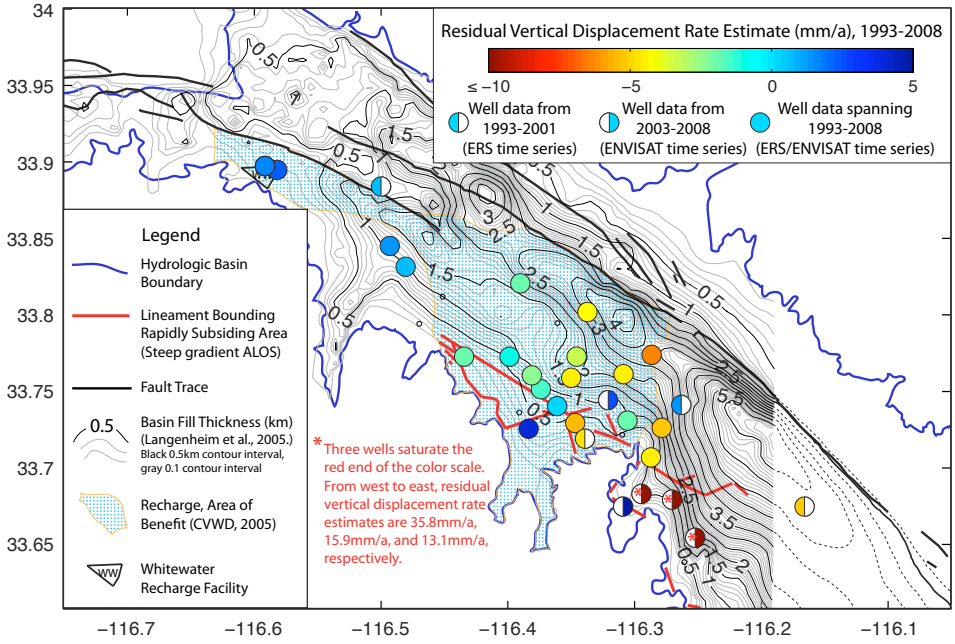
Residual Vertical Displacement Rate Estimate (mm/a), 1993-2008
≤ −10
−5
0
5
Well data from 1993-2001 (ERS time series)
Well data from 2003-2008 (ENVISAT time series)
Well data spanning 1993-2008 (ERS/ENVISAT time series)
Legend
Hydrologic Basin Boundary
Lineament Bounding Rapidly Subsiding Area (Steep gradient ALOS)
Fault Trace
Basin Fill Thickness (km) (Langenheim et al., 2005.) Black 0.5km contour interval, gray 0.1 contour interval
Recharge, Area of Benefit (CVWD, 2005)
Whitewater Recharge Facility
*Three wells saturate the red end of the color scale. From west to east, residual vertical displacement rate estimates are 35.8mm/a, 15.9mm/a, and 13.1mm/a, respectively.
34
33.95
33.9
33.85
33.8
33.75
33.7
33.65
−116.7
−116.6
−116.5
−116.4
−116.3
−116.2
−116.1

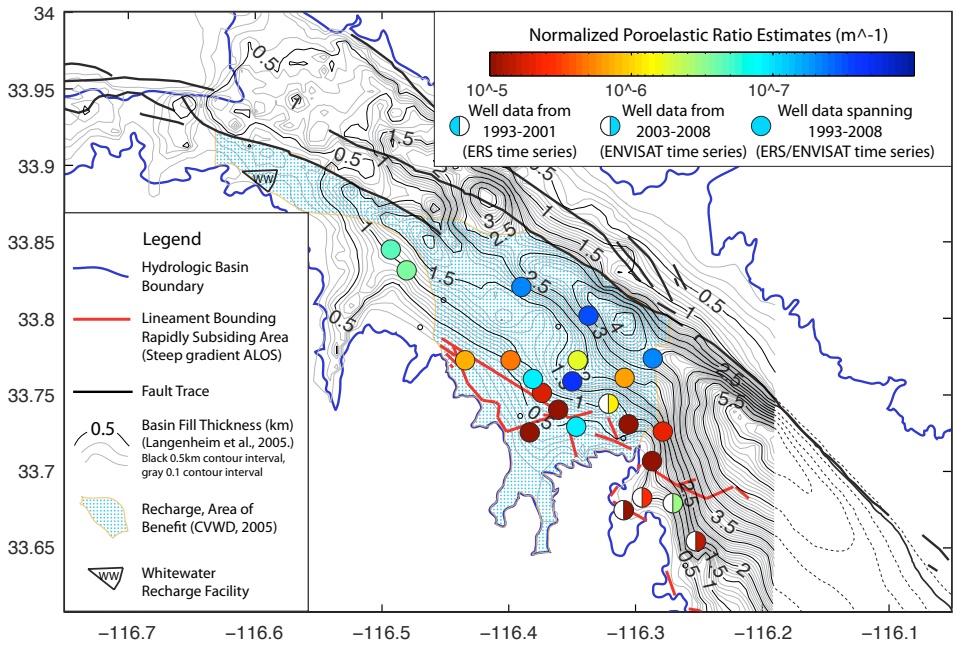
Normalized Poroelastic Ratio Estimates (m^-1)
10^-5
10^-6
10^-7
Well data from 1993-2001 (ERS time series)
Well data from 2003-2008 (ENVISAT time series)
Well data spanning 1993-2008 (ERS/ENVISAT time series)
Legend
Hydrologic Basin Boundary
Lineament Bounding Rapidly Subsiding Area (Steep gradient ALOS)
Fault Trace
Basin Fill Thickness (km) (Langenheim et al., 2005.) Black 0.5km contour interval, gray 0.1 contour interval
Recharge, Area of Benefit (CVWD, 2005)
Whitewater Recharge Facility
34
33.95
33.9
33.85
33.8
33.75
33.7
33.65
−116.7
−116.6
−116.5
−116.4
−116.3
−116.2
−116.1

7. ANALYSIS OF WATER WELL DRILLERS' SEDIMENT LOGS

7.1. Facies Classification

Characterization of hydrogeological units of an alluvial aquifer ideally includes knowledge of the geometry, interrelationships, and the hydrostratigraphy of the units hosting the groundwater reserve, and as in the case of Coachella Valley, often requires understanding of the system's ability to receive and distribute imported recharged water. Understanding geologic complexities of the subsurface is a key factor in the decision-making processes of water resource planning and management. Accurate hydrogeologic interpretations can be achieved using sedimentological data such as grain size and depositional properties (e.g. Anderson 1989; Neton *et al*. 1994; Scheibe & Freyberg 1995; Bertram & Texier 1999; Artimo *et al*. 2003). Such data reflect the style and relative velocity of sediment transport, and provide a basis for inferring depositional environment, and hydrogeologic parameters such as permeability and hydraulic conductivity (Neton *et al*. 1994; Scheibe & Freyberg 1995; Artimo *et al*. 2003).

This study applies concepts of sediment classification to assemble a generalized depositional facies analysis of the upper 300m of the Coachella Valley aquifer, dominantly based on grain size and sorting, and other details that may be included in water well drillers' logs. Without access to preserved sediment cores from the drilling of the aquifer, this study lacks data on smaller scale features of aquifer layers, such as cross-bedding or identification of paleosols. Cores and geophysical borehole records may greatly assist in further facies classification of the upper aquifer. Although in the following section I make interpretations with a limited data set, I show that the available sedimentological data from the driller logs may be utilized to yield meaningful results.

7.2. Data: Water Well Drillers' Logs

For 28 water wells in the central basin and western basin margin, sediment grain sizes with depth are consistently documented in well drillers' logs. However, the level of sedimentological details recorded in the drillers' log varies, with some field technicians recording detailed information about grain sizes and textures present over short depth intervals, and others recording less detail over much longer depth intervals. Occasionally logs are missing pages, and hence, the lower ~100m of data. Even with these discrepancies, the drillers' records, which span almost 3 decades of well installation, contain a great deal of information. The following section reviews the systematic cataloging and interpretation of 22 complete and relatively detailed well drillers' sediment records from the Upper Coachella Valley, and the process by which this information was used to assign depositional facies to the upper ~300m of the aquifer column at each well location. The goal is to transform the variable data contained in the drillers' logs to data useable in a statistical assessment or realistic conceptualization of lateral changes in the aquifer subsurface (e.g. Carr *et al*. 1966; Anderson 1989; Neton *et al*. 1994; Scheibe & Freyberg 1995; Carle *et al*. 1998). This assessment is used to conceptualize layers of the Coachella Valley aquifer subsurface.

The wells were installed between 1965-1992 by a variety of well drilling field technicians from a number of different drilling companies. Therefore, the well logs will naturally have some inconsistency and/or subjectivity in recording practices of the sedimentology. My method of cataloging driller logs illustrates as much of the information provided by the drilling field technicians as possible, while minimizing the "lumping" of data that is necessary to create a meaningful interpretation of the

subsurface. I estimate percentages of grain sizes present based on logged descriptions, infer sorting, and note the presence of cementation or free space. Along with sediment grain size, well depth is indicated in each well driller report and is usually level with the base of the outer gravel pack. Other data recorded in the logs are site parameters such as the perforated intervals of the well column, and groundwater levels at the time of installation. Frequently included in some records are terms relating to permeability of particular layers, including reference to cementation, free space (high porosity), and descriptions like "tight", "sticky", "hard", or "soft". Using the above information, I can attempt a systematic approximation of the characteristics defining certain alluvial fan deposits (Table 3.5), and demarcate vertical changes in depositional environment.

Table 3.5. Descriptions classifying depositional facies of alluvial basin deposits.

Depositional Facies	**General Description**
Playa Lake Deposit	Depth intervals where clay and/or cemented clay is the dominant feature. Lake deposits may also contain fine, medium or coarse sand, or small amounts of gravel.
Sheet Flood Deposit	Depth intervals of well sorted fine, medium or coarse sand. Some cementation may be present in the finest sheet deposits.
Stream Channel Deposit	Poorly sorted intervals of fine to very coarse-grained deposits. Lacking clay and cementation.
Sieve Deposit	Well-sorted gravel deposits.
Debris Flow Deposit	Poorly sorted intervals of the finest to the coarsest grain sizes, with distinct clay matrix and/or cementation.
Aeolian Dune Sand Deposit	Surface deposits of well-sorted wind-lain sands. Facies assigned only where surface deposit of well column matches surface deposit of Qs on geologic maps as evidence of dune structures is not available in the well driller logs (Sims, 1961; Rodgers, 1965; Dibblee, 2008).

7.3. Methods: Standardization of Sediment Reports

Figure 3.12a represents the first stage in the systematic cataloging of estimated grain size distribution and sorting of the different depth intervals. The data are anchored to a color axis at the bottom of the figure with a vertical black line between medium and coarse grain sand (1.0 on the Phi scale). This anchor is mostly used as a graphical link to the color scale, with the finest grained material on the left, and the coarsest on the right. Where a material is present in a layer, this is indicated in the color column above the color scale. Trace amounts of a particular material in a particular layer are indicated by white diagonal hachure marks. This first stage provides an initial assessment of grain size distribution of the well array. Preliminary results showed a conspicuous lack of correlation between grain-size distribution and the observed subsidence rate at the well sites, suggesting grain size percentage in a shallow well column may not be entirely indicative of hydrogeologic properties and surface displacement response to changes in groundwater level at depth. I therefore find it necessary to also include the available data on the grade of sorting into the analysis. I assume a particular depositional environment based on both grain size distribution and sorting. The alluvial fan depositional facies present in the upper 300m of the Coachella Valley aquifer are described in Table 3.5. This method of categorizing and interpreting well driller logs is an original method.

7.4. Methods: Interpreting Depositional Facies

Alluvial fan deposits in arid regions are largely transported by the intense yet infrequent storm and flood events, with relatively little sediment transport during the intervening periods. Vertical sequencing is usually irregular and inconsistent with

individual beds showing either no change in grain size, coarsening upward, or thinning upward (Boggs 1987; Neton *et al*. 1994). In general, a progradational fan will show strong thickening and coarsening upward, while a retrogradational fan will trend towards thinning and fining upward. Figure 3.12b shows the interpreted depositional facies to the sample sediment log in Figure 3.12a.

Deposition in the proximal alluvial fan environment tends to produce the coarsest and most poorly sorted of alluvial deposits. Rock falls, rock avalanches, and other deposits of the proximal fan environment tend to have strong porosity. These include the coarse-grained, clast-supported, and well-sorted gravel sieve deposits, thought to represent former rills and outwash plains or buried residual pavements (Bertram & Texier 1999; Milana 2010). Also coarse and clast-supported, the more poorly sorted stream deposits are common in the proximal alluvial fan. Another common facies type are debris flows, which are poorly sorted and often containing blocks and boulders, with muddy matrix. Typically, these matrix-rich conglomerates are impervious and non-porous, with the exception of where stream channels cut into the debris flow and remove fines (Bertram & Texier 1999).

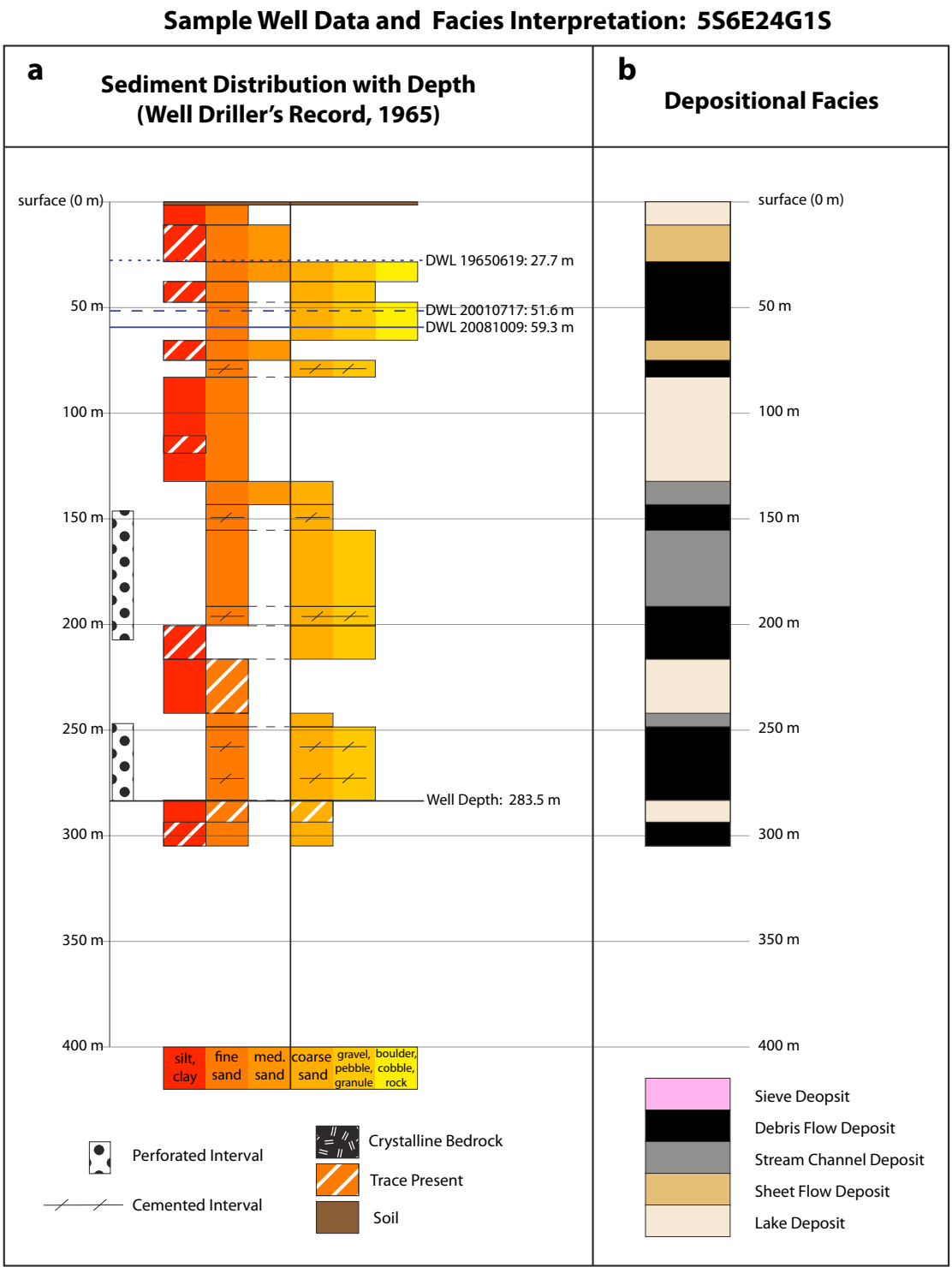

Figure 3.12. Sample Well 5S6E24G1S, graphic display of sediment distribution with depth (3.12a) and ascribed depositional facies (3.12b).

Stream channel, sieve, and debris flow deposits may also be found in the mid-fan. However, the mid fan environment is dominated by non-channelized flow of water and sediments. As the flow energy of the sediment and water mixture is dispersed by the fan lobe, the sediment falls out of suspension and is deposited in well-sorted, thin, and relatively laterally continuous lenses of silt, sand or gravel known as sheet flood deposits (Neton *et al*. 1994). Blair & McPherson (1994) also describe sheet flood deposits as having intervals of gravel and sand couplets and planar-bedded sand skirts, and provide evidence that sheet flood deposition is an important fan-building process. After deposition these types of flows lack cohesion, but may be moderately indurated by secondary carbonates in fine distributed crystal form (Bertram & Texier 1999). Porosity may also be enhanced by strong run-off activity.

Basinward of alluvial fan deposits in arid environments are often playa lake and dune deposits. These deposits are composed of the finest material, largely sand, silt, and clay, with occasional thin conglomerate layers (Boggs 1987). These deposits tend to be well sorted with only the rare occurrence of channel facies, and largely represent sediments winnowed and transported by wind and water. In terms of aquifer partitioning, fine-grained clay-rich layers like playa lake deposits play an important role, as do fault offsets that juxtapose lithologies. The delineation of the extent and continuity of confining layers largely determines vertical and horizontal connectivity of an aquifer, and is crucial in controlling artificial recharge. Faults often act as barriers to groundwater flow through separation of alluvial, fluvial and lacustrine hydraulic units. Lakebed deposits and fault-offset lithologies are both observable at the Coachella Valley basin surface, and are also known to be present in the subsurface of the aquifer. In terms of

aquifer transmissivity and well production, it is the coarser deposits that largely provide accessible groundwater resources.

The method used here for interpreting facies from water well driller logs is novel and uses a simple approach and application, but also is likely affected by the oversimplification of deposits in the recording data (well driller logs), by the assigning of a depositional facies (Fig. 3.12b), and in the mapping depositional facies. For example I am unable to differentiate a well sorted, medium sand-sized sheet flood deposit from a medium sand sized aeolian dune deposit without additional information besides the driller log. Nevertheless, my methodology attempts to extract the maximum information from the drillers' logs.

7.5. General Facies Trends

The distribution of depositional facies for the Coachella Valley wells is plotted in Figure 3.13, with each column representing the depositional facies with depth from the surface down. In general, the wells located in the central and northeastern parts of the basin (outside of the subsidence lobes) show the most frequent occurrences of thick sand-rich sheet flood deposits, interbedded with some significant stream channel facies, and the occasional occurrence of debris flows. Fine-grained lakebed deposits commonly occur in the well columns of the north central basin, but appear to have irregular lateral continuity. These observations imply that the north central well array is in an area dominated by mid-fan alluvial deposition.

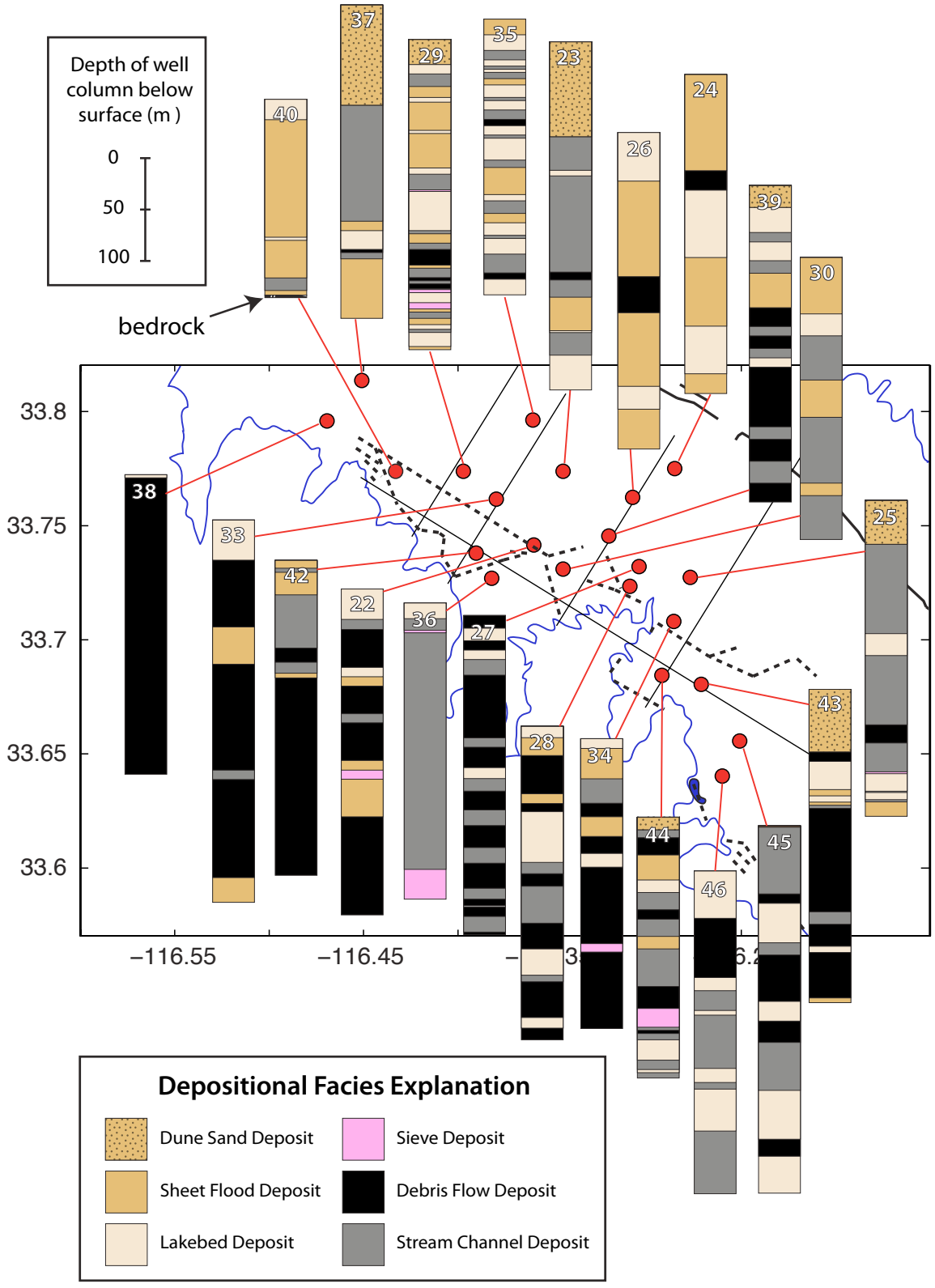

Figure 3.13. Depositional facies of well columns in study area.

The wells closer to the Santa Rosa Mountains range front show significantly more of the coarsest depositional facies, with very thick intervals of debris flow and stream channel deposits, and some significant sieve deposition as well (Fig. 3.13). Sheet flood and lakebed deposits are observed in the columns nearer the range front, but both occur with less frequency or have been scoured and obliterated by subsequent coarser grained deposition. These characteristics imply proximal fan deposition, consistent with proximity to the range front. Although lakebed deposits persist in various columns through the entire array in general these finest deposits are thickest and most abundant farthest from the range front and toward the southeast (Fig. 3.13). Although I focus on the San Jacinto and Santa Rosa Mountains as the sources of alluvium, the Little San Bernardino Mountains to the north may contribute some sediment as well.

7.6. Results of Depositional Facies Analysis

Using the compiled data on depositional facies, I contour gross percentages of coarse grained, dominantly proximal fan deposits, which include stream, sieve and debris flow deposits (Fig. 3.14). The contouring shows that the highest concentrations of coarse-grained alluvial deposits are concentrated near the steep southwestern boundary of the basin, with contours deflected to the northeast downstream of the two largest canyons. Concentrations of coarse deposits decrease to the northeast into the central basin. This facies trend is consistent with the expected overall fining of sedimentary deposits away from the range front and supports the validity of this analysis.

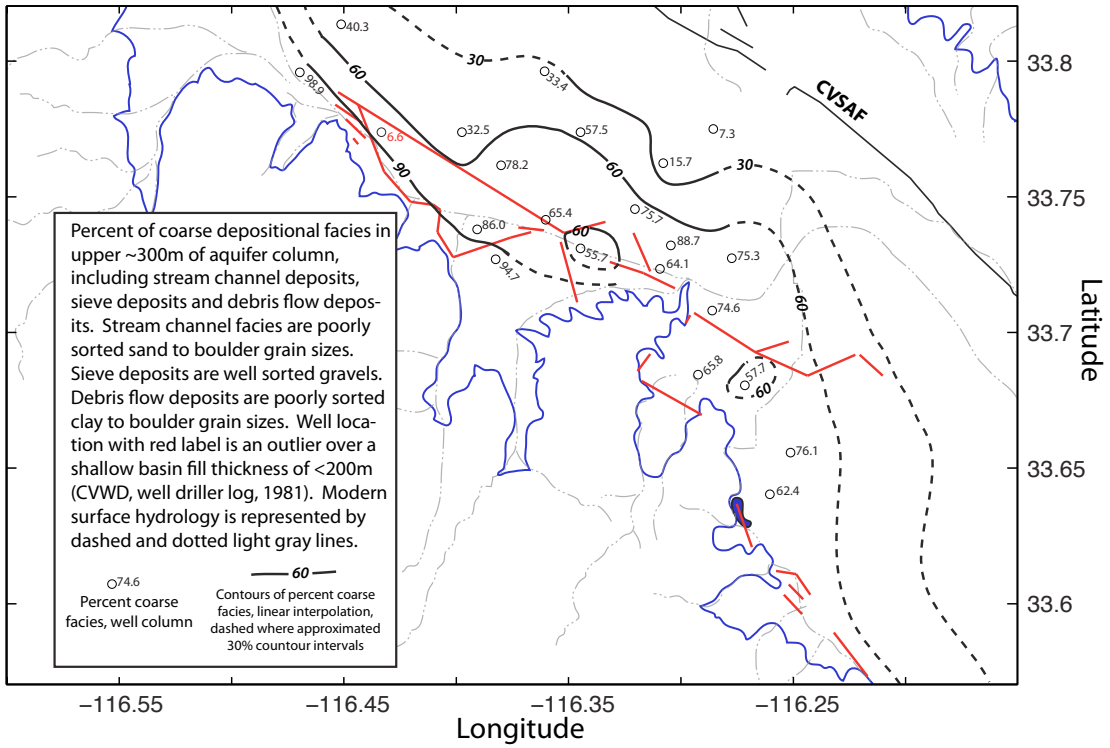

Figure 3.14. Contoured percentages of coarse depositional facies, upper ~300 m of the aquifer. Blue lines represent hydrologic basin boundary. Red lines locate the boundaries of abrupt subsidence. Light gray dashed and dotted line represent surface hydrology.

Compaction related subsidence in fine-grained aquifer layers may occur as a delayed response to prolonged overdraft conditions and, at certain pore stress thresholds, will begin to rapidly and permanently deform the fine grained aquitard and aquiclude layers (e.g. Riley 1969; Poland 1984). Sneed & Brandt (2007) concluded that the relationship between surface displacement and coeval groundwater levels at geodetic monuments in the Coachella Valley is complicated and not clearly defined. They attribute complications to the overprinting of seasonal and long-term changes in groundwater levels, and the delayed compaction of fine-grained layers, suggesting preconsolidation stresses may have been surpassed, inducing permanent compaction. To address the above questions, I contour gross percentages of lakebed facies, assuming

these dominantly clay and silt deposits may undergo compaction and rapid subsidence related to aquifer overdraft (Fig. 3.15).

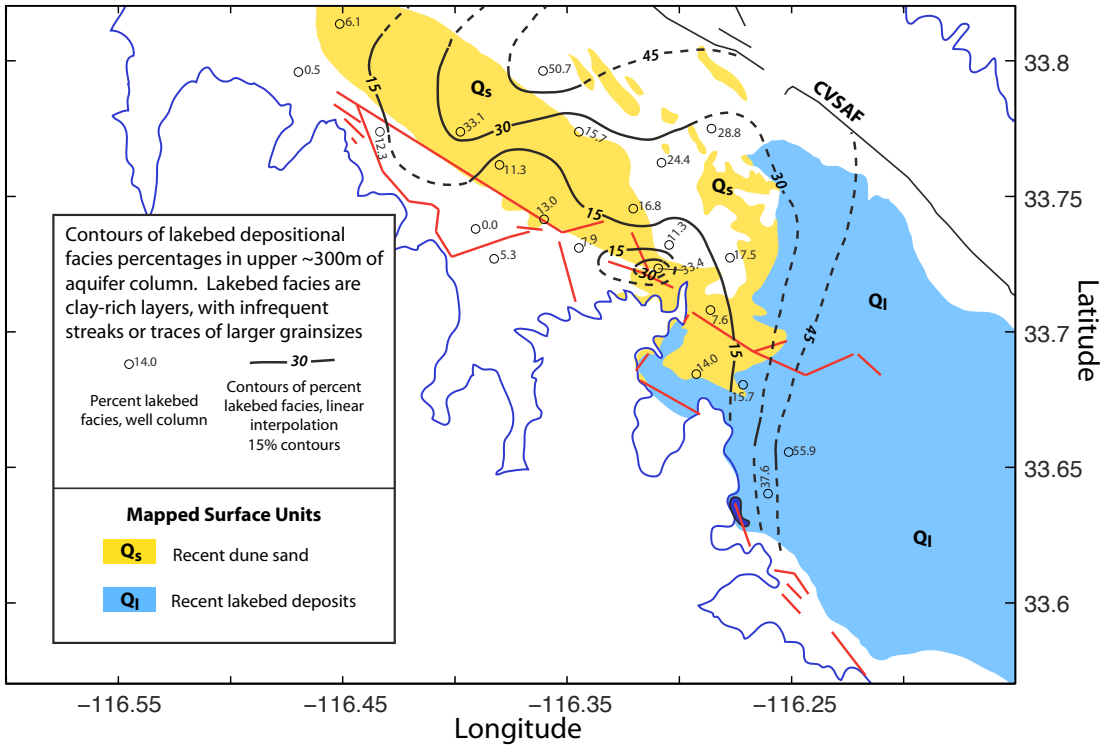

Figure 3.15. Contoured percentages of lakebed facies, upper ~300 m of the aquifer with mapped surface dune and lakebed deposits (modified from Sims, 1961; Rodgers, 1965; Dibblee, 2008).

The lowest concentrations of significant lakebed deposits are close to the southwestern basin margin (Fig. 3.15). This result is in agreement with the CVWD (2005, 2010) engineer's report, in which these areas are reported as unconfined. Where well data were not available, I use the mapped surface geology of the Quaternary lakebed deposits to guide the inferred southeastern contours of fine-grained percentages. The rapidly subsiding regions all have conspicuously low concentrations of lakebed deposits with the exception of the area east of lake Cahuilla where lakebed deposits are exposed at the surface. This contour plot (Fig. 3.15) indicates that processes other than the

compaction of basin-wide lakebeds are likely controlling the rate and locations of subsidence in the western basin margin. In the following section I discuss the groundwater aquifer in the western basin margin, as reflected by the interaction of groundwater flow barriers and anthropogenic surface displacement, complemented by a geophysical basin thickness model (Langenheim *et al*. 2005).

8. DISCUSSION

8.1. Synthesis of Basin Stratigraphy, Structure and Deformation

In this section I synthesize the broad variety of results obtained from InSAR, groundwater levels and well driller logs. I am also able to model surface displacement and suggest plausible hydrogeologic structures that may be controlling the enigmatic pattern of surface displacement. Mechanisms for the patterns of differential surface displacement in the western Coachella Valley basin margin considered in the following section are: 1) fine-grained localized lenses of compaction related to overdraft conditions and insufficient groundwater flow pathways to artificial recharge, 2) concentrated land use, either urban, recreational, or agricultural regions, and 3) the presence of vertical to sub-vertical groundwater flow barriers (e.g. faults). Surface displacement caused by compacting lenses of fine-grained material is explored with the deformation and stress change software Coulomb 3.3 (Toda *et al*. 2011), and I find this hypothesis to be the most plausible, although components of concentrated pumping and groundwater flow barriers cannot be completely discounted. Using the constraints from InSAR and the depositional facies analysis, I first construct cross-sections (Fig. 3.16), interpreting the structure of the

aquifer. These synthesized figures (Figs. 3.17-3.21) are the basis for the parameterization and iterations for the numerical models of surface displacement in the next section.

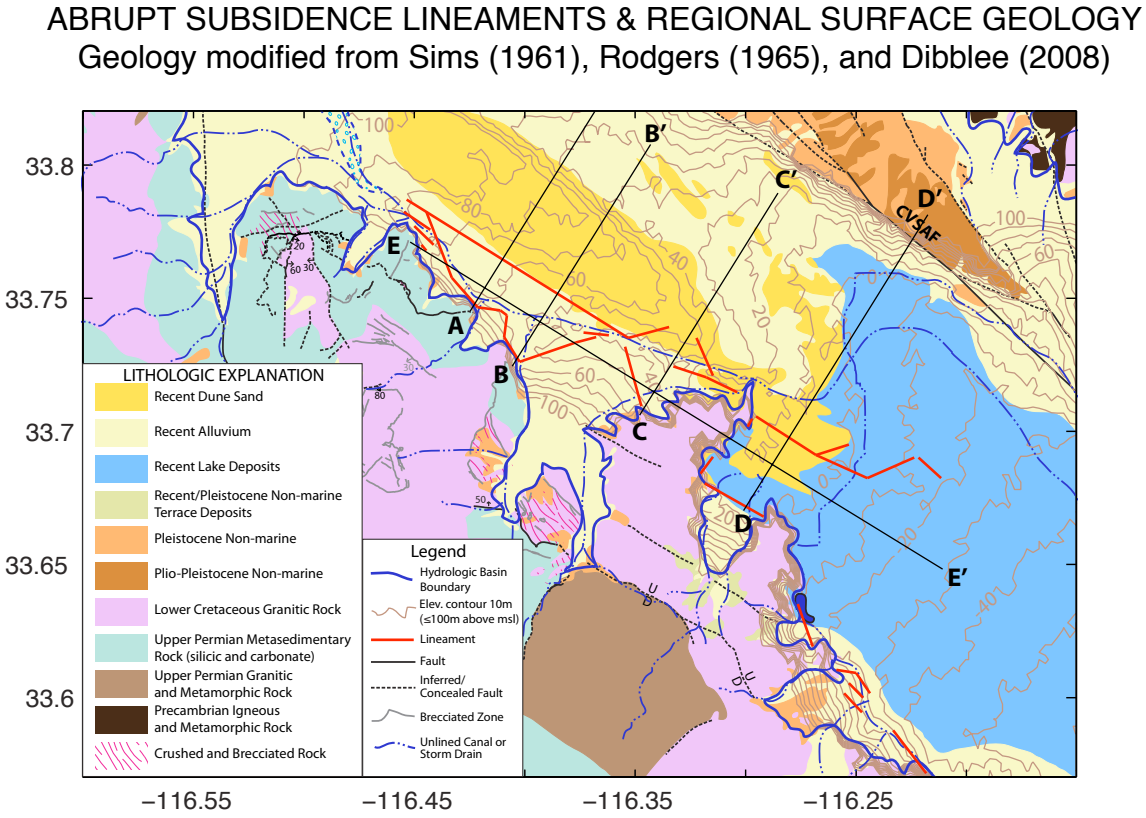

Figure 3.16. Compilation of regional surface geology in relation to rapid subsidence boundaries and cross-sections in the following Figures 3.17-3.21. Topography of the basin (≤100m above msl) is mapped at 10m contour intervals as well.

In the lines of cross-sections (Fig. 3.16), I directly compare surface displacement, surface elevation, the crystalline basement/sediment interface (Langenheim *et al*. 2005), and significant lakebed deposition from the hydrostratigraphic analysis. To map the rapid subsidence, I use the ALOS data between 2006-2009 (Fig. 3.2) because the L-band data provides the most spatially continuous data set. Topographic profiles are labeled where deposits other than generalized Quaternary alluvium are specified at the surface.

Some of the rapid subsidence rates occur in close proximity to the Whitewater River channel and to many of the local storm channels, which are both intermittently dry. I therefore also indicate the surface hydrology in the cross-sections. Cross-sections A-A' (Fig. 3.17) and B-B' (Fig. 3.18) span the shallow, gently sloping basin margin that underlies the northernmost lobe of rapid subsidence. Cross-section C-C' (Fig. 3.19) spans the middle subsidence lobe, which has a fairly steep crystalline basement/sediment interface at the basin margin, but flattens indicating a small semi-isolated depression in the crystalline basement rock below observed rapid subsidence. Cross-section D-D' (Fig. 3.20) spans the southernmost subsidence lobe, where the crystalline basement/sediment interface is steep, and basin thickness quickly reaches a maximum depth of 5.3 km. Perpendicular to the other section lines, cross-section E-E' (Fig. 3.21) trends NW, parallel to the swath of subsidence lobes, and intersecting both alluvial fill and uplifted crystalline basement.

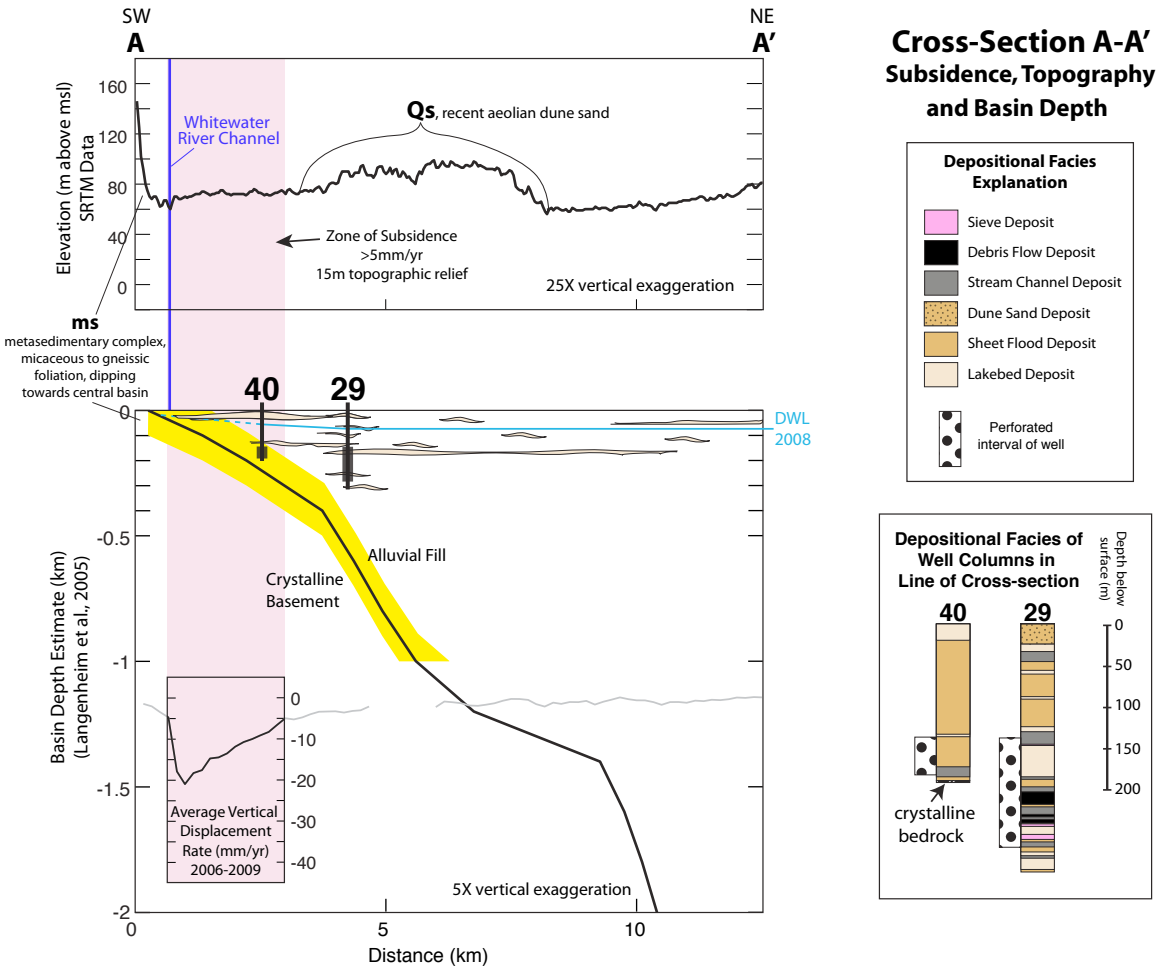

Figure 3.17. Compositional cross-section A-A' illustrating spatial relationship of surface topography, crystalline basement topography, subsidence, and depositional facies analyses of well columns.

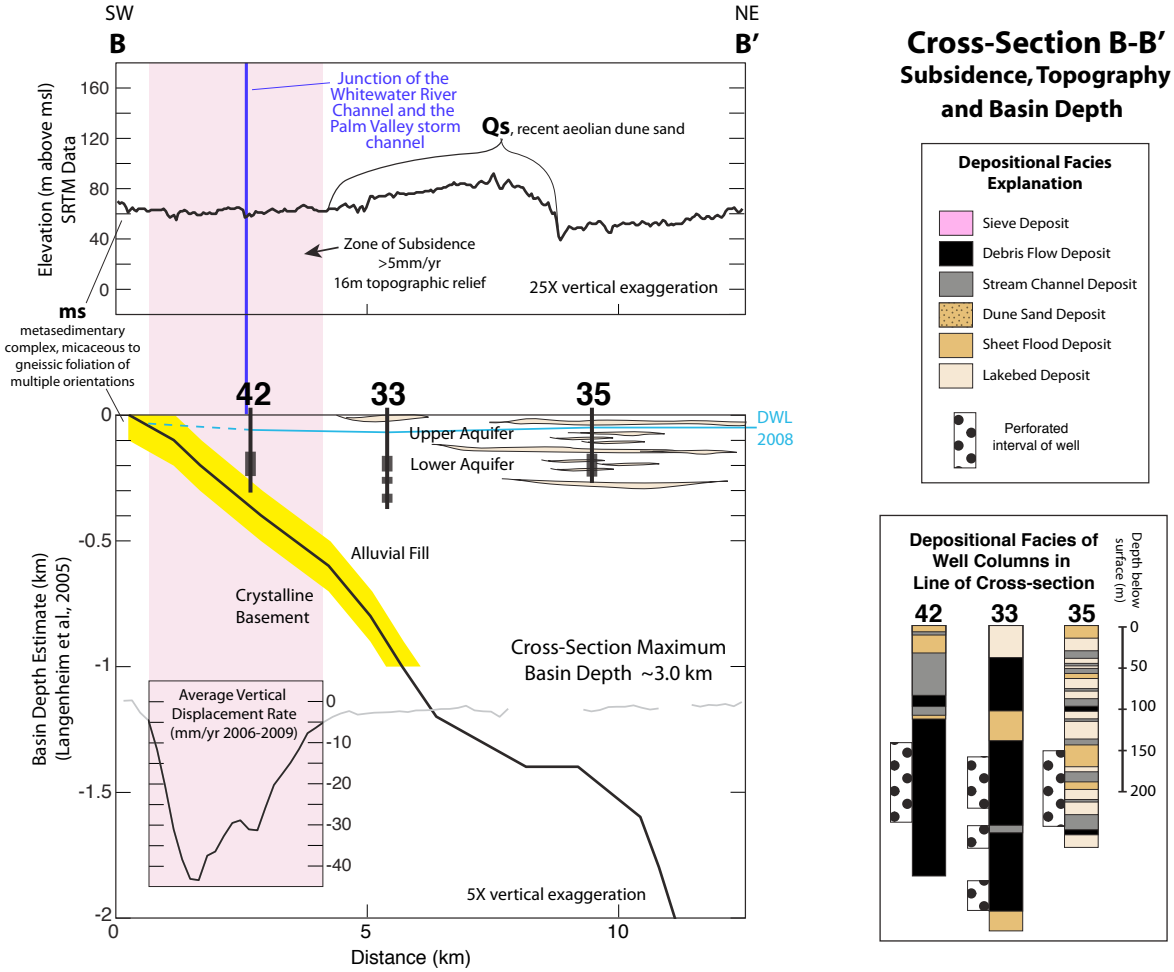

Figure 3.18. Compositional cross-section B-B' illustrating spatial relationship of surface topography, crystalline basement topography, subsidence, and depositional facies analyses of well columns.

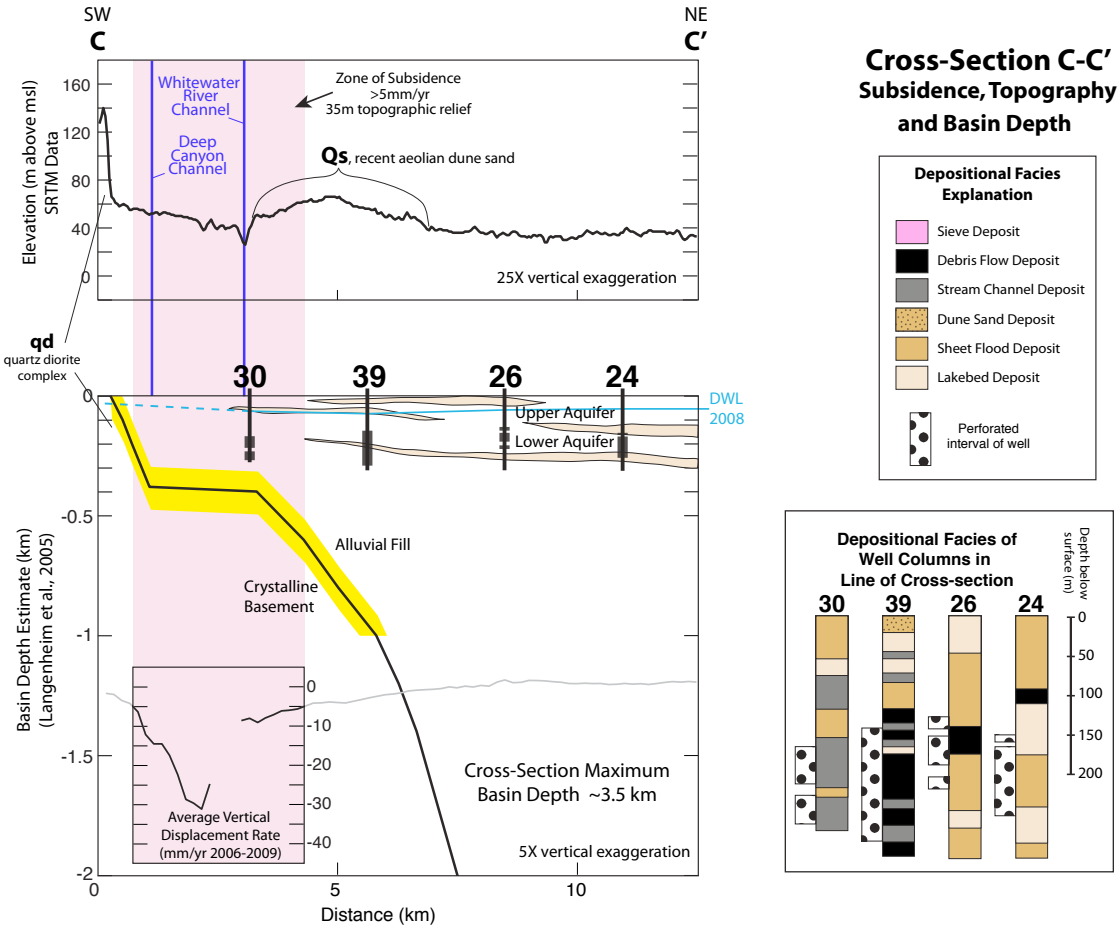

Figure 3.19. Compositional cross-section C-C' illustrating spatial relationship of surface topography, crystalline basement topography, subsidence, and depositional facies analyses of well columns.

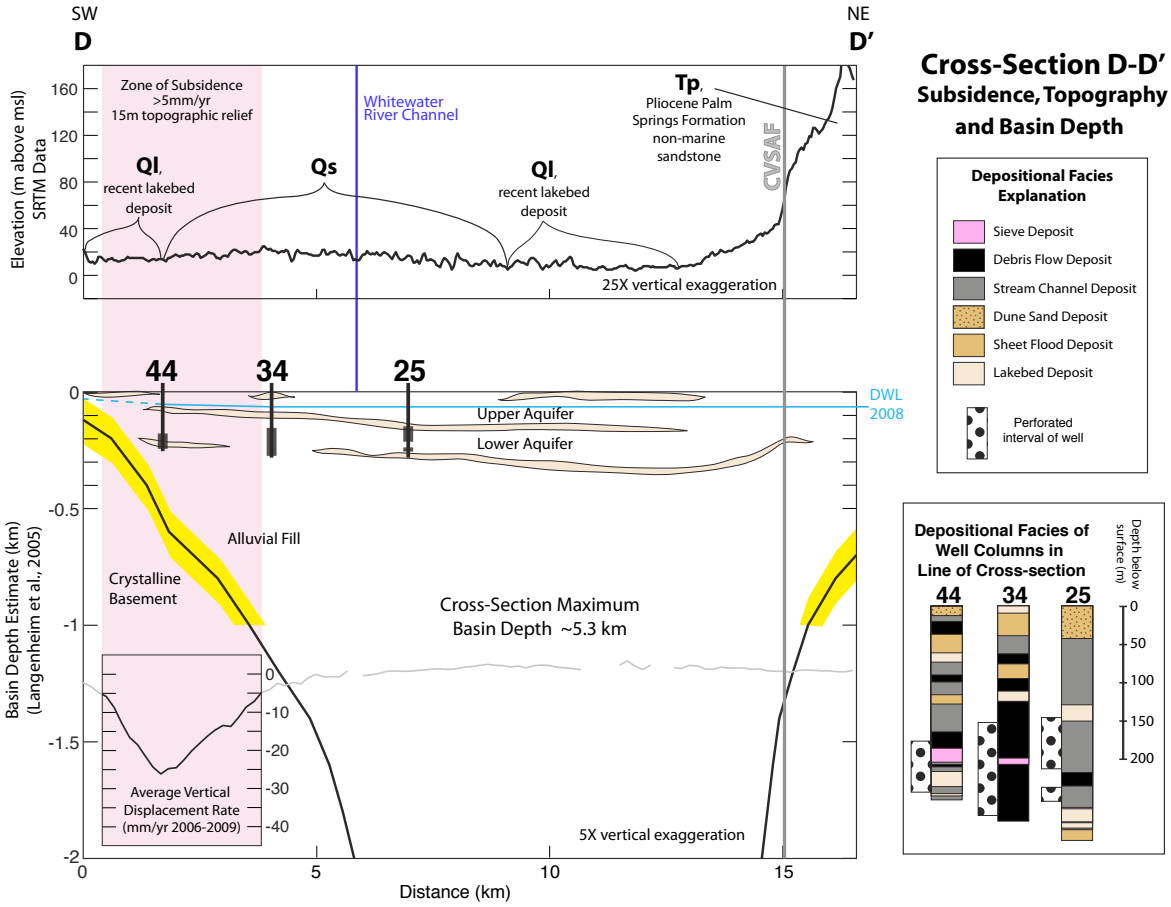

Figure 3.20. Compositional cross-section D-D' illustrating spatial relationship of surface topography, crystalline basement topography, subsidence, and depositional facies analyses of well columns.

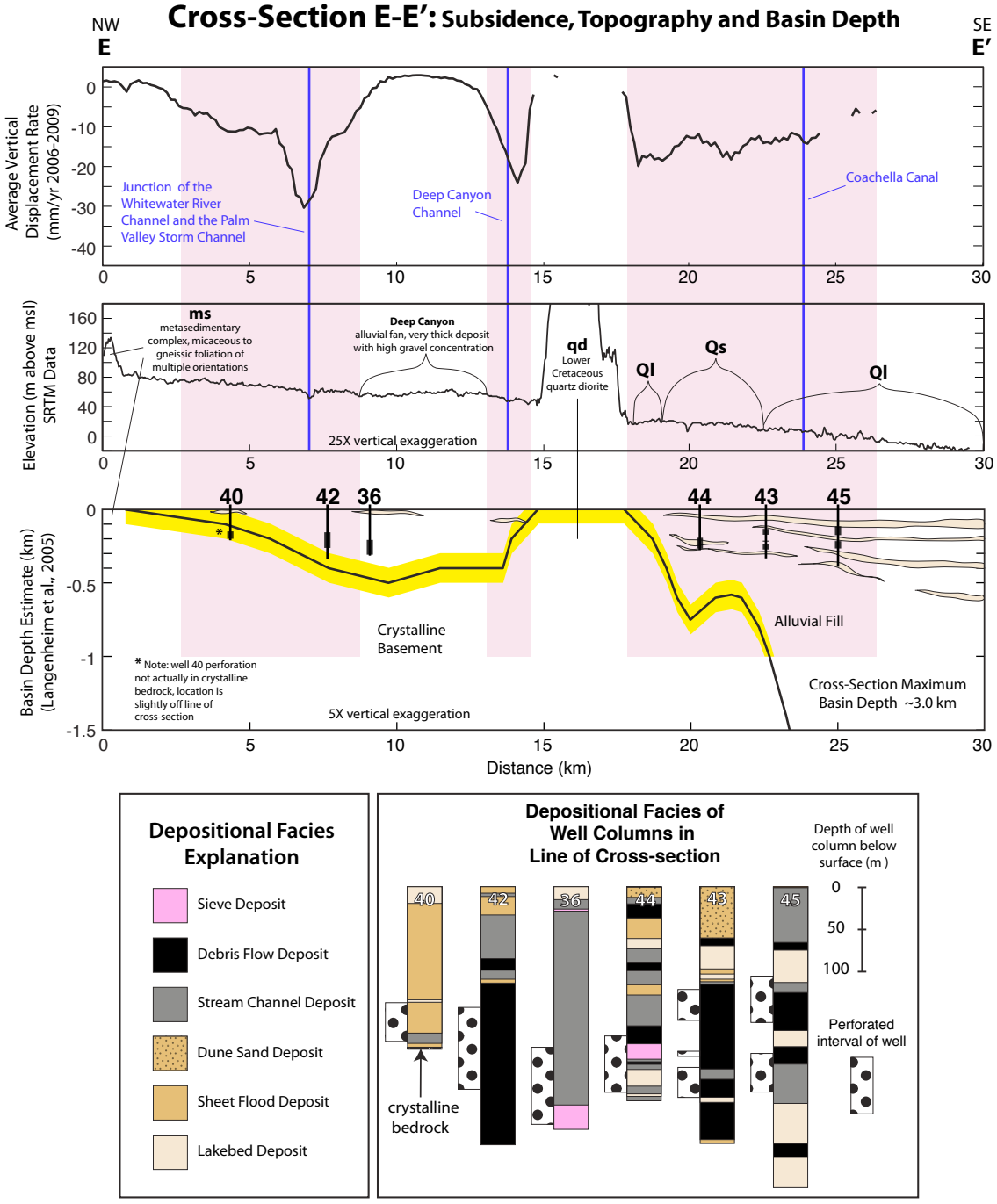

Figure 3.21. Compositional cross-section E-E' illustrating spatial relationship of surface topography, crystalline basement topography, subsidence, and depositional facies analyses of well columns.

The basin model from Langenheim *et al*. (2005) used in Figures 3.17-3.21 is constrained by gravity and seismic data, which locate sharp lithologic changes, and by aeromagnetic data, which indicate magnetic anomalies reflecting the presence of magnetic bodies in the mid to lower crust. For the Upper Coachella Valley this is generally indicative of the crystalline basement rock. Seismic velocity models reflect density variations, and may provide constraints on sharp lithologic interfaces that are represented in the gravity data by steep gradients. This non-unique, iterative modeling process will produce a geologically reasonable structure with minimal structural complexities (Langenheim *et al*. 2005). The authors utilize the density/depth function defined in Anderson *et al*. (2004), which introduces uncertainties in depth estimates of ~100m for depths less than 1 km (thick yellow line in Figures 3.17-3.21) and 100–300m for depths greater than 1 km. Faults may not always appear as gravity or magnetic anomalies, particularly those faults that cut through shallow alluvium, and may not be detectable in measurements or recognizable in data processing. There may be minor but locally significant topographic features in the basement interface that are not resolved.

Surface deformation plotted on Figure 3.17 indicates subsidence is concentrated in a gentle topographic depression on the southwest side of the Quaternary dune deposits and reaches a maximum subsidence rate of over 20 mm/yr. In cross-section A-A', the southwestern bounding lineament of the zone of subsidence is coincident with the Whitewater River Channel, and subsidence is greatest just inside this boundary, lessening gradually to the northeast. The rest of the cross-section is undergoing near zero subsidence rates between 2006-2009. Subsidence must be focused in this cross-section above basin depths of 50-300m as I assume the poroelastic response of the crystalline

bedrock to the alluvial aquifer is negligible, although some studies suggest bedrock is susceptible to hydraulic deformation where crevice pore space and clay-rich lithologies (argillite and shale) are present in the basement rock (Gourmelen *et al*. 2007). Notably, only minor layers of fine-grained lakebed deposits are observed in this cross-section below the depth of the water table and above the basement rock. Well 40 is recorded to have reached crystalline bedrock, which is consistent with the Langenheim et al. (2005) basin depth model. Well 29 is outside of the zone of rapid subsidence and illustrates a location that has been host to varying styles of deposition through time, but consists primarily of sand size sediments with some coarser materials concentrated lower in the well column. The array of depositional environments observed in well 29 suggests a period where coarse proximal fan deposition occurred interfingering with mid-fan and distal fan deposition.

The zone of subsidence in cross-section B-B' (Fig. 3.18) is broader in map view than section A-A', and also occurs in a shallow topographic depression southwest of the Quaternary dune sand deposits (Fig. 3.16). Again, the most rapid subsidence across the entire basin occurs near surface hydrology, where the Whitewater River is intersected by the Palm Valley storm Channel. The maximum observed subsidence rate in this cross-section between 2006-2009 is ~43 mm/yr, and near zero subsidence rates are observed towards the central basin. The broad zone of subsidence shows two troughs of subsidence, and is over a slightly deeper basin than section A-A', between 50-600m thick. Well 42, located within the zone of subsidence, bears a high concentration of debris flow deposits, indicating dominantly coarse and poorly sorted near-range front deposition. Well 42 is near the fluvial channel, and thick intervals of streambed

deposition in the mid-level well column, suggest a fairly consistent location of fluvial deposition through basin sedimentation. Outside of the zone of rapid subsidence, well 33 also bears thick coarse-grained depositional layers lower in the section, but is capped by a significant thickness of lakebed deposits. Based on groundwater levels for this well, this upper lakebed deposit is not likely in the saturated zone of the aquifer and therefore could only be a dominant contributor to surface subsidence if it is undergoing delayed compaction due to time-dependent dewatering of clay-rich deposits (Riley 1969; Poland 1984). Well 35 is over deeper basin thickness and hosts varying depositional facies through the vertical section. Coarse-grained layers are less frequent in well 35, and many lakebed and sheet flood deposits have been preserved in the section. Given the central basin location of well 35 and its close proximity to surface dune deposits, I suspect some layers ascribed the sheet flood facies in this column may instead be aeolian dune deposition.

Cross-section C-C' (Fig. 3.19) spans the middle subsidence lobe which overlies significantly different basement rock topography than cross-sections of the northern subsidence lobe (Figs. 3.17, 3.18). Instead of the gently sloping basement surface seen in previous cross-sections, it overlies a relatively flat shelf of crystalline basement rock at ~400m depth. Maximum observed subsidence rate is ~30 mm/yr and occurs midway between the two main fluvial channels of the Whitewater River and the Deep Canyon Channel which intersect downstream near Point Happy (Fig. 3.16). There are 4 wells in cross-section C-C', one of which, well 30, is centered over the middle subsidence lobe, above the edge of the buried crystalline basement shelf and very near the Whitewater River Channel. The facies analysis suggests this location has been the repeated and

persistent site of the local channel system. Well 39 overlies a steeper section of basement topography, and is vertically divided into a dominantly coarse-grained lower section and a dominantly fine-grained upper section, a likely representation of the progression of basin margin southwestward as the basin filled with alluvium. Wells 26 and 24 overlie the deep central basin and are locations where aquitard layers begin to persist enough to begin hydraulic separation of an upper and lower aquifer layer. Both wells 26 and 24 are dominated by distal fan depositional facies, with an apparent episode of debris flow deposition. The thick uppermost lakebed deposits in each well do not appear horizontally continuous, but are thick enough to impede vertical conductivity (CVWD 2005).

Cross-section D-D' (Fig. 3.20) spans the south lobe of rapid subsidence, crosses the central basin, approximates the location of the San Andreas fault, and identifies the mapped Quaternary lakebed and dune sand deposits at the surface. The zone of subsidence in this cross-section overlies a moderately sloped basement interface with a basin thickness between ~100-1000m. The gradient in subsidence rate for cross-section D-D' is not as steep as the gradients in the northern and middle lobes, and the maximum subsidence rate is ~26 mm/yr. Also unlike the cross-sections to the north, the rapid subsidence does not appear coincident with the surface hydrology, and the contact between the dune sand and other surface deposits is not coincident with the border of rapid subsidence. These differences may distinguish mechanisms of rapid subsidence. The wells in Figure 3.20 all have 2-3 significant lakebed deposits in the vertical section, consistent with the CVWD's report that lakebed deposits are more laterally continuous in this part of the aquifer (CVWD 2005). Percentages of coarse and fine-grained facies are similar for all three wells, and thick sections of the well-sorted sheet flood deposits are

less frequent in this area. Well 25 is dominated by streambed facies and would support a southwestward river channel migration in recent time, based on current location. If the line of cross-section extended further southwest, it would span the gently sloping basement rock interface of the La Quinta alluvial fan and its relatively thin (≤120m) alluvial accumulation. The La Quinta fan bears near zero subsidence rates and the steep subsidence gradient at the mouth of the fan is distinct, as are the steep gradients at the mouth of the Deep Canyon fan between the north and middle lobes.

Perpendicular to the other lines of cross-section, E-E' (Fig. 3.21) intersects all three subsidence lobes, the crystalline spur between Indian Wells and La Quinta, as well as the Deep Canyon alluvial fan. The Deep Canyon fan is a very coarse grained and thick accumulation of sediments reaching ~500m depth at its thickest point in the cross-section. Rapid subsidence between 15-30 mm/yr coincides with the modern storm channel system in the northern and middle lobes of rapid subsidence, while subsidence in the southern lobe is consistently 15 mm/yr and does not exhibit such sharp troughs in the graph. Although it is difficult to distinguish any mechanical basis for rapid subsidence in this long line of cross-section, the variations in basin thicknesses, topographic gradient, and hydrogeology are emphasized and the geologic complexity of the tectonic basin setting is observable. The depositional facies of the south lobe indicate a persistent occurrence of lakebed deposition at intervals in the upper 300m. Well sites 42 and 36 both overly basin depth of 300-500m, and between them is one of the steep subsidence gradient lineaments observed at the mouth of Deep Canyon (Fig. 3.2). Both columns are dominated by the coarsest depositional facies, with minor fine facies. The observation that rapid subsidence is occurring where clay-rich deposits are absent (well 42), and

relatively no subsidence is occurring where the section is capped with a clay-rich facies (well 36) supports the previous statement that delayed compaction of basin-wide fine-grained lakebed facies is not a reasonable explanation for residual subsidence. However, the compaction of localized lenses of the clay-rich material remains a possible explanation of deformation patterns, as some lenses may not have been resolved by the hydrostratigraphic analysis.

Wells 44, 43, and 45 are all within the south lobe of rapid subsidence and all exhibit significant lakebed deposition. The wells in this part of the basin share a characteristic depositional sequence of significant lakebed facies interbedded and alternating with significantly thick deposits of the coarsest material (See also Fig. 3.13), with some relatively minor variations. This alternating depositional style may be indicative of pulses in tectonic activity, where episodes of broad subsidence and basin-wide lakebed deposition precede quiescent intervals when weathering, erosion, and transport of source material to the alluvial fans can occur on a large scale. More likely the Salton Trough is simply subject to periodic filling of the lake. The significant difference in elevation between subsidence lobes to the north and south of Point Happy appears to play a significant role in depositional styles of the upper aquifer layers, consistent with high stands of Ancient Lake Cahuilla.

8.2. Modeling Surface Deformation

To test whether compaction of fine-grained lenses at depth in the aquifer is a feasible explanation for surface displacement patterns observed in the western basin margin, I construct models of closing on horizontal to sub-horizontal planes in an elastic

half space using the deformation and stress change software Coulomb 3.3 (Toda *et al*. 2011). Although the modeling of surface displacement produces non-unique solutions, it provides insight to plausible displacement patterns related to compacting bodies at varying depths in the subsurface. I vary the model inputs to explore the effects of depth, width, dip and magnitudes of closure (compaction) in the model aquifer. Thickness of compacting layers are not represented in the modeling, although presumably a layer compacting at several millimeters per year would need to be of significant thickness (3m or more) to undergo compaction for decades. The models are not hydrologic models and do not account for inter-granular displacement of aquifer material and do not discriminate between elastic and inelastic hydraulic deformation. The method is also only an approximation of deformation since it does not directly model the compaction process. A similar modeling approach was used by Bawden *et al*. (2001) to model subsidence in the San Fernando Valley near Los Angeles. To replicate the peaks, troughs, asymmetry, and slopes of the surface displacement observed with InSAR, I use the hydrostratigraphic analysis as first order constraints on the locations and magnitudes of compaction in the aquifer cross-sections.

Figure 3.22a focuses in on the subsiding area of cross-section A-A' (Fig. 3.17), where the most rapid subsidence occurs near the basin margin. By trial and error, I approximate the asymmetric subsidence curve by modeling surface displacement related to a single shallow (25m depth) compacting layer, with tapering compaction towards the basin center and a sharper tapering of compaction towards the basin margin. Tapering the compaction is required because uniform layers with constant closure cannot reproduce the observed cross-sectional displacement of subsidence. Model tapering is

accomplished with multiple dislocations at one depth, varying in their lateral width and relative distribution. As observed in Figure 3.17, significantly thick lakebed facies exist in the upper aquifer and compaction of this clay-rich stratigraphy may be interpreted as delayed compaction related to historical dehydration of near surface aquitard layers. Between 2003-2008 ground water levels decreased up to 2m/a at well 40 (Fig. 3.17), supporting the plausibility of overdraft related compaction. The shallow basin thickness at this site vertically limits the depth of water-bearing deposits (Fig. 3.22a) and as a result limits accessibility to artificial recharge water, the majority of which flows into the lower aquifer (CVWD 2005). Multiple lakebed facies appear in well column 29 (Fig. 3.22a), yet subsidence is not as extreme at this location. This implies not all clay-rich deposits are undergoing compaction. My interpretation is that shallow lenses in a formerly saturated zone of the aquifer are now in the unsaturated zone and their compaction may be contributing to surface displacement patterns.

Figure 3.22b focuses in on the subsiding area of cross-section B-B' (Fig. 3.18). This subsidence profile has two troughs and crosses one of the most rapidly subsiding locations in the study area. Since well 42 does not exhibit significant lakebed deposition, I model narrow sections of compaction that do not intersect the well column. By modeling surface displacement related to staggered and roughly tapered compacting layers (one towards the basin margin of well 42, and one stratigraphically below the well column) observed surface displacement may be roughly replicated. Unlike the modeled displacement in Figure 3.22a, modeled displacement in Figure 3.22b is related to deeper aquifer compaction.

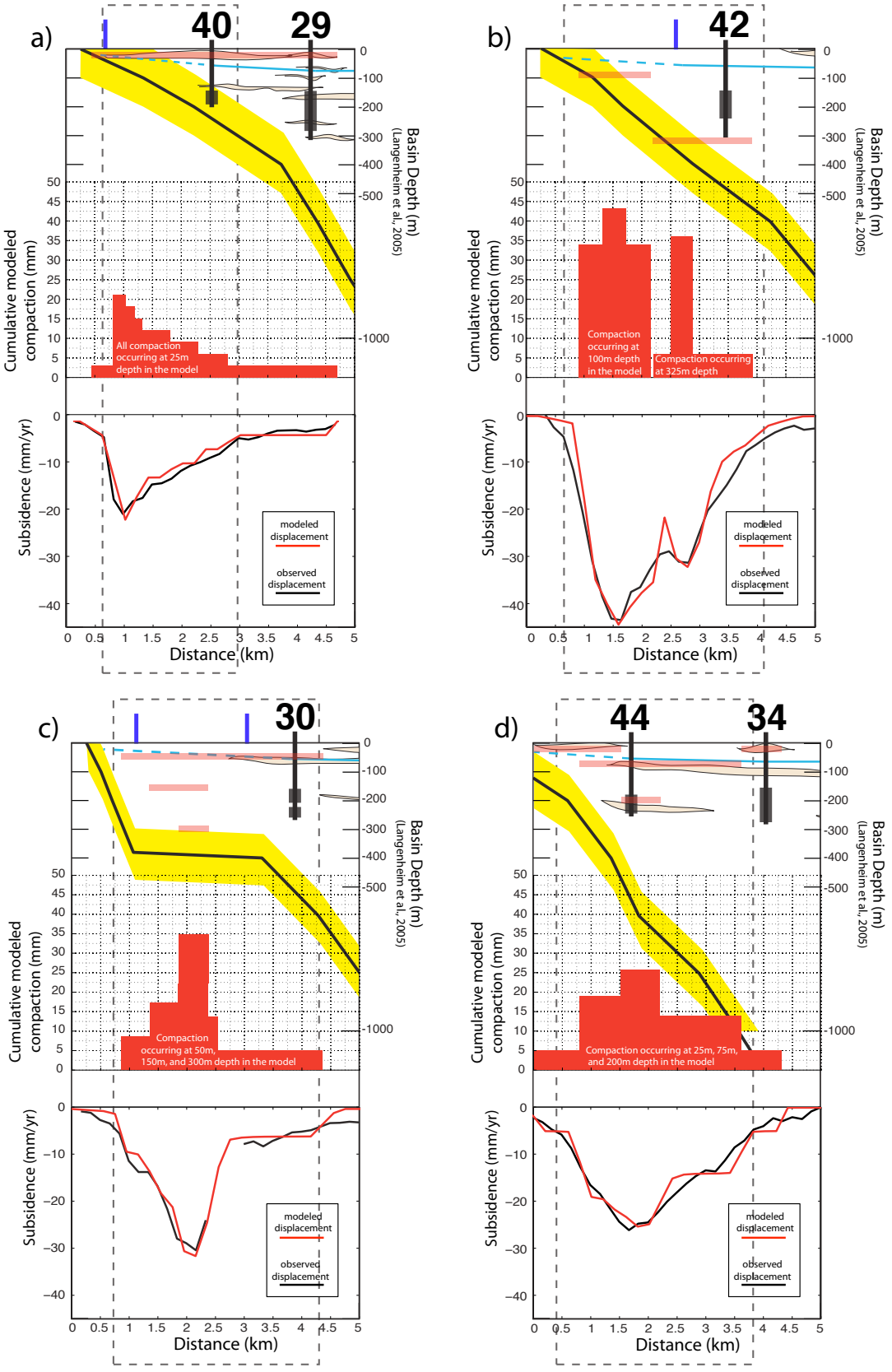

Figure 3.22. Elastic half-space model comparison with data observations. Figures 3.22a, b, c, and d correspond to cross-sections A-A', B-B', C-C', and D-D', respectively.

Figure 3.22c focuses in on the subsiding area of cross-section C-C' (Fig. 3.19). I observe a stair-step pattern in the subsidence curve and model compaction occurring at different depths in the aquifer. Approximating the lakebed observed in the hydrostratigraphy of well 30, I model compaction in a broad layer at 50m depth in the aquifer with more narrow sections of compaction occurring at 150m and 300m depth in the aquifer. By staggering the depths of compacting layers I am able to roughly replicate the stair-step pattern observed in the InSAR data. Varying the magnitude of compaction in the different layers allows for the replication of the general subsidence trend with a steep sided trough of maximum subsidence. As this cross-section contains a shelf-like section of the crystalline basement topography and a gentle topographic low at the surface it is not unreasonable to presume this area may contain isolated lenses of clay-rich material, justifying the hypothetical locations in the aquifer column for compaction. The broad upper layer of modeled compaction is near the level of the groundwater table and may be interpreted as delayed compaction due to continuous overdraft conditions. However, compaction in deeper deposits may also be causing some portion of observed surface deformation.

Figure 3.22d focuses in on the subsiding area of cross-section D-D' (Fig. 3.20). Using the mapped surface geology and hydrostratigraphy from wells 44 and 34, I approximate where in the subsurface compaction may be occurring and model compaction at 25m, 75m and 200m depth. The subsidence profile in this location has more gentle gradients than the other cross-sections, and compaction may be occurring above and/or below the groundwater table.

Observed subsidence may be replicated to a first order by elastic models of compaction at depth in the aquifer. What is not addressed in the models is what determines where the termination of a compacting layer may be or the shape of the compacting body, including the stratigraphic thickness. For example, are the fine-grained layers truncated abruptly by offset stratigraphy, or do they pinch out in tapered lenses?

8.3. Aquifer Partitioning

The alluvial aquifer near the base of the Santa Rosa Mountains is considered unconfined, with interfingering discontinuous lenses of sand, gravel, and clay (CVWD 2005). Eastward of the mountain front, the presence of fine-grained aquitard layers increases and may impede vertical groundwater flow. Although aquitard layers are not laterally continuous and are not considered tight or persistent enough to be considered aquicludes (CVWD 2005), the general structure of the aquifer is an upper and lower aquifer layer separated by this semi-discontinuous confining layer. From Indio to the southeast, the confining layer becomes a persistent 30-60m thick deposit of lacustrine clay and silt, classifying the upper aquifer south of Indio as semi-perched (Sneed *et al*. 2001 & 2002; Sneed & Brandt 2007). The upper aquifer layer is present through the entire Coachella Valley, generally 45 to 90m thick. The lower water-bearing layer, ranges in thickness from 150-600m, the top of which is ~90-180m below the surface.

Tapered lenses of compaction that vertically partition the aquifer may explain the observed differential subsidence, as shown by the elastic models. Vertical partitioning can be achieved by the presence of fine-grained aquitard layers that impede vertical groundwater flow and can have a time dependent response to pore pressure differentials

in the aquifer column. Inelastic compaction of aquitard layers is observable, in particular where prolonged overdraft conditions exist.

The northeast boundary of abrupt subsidence in the northern subsidence lobes is coincident with the surface contact between the recent dune sand deposits and the Quaternary alluvium, which is exposed in a slight topographic depression (Fig. 3.16). This may have provided an isolated environment for discontinuous fine-grained deposition. Assuming dune deposition and the adjacent topographic low have been persistent through the Quaternary, this area could have developed draped lenses of lacustrine deposits interbedded and interfingering with coarser alluvial facies. Contrasting transmissivities and poroelastic properties of the various interfingering depositional facies can cause differential surface displacement (Carver 1971). Also thin clay-rich layers under overdraft conditions will dewater and compact more quickly than thick layers of the same composition, as thick clay-rich layers do not allow pore fluid to escape as readily. Varying lateral thickness of a dewatering clay-rich layer can result in differential surface displacement as compaction occurs at different rates (Riley 1969; Carver 1971).

Abrupt truncation of an aquitard layer in an alluvial aquifer is often indicative of faulting, which can horizontally partition an alluvial aquifer. Vertical and sub-vertical fault planes can offset transmissive layers, juxtaposing transmissive layers against relatively impermeable layers (Caine & Minor 2011), and/or producing relatively impermeable fault gouge disrupting horizontal connectivity between transmissive layers (Caine & Minor, 2011). Buried faults in the subsurface may also act as semi-permeable barriers to groundwater flow, and, in fact, the linear presentation of the abrupt subsidence

boundaries do bear similar orientations to the fault segments visible at the surface of the study area (Figure 3.16) in the late-Cretaceous faults and brecciated zones mapped in the Santa Rosa Mountains (Erskine & Wenk 1985) as well as the trace of the San Andreas fault to the northeast. I mention again the fault and minor cross faults concealed by Quaternary alluvium that were posited by the Biehler *et al*. 1964, based on gravimetric data. A buried fault system could readily cause differential subsidence if the system isolated a section of the producing aquifer and limited access to natural and/or artificial recharge.

Holocene faulting may also be evidenced by stream capture in a topographic sag, through the accumulation of fine-grained sediment in a crack or depression (Wentworth *et al*. 2010). Even narrow topographic steps (on the order of ~2m) can support the presence of underlying fault structures where little or no convincing evidence for the fault location can be observed at the alluvial surface (Wentworth *et al*. 2010). The depositional facies analysis of well columns near the modern Whitewater Channel indicate persistent streambed facies (Fig. 3.18, well 42; Fig. 3.20, well 30) and may imply the location of fluvial deposition the Upper Coachella has remained fairly stable through the Holocene, supporting the possibility of tectonic stream capture.

This tempting interpretation is refuted by the lack of fault traces appearing at the western basin margin and by the lack active seismicity. Groundwater flow barriers without visible fault traces at the alluvial surface may be evidenced by a step in groundwater levels or hydraulic head and by differential surface displacement. Surprisingly, the groundwater table elevation across the rapid subsidence boundaries shows little to no change in elevation. Since the 1970's groundwater levels at the well

sites in the study area are being lowered on the order of 1-2m/a, both within and outside of the abrupt subsidence boundaries, and currently are ~50-100 meters below the ground surface. If the partitioning of the aquifer reaches the level of the groundwater table, it is reasonable to assume groundwater levels across these features would be offset, as they are across the Garnet Hill Banning and CVSAF, known active faults and groundwater flow barriers (CVWD 2005); however, groundwater levels at well sites suggest this is not the case. The groundwater table is uniform across the steep displacement gradients, usually just slightly higher in elevation within the subsidence lobes, implying that any horizontal aquifer partitioning would be in deeper deposits.

Variation in land use and development of surface structures can cause differential surface displacement by the artificial loading of unconsolidated sediments (Mazzotti *et al*. 2009), and varied irrigation practices. For example, an area with primarily residential wooden buildings will exhibit slower subsidence rates (presumably natural sediment compaction processes) than an area near an airport, industrial buildings or other large structures. As the abrupt subsidence boundaries encompass both residential and commercial regions, as well as numerous golf courses, all of which can also be found outside of the subsidence lobes I find that there is no apparent land use correlation with the locations of the subsidence lobes (Fig. 3.23). I currently have no data indicating where groundwater pumping is concentrated, or where groundwater needed for use at the surface might be extracted in situ. The location of major production wells within and near the study area would aid in the interpretation of surface displacement patterns, however this data has not yet been made available.

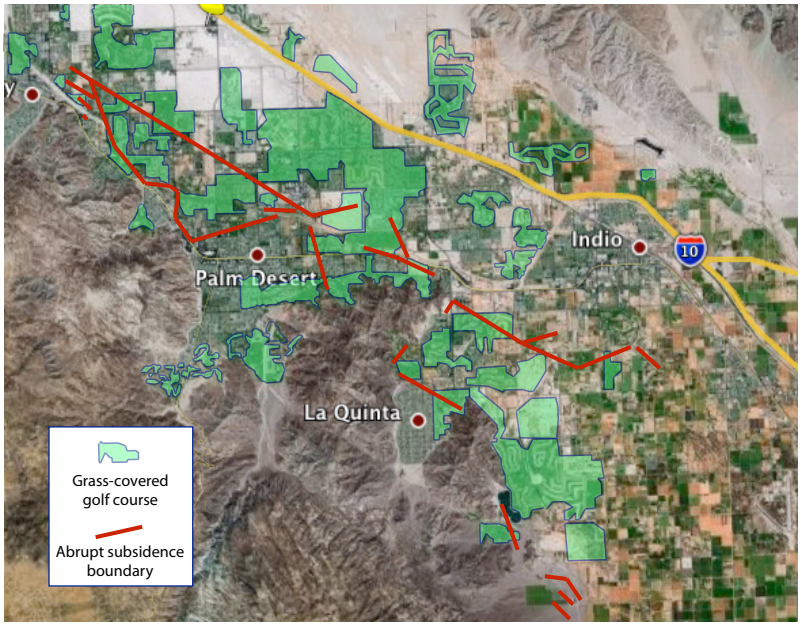

Figure 3.23. Satellite image from GoogleEarth, with golf courses locations compiled from public land use records and satellite photos. There are no visible surface features that readily align with subsidence boundaries.

8.4. Implications for Aquifer Management

The general trend of groundwater flow is southeastward from the Whitewater Recharge Facility. From Cathedral City, groundwater flow is predominated by bedding plane parallel movement, due to significantly lower bedding-normal permeabilities in the interbedded sands, silts and clays of this region of the aquifer (CVWD 2005). Subsurface inflow to the lower aquifer is greater than the subsurface inflow to the upper aquifer (CVWD 2005). Stratigraphically atop the crystalline basement rock, the lower aquifer primarily consists of the debris-rich Plio-Pleistocene Ocotillo Formation. The formation is often warped and faulted and is unconformably overlain by the relatively undisturbed recent alluvium in the Coachella Valley (CVWD 2005). The Ocotillo Formation is a fanglomerate composed of semi-consolidated, dominantly poorly bedded sandstone and conglomerate and the upper most layers are present at depths of 90-120m below the

surface near Palm Springs and Cathedral City (CVWD 2005). I suspect the Ocotillo deposits may provide subsurface controls on groundwater flow and pressure gradients, particularly where deformed or displaced layers encounter relatively impermeable fine-grained deposits. Varying levels of consolidation and cementation can greatly alter depositional structures and hydrogeologic properties (Scheibe & Freyberg 1995) and may be a contributing factor to displaced preferential flow paths in the water bearing material (Sneed & Brandt 2007; Philibosian 2011).

With the initiation of artificial recharge at the Whitewater Facility in the early 1970's, an analog model of groundwater levels for the Upper Coachella Valley (Tyley 1974) predicted recovery and stabilization of groundwater levels from the Whitewater Facility south to the Coachella Canal, and north into the Garnet Hill subbasin. Observable recovery was expected to reach southeast to Indio by the early 1990's and effectively recharge the entire area by 2000. Wisely & Schmidt (2005) observe subsidence on the order of 5 mm/yr in a NW-SE trending ellipse in the central basin, between 1992-2000 (Fig. 3.3a), encompassing the cities of Coachella and Indio. After 2000, vertical displacement rates in the central basin approach zero in most areas (Fig. 3.3b), and slight uplift is observed in some locations between 2006-2009 (Fig. 3.2). Recent InSAR data supports the prediction made by Tyley (1974) for the central basin, but highlights potential aquifer management issues for the western basin margin.

I suggest the areas of rapid and prolonged subsidence in the western basin margin are not being effectively recharged by the inflow from the Whitewater Facility. Sneed & Brandt (2007) show decreasing groundwater levels in both the upper and lower aquifers layers of the Coachella Valley since the 1970's, even after the installation of the

Whitewater Recharge Facility. The boundary for the area of benefit in the Upper Coachella Valley, as defined by the CVWD (Fig. 3.7) is vertically limited in its capacity for recharge due to the relatively shallow basement rock topography and the southeastward direction of groundwater flow. As discussed in previous sections, subsurface features related to the steep subsidence boundaries may also be disrupting horizontal hydraulic connectivity.

Future work in the Coachella Valley may include permanent scatterer InSAR for the Lower Coachella Valley where the InSAR coverage is not spatially continuous. I suggest the incorporation of the hydrostratigraphic analysis of the upper 300m of aquifer into a detailed groundwater modeling framework to better manage groundwater resources and control land subsidence. It is also possible that channel instability may be a contributor to steep subsidence troughs, and that examination of subsidence within the unlined storm channels be more closely assessed. Geophysical tools useful for identification of subsurface fault structures in the upper aquifer include ground-penetrating radar, seismic refraction surveys, gravity and magnetic studies, and borehole geophysical testing (Langsholt *et al*. 1998; Anderson *et al*. 2004; Langenheim *et al*. 2005; Wentworth *et al*. 2010; Artimo *et al*. 2003). Stratigraphic data such as strike and dip of strata through the aquifer column, and the lateral extent and shape of interbedded deposits would also compliment the development of a 3D computer model of the aquifer of the western basin margin. The most valuable additional data for determining the Quaternary history of the proposed buried fault system would be detailed NE trending seismic reflection profiles (e.g. Wentworth *et al*. 2010). Such data would ideally locate structural features and provide evidence of discontinuities in material properties. Lastly, the

location of major production wells for the Coachella Valley would greatly assist in the understanding of the observed subsidence and interpretations of aquifer deformation.

9. CONCLUSIONS

The major findings of this study include the persistent pattern of rapid subsidence (5-48 mm/yr) in the western Coachella Valley basin margin, consistent with earlier observations of Sneed and Brandt (2007). Using a unique combination of data and methodology, I have analyzed the surface deformation of this primary California aquifer and modeled subsurface compaction to explain how differential displacement may be achieved. Part of the deformation analysis involved the application of the HII method (Wisely & Schmidt 2010) to the Coachella Valley aquifer. Sensitivity testing of the HII method indicates the groundwater level data sampling frequency typical in the Upper Coachella Valley (3× yearly) is less than optimal, but still may yield meaningful results. Sensitivity testing also indicates inelastic subsidence (compaction) rates may be overestimated (Fig. 3.11a) and the poroelasticity may be underestimated (Fig. 3.11b). I calculate a systematic error of ±0.5 mm/yr associated with the offset in temporal sampling of InSAR and groundwater levels in the application of the HII method. The HII method confirms that some portion of observed surface displacement is likely to be inelastic compaction of the dewatering aquifer skeleton. However, the generalized depositional facies analysis and modeling of aquifer compaction both show that compaction of basin-wide lakebed deposits is not what is controlling the pattern of observed surface displacement in the western Coachella Valley. The most reasonable explanation for this enigmatic surface displacement is the compaction of discontinuous

lenses of fine-grained aquitard layers isolated and focused on the west side of the basin. More data is necessary to confirm this stratigraphic interpretation of the groundwater aquifer, such as seismic data, drill cores, and geophysical borehole testing.

I considered several mechanisms as controls on the rapid subsidence lobes, including buried faults that bound, semi-confined aquifer blocks. Evidence for buried faults include the systematic lineaments that appear at the ~5 mm/yr subsidence rate contour (Fig. 3.3), the possibility of tectonic stream capture and, apparently disrupted access to artificial recharge. Evidence refuting the presence of buried faults includes the lack of active seismicity, no surface scarps or traces, and no obvious step in the groundwater levels that would indicate horizontal flow barriers. No apparent land use correlation or known well pumping is indicated in the available hydrologic data. Thus, I conclude the unique pattern of subsidence is most plausibly related to the delayed compaction of discontinuous lenses of fine-grained lakebed deposition, either above and/or below the groundwater table (Figs. 3.22). As the hydrostratigraphic analysis indicates, there are other fine-grained layers in the aquifer outside of the subsidence lobes. I surmise that this indicates that such layers within the subsiding lobes are unable to access artificial recharge, and that outside of the subsiding lobes the artificial recharge is inhibiting the compaction of fine-grained layers or lenses. The depositional facies analysis successfully provided gross constraints for the modeling and first order replication of subsurface compaction. Hydrogeologic structures controlling the locations of abrupt subsidence may be sharply bound by either deformation of the Ocotillo Formation at depth in the aquifer or by the contact between the Quaternary alluvium and the recent aeolian dune sand deposits.

CHAPTER IV

COMPILATION OF SURFACE CREEP ON CALIFORNIA FAULTS AND COMPARISON OF WG-07 DEFORMATION MODEL TO PACIFIC-NORTH AMERICAN PLATE MOTION

This work was published in 2007 as Appendix P in The Uniform California Earthquake Rupture Forecast, version 2 (UCERF 2), a USGS Open-File Report 2007-1437 and California Geological Survey Special Report 203. I performed the strain tensor analysis and formatted the computer code to run on the RefGF fault database for all of California. My co-author David Schmidt developed and executed the creep compilation and analysis for the project, and my co-author Ray Weldon developed and executed the line integral analysis and also drafted the main body of the report. This project is currently under revision for UCERF 3, and will be re-published by Summer 2012.

1. INTRODUCTION

This study contains 3 sections that 1) documents published observations of surface creep on California faults, 2) constructs line integrals across the WG-07 deformation model to compare to the Pacific–North America plate motion, and 3) constructs strain tensors of volumes across the WG-07 deformation model to compare to the Pacific–North America plate motion.

Observation of creep on faults is a critical part of our earthquake rupture model because the moment released as earthquakes on faults is reduced from what would be inferred directly from the fault's slip rate, if the fault is observed to creep. The rate of

creep relative to the slip rate is used to infer the average depth of creep, and the depth of creep is used to reduce the surface area of the fault that generates earthquakes in our model. This reduction of surface area of rupture is described by an "aseismicity factor," assigned to each fault in UCERF 2. An aseismicity factor of less than 1 is only assigned to faults that slip during the interseismic period. Afterslip following earthquakes on modeled faults and inferred widely distributed shear in C-zones is handled by a reduction in slip rate, rather than a reduction of fault area, because these processes are believed to span the seismogenic portion of the fault. These "aseismic" processes are not covered in this study.

Parts Two and Three of this study compare the WG-07 deformation model and the seismic source model it generates (UCERF 2.3) to the strain generated by the Pacific-North American plate motion. The concept is that plate motion generates essentially all of the elastic strain in the vicinity of the plate boundary that can be released as earthquakes. Adding up the slip rates on faults and all others sources of deformation (such as C-zones and distributed background seismicity) should approximately yield the plate motion. This addition is usually accomplished by one of three approaches: 1) line integrals that sum deformation along discrete paths through the deforming zone between the two plates, 2) seismic moment tensors that add up seismic moment of a representative set of earthquakes generated by a crustal volume spanning the plate boundary, and 3) strain tensors generated by adding up the strain associated with all of the faults in a crustal volume spanning the plate boundary. In this study we apply approaches 1 and 3. We cannot apply the moment tensor approach because most of the seismic moment released in the historical period in California predates the instrumental period, so we

don't know the source parameters need to determine a seismic moment tensor. The scalar moment of the historical period has been compared to that produced by UCERF 2.3 in the Main Report, and they match to within uncertainties. As discussed in detail in Parts Two and Three of this study, the strain inferred from our current model (UCERF 2.3) matches the plate motion in both rate and style to 5-10%, well within the uncertainties.

2. PART ONE: SURFACE CREEP OBSERVATIONS

Surface creep commonly refers to aseismic fault slip occurring at or near the surface with slip rates on the order of cm/yr or less (*Wesson*, 1988). Fault creep can be continuous in time or consist of a series of steps (creep events). Steady creep that persists for several decades is often referred to as interseismic creep. Accelerated surface slip can also be observed following a major earthquake in which case it is referred to as afterslip. Short-term fluctuations in creep rate that deviate from long-term rates for weeks or months can be referred to as transient creep or triggered creep in the case where a localized stress perturbation is imposed (*Burford*, 1988).

Evidence for surface creep is well documented along the San Andreas fault system (Fig. 4.1). Most observations were collected using alignment arrays (*Burford and Harsh*, 1980), creepmeters (*King et al*., 1977), and geodolite networks. Offset cultural features, such as curbs and buildings, provide an additional record of faulting. Occasionally, surface creep is inferred from GPS-derived models of the regional deformation.

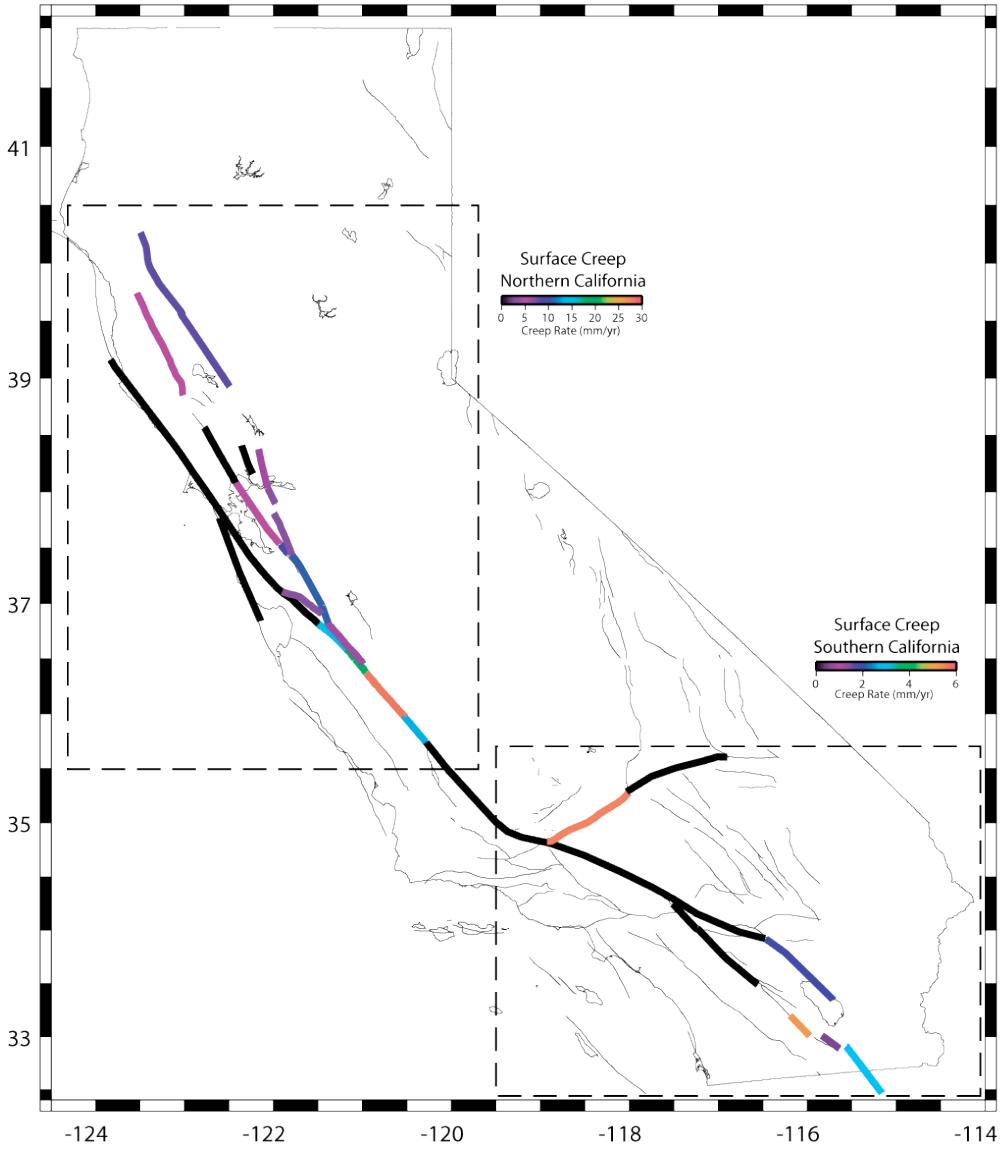

Figure 4.1. Map of creep rates of California faults. Note that the range of creep rates is different in northern and southern California. Heavy black lines indicate documented absence of creep. Locations of all known sites with published creep rate observations are shown in more detailed maps of northern and southern California (Figures 4.2 and 4.3) and numbers are summarized in Table 4.1.

In this part of the study we summarize the observational data on surface creep along the San Andreas fault system. The two primary sources for this data set include *Louie et al*. (1985) and *Galehouse and Lienkaemper* (2003) for southern and northern California, respectively. These summaries are supplemented with additional sources. We have focused on interseismic observations and have purposefully avoided results that are dominated by transient behavior or otherwise influenced by nearby seismic events. Where multiple observations are available at a particular location, the most consistent observation is used based on the information provided in each source. We have also included data on faults where no surface creep is found despite repeated surveys. Uncertainties are routinely not reported, especially in early work. Occasionally we have inferred an uncertainty from ancillary information in each source or left the uncertainty undefined. A creep rate of zero is recorded in cases where no creep is observed within instrument error.

It is not known if creep is limited to the San Andreas system (with the possible exception of the western Garlock) or simply that the San Andreas system slips more rapidly and has been more intensively investigated so the creep is more easily observed. Because slip is usually only a fraction of a fault's slip rate it would be very difficult to recognize creep on most Californian faults that have slip rates less than 1 mm/yr.

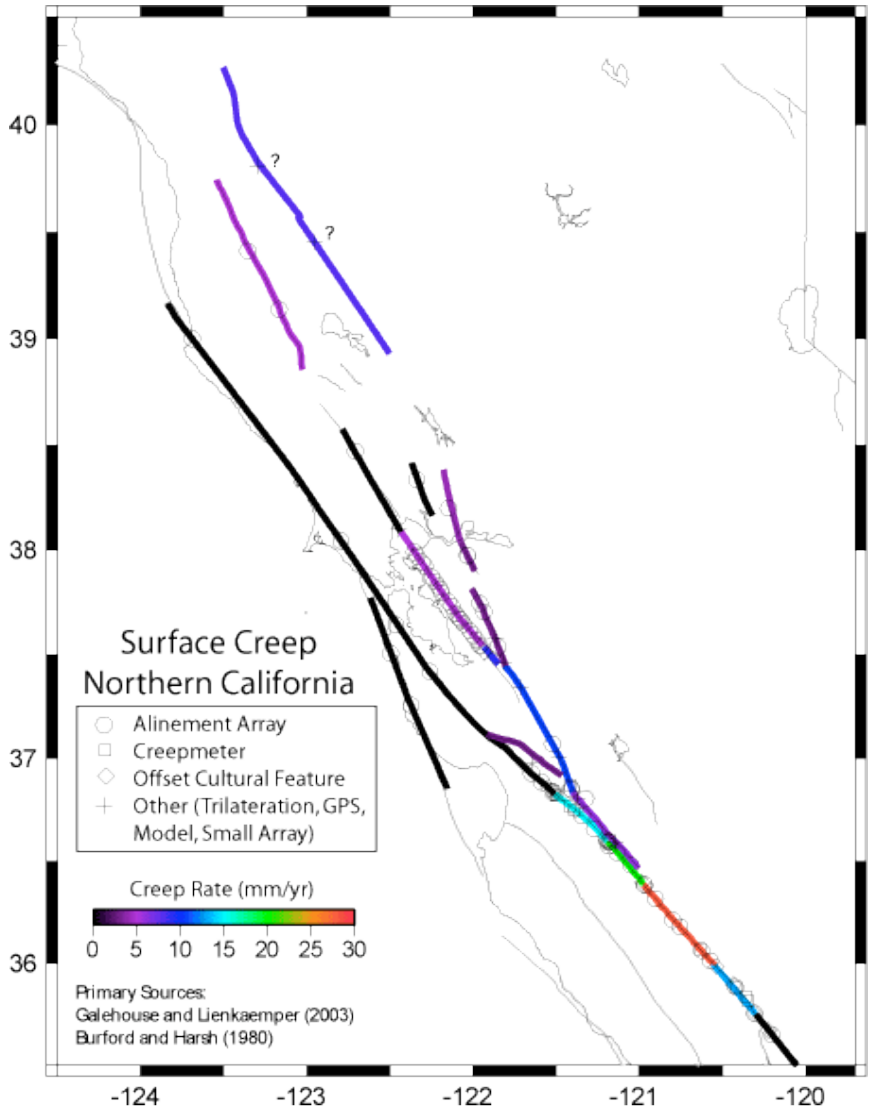

Figure 4.2. Details of creep observations in Northern California. Colors indicate creep rate and bold black lines indicate a documented absence of creep. Small (faint) symbols indicate the locations of creep observations that are summarized in Table 4.1.

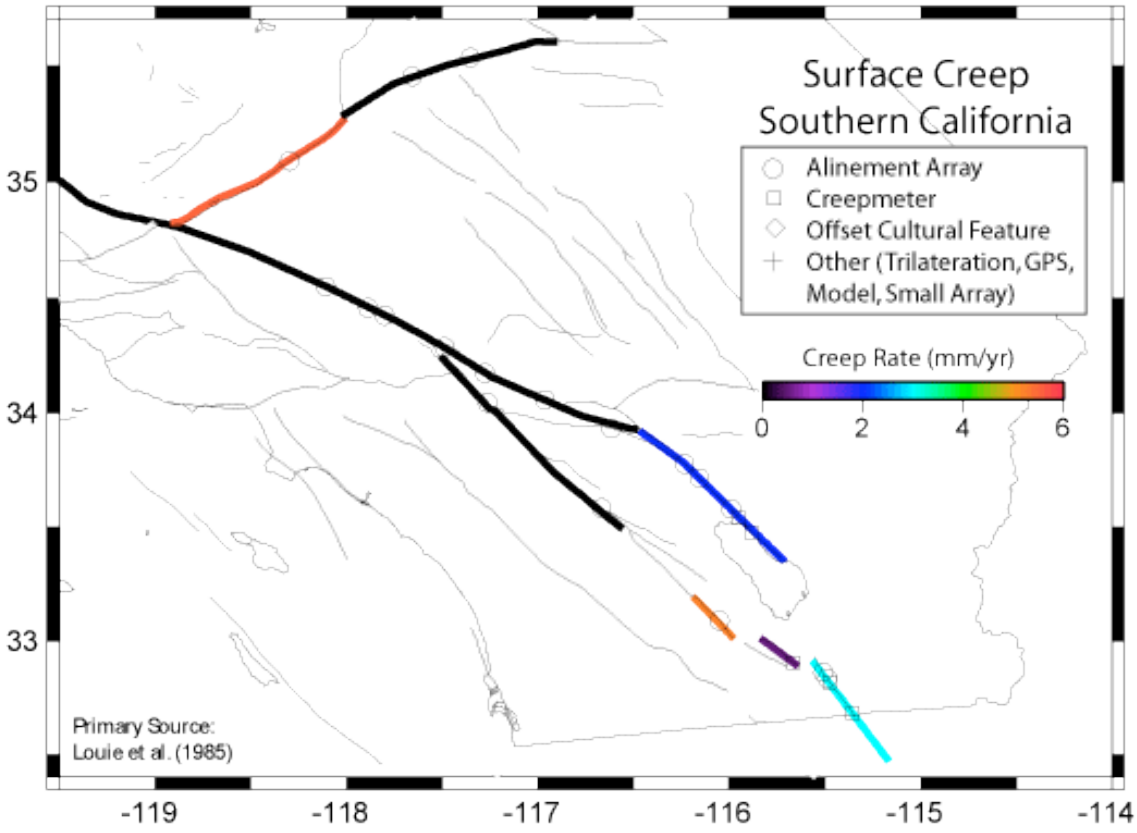

Figure 4.3. Details of creep observations in Southern California. Colors indicate creep rate and bold black lines indicate a documented absence of creep. Small (faint) symbols indicate the locations of creep observations that are summarized in Table 4.1.

Table 4.1. (following pages) List of surface creep observations in California. Entries are sorted alphabetically by fault name, and then by latitude. Measurement error (sigma) is denoted as 'Und' for undefined when a value is not given by the source. Instruments types are listed as follows: AA=alignment array, CM=creepmeter, Cult=cultural offset features, Geod=small geodetic array, Mod=inferred from model, Tri=trilateration. Types of surface creep observations are listed as follows: I=interseismic creep, A=afterslip creep, T=transient or triggered creep.

CREEPING FAULT DATA

Longitude	Latitude	Creep Rate (mm/yr)	Sigma (mm/yr)	Creep Type	Inst. Type	Start Date	End Date	Source
Bartlet Springs Fault								
-122.9526	39.4539	8.2	2	I	Mod	1991	1995	Freymueller et al. (1999)
Calaveras Fault								
-121.9598	37.7458	0.2	0.1	I	AA	1980	1989	Galehouse & Lienkaemper (2003)
-121.9359	37.7044	2.8	0.5	I	AA	1965	1977	Lisowski & Prescott (1981)
-121.8642	37.581	2.9	0.3	I	Geod	1965	1976	Prescott et al. (1981)
-121.8508	37.5358	3.6	0.5	I	AA	1997	2001	Galehouse & Lienkaemper (2003)
-121.812	37.4578	2.2	0.5	I	Geod	1970	1979	Prescott et al. (1981)
-121.7139	37.3417	9.4	0.4	I/A	Geod	1977	1984	Oppenheimer et al. (1990)
-121.5242	37.0699	14	2	I	AA	1968	1989	Galehouse & Lienkaemper (2003)
-121.4826	37.0096	13	2	I	Geod	1972	1979	Lisowski & Prescott (1981)
-121.4128	36.8699	13	Und	I/A	CM	1971	1983	Schulz (1982)
-121.4128	36.8496	12.2	0.2	I/A	AA	1979	1989	Galehouse & Lienkaemper (2003)
-121.4053	36.8496	6.4	0.2	I/A	AA	1979	1989	Galehouse & Lienkaemper (2003)
-121.3736	36.805	5	3	I	Geod	1975	1979	Lisowski & Prescott (1981)
-121.3233	36.805	6.2	0.1	I	AA	1973	1986	Wilmesher & Baker (1987)
-121.1425	36.5932	10	3	I	Geod	1975	1979	Lisowski & Prescott (1981)
Concord Fault								
-122.0372	37.9758	2.7	0.03	I	AA	1979	2001	Galehouse & Lienkaemper (2003)
-122.0342	37.972	3.6	0.04	I	AA	1979	2001	Galehouse & Lienkaemper (2003)
Garlock Fault								
-117.352	35.532	0	Und	I	AA	1971	1983	Louie et al. (1985)
-117.656	35.452	0	Und	I	AA	1971	1983	Louie et al. (1985)
-118.299	35.0898	5.7	1.5	I	AA	1971	1982	Louie et al. (1985)
Green Valley Fault								
-122.1495	38.1986	4.4	0.1	I	AA	1984	2001	Galehouse & Lienkaemper (2003)
Hayward Fault								
-122.3546	37.9891	5	0.1	I	AA	1968.33	1993.06	Lienkaemper et al. (2001)
-122.3379	37.969	4.8	0.2	I	AA	1980.61	1999.89	Lienkaemper et al. (2001)
-122.3083	37.9425	4.9	0.4	I	AA	1989.75	1999.68	Lienkaemper et al. (2001)
-122.2918	37.9246	4.4	0.3	I	AA	1989.75	1999.87	Lienkaemper et al. (2001)
-122.2506	37.8719	4.6	0.1	I	AA	1966.91	1999.66	Lienkaemper et al. (2001)
-122.2304	37.8484	3.8	0.1	I	AA	1974.26	1999.70	Lienkaemper et al. (2001)
-122.209	37.8264	3.7	0.2	I	AA	1993.11	1999.89	Lienkaemper et al. (2001)
-122.1975	37.8101	3.7	0.1	I	AA	1970.29	1999.70	Lienkaemper et al. (2001)
-122.1882	37.7951	3.6	0.3	I	AA	1974.27	1999.66	Lienkaemper et al. (2001)
-122.1504	37.7546	3.7	0.5	I	AA	1989.69	1999.89	Lienkaemper et al. (2001)
-122.1285	37.7319	5.9	0.5	I	AA	1993.39	1999.68	Lienkaemper et al. (2001)
-122.1045	37.695	5.5	0.9	I	AA	1992.62	1999.66	Lienkaemper et al. (2001)
-122.0899	37.6798	5	0.1	I	AA	1967.17	1999.83	Lienkaemper et al. (2001)
-122.0804	37.6703	4.4	0.1	I	AA	1980.48	1999.83	Lienkaemper et al. (2001)
-122.0727	37.6627	4	0.6	I	AA	1977.07	1999.68	Lienkaemper et al. (2001)
-122.0579	37.6481	6.7	0.5	I	AA	1994.59	1999.68	Lienkaemper et al. (2001)
-122.0222	37.6143	5.1	0.7	I	AA	1994.59	1999.70	Lienkaemper et al. (2001)
-122.0008	37.5925	5.1	0.2	I	AA	1979.73	1999.83	Lienkaemper et al. (2001)

-121.9797	37.5664	6	1.3	I	AA	1983.76	1988.85	Lienkaemper et al. (2001)
-121.9607	37.5422	5.6	0.3	I	AA	1979.73	1989.81	Lienkaemper et al. (2001)
-121.9548	37.5361	8.9	0.6	I	Cult	1940.3	1987.64	Lienkaemper et al. (2001)
-121.9343	37.5125	9.5	0.6	I	Cult	1967.7	1987.64	Lienkaemper et al. (2001)
-121.9316	37.5097	8.2	0.4	I	Cult	1968.7	1982.3	Lienkaemper et al. (2001)
Imperial Fault								
-115.51	32.862	13	8	I	AA	1974	1979	Louie et al. (1985)
-115.488	32.837	5.4	Und	I/T	AA	1967	1978	Louie et al. (1985)
-115.4787	32.8202	5	Und	I	CM	?	1979	Louie et al. (1985)
-115.356	32.683	1	Und	I	?	?	1977	Goulty et al. (1978)
-115.356	32.683	1.4	Und	I	CM	1975	1979	Louie et al. (1985)
-115.356	32.683	6	Und	A	CM	1980	1984	Louie et al. (1985)
Maacama Fault								
-123.3559	39.4125	6.5	0.1	I	AA	1991	2001	Galehouse & Lienkaemper (2003)
-123.1664	39.1392	4.4	0.2	I	AA	1993	2001	Galehouse & Lienkaemper (2003)
Rodgers Creek Fault								
-122.7083	38.4701	0.4	0.5	I	AA	1980	1986	Galehouse & Lienkaemper (2003)
-122.6405	38.3478	1.6	0.1	I	AA	1986	2000	Galehouse & Lienkaemper (2003)
-122.4469	38.0987	1.4	1.1	I	Tri	1978	1988	Lienkaemper et al. (1991)
San Andreas Fault								
-123.6895	39.0000	0.5	0.10	I	AA	1981	2000	Galehouse & Lienkaemper (2003)
-122.7969	38.0441	0.2	0.0	I	AA	1985	2001	Galehouse & Lienkaemper (2003)
-122.4646	37.6443	-0.3	0.02	I	AA	1980	1994	Galehouse & Lienkaemper (2003)
-122.2605	37.4171	0.3	0.1	I	AA	1989	2000	Galehouse & Lienkaemper (2003)
-121.6483	36.9267	0.8	0.4	I	AA	1967	1972	Burford & Harsh (1980)
-121.5851	36.8827	0.1	0.1	I	AA	1989	1998	Galehouse & Lienkaemper (2003)
-121.5453	36.8549	8	0.2	I	Cult	1942	1978	Burford & Harsh (1980)
-121.52	36.84	9	Und	I/T	CM	1969	1976	Burford (1988)
-121.5250	36.8392	13.3	0.2	I	Cult	1926	1978	Burford & Harsh (1980)
-121.5200	36.8367	14	0.4	I	AA	1968	1977	Burford & Harsh (1980)
-121.5207	36.8351	10.4	0.2	I	AA	1990	2001	Galehouse & Lienkaemper (2003)
-121.50	36.82	8.1	Und	I/T	CM	1969	1976	Burford (1988)
-121.42	36.77	10.9	Und	I/T	CM	1969	1976	Burford (1988)
-121.390	36.75	12.3	Und	I/T	CM	1958	1976	Burford (1988)
-121.3839	36.7495	12.3	0.2	I	Cult	1948	1976	Burford & Harsh (1980)
-121.3467	36.7200	13.5	0.4	I	AA	1972	1977	Burford & Harsh (1980)
-121.2717	36.6583	14	0.4	I	AA	1973	1977	Burford & Harsh (1980)
-121.23	36.65	13.8	Und	I/T	CM	1969	1976	Burford (1988)
-121.2017	36.6050	19.9	0.4	I	AA	1972	1977	Burford & Harsh (1980)
-121.19	36.6	20.3	Und	I/T	CM	1969	1976	Burford (1988)
-121.1943	36.5988	19	0.2	I	Cult	1937	1966	Brown & Wallace (1968)
-121.1850	36.5950	22.7	0.4	I	AA	1972	1977	Burford & Harsh (1980)
-121.1845	36.5933	22.9	0.4	I	AA	1967	1978	Burford & Harsh (1980)
-121.1841	36.5902	22	0.2	I	Cult	1945	1978	Burford & Harsh (1980)
-121.18	36.59	21.2	Und	I/T	CM	1969	1976	Burford (1988)
-121.1835	36.5740	23.1	0.4	I	AA	1970	1973	Burford & Harsh (1980)
-121.1630	36.5735	8	0.2	I	Cult	1951	1966	Brown & Wallace (1968)
-121.1350	36.5433	23.1	0.4	I	AA	1972	1977	Burford & Harsh (1980)
-121.0517	36.4817	21.9	0.4	I	AA	1967	1974	Burford & Harsh (1980)

-120.9823	36.3972	25	0.2	I	Cult	1908	1966	Brown & Wallace (1968)
-120.9750	36.3883	31.3	0.4	I	AA	1970	1976	Burford & Harsh (1980)
-120.969	36.3883	23.2	1	I	GPS	1967	2003	Titus et al. (2005)
-120.9693	36.3833	33.3	0.4	I	AA	1967	1971	Burford & Harsh (1980)
-120.9687	36.3828	28	0.2	I	Cult	1941	1966	Brown & Wallace (1968)
-120.9017	36.3167	31.4	0.4	I	AA	1970	1977	Burford & Harsh (1980)
-120.7983	36.2133	17.3	0.4	I	AA	1968	1977	Burford & Harsh (1980)
-120.7567	36.1800	26	0.4	I	AA	1970	1977	Burford & Harsh (1980)
-120.798	36.18	26.7	1	I	GPS	1970	2003	Titus et al. (2005)
-120.63	36.07	22.1	Und	I/T	CM	1972	1987	Burford (1988)
-120.6283	36.0650	30	0.4	I	AA	1968	1979	Burford & Harsh (1980)
-120.628	36.065	24.9	1	I	GPS	1968	2003	Titus et al. (2005)
-120.5717	36.0150	23.8	0.4	I	AA	1970	1979	Burford & Harsh (1980)
-120.5357	35.9837	25	0.2	I	Cult	1946	1966	Wallace & Roth (1967)
-120.4337	35.8951	22	0.2	I	Cult	1932	1978	Burford & Harsh (1980)
-120.4217	35.8850	14.6	0.4	I	AA	1968	1979	Burford & Harsh (1980)
-120.42	35.88	8.3	Und	I/T	CM	1972	1987	Burford (1988)
-120.36	35.84	3.97	Und	I/T	CM	1971	1987	Burford (1988)
-120.35	35.82	3.25	Und	I/T	CM	1972	1987	Burford (1988)
-120.3072	35.7567	18	0.2	I	Cult	1908	1978	Burford & Harsh (1980)
-120.3071	35.7566	4	0.4	I	AA	1966	1979	Burford & Harsh (1980)
-120.2267	35.6728	0	0.2	I	Cult	1937	1966	Brown & Wallace (1968)
-120.2050	35.6517	0	0.4	I	AA	1975	1977	Burford & Harsh (1980)
-118.11	34.55	0	0.5	I	AA	1970	1984	Louie et al. (1985)
-117.888	34.457	0	0.2	I	AA	1970	1984	Louie et al. (1985)
-117.8	34.422	0	1	I	AA	1970	1981	Louie et al. (1985)
-117.49	34.2858	0	0.5	I	AA	1970	1984	Louie et al. (1985)
-117.276	34.174	0	1	I	AA	1970	1983	Louie et al. (1985)
-116.964	34.058	0	0.4	I	AA	1970	1983	Louie et al. (1985)
-116.616	33.9325	2	Und	I	AA	1972	1982	Louie et al. (1985)
-116.234	33.777	1.5	0.6	I	AA	1970	1984	Louie et al. (1985)
-116.156	33.715	2	1	I/T	AA	1970	1984	Louie et al. (1985)
-115.99	33.58	1.7	Und	A	AA	1967	1983	Louie et al. (1985)
-115.949	33.541	0	0.1	I	CM	1970	1984	Louie et al. (1985)
-115.887	33.482	0.7	Und	I	CM	1981	1984	Louie et al. (1985)
				San Jacinto Fault				
-117.264	34.0442	0	1	I	AA	1973	1983	Louie et al. (1985)
-116.669	33.5861	0	2	I	AA	1977	1984	Louie et al. (1985)
-116.05	33.09	5.2	3	I/A	AA	1971	1984	Louie et al. (1985)
				Sargent Fault				
-121.6462	36.9763	2.9	0.7	I	Geod	1970	1975	Prescott & Burford (1976)
				Superstition Hills Fault				
-115.6633	32.9045	0.5	Und	I	CM	1968	1979	Louie et al. (1985)
				West Napa Fault				
-122.3393	38.3353	0.1	0.1	I	AA	1980	1999	Galehouse & Lienkaemper (2003)

3. PART TWO: LINE INTEGRALS ACROSS THE PACIFIC-NORTH AMERICA PLATE BOUNDARY

To test the WG-07 deformation model, four line integrals were constructed across the model in California. We used the method of Humphreys and Weldon (1994) to accumulate uncertainty along the path, and used several input values, including uncertainties in the rake and orientation of the faults, deformation between stable North America and California (Fig. 4.4), and block rotations, from Humphreys and Weldon (1994) where our model did not contain data. The paths were chosen, from south to north, to cross the plate boundary 1) across the Salton Depression, Peninsula Ranges and Continental Borderland south of Los Angeles, 2) through the Mojave Desert and the Transverse Ranges just north of Los Angeles, 3) across the Eastern California Shear Zone, Sierra Nevada and Central California near Parkfield, and 4) through Northern California near the latitude of the Bay Area (Fig. 4.5). Paths 1-3 repeat those of Humphreys and Weldon (1994) and yield very similar results. Deformation along all paths sums to values that overlap in uncertainty with the Pacific-North America plate rate (Fig. 4.6). While this appears to be a powerful vindication of our model, it should not be too unexpected because past Working Group models, upon which this one is built, have been "tuned" to match the known plate rate, by choosing preferred values from uncertain slip rates that add up to the plate rate.

Line integrals are very sensitive to the path chosen. As can be seen in Figure 4.5, it is easy to slightly change the path to avoid or add discontinuous structures or cross longer faults where their geometry, slip rate, dip or rake vary. Thus, the uncertainties reflected in Figure 4.6 should be considered minimums, which do not take into account

possible different paths. In addition, line integral paths that cross-rotating blocks must correctly account for rotations that are not explicitly included in our deformation model. We have used the rotations determined by Humphreys and Weldon (1994), but it is unlikely, particularly in southern California, that all of the rotations are known and well characterized. This may be the reason for the systematic more westerly direction we determine for all three southern paths and the underestimate in rate for the most complex Transverse Ranges path, which crosses rotating blocks.

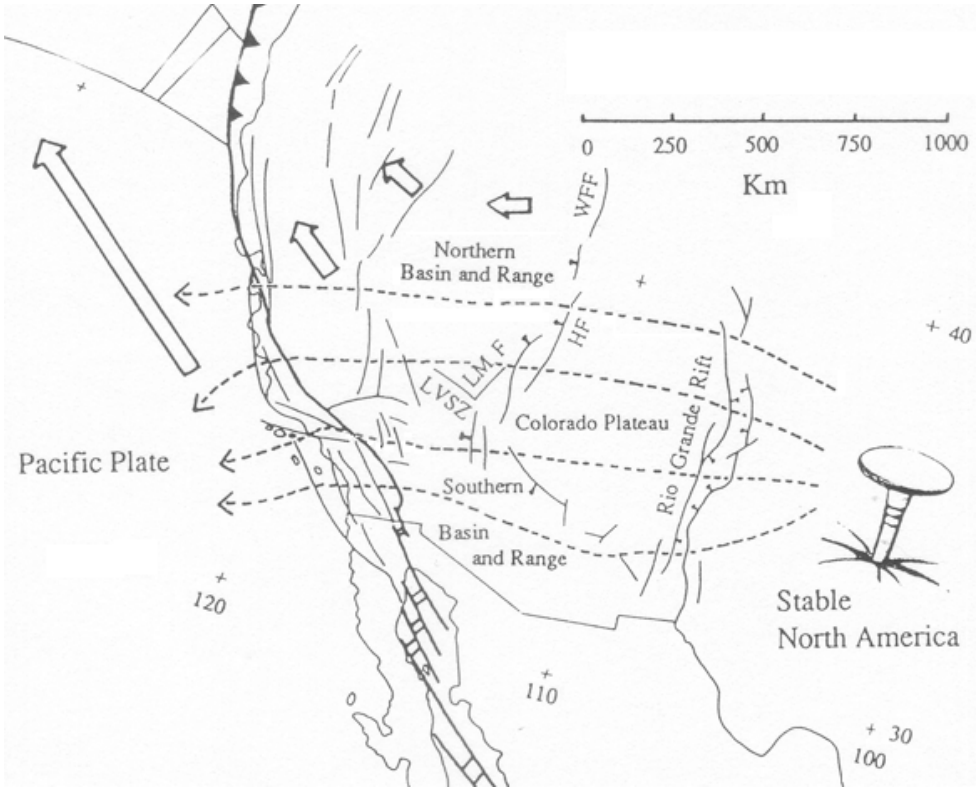

Figure 4.4. Approximate location of line integrals across the Pacific–North America plate boundary; modified from Humphreys and Weldon (1994). Because the WG-07 model does not extend significantly east of California, we used the values for deformation east of California from Humphreys and Weldon (1994) to complete the paths between the Pacific and North American plates. Due to the influence of the Juan de Fuca subduction zone (bold teeth on NW end of figure) no path was constructed for northernmost California.

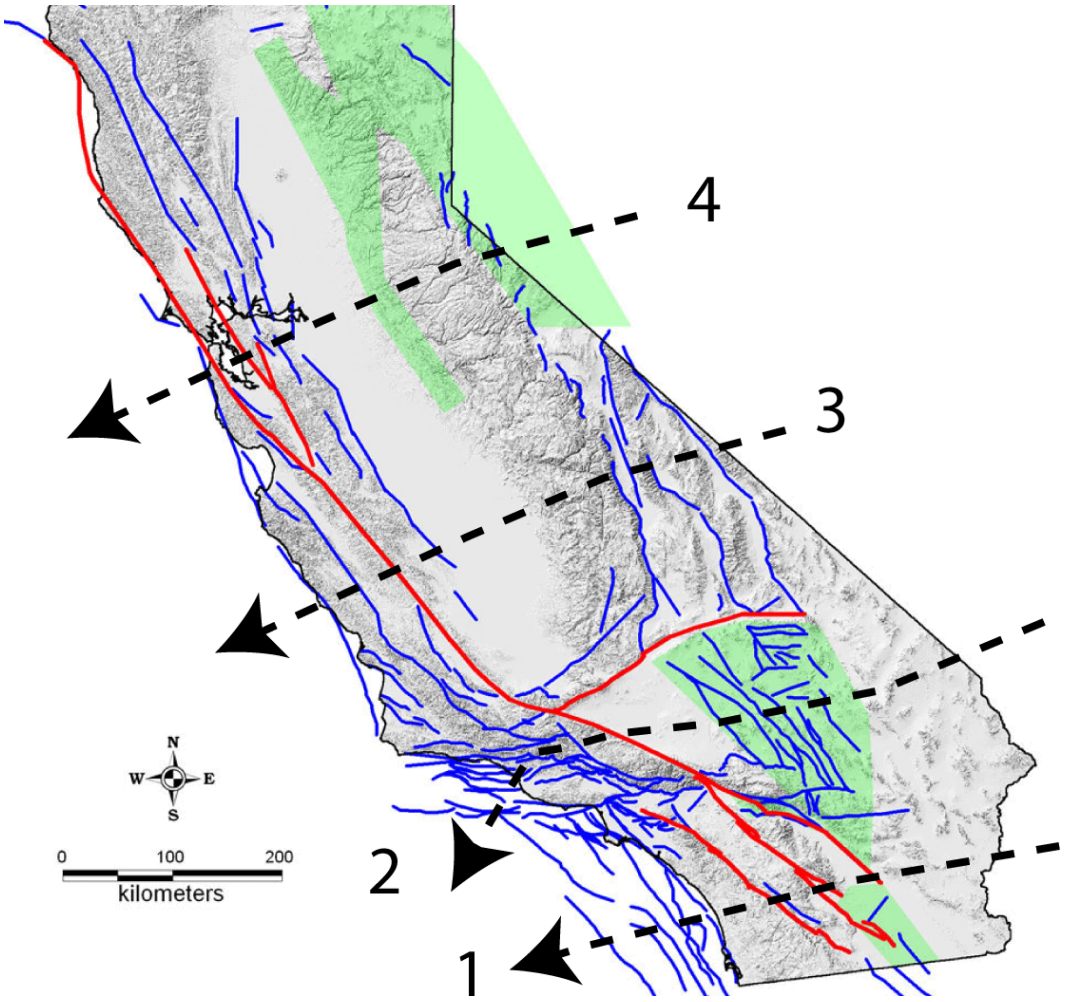

Figure 4.5. Approximate location of line integrals 1) Peninsular Ranges path, 2) Transverse Ranges path, 3) Central California path, and 4) Northern California path. Deformation east of the modeled area is included from Humphreys and Weldon (1994). Red lines are A-Faults, blue B-Faults, and green polygons are C-zones, which are modeled as vertical faults with simple shear appropriately oriented.

Figure 4.6. (on next page) Vector sum of line integrals compared to the expected Pacific North America plate motion. The tip of the vectors are the best estimate from Monte Carlo sampling of the uncertainties associated with all inputs and the uncertainty contours are 30 and 90% (following Humphreys and Weldon, 1994; which used 30, 60 and 90% - the 60% range is left off here for clarity). The pluses are the sum of the individual fault slip vectors (and rotations), and are distinct from the best estimates because the individual fault uncertainties are quite asymmetric. Note the plate motion varies slightly from path to path, becoming more northerly to the north.

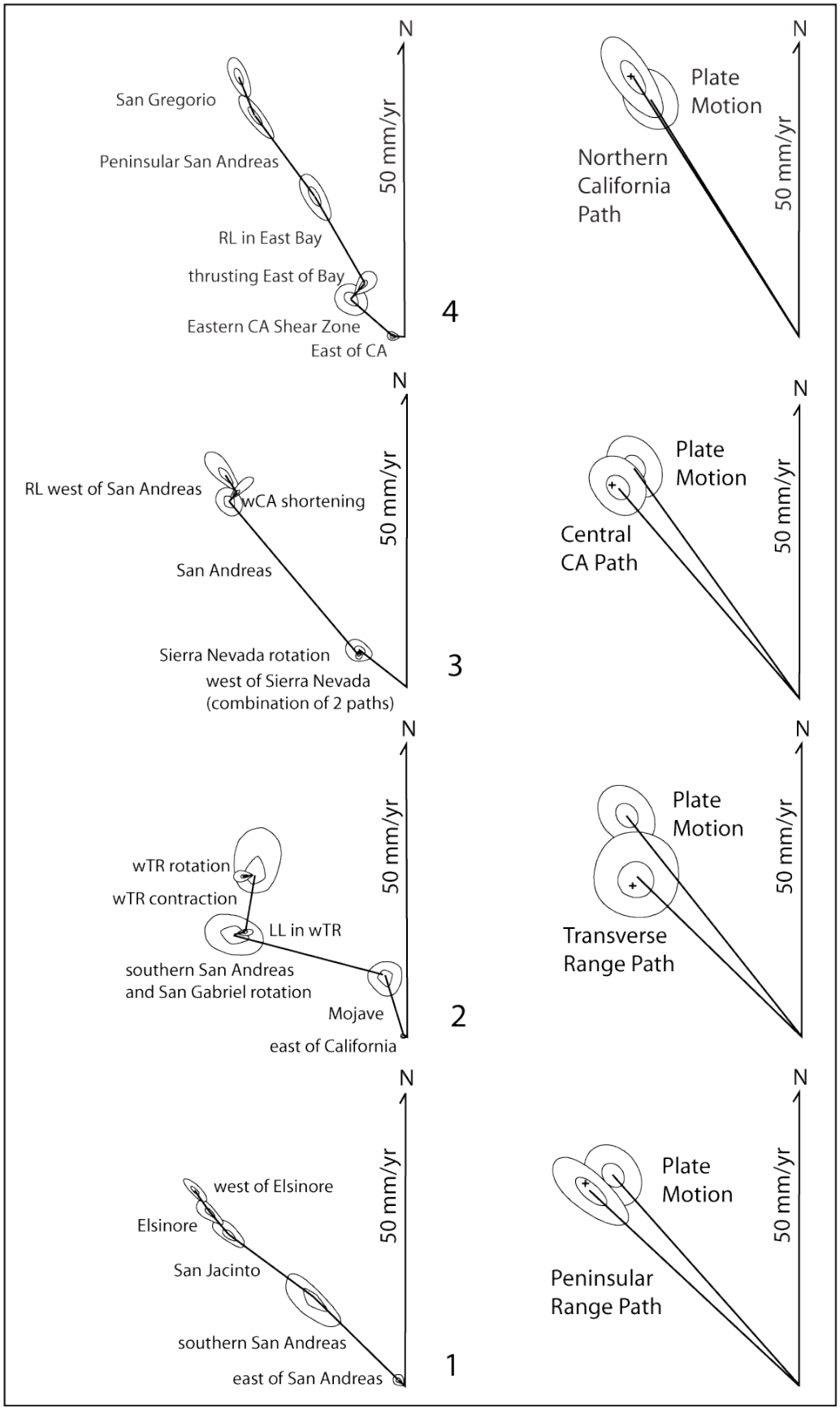
N
San Gregorio
Peninsular San Andreas
RL in East Bay
thrusting East of Bay
Eastern CA Shear Zone
East of CA
50 mm/yr
4
N
Plate
Motion
Northern
California
Path
50 mm/yr
N
RL west of San Andreas
wCA shortening
San Andreas
Sierra Nevada rotation
west of Sierra Nevada
(combination of 2 paths)
50 mm/yr
3
N
Plate
Motion
Central
CA Path
50 mm/yr
N
wTR rotation
wTR contraction
LL in wTR
southern San Andreas
and San Gabriel rotation
Mojave
east of California
50 mm/yr
2
N
Plate
Motion
Transverse
Range Path
50 mm/yr
N
west of Elsinore
Elsinore
San Jacinto
southern San Andreas
east of San Andreas
50 mm/yr
1
N
Plate
Motion
Peninsular
Range Path
50 mm/yr

WG-07 does not include a number of inputs that are required to construct line integrals and to estimate their uncertainty. First, WG-07 does not any information about deformation east of a narrow buffer zone east of California. To complete the analysis we used the values for Humphreys and Weldon (1994) for the southern 4 paths and made an estimate of the rate of extension across the northern Basin and Range for the northernmost path. Second, there are no rotations explicitly included in WG-07. Integrating along paths that cross rotating blocks accumulates deformation associated with the deformation, so must be explicitly included in the analysis. To do so we used the rotations estimated by Humphreys and Weldon (1994). Finally, the WG-07 model does not contain estimates of uncertainty in strike, dip, and rake of faults. Again, we used the uncertainties from Weldon and Humphreys (1994) for faults that they considered and added uncertainties with similar ranges to those faults they did not consider. To estimate how uncertainties accumulate along the path of the line integral, we used the Humphreys and Weldon (1994) approach of Monte Carlo sampling the uncertainties of individual faults that the path includes. An analytical approach was not possible because many of the uncertainties are highly asymmetrical. The results of this uncertainty analysis are represented by uncertainty ellipses that approximate uncertainty thresholds in the final results (Fig. 4.6).

At least two of the paths (Northern California and Peninsular Ranges) appear to accumulate slightly more deformation than the plate rate (Fig. 4.6). This is surprising given that the line integrals do not include distributed deformation (represented in WG-07 model as "background" seismicity). This is in contrast to our strain tensors (discussed in Part Three), which include background seismicity, yet generally yield just under the plate

rate. The answer to this possible discrepancy (it is all within reasonable uncertainties, so may not be significant) is that the line integrals are generally chosen to cross the faults where the slip rates are best known and the faults are simple, straight, and generally parallel to the plate boundary (except for the Transverse Ranges path, which has the lowest total rate; Figure 4.6). In contrast, the strain tensors combine deformation in large crustal volumes, so include both regions where simple and complex faults occur and, in discontinuous fault zones, the gaps in between. It is possible that by choosing the "best" paths and slip rates we are biasing the result towards higher slip rates that may not be representative of the fault as a whole. This is especially true for discontinuous zones where the slip rate used often comes from the middle of a fault where the slip rate is the highest and the actual slip rate tapers to each end of individual strands. A line integral could cross the fault in the middle, where the rate is high, whereas the strain tensor would include the gaps (and tapered ends, if they have lower slip rates) in between as well.

It is also possible that the actual plate rate is higher than the widely accepted rate (~48 mm/yr); recent GPS and VLBI studies suggest the rate is 5-10% higher (e.g. Wdowinski et al., 2007). If this is the case, then picking paths along simple, well studied paths may yield values that approach the real plate rate, whereas the volumes considered in the strain tensor approach would include regions where the deformation is expressed in a few simple faults and others where it is more distributed and thus more difficult to capture in a simple model.

4. PART THREE: STRAIN TENSOR ANALYSIS

To test our deformation and seismic source models, we have constructed strain tensors across the Pacific-North American plate boundary and compared them to predictions from the far field plate motion. We used the Kostrov (1974) method as presented in Aki and Richards (1984). Molnar (1983; 1979; et al., 2007; Chen and Molnar, 1977) and many others have discussed the relative merits of using symmetrical strain tensors (as we do) versus asymmetrical tensors or a combination of rotational and irrotational components of the deformation field. We finesse this issue to some extent by comparing principle strain axes from our symmetrical strain tensors to those resulting from a single ideally-oriented (plate boundary parallel) fault, with the plate rate of slip, embedded in the same volume as the distributed deformation we consider. The fact that the distributed deformation almost exactly equals the strain inferred from the Pacific-North America plate motion in both rate and style suggest that symmetrical tensors adequately capture the deformation. We have analyzed ten 3D volumes spanning our model, oriented perpendicular to the plate boundary (Fig. 4.7; results presented in Table 4.2). We have cut off northernmost California north of the Mendocino triple junction because of the possible influence of the Juan de Fuca subduction zone. We also limited the southern end of the model to approximately the US Mexico border because the coverage of faults drops into Mexico and we have no C- zones south of the US border (Figure 4.7).

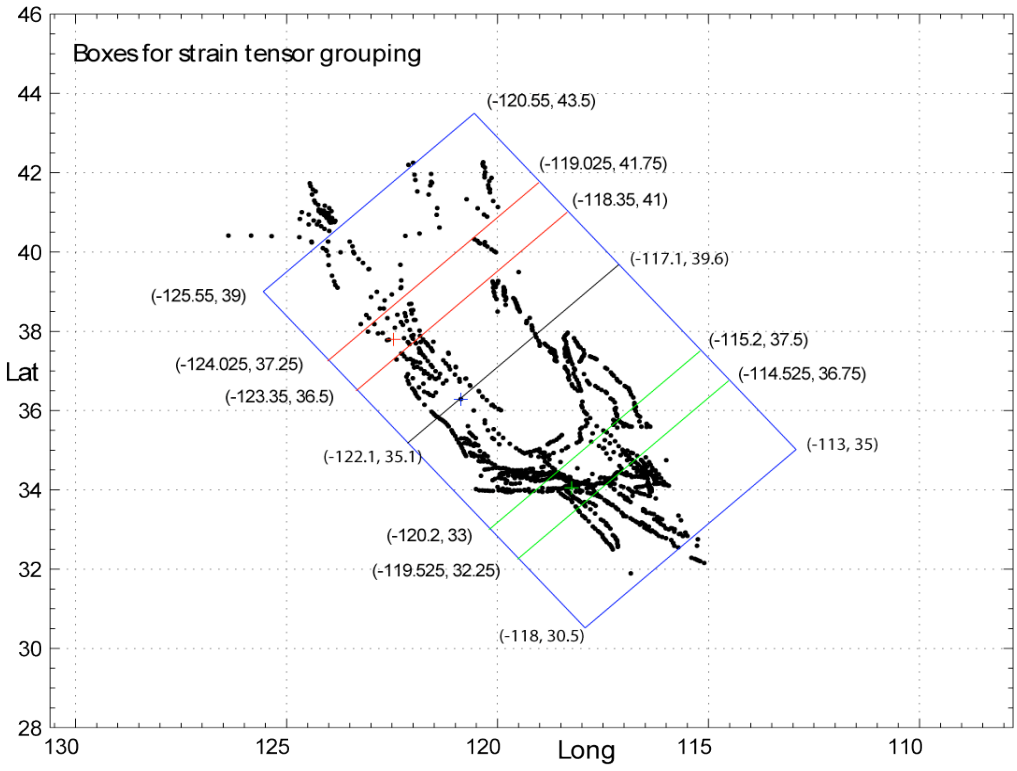

Figure 4.7. Volumes considered for strain tensor analysis (depths of each volume included in Appendix B, Table B.1). Small +s are the ends points of individual linear portions of faults or fault sections. Blue box is the "entire" region considered (it is smaller than the WG -07 model because we limited it at the Mendocino triple junction and the Mexican border). Black line separates the northern and southern volumes, divided at the southern end of the Creeping section of the San Andreas fault. Red and green are the San Francisco and Los Angeles regions, respectively.

For the entire region, our deformation model accounts for ~90% (91.4) of the plate motion (summarized in Table 4.2; tensors are in Appendix B Table B.1, and input values are found in Table B.2). This is almost certainly within the calculation uncertainty, which includes the slip rates on the faults, the rate of background seismicity and aftershocks, the depths of the faults and the thickness of the block being deformed. If significant, the small additional 10% of strain generated by the plate motion may be aseismic strain that is off our modeled faults (Aseismic strain on the faults would be included in the fault's slip rate, and thus in our deformation model; however, for

unmodeled faults, i.e. our "background," we can only "account" for the seismically observed component). Alternatively, we may have incompletely estimated the background rate because it does not formally include aftershocks.

Table 4.2.
1) Percentage of Pacific – North America plate motion accommodated by the model (calculated as the ratio of the maximum principle strain axes presented in Appendix B, Table B.1).
2) Angular difference between the orientation of principle strain axes of the model and average Pacific – North America plate motion of N42W; positive is more northerly and negative more westerly. Most of the difference from north to south is the variation of the direction of plate motion across the region (~15°).
3) Percentage of thickening or thinning of the block relative to the simple shear component (ideal Pacific – North America plate motion has only simple shear and thus no block thickening or thinning).
4) These values do not average to the State total because each box is calculated with the average depth of all of the faults in the box. If one fixes the thickness of the boxes to the State average (~13 km) one would calculate 87.9% for the northern ½ and 99.0% for the southern ½ (see Appendix B Table B.1). Since the average depth of faulting is a real difference between northern and southern California it is more appropriate to use the different average depths of each to compare to the plate boundary total.
5) This value is very sensitive to the rate and orientation of shear applied to the Imperial C-zone and the spatial cut off of the block being considered (since the density of mapped faults drops dramatically into Mexico). An early calculation using the Imperial C-zone of Rate Model 2.2 and a slightly different spatial cut off yielded 115%. Because the Imperial C-zone is given zero value in our current source model, the percent of shear in our source model is as accurate as other boxes.

Summary of Strain Tensor Analysis

Block	**Deformation Model (1)**	**Source Model (1)**	**Angular Difference (2)**	**Vertical change (3)**
Entire Region	91.4%	65.0%	0.1°	4.2%
North 1/2	95.2%(4)	56.1%	7.0°	1.7%
South 1/2	95.5%(4)	78.7%	-6.2°	9.0%
San Francisco	91.4%	67.8%	7.8°	2.1%
North of San Francisco	92.7%	65.0%	-10.6°	3.1%
Los Angeles	101.3%	84.7%	-9.5°	16.4%
South of Los Angeles	85.7%(5)	68.8%(5)	-5.5°	0.7%

For the entire region, our seismic source model accounts for ~70% (65.0% plus an estimated 5% aftershocks that are not included in the model) of the plate motion. This is very consistent with the global average seismic component of strike slip plate boundaries (Bird and Kagan, 2004).

To explore the differences between northern and southern California we split the region approximately in half, perpendicular to the plate boundary, through the northern end of the Parkfield section of the San Andreas fault (or southern end of the Creeping section). The deformation model yields 95.2% for the northern half of the State and 95.5% for the southern. The apparent discrepancy with the entire region (91.4%) is due to different block thicknesses for the different parts of the State. We use the average depth of all the faults in each block being considered to define the block thickness. For the entire State this is 13.0 km, whereas for Northern CA it is 12.0 km and for Southern CA it is 13.5 km (note that it is not the average because there are more faults in the Southern California block). If one were to use the 13.0 average depth for the entire State the Northern California part of our model would have 87.9% and southern California 99.0% of the plate rate; however, since the difference in average depth of faulting is likely to be real, the ~95% values for each half of the State are probably correct.

The similarity of these values to each other and the plate rate strongly suggests that our model accurately captures the strain driving deformation across the plate boundary. In addition, the direction of calculated principle strain axes and small fraction of thickening of the boxes is consistent with the transform plate margin (Table 4.2).

The seismic component for Northern and Southern California are 56.1% and 78.7% respectively. This difference is almost certainly significant and is due to the fact

that the Northern California block contains the Creeping section of the San Andreas fault, major faults in the Bay Area that have significant aseismicity factors and the large Eastern CA C-zone that is given a 50% aseismicity factor. In addition, the Southern CA block has many more B faults that are reverse in style, which due to their low dip and lack of aseismicity contribute significantly to the seismic component of the strain. Thus, the difference between Northern and Southern California probably represent real differences in the seismic component of the strain release across the plate boundary and not a bias in the model.

This real distinction between Southern and Northern California suggest that drawing conclusions from blocks smaller than the entire State may be dangerous. However, to explore possible regional differences we also consider ~100 km wide boxes centered on the San Francisco and Los Angeles regions and similar-sized boxes to the north and south.

The San Francisco block yields a deformation strain rate of 91.4% of the plate total and a seismic rate of 67.8% of the plate rate, essentially identical with the entire State. The block to the north of San Francisco gives similar results of 92.7% and 65.0% respectively. We also looked at the western halves of these blocks (essentially the San Andreas system) and found no significant differences between the Bay Area and the region to the north (early calculations suggesting a difference were biased by errors in the dimensions and shear directions of the C-zones in Rate Model 2.2).

The Los Angeles block yields a deformation strain rate of 101.3% of the plate total and a seismic rate of 84.7% of the plate rate. These values are 5-10% higher than elsewhere and may indicate real differences in the LA region, a slight bias in the data, or

that the block is too small to accurately represent the plate rate. This block contains no known creeping faults, a relatively low slip rate C-zone (Mojave), and a large number of thrusts, so the slightly higher values may reflect a real regional difference.

If the LA rate is too high, it is likely to be because the LA region has a relatively large number of B faults that as a group may have slightly over-estimated slip rates. Finally, it is possible that a slight excess in strain in this block may be balanced by a deficit elsewhere. For example, Humphreys and Weldon (1994) have argued that the loss of surface area along the transform boundary from compression in the Transverse Ranges (largely included within the LA block) is balanced by creation of surface area in the Salton Depression and, potentially Eastern California. So it may simply require a larger region than the LA block to exactly account for the plate deformation.

The southernmost block, between LA and the Mexican border, yields a deformation strain rate of 85.3% of the plate total and a seismic rate of 68.8% of the plate rate. While the deformation rate may be lower than other blocks, the value is very sensitive to where the boundary is drawn (since the distribution of known faults drops rapidly to the south) and the rate assigned to the Imperial Valley C-zone. Earlier estimates using the higher rate on the Imperial C-zone in Rate Model 2.2 and a slightly different spatial cut-off yielded a deformation strain rate of ~115% of the plate rate. The seismic rate, that approximately matches the State average value, is less sensitive because the Imperial C-zone is modeled as being completely aseismic, so its rate does not affect the seismic source model at all.

CHAPTER V

CONCLUSION

In this dissertation I describe my research related to the hydrogeology and surface deformation of two primary California alluvial aquifers embedded in the southern San Andreas fault system, the San Bernardino Basin and the Upper Coachella Valley. Groundwater is an invaluable and vulnerable resource, especially in the arid southwestern United States. There has been a recent growth in public awareness surrounding the issues of excessive groundwater mining, including concern over clean water and sustainability practices. As a geophysicist and hydrogeologist, my focus has been on the differential surface displacement related to groundwater removal and the potential loss of aquifer storage capacity through compaction. I use these heavily pumped and artificially recharged groundwater basins as case studies to investigate the interplay between groundwater hydraulics and aquifer structures of these fault-bound basins. Overdraft-induced land subsidence is a major societal issue addressed in each of these case studies. I focus on the differentiation of the elastic and inelastic hydraulic deformation and make efforts to account for tectonic components of surface displacement. In both aquifer basins I consistently observed differential surface displacement using satellite interferometry.

In Chapter II, I analyze the relationship between shifting groundwater levels and surface displacement in the San Bernardino Basin and develop the HII method for aquifer characterization. I remotely estimate poroelastic material properties and observe a 4 mm/yr range in residual vertical surface displacement rates that is not related to coeval

changes in groundwater levels. Between 1995-2000, in a narrow zone of residual subsidence near the San Jacinto fault, where many normalized poroelastic ratios trend higher than expected, I find permanent compaction of clay-rich strata to be the most likely explanation for 0.5-2.0 mm/yr of residual subsidence. This permanent compaction is likely a result of delayed compaction due to previous overdraft conditions and/or a result of the installation of deep production wells during the span of the InSAR time series. Observations of localized subsidence within stepovers of the San Jacinto fault zone and relative uplift at the range fronts are consistent with current basin development models; however, interseismic strain modeling of the regional faults does not reproduce the surface displacement pattern or magnitude of these observations.

Overall this study highlights complexity in the tectonically active, fault-bound San Bernardino Basin aquifer and formalizes a method of remote aquifer characterization. The HII method is greatly assisted by continuous monitoring of groundwater levels, frequent SAR scene acquisitions, and minimal atmospheric interference, and is applicable in other groundwater basins where surface displacement patterns appear correlated to seasonally changing groundwater levels. Under these conditions the HII method estimates any overprinted inelastic hydraulic process like fine-grained compaction, or long-term process like interseismic deformation. Lower frequency sampling for groundwater levels in the Coachella Valley prompted sensitivity testing of the HII method, indicating typical sampling frequency in the Upper Coachella Valley of 3× yearly is less than optimal, but still may yield meaningful results.

Several lithologic descriptions from drillers' logs and a handful of geophysical logs that I came across while searching through groundwater archives of the San

Bernardino aquifer provided significant insight. This urged me to seek out drillers' logs for use in my study of the Coachella Valley aquifer in Chapter III. I convert descriptive data available ~30 drillers' logs to a systematic hydrostratigraphic and depositional facies analysis of the upper ~300m of the aquifer of the southwestern basin. This facies analysis is used in conjunction with the HII method in order to interpret sharply bound lobes of persistent rapid subsidence observed near the western basin margins.

Overall, this study illuminates the dynamically deforming Coachella Valley aquifer and contributes to the understanding of groundwater management and successful aquifer recharge efforts. Location of groundwater flow barriers in shallow alluvium may indicate seismic risks, including liquefaction in an earthquake, and it is important to assess groundwater flow barriers with earthquake potential in mind.

Earthquake potential in California is the basis for the data compilations and analysis discussed in Chapter III. Far-field plate boundary rates are compared to deformation and seismic source models through the compilation of documented observations of surface creep on California faults and models of fault slip rates. Major finding show that when taking aseismic deformation into consideration, the seismic source models of plate movement are consistent with strain estimated from fault slip observations. The fact that the distributed deformation almost exactly equals the strain inferred from the Pacific-North America plate motion in both rate and style suggest that symmetrical tensors adequately capture the deformation.

In summary, my dissertation explores two diverse alluvial aquifer basins of southern California and their responses to aquifer mining, recharge and overdraft. The primary data is a collection of InSAR data showing significant differential surface

displacement between 1993-2009. My work contributes to the on-going studies of the San Bernardino Basin and Upper Coachella Valley aquifers, two structural basins filled with heterogeneous sedimentary deposits shed off rapidly uplifting mountain ranges along the San Andreas fault zone. The HII method developed in Chapter II and tested in Chapter III offers avenues for the separation and interpretation of overprinted deformation signals, common in the arid basins of the American southwest.

APPENDIX A

SUPPORTING INFORMATION FOR SAN BERNARDINO

We provide, in Table A.1, the estimated model parameters and uncertainties from the application of the HII method at 60 well sites in the San Bernardino basin, California. The 60 sites are labeled in Fig. A.1, and are the same sites shown in Figs 2.5(a) and 2.5(b) in Chapter II. Where well sites are closely clustered a red circle is used for group labeling. As stated in the body text, the variation in both residual vertical displacement rates and normalized poroelastic ratios, particularly within the San Jacinto fault zone, led us to test for correlations between the model parameter estimates and site-specific characteristics. The one resolvable correlation is identified in Chapter II (Fig. 2.6). Figs A.2(a-f) test for correlations between residual vertical displacement rate with the range of measured groundwater level change during the study period (a), average depth to groundwater (b), and with the normalized poroelastic ratios (c). We also test for correlation between normalized poroelastic ratios and basin depth (d), average depth to groundwater (e), and measured groundwater level change during the study period (f). We find no resolvable correlations in these plots.

Table A.1. List of well sites, estimated model parameters and uncertainties

Well	Longitude	Latitude	Normalized Poroelastic Ratio (m^-1)	+/-	Residual vertical displacement (mm/yr)	+/-
101001	-117.2072	34.1015	1.4E-06	5.2E-07	0.7	0.4
106901	-117.1419	34.1140	3.6E-05	9.0E-05	1.5	0.4
135601	-117.1292	34.0711	2.1E-05	5.2E-05	-0.3	0.4
154501	-117.2351	34.0685	3.1E-06	9.2E-07	-1.1	0.5
161801	-117.3332	34.1147	4.2E-07	1.4E-07	-1.1	0.4
171801	-117.1617	34.0428	1.6E-05	5.6E-05	0.4	0.9
172001	-117.1596	34.0430	5.3E-06	5.6E-06	0.7	0.6
172301	-117.2489	34.0698	1.8E-06	4.2E-07	-0.7	0.8
172701	-117.1258	34.0698	1.3E-05	1.2E-05	0.1	0.7
176701	-117.2841	34.0744	2.4E-06	6.1E-07	-0.1	0.5
177301	-117.3162	34.0558	2.2E-06	2.4E-06	-0.3	0.4
177501	-117.3193	34.0507	3.7E-06	5.4E-06	-1.0	0.5
179901	-117.2902	34.0677	1.4E-06	4.1E-07	0.4	0.4
180301	-117.3063	34.0523	1.9E-06	9.8E-07	-1.1	0.3
182601	-117.0782	34.0254	3.0E-08	9.5E-09	-2.0	0.3
191101	-117.3454	34.1429	3.6E-06	1.3E-06	-0.7	0.3
191201	-117.3298	34.1148	2.6E-06	1.1E-05	-1.2	0.3
196501	-117.2666	34.1098	2.6E-06	9.7E-07	-0.5	0.4
204401	-117.1959	34.0538	2.9E-06	1.6E-06	-0.2	0.2
206201	-117.3301	34.1218	2.7E-06	6.3E-07	-0.8	0.3
208601	-117.2505	34.1051	2.8E-06	7.5E-07	0.1	0.6
211001	-117.1117	34.0741	1.0E-05	1.7E-05	-1.2	0.7
211101	-117.1252	34.0764	1.5E-05	3.2E-05	-0.3	0.8
212201	-117.1211	34.0737	9.2E-06	1.6E-05	-1.1	0.7
213201	-117.3385	34.1209	1.1E-06	2.6E-07	-0.6	0.5
214701	-117.3118	34.1187	2.0E-06	9.4E-07	-0.7	0.5
227801	-117.2947	34.0810	6.5E-07	1.3E-07	-0.4	0.3
261701	-117.3234	34.1040	3.6E-06	9.2E-07	-1.5	0.4
261801	-117.3050	34.1038	8.5E-06	1.9E-06	-1.7	0.6
261901	-117.3088	34.1041	8.3E-06	2.3E-06	-1.9	0.4
262001	-117.3118	34.1033	6.3E-06	1.7E-06	-1.6	0.4
262101	-117.3136	34.1078	7.0E-06	2.1E-06	-1.9	0.5
324901	-117.3681	34.1877	3.7E-06	1.8E-06	0.1	0.3
395801	-117.3083	34.1034	9.2E-06	2.1E-05	-1.2	0.5
1N4W7J1	-117.3346	34.1841	1.8E-05	4.5E-05	0.1	0.5
1N5W10J1	-117.3694	34.1832	4.1E-06	3.8E-06	0.2	0.2
1N5W12M2	-117.3654	34.1858	5.1E-06	4.0E-06	0.4	0.4
1N5W21K1S	-117.4061	34.1575	5.1E-06	1.5E-06	1.7	0.3
1N5W27D2S	-117.3975	34.1483	6.4E-06	2.3E-06	0.5	0.2
1N5W28J2S	-117.4003	34.1411	5.9E-06	2.3E-06	-0.6	0.4
1N5W29Q1S	-117.4264	34.1372	1.5E-06	5.5E-07	1.0	0.5
1N5W34D1S	-117.4007	34.1343	6.5E-06	5.4E-06	0.4	0.6
1N5W34D2S	-117.4007	34.1343	7.0E-06	5.8E-06	0.4	0.6
1N5W34D3S	-117.4007	34.1343	7.1E-06	5.9E-06	0.3	0.6
1N5W34D4S	-117.4007	34.1343	7.1E-06	2.7E-06	0.3	0.6
1S4W10B2S	-117.2864	34.1042	2.0E-06	4.7E-07	-0.2	0.4
1S4W10B3S	-117.2864	34.1042	6.8E-06	2.0E-06	-0.9	0.3
1S4W10F1S	-117.2913	34.1026	1.4E-05	3.9E-06	-1.4	0.4
1S4W16J1	-117.2977	34.0816	7.8E-06	2.3E-06	2.0	0.6
1S4W22D2S	-117.2952	34.0774	1.1E-06	3.2E-07	0.6	0.3
1S4W22D4S	-117.2952	34.0774	9.4E-07	2.9E-07	0.2	0.3
1S4W22D7S	-117.2952	34.0774	2.5E-06	7.3E-07	0.4	0.4
1S4W2D6S	-117.2744	34.1185	4.7E-06	2.6E-06	-0.6	0.3
1S4W2D7S	-117.2744	34.1185	4.3E-06	2.6E-06	-0.4	0.4
1S4W2N2S	-117.2755	34.1082	3.5E-06	9.3E-06	-0.1	0.4
1S4W2P2S	-117.2742	34.1100	4.1E-06	3.1E-06	-0.2	0.4
1S4W2Q4S	-117.2665	34.1099	4.4E-06	2.0E-06	-0.5	0.3
1S4W4E4S	-117.3117	34.1151	1.2E-05	3.4E-06	-1.5	0.5
1S4W4E5S	-117.3117	34.1151	7.1E-06	1.8E-06	-1.2	0.5
1S4W4E6S	-117.3117	34.1151	3.3E-06	1.1E-06	-0.8	0.4

Figure A.1. Labeled well locations for San Bernardino basin

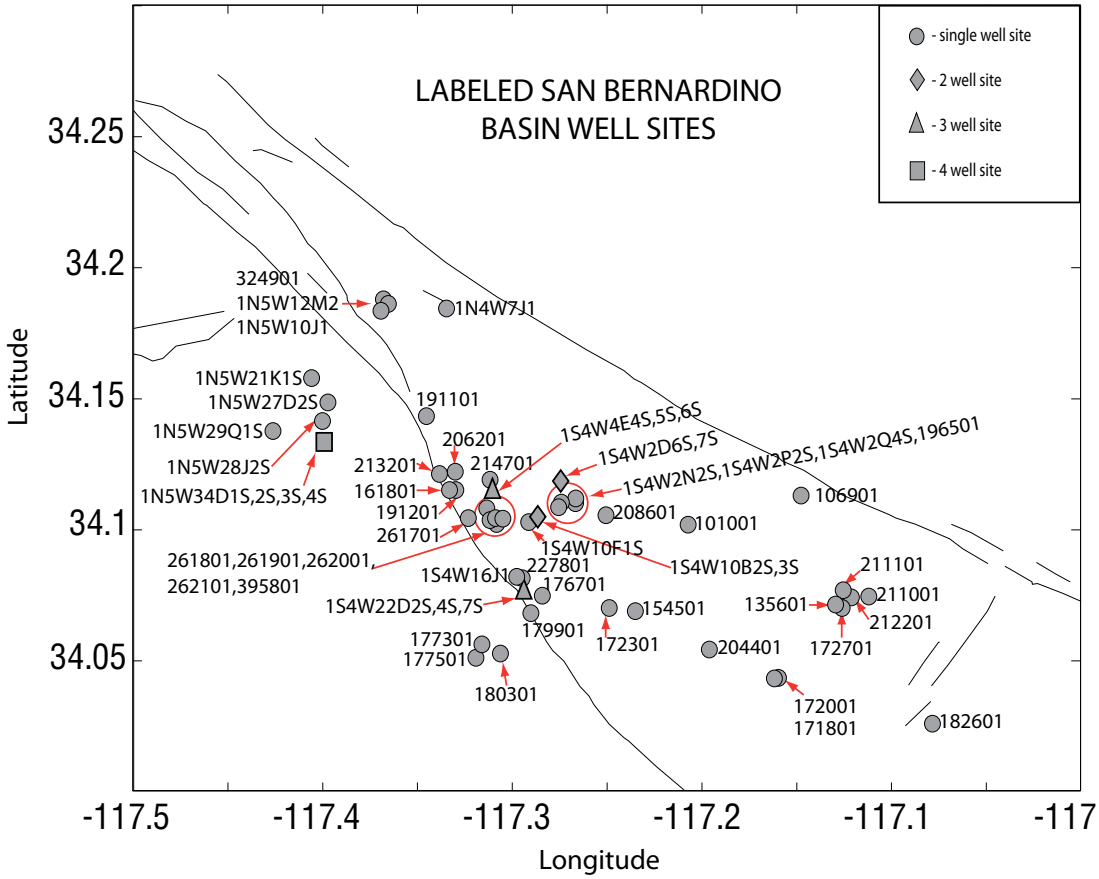

Figure A.2a. Correlation Plot

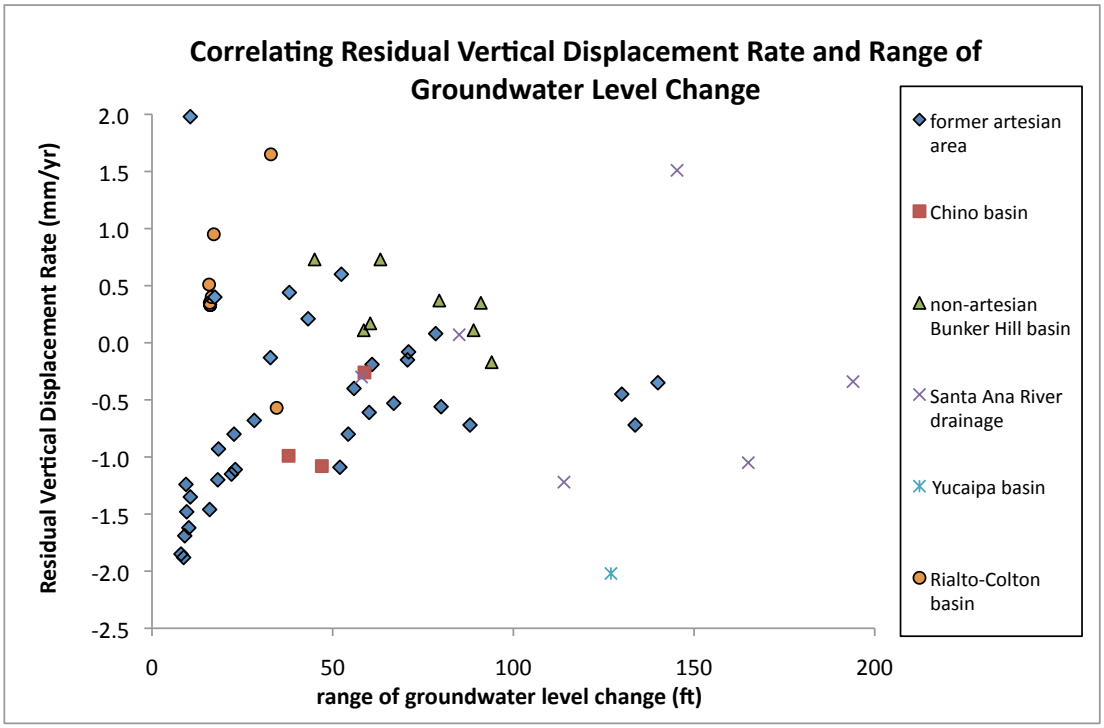

Figure A.2b. Correlation Plot

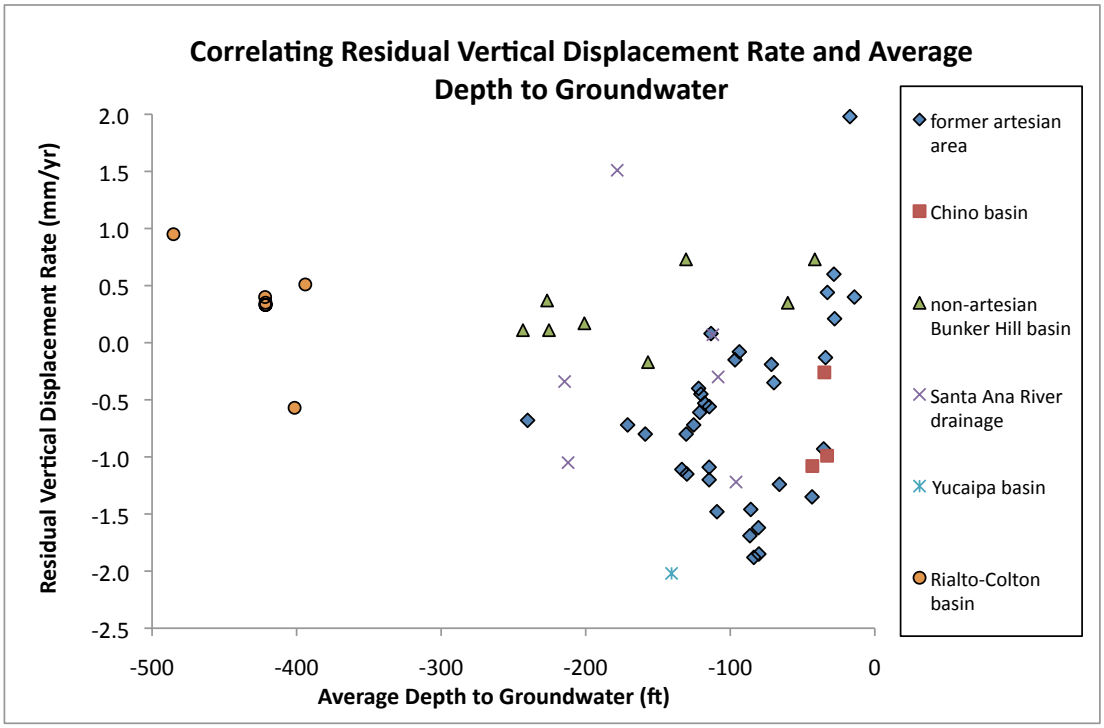

Figure A.2c. CorrelationPlot

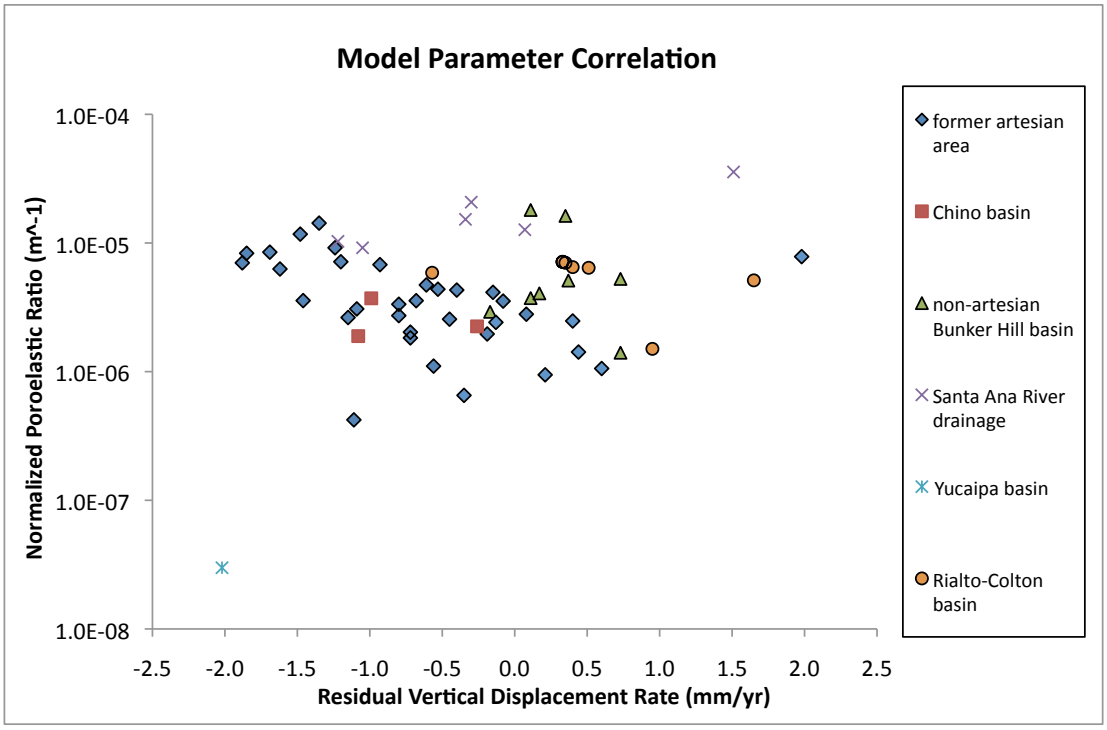

Figure A.2d. Correlation Plot

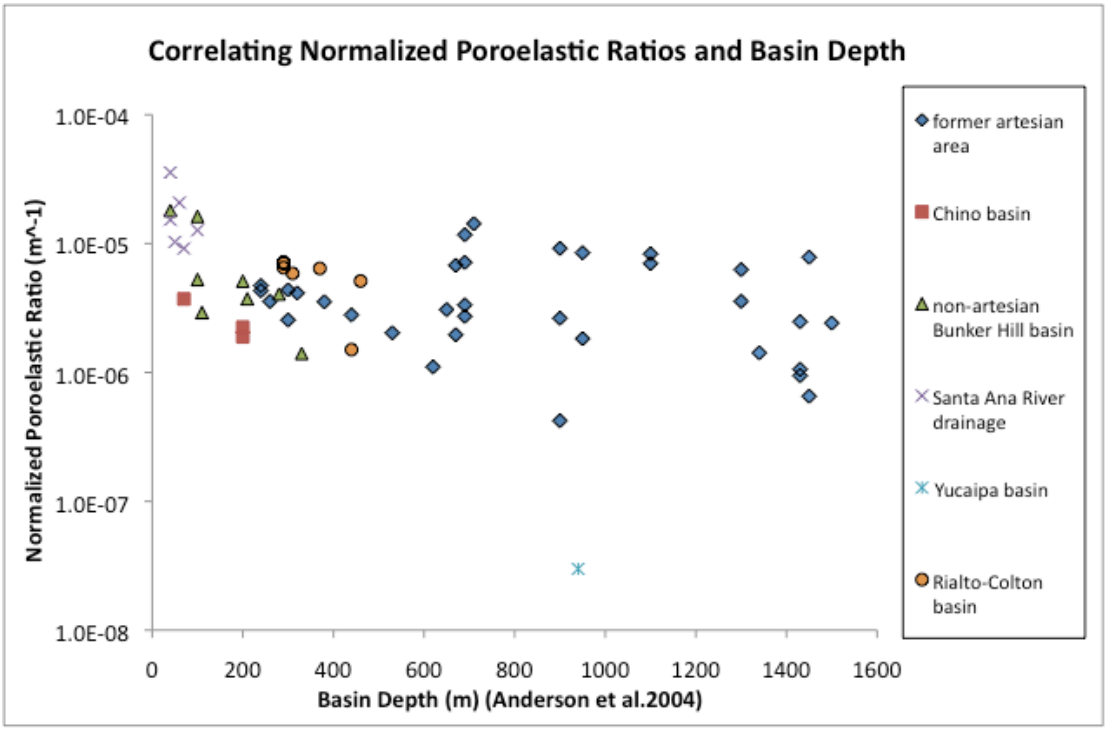

Figure A.2e. Correlation Plot

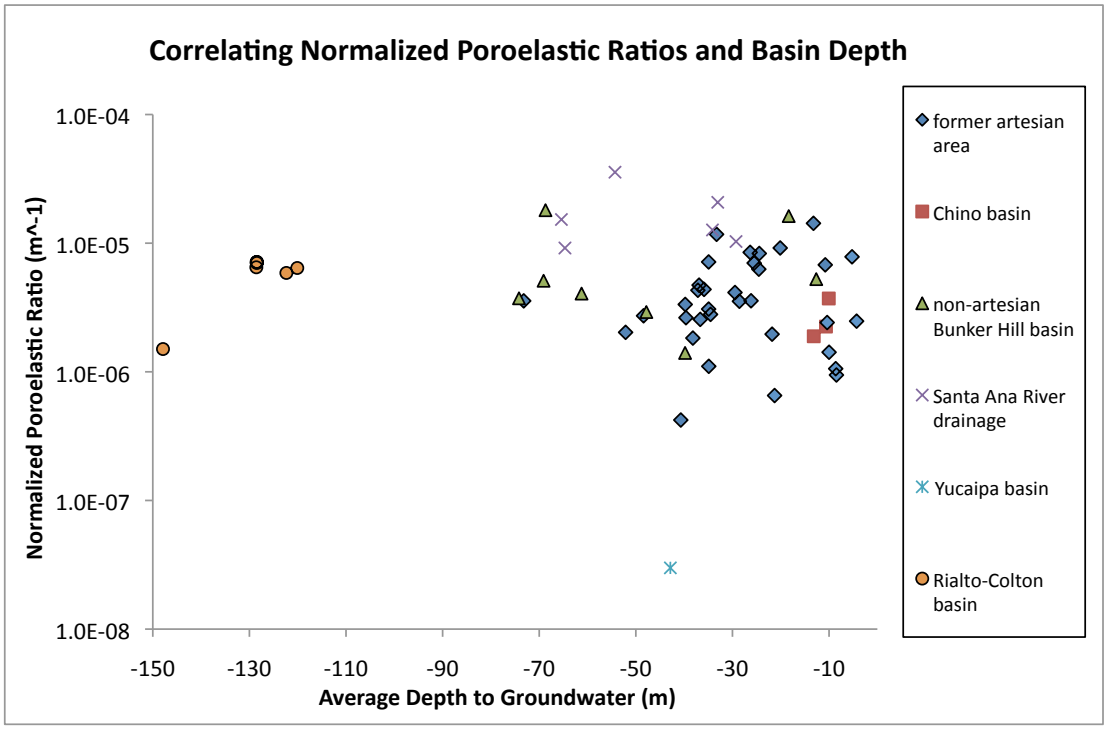

Figure A.2f. Correlation Plot

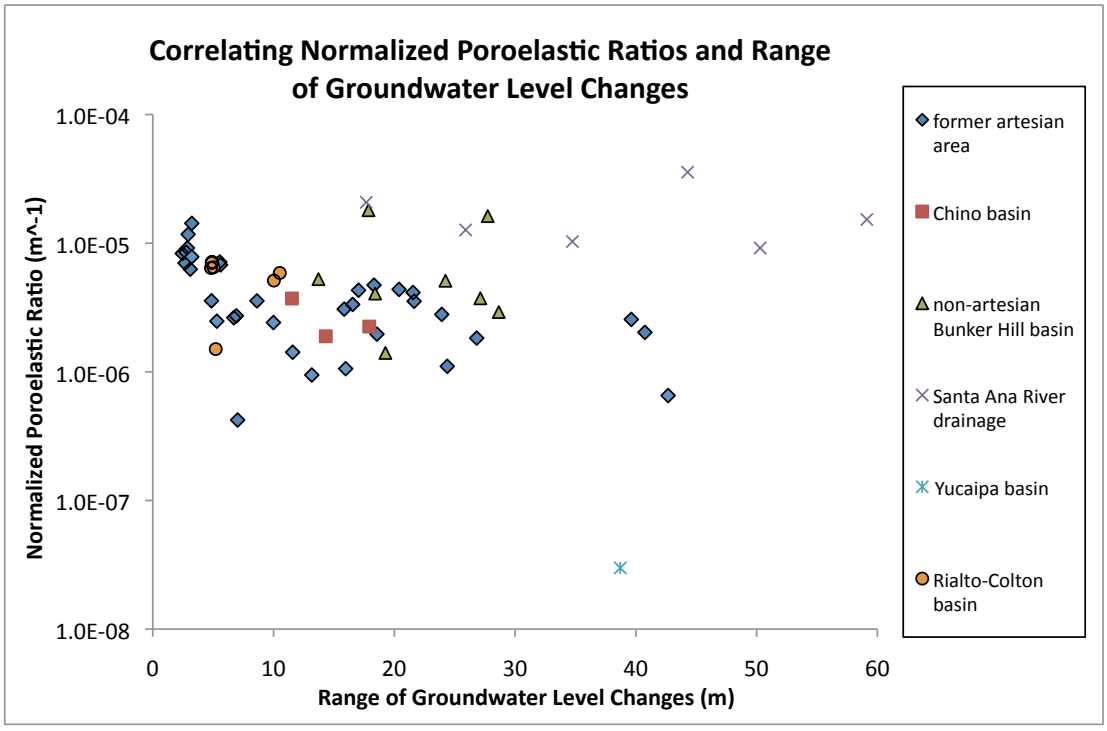

APPENDIX B

STRAIN TENSORS FOR VOLUMES IN FIGURE 4.7

All faults are rotated so that "N" is plate margin parallel, ~42° CW.
M is the moment tensor for simple single fault boxes.
SR is the strain rate matrix for simple single fault boxes.
V columns are the eigenvectors for **D** (eigenvalues for SR and M).
MsumS is the summed Moment tensor for each grouping of faults with a 10% increase from background seismicity (dyne·km)
MsumA is summed Moment tensor for each grouping of faults with a 10% increase from background seismicity, and a 10% decrease in moment, and incorporates an aseismicity factor.
SRS is the strain rate matrix including background seismicity (yr^{-1})
SRA is the strain rate matrix including background seismicity and decreased moments and aseismicity factor
Vs columns are the eigenvectors for **Ds** (eigenvalues for SRS and MsumS)
Va columns are the eigenvectors for **Da** (eigenvalues for SRA and MsumA)

EQUATIONS (from Aki and Richards, 1980)
$\mu = 3.3e+21$ dyne/km^2
$M_o \approx \mu As$, where $\mu = 3.3e+21$ dyne/km^2
A = rupture area
s = slip
Δ = dip
Γ = rake
S = strike

$M_{xx} = -M_o ((\sin \Delta \cos \Gamma \sin 2S) + (\sin 2\Delta \sin \Gamma \sin^2 S))$

$M_{xy} = M_o ((\sin \Delta \cos \Gamma \cos 2S) + (0.5*\sin 2\Delta \sin \Gamma \sin 2S)) = M_{yx}$

$M_{xz} = -M_o ((\cos \Delta \cos \Gamma \cos S) + (\cos 2\Delta \sin \Gamma \sin S)) = M_{zx}$

$M_{yy} = M_o ((\sin \Delta \cos \Gamma \sin 2S) - (\sin 2\Delta \sin \Gamma \cos^2 S))$

$M_{yz} = -M_o ((\cos \Delta \cos \Gamma \sin S) - (\cos 2\Delta \sin \Gamma \cos S)) = M_{zy}$

$M_{zz} = M_o (\sin 2\Delta \sin \Gamma)$

$$\dot{\varepsilon} \cong (1/2\mu VT)\sum_{n=1}^{N} M_{ij}$$

Table B.1. Calculated strain tensors for the volumes represented in Figure 4.7.

Entire Block
Fault Surface Area: 16435.9 km^2
Block volume: 1.2294e+7 km^3

Strike: Due N
Dip: Vertical
Rake: 180 (right lateral)

Slip Rate: 47 mm/yr
Depth = 13.0 km

M =

1.0e+27 *

0	-2.5492	0
-2.5492	0	0
0	0	0

MsumS =

1.0e+27 *

-0.0429	-2.2759	0.0436
-2.2759	-0.0545	-0.0029
0.0436	-0.0029	0.0974

MsumA =

1.0e+27 *

-0.0825	-1.6101	0.0386
-1.6101	-0.0053	-0.0030
0.0386	-0.0030	0.0878

SR =

0	-0.0314	0
-0.0314	0	0
0	0	0

SRS =

-0.0005	-0.0280	0.0005
-0.0280	-0.0007	-0.0000
0.0005	-0.0000	0.0012

SRA =

-0.0010	-0.0198	0.0005
-0.0198	-0.0001	-0.0000
0.0005	-0.0000	0.0011

V =

-0.7071	0	-0.7071
-0.7071	0	0.7071
0	1.0000	0

Vs =

0.7062	-0.0026	0.7080
0.7079	0.0193	-0.7061
-0.0119	0.9998	0.0154

Va =

0.7155	-0.0033	0.6986
0.6984	0.0243	-0.7153
-0.0147	0.9997	0.0197

D =

-0.0314	0	0
0	0	0
0	0	0.0314

Ds =

-0.0287	0	0
0	0.0012	0
0	0	0.0275

Da =

-0.0204	0	0
0	0.0011	0
0	0	0.0193

North Block
Fault Surface Area: 7428.0 km^2
Block volume: 5.5561e+6 km^3

Strike: Due N
Dip: Vertical
Rake: 180 (right lateral)

Slip Rate: 47 mm/yr
Depth: 12.0 km

M =

1.0e+27 *

0	-1.1521	0
-1.1521	0	0
0	0	0

MsumS =

1.0e+27 *

0.2773	-1.0750	0.0020
-1.0750	-0.2575	-0.0124
0.0020	-0.0124	-0.0199

MsumA=

1.0e+26 *

2.0381	-6.2322	0.0164
-6.2322	-1.8610	-0.1152
0.0164	-0.1152	-0.1771

SR =

0	-0.0314	0
-0.0314	0	0
0	0	0

SRS =

0.0076	-0.0293	0.0001
-0.0293	-0.0070	-0.0003
0.0001	-0.0003	-0.0005

SRA =

0.0056	-0.0170	0.0000
-0.0170	-0.0051	-0.0003
0.0000	-0.0003	-0.0005

V =

-0.7071	0	-0.7071
-0.7071	0	0.7071
0	1.0000	0

Vs =

0.6158	-0.0113	-0.7878
0.7878	-0.0013	0.6159
0.0080	0.9999	-0.0081

Va =

0.5921	-0.0175	-0.8057
0.8058	-0.0036	0.5922
0.0133	0.9998	-0.0120

D =

-0.0314	0	0
0	0	0
0	0	0.0314

Ds =

-0.0299	0	0
0	-0.0005	0
0	0	0.0305

Da =

-0.0176	0	0
0	-0.0005	0
0	0	0.0181

West Half Of North Block
Fault Surface Area: 7366.1 km^2
Block volume: 2.7549e+6 km^3

Strike: Due N
Dip: Vertical
Rake: 180 (right lateral)

Slip Rate: 38 mm/yr
Depth: 11.9 km

M =

1.0e+26 *

0	-9.2371	0
-9.2371	0	0
0	0	0

MsumS =

1.0e+26 *

2.7188	-9.1027	0.0395
-9.1027	-2.8538	-0.1544
0.0395	-0.1544	0.1350

MsumA=

1.0e+26 *

1.9789	-5.4016	0.0355
-5.4016	-2.1004	-0.1389
0.0355	-0.1389	0.1215

SR =

0	-0.0508	0
-0.0508	0	0
0	0	0

SRS =

0.0150	-0.0501	0.0002
-0.0501	-0.0157	-0.0008
0.0002	-0.0008	0.0007

SRA =

0.0109	-0.0297	0.0002
-0.0297	-0.0116	-0.0008
0.0002	-0.0008	0.0007

V =

-0.7071	0	-0.7071
-0.7071	0	0.7071
0	1.0000	0

Vs =

0.5946	-0.0168	0.8038
0.8040	-0.0004	-0.5947
0.0103	0.9999	0.0133

Va =

0.5685	-0.0249	0.8223
0.8226	-0.0020	-0.5687
0.0158	0.9997	0.0193

D =

-0.0508	0	0
0	0	0
0	0	0.0508

Ds =

-0.0527	0	0
0	0.0007	0
0	0	0.0520

Da =

-0.0321	0	0
0	0.0007	0
0	0	0.0314

San Francisco Block
Fault Surface Area: 1481.0 km^2
Block volume: 1.1078e+6 km^3

Strike: Due N
Dip: Vertical
Rake: 180 (right lateral)

Slip Rate: 47 mm/yr
Depth: 13.2 km

M =

1.0e+26 *

0	-2.2970	0
-2.2970	0	0
0	0	0

MsumS =

1.0e+26 *

0.5347	-1.9977	0.0139
-1.9977	-0.5811	-0.0316
0.0139	-0.0316	0.0464

MsumA =

1.0e+26 *

0.4132	-1.4749	0.0123
-1.4749	-0.4553	-0.0291
0.0123	-0.0291	0.0421

SR =

0	-0.0314	0
-0.0314	0	0
0	0	0

SRS =

0.0073	-0.0273	0.0002
-0.0273	-0.0079	-0.0004
0.0002	-0.0004	0.0006

SRA =

0.0057	-0.0202	0.0002
-0.0202	-0.0062	-0.0004
0.0002	-0.0004	0.0006

V =

-0.7071	0	-0.7071
-0.7071	0	0.7071
0	1.0000	0

Vs =

0.6045	-0.0167	0.7964
0.7966	0.0029	-0.6046
0.0078	0.9999	0.0151

Va =

0.5989	-0.0208	0.8006
0.8008	0.0031	-0.5989
0.0100	0.9998	0.0185

D =

-0.0314	0	0
0	0	0
0	0	0.0314

Ds =

-0.0287	0	0
0	0.0006	0
0	0	0.0281

Da =

-0.0213	0	0
0	0.0006	0
0	0	0.0207

North of San Francisco Block
Fault Surface Area: 2994.0 km^2
Block volume: 2.2395e+6 km^3

Strike: Due N
Dip: Vertical
Rake: 180 (right lateral)

Slip Rate: 47 mm/yr
Depth: 11.6 km

M =

1.0e+26 *

0	-4.6437	0
-4.6437	0	0
0	0	0

MsumS =

1.0e+26 *

1.6445	-4.0717	-0.0005
-4.0717	-1.5153	-0.0195
-0.0005	-0.0195	-0.1293

MsumA =

1.0e+26 *

1.2586	-2.8266	-0.0005
-2.8266	-1.1422	-0.0175
-0.0005	-0.0175	-0.1163

SR =

0	-0.0314	0
-0.0314	0	0
0	0	0

SRS =

0.0111	-0.0275	-0.0000
-0.0275	-0.0103	-0.0001
-0.0000	-0.0001	-0.0009

SRA =

0.0085	-0.0191	-0.0000
-0.0191	-0.0077	-0.0001
-0.0000	-0.0001	-0.0008

V =

-0.7071	0	-0.7071
-0.7071	0	0.7071
0	1.0000	0

Vs =

0.5649	-0.0041	-0.8251
0.8251	-0.0019	0.5649
0.0039	1.0000	-0.0023

Va =

0.5519	-0.0052	-0.8339
0.8339	-0.0027	0.5519
0.0051	1.0000	-0.0029

D =

-0.0314	0	0
0	0	0
0	0	0.0314

Ds =

-0.0291	0	0
0	-0.0009	0
0	0	0.0300

Da =

-0.0204	0	0
0	-0.0008	0
0	0	0.0212

West Half of North of San Francisco Block
Fault Surface Area: 2994.0 km^2
Block volume: 1.1197e+6 km^3

Strike: Due N
Dip: Vertical

Rake: 180 (right lateral)
Slip Rate: 38 mm/yr
Depth: 11.6 km

M =

1.0e+26 *

0	-3.7545	0
-3.7545	0	0
0	0	0

MsumS =

1.0e+26 *

1.6720	-3.4216	0.0057
-3.4216	-1.6843	-0.0140
0.0057	-0.0140	0.0123

MsumA =

1.0e+26 *

1.2594	-2.5197	0.0052
-2.5197	-1.2704	-0.0126
0.0052	-0.0126	0.0110

SR =

0	-0.0508	0
-0.0508	0	0
0	0	0

SRS =

0.0226	-0.0463	0.0001
-0.0463	-0.0228	-0.0002
0.0001	-0.0002	0.0002

SRA =

0.0170	-0.0341	0.0001
-0.0341	-0.0172	-0.0002
0.0001	-0.0002	0.0001

V =

-0.7071	0	-0.7071
-0.7071	0	0.7071
0	1.0000	0

Vs =

-0.5290	-0.0040	-0.8486
-0.8486	-0.0003	0.5290
-0.0023	1.0000	-0.0032

Va =

-0.5250	-0.0048	-0.8511
-0.8511	-0.0003	0.5251
-0.0028	1.0000	-0.0039

D =

-0.0508	0	0
0	0	0
0	0	0.0508

Ds =

-0.0517	0	0
0	0.0002	0
0	0	0.0515

Da =

-0.0382	0	0
0	0.0001	0
0	0	0.0381

South Block
Fault Surface Area: 8711.6 km^2
Block volume: 6.5162e+6 km^3

Strike: Due N
Dip: Vertical
Rake: 180 (right lateral)

Slip Rate: 47 mm/yr
Depth: 13.5 km

M =

1.0e+27 *

0	-1.3512	0
-1.3512	0	0
0	0	0

MsumS =

1.0e+27 *

-0.3202	-1.2009	0.0416
-1.2009	0.2030	0.0095
0.0416	0.0095	0.1172

MsumA =

1.0e+26 *

-2.8807	-9.8225	0.3613
-9.8225	1.8256	0.0837
0.3613	0.0837	1.0551

SR =

0	-0.0314	0
-0.0314	0	0
0	0	0

SRS =

-0.0074	-0.0279	0.0010
-0.0279	0.0047	0.0002
0.0010	0.0002	0.0027

SRA =

-0.0067	-0.0228	0.0008
-0.0228	0.0042	0.0002
0.0008	0.0002	0.0025

V =

-0.7071	0	-0.7071
-0.7071	0	0.7071
0	1.0000	0

Vs =

-0.7786	0.0101	-0.6275
-0.6270	0.0309	0.7784
0.0273	0.9995	-0.0177

Va =

-0.7850	0.0110	-0.6194
-0.6189	0.0323	0.7848
0.0287	0.9994	-0.0186

D =

-0.0314	0	0
0	0	0
0	0	0.0314

Ds =

-0.0300	0	0
0	0.0027	0
0	0	0.0272

Da =

-0.0247	0	0
0	0.0025	0
0	0	0.0223

Los Angeles Block
Fault Surface Area: 1537.1 km^2
Block volume: 1.1498e+6 km^3

Strike: Due N
Dip: Vertical
Rake: 180 (right lateral)

Slip Rate: 47 mm/yr
Depth: 13.7 km

M =

1.0e+26 *

0	-2.3840	0
-2.3840	0	0
0	0	0

MsumS =

1.0e+26 *

-0.9139	-2.0952	-0.0925
-2.0952	0.5232	-0.0275
-0.0925	-0.0275	0.3907

MsumA =

1.0e+26 *

-0.7203	-1.7544	-0.0832
-1.7544	0.3686	-0.0247
-0.0832	-0.0247	0.3517

SR =

0	-0.0314	0
-0.0314	0	0
0	0	0

SRS =

-0.0120	-0.0276	-0.0012
-0.0276	0.0069	-0.0004
-0.0012	-0.0004	0.0051

SRA =

-0.0095	-0.0231	-0.0011
-0.0231	0.0049	-0.0003
-0.0011	-0.0003	0.0046

V =

-0.7071	0	-0.7071
-0.7071	0	0.7071
0	1.0000	0

Vs =

-0.8135	-0.0152	-0.5814
-0.5807	-0.0346	0.8134
-0.0325	0.9993	0.0193

Va =

-0.8048	-0.0144	-0.5934
-0.5926	-0.0386	0.8046
-0.0345	0.9992	0.0225

D =

-0.0314	0	0
0	0	0
0	0	0.0314

Ds =

-0.0318	0	0
0	0.0052	0
0	0	0.0266

Da =

-0.0266	0	0
0	0.0047	0
0	0	0.0219

South of Los Angeles Block
Fault Surface Area: 3613.4 km^2
Block volume: 2.7028e+6 km^3

Strike: Due N
Dip: Vertical
Rake: 180 (right lateral)

Slip Rate: 47 mm/yr
Depth: 14.0 km

M =

1.0e+26 *

0	-5.6044	0
-5.6044	0	0
0	0	0

MsumS =

1.0e+26 *

-0.9318	-4.6876	0.2257
-4.6876	0.8885	-0.1002
0.2257	-0.1002	0.0433

MsumA =

1.0e+26 *

-0.9208	-3.7189	0.1985
-3.7189	0.8818	-0.0908
0.1985	-0.0908	0.0390

SR =

0	-0.0314	0
-0.0314	0	0
0	0	0

SRS =

-0.0052	-0.0263	0.0013
-0.0263	0.0050	-0.0006
0.0013	-0.0006	0.0002

SRA =

-0.0052	-0.0208	0.0011
-0.0208	0.0049	-0.0005
0.0011	-0.0005	0.0002

V =

-0.7071	0	-0.7071
-0.7071	0	0.7071
0	1.0000	0

Vs =

0.7717	-0.0121	0.6359
0.6356	0.0506	-0.7704
-0.0228	0.9986	0.0468

Va =

0.7861	-0.0115	0.6180
0.6175	0.0562	-0.7845
-0.0257	0.9984	0.0513

D =

-0.0314	0	0
0	0	0
0	0	0.0314

Ds =

-0.0269	0	0
0	0.0002	0
0	0	0.0267

Da =

-0.0216	0	0
0	0.0002	0
0	0	0.0214

North Block with 13 km depth
Fault Surface Area: 7428.0 km^2
Block volume: 6.0192e+6 km^3

Strike: Due N
Dip: Vertical
Rake: 180 (right lateral)

Slip Rate: 47 mm/yr
Depth: 13.0 km

M =

1.0e+27 *

0	-1.2481	0
-1.2481	0	0
0	0	0

MsumS =

1.0e+27 *

0.2773	-1.0750	0.0020
-1.0750	-0.2575	-0.0124
0.0020	-0.0124	-0.0199

MsumA

1.0e+26 *

2.0381	-6.2322	0.0164
-6.2322	-1.8610	-0.1152
0.0164	-0.1152	-0.1771

SR =

0	-0.0314	0
-0.0314	0	0
0	0	0

SRS =

0.0070	-0.0271	0.0000
-0.0271	-0.0065	-0.0003
0.0000	-0.0003	-0.0005

SRA =

0.0051	-0.0157	0.0000
-0.0157	-0.0047	-0.0003
0.0000	-0.0003	-0.0004

V =

-0.7071	0	-0.7071
-0.7071	0	0.7071
0	1.0000	0

Vs =

0.6158	-0.0113	-0.7878
0.7878	-0.0013	0.6159
0.0080	0.9999	-0.0081

Va =

0.5921	-0.0175	-0.8057
0.8058	-0.0036	0.5922
0.0133	0.9998	-0.0120

D =

-0.0314	0	0
0	0	0
0	0	0.0314

Ds =

-0.0276	0	0
0	-0.0005	0
0	0	0.0281

Da =

-0.0162	0	0
0	-0.0004	0
0	0	0.0167

South Block with 13 km depth
Fault Surface Area: 8711.6 km^2
Block volume: 6.2749e+6 km^3

Strike: Due N
Dip: Vertical
Rake: 180 (right lateral)

Slip Rate: 47 mm/yr
Depth: 13.0 km

M =

1.0e+27 *

0	-1.3011	0
-1.3011	0	0
0	0	0

MsumS =

1.0e+27 *

-0.3202	-1.2009	0.0416
-1.2009	0.2030	0.0095
0.0416	0.0095	0.1172

MsumA =

1.0e+26 *

-2.8807	-9.8225	0.3613
-9.8225	1.8256	0.0837
0.3613	0.0837	1.0551

SR =

0	-0.0314	0
-0.0314	0	0
0	0	0

SRS =

-0.0077	-0.0290	0.0010
-0.0290	0.0049	0.0002
0.0010	0.0002	0.0028

SRA =

-0.0070	-0.0237	0.0009
-0.0237	0.0044	0.0002
0.0009	0.0002	0.0025

V =

-0.7071	0	-0.7071
-0.7071	0	0.7071
0	1.0000	0

Vs =

-0.7786	0.0101	-0.6275
-0.6270	0.0309	0.7784
0.0273	0.9995	-0.0177

Va =

-0.7850	0.0110	-0.6194
-0.6189	0.0323	0.7848
0.0287	0.9994	-0.0186

D =

-0.0314	0	0
0	0	0
0	0	0.0314

Ds =

-0.0311	0	0
0	0.0028	0
0	0	0.0283

Da =

-0.0257	0	0
0	0.0026	0
0	0	0.0231

Table B.2. Input for strain tensors and line integrals.

Fault sections are assigned the following numbers so that it is easier to account for what faults are in what strain tensors or line integral.

Section Name	sect #
Green Valley (So)	1
Mount Diablo Thrust	2
Concord	3
Calaveras (No)	4
Calaveras (Central)	5
Greenville (No)	6
Greenville (So)	7
Monte Vista-Shannon	8
Ortigalita	9
Rinconada	10
Monterey Bay-Tularcitos	11
San Gregorio (No)	12
Mendocino	13
Honey Lake	14
Table Bluff	15
Little Salmon (Offshore)	16
Little Salmon (Onshore)	17
Big Lagoon-Bald Mtn	18
Trinidad	19
Fickle Hill	20
McKinleyville	21
Mad River	22
Collayomi	23
Bartlett Springs	24
Rodgers Creek	25
San Andreas (Offshore)	26
San Andreas (North Coast)	27
San Jacinto (Superstition Mtn)	28
San Gregorio (So)	29
Hosgri	30
San Juan	31
San Andreas (Parkfield)	32
Gillem-Big Crack	33
Cedar Mtn-Mahogany Mtn	34
Likely	35
Surprise Valley	36
Hat Creek-McArthur-Mayfield	37
Robinson Creek	38
Mono Lake	39
Hartley Springs	40
Hilton Creek	41
Round Valley	42
Fish Slough	43
White Mountains	44

Death Valley (No of Cucamongo)	45
Death Valley (No)	46
Owl Lake	47
Garlock (East)	48
Garlock (West)	49
Hunter Mountain-Saline Valley	50
Deep Springs	51
Point Reyes	52
Zayante-Vergeles	53
Quien Sabe	54
Calaveras (So)	55
San Andreas (Santa Cruz Mtn)	56
San Andreas (Creeping Segment)	57
Pleito	58
So Sierra Nevada	59
Owens Valley	60
Independence	61
Birch Creek	62
San Andreas (Peninsula)	63
Hayward (No)	64
Hayward (So)	65
West Napa	66
Green Valley (No)	67
Hunting Creek-Berryessa	68
Battle Creek	69
Los Osos	70
San Luis Range (So Margin)	71
Lions Head	72
Santa Ynez (West)	73
Mission Ridge-Arroyo Parida-Santa Ana	74
Santa Ynez (East)	75
San Cayetano	76
Cleghorn	77
North Frontal (West)	78
North Frontal (East)	79
Helendale-So Lockhart	80
Lenwood-Lockhart-Old Woman Springs	81
Gravel Hills-Harper Lk	82
Blackwater	83
Calico-Hidalgo	84
Pisgah-Bullion Mtn-Mesquite Lk	85
So Emerson-Copper Mtn	86
Johnson Valley (No)	87
Landers	88
Pinto Mtn	89
Burnt Mtn	90
Eureka Peak	91
Elmore Ranch	92
Imperial	93
Superstition Hills	94

San Jacinto (Borrego)	95
San Jacinto (Coyote Creek)	96
Elsinore (Julian)	97
Elsinore (Coyote Mountain)	98
Laguna Salada	99
San Jose	100
Hollywood	101
Palos Verdes	102
Santa Rosa Island	103
Santa Cruz Island	104
Verdugo	105
Sierra Madre (San Fernando)	106
Sierra Madre	107
Simi-Santa Rosa	108
Oak Ridge (Onshore)	109
Ventura-Pitas Point	110
Red Mountain	111
San Jacinto (San Bernardino)	112
Coronado Bank	113
Newport-Inglewood (Offshore)	114
Rose Canyon	115
Clamshell-Sawpit	116
Cucamonga	117
Channel Islands Thrust	118
Northridge	119
Great Valley 1	120
Great Valley 3, Mysterious Ridge	121
Great Valley 2	122
Great Valley 4a, Trout Creek	123
Great Valley 5, Pittsburg Kirby Hills	124
Great Valley 7	125
Great Valley 8	126
Great Valley 10	127
Great Valley 11	128
Great Valley 12	129
Great Valley 14 (Kettleman Hills)	130
Great Valley 13 (Coalinga)	131
San Joaquin Hills	132
Little Lake	133
Tank Canyon	134
Elysian Park (Upper)	135
Carson Range (Genoa)	136
Antelope Valley	137
Maacama-Garberville	138
Goose Lake	139
Great Valley 9	140
Raymond	141
Casmalia (Orcutt Frontal)	142
Los Alamos-West Baseline	143
Pitas Point (Lower, West)	144

Pitas Point (Lower)-Montalvo	145
Anacapa-Dume, alt 1	146
Malibu Coast, alt 1	147
Santa Monica, alt 1	148
Santa Susana, alt 1	149
Holser, alt 1	150
Newport-Inglewood, alt 1	151
Whittier, alt 2	152
Chino, alt 1	153
Puente Hills	154
Panamint Valley	155
Death Valley (Black Mtns Frontal)	156
Death Valley (So)	157
San Gabriel	158
Earthquake Valley	159
White Wolf	160
San Andreas (San Bernardino N)	161
San Andreas (San Bernardino S)	162
San Andreas (San Gorgonio Pass-Garnet Hlll)	163
San Andreas (Cholame) rev	164
San Andreas (Mojave N)	165
San Andreas (Big Bend)	166
San Jacinto (San Jacinto Valley) rev	167
San Jacinto (San Jacinto Valley, stepover)	168
San Jacinto (Anza, stepover)	169
San Jacinto (Clark) rev	170
San Jacinto (Anza) rev	171
San Andreas (Coachella) rev	172
Elsinore (Glen Ivy) rev	173
Elsinore (Glen Ivy stepover)	174
Elsinore (Temecula stepover)	175
Elsinore (Temecula) rev	176
San Andreas (Carrizo) rev	177
San Andreas (Mojave S)	178
West Tahoe	179
North Tahoe	180
Garlock (Central)	181
Great Valley 4b, Gordon Valley	182
Czone_Foothill_Flt_Sys	183
Czone_Mohawk_Honey_Lake	184
Czone_NE_Cal	185
Czone_Western_Nevada	186
Czone_ECSZ	187
Czone_Imperial_Valley	188
Czone_San_Gorgonio_Knot	189

Columns below are:
1) section id corresponding to the section name above,
2) average strike
3) dip
4) slip rate (mm/yr)
5) rake
6) area (km2)

Entire box fault list

1	-13.90394173	90.0	5.0	180.0	352.2605374
2	-49.1812574	38.0	2.0	90.0	325.1186408
3	-26.30146625	90.0	4.0	180.0	274.9149512
4	156.6543651	90.0	6.0	180.0	587.701315
5	149.2044787	90.0	15.0	180.0	647.8842615
6	146.1013812	90.0	2.0	180.0	397.9174292
7	152.1869967	90.0	2.0	180.0	353.5976168
8	124.616856	45.0	0.4	90.0	223.2353262
9	150.1407721	90.0	1.0	180.0	771.4763872
10	143.3101458	90.0	1.0	180.0	1907.732537
11	-40.71480928	90.0	0.5	150.0	1168.202861
12	158.0271488	90.0	7.0	180.0	1315.361936
14	-49.89690553	90.0	2.5	180.0	631.7722196
23	-33.29049806	90.0	0.6	180.0	284.866272
24	-29.72039639	90.0	6.0	180.0	2610.370283
25	-29.55398905	90.0	9.0	180.0	748.3496166
27	-35.20740864	90.0	24.0	180.0	2082.92384
28	119.5330218	90.0	5.0	180.0	325.8234224
29	-23.69506075	90.0	3.0	180.0	795.1433645
30	-31.45025707	80.0	2.5	180.0	1182.228217
31	152.7601348	90.0	1.0	180.0	880.2721048
32	-40.06046446	90.0	34.0	180.0	371.5908331
33	2.639363974	60.0	1.0	-90.0	412.7778823
35	-39.09484109	90.0	0.3	180.0	703.7458117
36	-8.469508945	50.0	1.3	-90.0	1093.999405
37	166.6909233	60.0	1.5	-90.0	1071.51036
38	27.60097107	50.0	0.5	-90.0	283.0106569
39	-17.32529623	50.0	2.5	-90.0	436.119332
40	-16.40517436	50.0	0.5	-90.0	418.5515684
41	-28.26264248	50.0	2.5	-90.0	497.3720676
42	-19.63609881	50.0	1.0	-90.0	734.7058252
43	-0.763531401	50.0	0.2	-90.0	440.6973324
44	-8.155249112	90.0	1.0	180.0	1438.322766
45	-38.13955154	90.0	5.0	-150.0	998.3320045
46	-39.47764013	90.0	5.0	180.0	1384.998125
47	57.5799599	90.0	2.0	0.0	302.3648728
48	90.97338746	90.0	3.0	0.0	519.2524931
49	58.68246799	90.0	6.0	0.0	1434.369921
50	-42.70915639	90.0	2.5	-150.0	897.186127
51	-155.4450827	50.0	0.8	-90.0	429.8624005
52	-52.95645863	50.0	0.3	90.0	557.1501174
53	-53.83569315	90.0	0.1	150.0	694.410828
54	-35.81342396	90.0	1.0	180.0	228.4533227
55	-19.36050843	90.0	15.0	180.0	212.6143623

56	-48.23350832	90.0	17.0	180.0	931.622146
57	137.0467275	90.0	34.0	180.0	1461.712439
58	90.96516861	46.0	2.0	90.0	823.8165132
59	1.648681567	50.0	0.1	-90.0	1996.236994
60	-18.63193849	90.0	1.5	180.0	1156.944725
61	-29.13491508	50.0	0.2	-90.0	1028.809314
62	-23.72819163	50.0	0.7	-90.0	262.7874641
63	-36.43547045	90.0	17.0	180.0	1098.740252
64	-33.78942937	90.0	9.0	180.0	417.7729511
65	-37.54659649	90.0	9.0	180.0	629.4265908
66	-21.46254698	90.0	1.0	180.0	295.6716887
67	-11.80178756	90.0	5.0	180.0	196.7419607
68	-26.42025354	90.0	6.0	180.0	715.7943749
69	75.2161373	75.0	0.5	-90.0	330.6193806
70	118.1932757	45.0	0.5	90.0	627.9021117
71	-53.45414684	45.0	0.2	90.0	901.6030524
72	-60.94741837	75.0	0.02	90.0	428.2089517
73	91.53917223	70.0	2.0	0.0	660.4970173
74	85.97858425	70.0	0.4	90.0	556.7324572
75	81.79635089	70.0	2.0	0.0	967.4692671
76	-87.46279808	42.0	6.0	90.0	1005.025735
77	97.42274035	90.0	3.0	0.0	391.8568763
78	81.0430746	49.0	1.0	90.0	1043.012394
79	96.56236988	41.0	0.5	90.0	677.9678743
80	-39.12921405	90.0	0.6	180.0	1459.194151
81	-46.7459093	90.0	0.9	180.0	1915.824787
82	-48.64022845	90.0	0.7	180.0	741.9517328
83	-35.10899493	90.0	0.5	180.0	719.9929387
84	-37.5802822	90.0	1.8	180.0	1624.325036
85	-30.08623793	90.0	0.8	180.0	1158.807383
86	-38.60003052	90.0	0.6	180.0	761.8356905
87	-39.10629038	90.0	0.6	180.0	559.7724348
88	-30.01951978	90.0	0.6	180.0	1427.15399
89	85.22576491	90.0	2.5	0.0	1147.810881
90	174.5662819	67.0	0.6	180.0	364.698984
91	-15.03776157	90.0	0.6	180.0	282.7409352
92	-140.3402293	90.0	1.0	0.0	330.5337807
94	130.0261945	90.0	4.0	180.0	455.8638615
95	133.0591279	90.0	4.0	180.0	448.4687641
96	132.7847548	90.0	4.0	180.0	681.5267123
97	-54.21481916	84.0	5.0	180.0	1426.064922
98	-54.72870569	82.0	4.0	180.0	517.2782765
100	-115.5014465	74.0	0.5	30.0	322.7750225
101	-103.5286384	70.0	1.0	30.0	309.8676158
102	-37.487553	90.0	3.0	180.0	1347.941142
103	-88.83687151	90.0	1.0	30.0	500.518891
104	98.20113999	90.0	1.0	30.0	919.0425243
105	-59.4703495	55.0	0.5	90.0	513.4860698
106	-80.72085333	45.0	2.0	90.0	332.5567324
107	-71.36903256	53.0	2.0	90.0	1011.960387
108	-104.490274	60.0	1.0	30.0	501.7696116
109	69.26845481	65.0	4.0	90.0	1001.423579
110	-96.91243096	64.0	1.0	60.0	681.8182794
111	-88.49559245	56.0	2.0	90.0	1709.590867
112	135.4487212	90.0	6.0	180.0	725.7316865
113	146.5658988	90.0	3.0	180.0	1602.234945

114	136.892991	90.0	1.5	180.0	677.5214596
115	-22.34428898	90.0	1.5	180.0	538.0570886
116	-116.2164686	50.0	0.5	90.0	293.2582356
117	-102.9544062	45.0	5.0	90.0	308.8457378
118	-95.53554943	20.0	1.5	90.0	1263.025782
119	111.2067365	35.0	1.5	90.0	546.4077678
120	177.8707637	15.0	0.1	90.0	438.7774436
121	157.2347183	20.0	1.25	90.0	751.4722058
122	-177.4361483	15.0	0.1	90.0	219.814698
123	155.0240167	20.0	1.25	90.0	280.2728708
124	158.9503977	90.0	1.0	180.0	318.9877681
125	134.1495367	15.0	1.5	90.0	447.8304393
126	158.509447	15.0	1.5	90.0	409.7238976
127	152.044083	15.0	1.5	90.0	216.6055935
128	131.4158411	15.0	1.5	90.0	245.7755835
129	152.7743111	15.0	1.5	90.0	175.20183
130	125.243537	22.0	1.5	90.0	922.2551011
131	136.0738421	15.0	1.5	90.0	743.7333501
132	114.3710172	23.0	0.5	90.0	730.0961398
133	-32.32791145	90.0	0.7	180.0	516.1473104
134	-179.1153138	50.0	1.0	-90.0	173.0268
135	-74.77190832	50.0	1.3	90.0	315.7264484
136	-4.787476878	50.0	2.0	-90.0	902.3629356
137	-18.92809284	50.0	0.8	-90.0	697.5579714
138	-30.75838308	90.0	9.0	180.0	2650.92268
139	167.3110345	50.0	0.1	-90.0	742.9481705
140	147.1231386	15.0	1.5	90.0	391.534555
141	-102.0156306	79.0	1.5	60.0	357.2379105
142	115.9631537	75.0	0.25	90.0	300.7047166
143	121.3539072	30.0	0.7	90.0	555.4398079
144	-86.88273588	13.0	2.5	90.0	1127.167395
145	-90.68338948	16.0	2.5	90.0	1349.133993
146	-95.58631598	45.0	3.0	60.0	1115.785685
147	-86.88902897	75.0	0.3	30.0	305.0807665
148	-107.1865129	75.0	1.0	30.0	267.3928918
149	-81.00101994	55.0	5.0	90.0	540.6694611
150	97.14864255	58.0	0.4	90.0	430.0512147
151	-41.18499123	88.0	1.0	180.0	980.5495407
152	-66.26707221	75.0	2.5	150.0	674.8205057
153	145.5857064	50.0	1.0	150.0	285.8834667
154	-69.61224038	25.0	0.7	90.0	835.6808537
155	-26.20413101	90.0	2.5	-150.0	1424.455959
156	166.169094	60.0	4.0	-150.0	1141.450665
157	-39.08392655	90.0	4.0	180.0	544.5739578
158	-50.88756761	61.0	1.0	180.0	1198.650564
159	126.7503977	90.0	2.0	180.0	382.7808363
160	50.72426682	75.0	2.0	60.0	957.6234018
161	121.5025573	90.0	22.0	180.0	451.939471
162	119.6950615	90.0	16.0	180.0	555.4873932
163	-70.15887366	58.0	10.0	180.0	842.9906736
164	-38.77273545	90.0	34.0	180.0	750.1661168
165	109.0983977	90.0	27.0	180.0	556.4521839
166	107.8265824	90.0	34.0	180.0	751.0052959
167	132.5664412	90.0	18.0	180.0	297.2277484
168	133.7954068	90.0	9.0	180.0	389.4844726
169	133.6890589	90.0	9.0	180.0	418.6002533

170	123.9291666	90.0	14.0	180.0	786.1407635
171	126.3629159	90.0	18.0	180.0	775.3124464
172	134.3923341	90.0	20.0	180.0	770.4324219
173	128.4342973	90.0	5.0	180.0	340.8997751
174	125.6662397	90.0	2.5	180.0	147.7212713
175	121.9282013	90.0	2.5	180.0	167.2703989
176	139.8740358	90.0	5.0	180.0	567.6202284
177	134.2110011	90.0	34.0	180.0	891.2256909
178	115.5150341	90.0	29.0	180.0	1278.981072
179	-9.650717124	50.0	0.6	-90.0	870.3468101
180	17.3334952	50.0	0.43	-90.0	332.1269999
181	71.01763089	90.0	7.0	0.0	1276.136888
182	161.8312481	20.0	1.25	90.0	416.0902731
183	-35	75	0.1	-150	4320
184	-25	90	4	180	1320
186	-45	90	8	180	3450
187	-47	90	4	180	3285
188	-35	90	10	180	1134
189	-67	90	4	180	1836

Entire box partial faults

Ratios of how much of fault is in the box in order of list below
[8/9,3/4,3/4,3/10,1/2]

26	-21.77760019	90.0	24.0	180.0	1497.568185
34	-13.31002153	60.0	1.0	-90.0	852.9483267
93	-34.82908488	82.0	20.0	180.0	674.6529593
99	-49.22951965	90.0	3.5	180.0	1322.89065
185	-45	90	4	180	3675

North box fault list

1	-13.90394173	90.0	5.0	180.0	352.2605374
2	-49.1812574	38.0	2.0	90.0	325.1186408
3	-26.30146625	90.0	4.0	180.0	274.9149512
4	156.6543651	90.0	6.0	180.0	587.701315
5	149.2044787	90.0	15.0	180.0	647.8842615
6	146.1013812	90.0	2.0	180.0	397.9174292
7	152.1869967	90.0	2.0	180.0	353.5976168
8	124.616856	45.0	0.4	90.0	223.2353262
9	150.1407721	90.0	1.0	180.0	771.4763872
11	-40.71480928	90.0	0.5	150.0	1168.202861
12	158.0271488	90.0	7.0	180.0	1315.361936
14	-49.89690553	90.0	2.5	180.0	631.7722196
23	-33.29049806	90.0	0.6	180.0	284.866272
24	-29.72039639	90.0	6.0	180.0	2610.370283
25	-29.55398905	90.0	9.0	180.0	748.3496166
27	-35.20740864	90.0	24.0	180.0	2082.92384
29	-23.69506075	90.0	3.0	180.0	795.1433645
33	2.639363974	60.0	1.0	-90.0	412.7778823
35	-39.09484109	90.0	0.3	180.0	703.7458117
36	-8.469508945	50.0	1.3	-90.0	1093.999405
37	166.6909233	60.0	1.5	-90.0	1071.51036
38	27.60097107	50.0	0.5	-90.0	283.0106569
39	-17.32529623	50.0	2.5	-90.0	436.119332

40	-16.40517436	50.0	0.5	-90.0	418.5515684
52	-52.95645863	50.0	0.3	90.0	557.1501174
53	-53.83569315	90.0	0.1	150.0	694.410828
54	-35.81342396	90.0	1.0	180.0	228.4533227
55	-19.36050843	90.0	15.0	180.0	212.6143623
56	-48.23350832	90.0	17.0	180.0	931.622146
57	137.0467275	90.0	34.0	180.0	1461.712439
63	-36.43547045	90.0	17.0	180.0	1098.740252
64	-33.78942937	90.0	9.0	180.0	417.7729511
65	-37.54659649	90.0	9.0	180.0	629.4265908
66	-21.46254698	90.0	1.0	180.0	295.6716887
67	-11.80178756	90.0	5.0	180.0	196.7419607
68	-26.42025354	90.0	6.0	180.0	715.7943749
69	75.2161373	75.0	0.5	-90.0	330.6193806
120	177.8707637	15.0	0.1	90.0	438.7774436
121	157.2347183	20.0	1.25	90.0	751.4722058
122	-177.4361483	15.0	0.1	90.0	219.814698
123	155.0240167	20.0	1.25	90.0	280.2728708
124	158.9503977	90.0	1.0	180.0	318.9877681
125	134.1495367	15.0	1.5	90.0	447.8304393
126	158.509447	15.0	1.5	90.0	409.7238976
127	152.044083	15.0	1.5	90.0	216.6055935
128	131.4158411	15.0	1.5	90.0	245.7755835
129	152.7743111	15.0	1.5	90.0	175.20183
136	-4.787476878	50.0	2.0	-90.0	902.3629356
137	-18.92809284	50.0	0.8	-90.0	697.5579714
138	-30.75838308	90.0	9.0	180.0	2650.92268
139	167.3110345	50.0	0.1	-90.0	742.9481705
140	147.1231386	15.0	1.5	90.0	391.534555
179	-9.650717124	50.0	0.6	-90.0	870.3468101
180	17.3334952	50.0	0.43	-90.0	332.1269999
182	161.8312481	20.0	1.25	90.0	416.0902731
183	-35	75	0.1	-150	4320
184	-25	90	4	180	1320
186	-45	90	8	180	3450

North box partial faults

Ratios of how much of fault is in the box in order of list below
[2/7,8/9,12/25,1/2,3/4,3/5,1/3,1/2]

10	143.3101458	90.0	1.0	180.0	1907.732537
26	-21.77760019	90.0	24.0	180.0	1497.568185
30	-31.45025707	80.0	2.5	180.0	1182.228217
32	-40.06046446	90.0	34.0	180.0	371.5908331
34	-13.31002153	60.0	1.0	-90.0	852.9483267
41	-28.26264248	50.0	2.5	-90.0	497.3720676
131	136.0738421	15.0	1.5	90.0	743.7333501
185	-45	90	4	180	3675

West half of North box fault list

1	-13.90394173	90.0	5.0	180.0	352.2605374
2	-49.1812574	38.0	2.0	90.0	325.1186408
3	-26.30146625	90.0	4.0	180.0	274.9149512
4	156.6543651	90.0	6.0	180.0	587.701315

5	149.2044787	90.0	15.0	180.0	647.8842615
6	146.1013812	90.0	2.0	180.0	397.9174292
7	152.1869967	90.0	2.0	180.0	353.5976168
8	124.616856	45.0	0.4	90.0	223.2353262
9	150.1407721	90.0	1.0	180.0	771.4763872
11	-40.71480928	90.0	0.5	150.0	1168.202861
12	158.0271488	90.0	7.0	180.0	1315.361936
23	-33.29049806	90.0	0.6	180.0	284.866272
24	-29.72039639	90.0	6.0	180.0	2610.370283
25	-29.55398905	90.0	9.0	180.0	748.3496166
27	-35.20740864	90.0	24.0	180.0	2082.92384
29	-23.69506075	90.0	3.0	180.0	795.1433645
52	-52.95645863	50.0	0.3	90.0	557.1501174
53	-53.83569315	90.0	0.1	150.0	694.410828
54	-35.81342396	90.0	1.0	180.0	228.4533227
55	-19.36050843	90.0	15.0	180.0	212.6143623
56	-48.23350832	90.0	17.0	180.0	931.622146
57	137.0467275	90.0	34.0	180.0	1461.712439
63	-36.43547045	90.0	17.0	180.0	1098.740252
64	-33.78942937	90.0	9.0	180.0	417.7729511
65	-37.54659649	90.0	9.0	180.0	629.4265908
66	-21.46254698	90.0	1.0	180.0	295.6716887
67	-11.80178756	90.0	5.0	180.0	196.7419607
68	-26.42025354	90.0	6.0	180.0	715.7943749
120	177.8707637	15.0	0.1	90.0	438.7774436
121	157.2347183	20.0	1.25	90.0	751.4722058
122	-177.4361483	15.0	0.1	90.0	219.814698
123	155.0240167	20.0	1.25	90.0	280.2728708
124	158.9503977	90.0	1.0	180.0	318.9877681
125	134.1495367	15.0	1.5	90.0	447.8304393
126	158.509447	15.0	1.5	90.0	409.7238976
127	152.044083	15.0	1.5	90.0	216.6055935
128	131.4158411	15.0	1.5	90.0	245.7755835
129	152.7743111	15.0	1.5	90.0	175.20183
138	-30.75838308	90.0	9.0	180.0	2650.92268
140	147.1231386	15.0	1.5	90.0	391.534555
182	161.8312481	20.0	1.25	90.0	416.0902731

West half of North box partial faults

Ratios of how much of fault is in the box in order of list below
[2/7,8/9,12/25,1/2,1/3]

10	143.3101458	90.0	1.0	180.0	1907.732537
26	-21.77760019	90.0	24.0	180.0	1497.568185
30	-31.45025707	80.0	2.5	180.0	1182.228217
32	-40.06046446	90.0	34.0	180.0	371.5908331
131	136.0738421	15.0	1.5	90.0	743.7333501

San Francisco box fault list

1	-13.90394173	90.0	5.0	180.0	352.2605374
3	-26.30146625	90.0	4.0	180.0	274.9149512
14	-49.89690553	90.0	2.5	180.0	631.7722196
64	-33.78942937	90.0	9.0	180.0	417.7729511
66	-21.46254698	90.0	1.0	180.0	295.6716887

67	-11.80178756	90.0	5.0	180.0	196.7419607
123	155.0240167	20.0	1.25	90.0	280.2728708
124	158.9503977	90.0	1.0	180.0	318.9877681
182	161.8312481	20.0	1.25	90.0	416.0902731

San Francisco box partial faults

Ratios of how much of fault is in the box in order of list below
[1/2,1/8,1/4,1/3,2/3,3/7,2/3,1/5,3/4,1/2,1/2,1/5,1/3]

2	-49.1812574	38.0	2.0	90.0	325.1186408
4	156.6543651	90.0	6.0	180.0	587.701315
6	146.1013812	90.0	2.0	180.0	397.9174292
12	158.0271488	90.0	7.0	180.0	1315.361936
25	-29.55398905	90.0	9.0	180.0	748.3496166
27	-35.20740864	90.0	24.0	180.0	2082.92384
52	-52.95645863	50.0	0.3	90.0	557.1501174
63	-36.43547045	90.0	17.0	180.0	1098.740252
65	-37.54659649	90.0	9.0	180.0	629.4265908
68	-26.42025354	90.0	6.0	180.0	715.7943749
121	157.2347183	20.0	1.25	90.0	751.4722058
183	-35	75	0.1	-150	4320
186	-45	90	8	180	3450

North of San Francisco box fault list

23	-33.29049806	90.0	0.6	180.0	284.866272
24	-29.72039639	90.0	6.0	180.0	2610.370283
33	2.639363974	60.0	1.0	-90.0	412.7778823
35	-39.09484109	90.0	0.3	180.0	703.7458117
36	-8.469508945	50.0	1.3	-90.0	1093.999405
37	166.6909233	60.0	1.5	-90.0	1071.51036
69	75.2161373	75.0	0.5	-90.0	330.6193806
120	177.8707637	15.0	0.1	90.0	438.7774436
122	-177.4361483	15.0	0.1	90.0	219.814698
138	-30.75838308	90.0	9.0	180.0	2650.92268
139	167.3110345	50.0	0.1	-90.0	742.9481705
184	-25	90	4	180	1320

North of San Francisco box partial faults

Ratios of how much of fault is in the box in order of list below
[1/3,8/9,4/7,3/4,1/2,1/2,1/2,1/3]

25	-29.55398905	90.0	9.0	180.0	748.3496166
26	-21.77760019	90.0	24.0	180.0	1497.568185
27	-35.20740864	90.0	24.0	180.0	2082.92384
34	-13.31002153	60.0	1.0	-90.0	852.9483267
68	-26.42025354	90.0	6.0	180.0	715.7943749
121	157.2347183	20.0	1.25	90.0	751.4722058
185	-45	90	4	180	3675
186	-45	90	8	180	3450

West half of North of San Francisco box fault list

23	-33.29049806	90.0	0.6	180.0	284.866272
24	-29.72039639	90.0	6.0	180.0	2610.370283
120	177.8707637	15.0	0.1	90.0	438.7774436
122	-177.4361483	15.0	0.1	90.0	219.814698
138	-30.75838308	90.0	9.0	180.0	2650.92268

West half of North of San Francisco box partial faults

Ratios of how much of fault is in the box in order of list below
[1/2,8/9,4/7,1/2,1/2]

25	-29.55398905	90.0	9.0	180.0	748.3496166
26	-21.77760019	90.0	24.0	180.0	1497.568185
27	-35.20740864	90.0	24.0	180.0	2082.92384
68	-26.42025354	90.0	6.0	180.0	715.7943749
121	157.2347183	20.0	1.25	90.0	751.4722058

South box fault list

28	119.5330218	90.0	5.0	180.0	325.8234224
31	152.7601348	90.0	1.0	180.0	880.2721048
42	-19.63609881	50.0	1.0	-90.0	734.7058252
43	-0.763531401	50.0	0.2	-90.0	440.6973324
44	-8.155249112	90.0	1.0	180.0	1438.322766
45	-38.13955154	90.0	5.0	-150.0	998.3320045
46	-39.47764013	90.0	5.0	180.0	1384.998125
47	57.5799599	90.0	2.0	0.0	302.3648728
48	90.97338746	90.0	3.0	0.0	519.2524931
49	58.68246799	90.0	6.0	0.0	1434.369921
50	-42.70915639	90.0	2.5	-150.0	897.186127
51	-155.4450827	50.0	0.8	-90.0	429.8624005
58	90.96516861	46.0	2.0	90.0	823.8165132
59	1.648681567	50.0	0.1	-90.0	1996.236994
60	-18.63193849	90.0	1.5	180.0	1156.944725
61	-29.13491508	50.0	0.2	-90.0	1028.809314
62	-23.72819163	50.0	0.7	-90.0	262.7874641
70	118.1932757	45.0	0.5	90.0	627.9021117
71	-53.45414684	45.0	0.2	90.0	901.6030524
72	-60.94741837	75.0	0.02	90.0	428.2089517
73	91.53917223	70.0	2.0	0.0	660.4970173
74	85.97858425	70.0	0.4	90.0	556.7324572
75	81.79635089	70.0	2.0	0.0	967.4692671
76	-87.46279808	42.0	6.0	90.0	1005.025735
77	97.42274035	90.0	3.0	0.0	391.8568763
78	81.0430746	49.0	1.0	90.0	1043.012394
79	96.56236988	41.0	0.5	90.0	677.9678743
80	-39.12921405	90.0	0.6	180.0	1459.194151
81	-46.7459093	90.0	0.9	180.0	1915.824787
82	-48.64022845	90.0	0.7	180.0	741.9517328
83	-35.10899493	90.0	0.5	180.0	719.9929387
84	-37.5802822	90.0	1.8	180.0	1624.325036
85	-30.08623793	90.0	0.8	180.0	1158.807383
86	-38.60003052	90.0	0.6	180.0	761.8356905
87	-39.10629038	90.0	0.6	180.0	559.7724348

88	-30.01951978	90.0	0.6	180.0	1427.15399
89	85.22576491	90.0	2.5	0.0	1147.810881
90	174.5662819	67.0	0.6	180.0	364.698984
91	-15.03776157	90.0	0.6	180.0	282.7409352
92	-140.3402293	90.0	1.0	0.0	330.5337807
94	130.0261945	90.0	4.0	180.0	455.8638615
95	133.0591279	90.0	4.0	180.0	448.4687641
96	132.7847548	90.0	4.0	180.0	681.5267123
97	-54.21481916	84.0	5.0	180.0	1426.064922
98	-54.72870569	82.0	4.0	180.0	517.2782765
100	-115.5014465	74.0	0.5	30.0	322.7750225
101	-103.5286384	70.0	1.0	30.0	309.8676158
102	-37.487553	90.0	3.0	180.0	1347.941142
103	-88.83687151	90.0	1.0	30.0	500.518891
104	98.20113999	90.0	1.0	30.0	919.0425243
105	-59.4703495	55.0	0.5	90.0	513.4860698
106	-80.72085333	45.0	2.0	90.0	332.5567324
107	-71.36903256	53.0	2.0	90.0	1011.960387
108	-104.490274	60.0	1.0	30.0	501.7696116
109	69.26845481	65.0	4.0	90.0	1001.423579
110	-96.91243096	64.0	1.0	60.0	681.8182794
111	-88.49559245	56.0	2.0	90.0	1709.590867
112	135.4487212	90.0	6.0	180.0	725.7316865
113	146.5658988	90.0	3.0	180.0	1602.234945
114	136.892991	90.0	1.5	180.0	677.5214596
115	-22.34428898	90.0	1.5	180.0	538.0570886
116	-116.2164686	50.0	0.5	90.0	293.2582356
117	-102.9544062	45.0	5.0	90.0	308.8457378
118	-95.53554943	20.0	1.5	90.0	1263.025782
119	111.2067365	35.0	1.5	90.0	546.4077678
130	125.243537	22.0	1.5	90.0	922.2551011
132	114.3710172	23.0	0.5	90.0	730.0961398
133	-32.32791145	90.0	0.7	180.0	516.1473104
134	-179.1153138	50.0	1.0	-90.0	173.0268
135	-74.77190832	50.0	1.3	90.0	315.7264484
141	-102.0156306	79.0	1.5	60.0	357.2379105
142	115.9631537	75.0	0.25	90.0	300.7047166
143	121.3539072	30.0	0.7	90.0	555.4398079
144	-86.88273588	13.0	2.5	90.0	1127.167395
145	-90.68338948	16.0	2.5	90.0	1349.133993
146	-95.58631598	45.0	3.0	60.0	1115.785685
147	-86.88902897	75.0	0.3	30.0	305.0807665
148	-107.1865129	75.0	1.0	30.0	267.3928918
149	-81.00101994	55.0	5.0	90.0	540.6694611
150	97.14864255	58.0	0.4	90.0	430.0512147
151	-41.18499123	88.0	1.0	180.0	980.5495407
152	-66.26707221	75.0	2.5	150.0	674.8205057
153	145.5857064	50.0	1.0	150.0	285.8834667
154	-69.61224038	25.0	0.7	90.0	835.6808537
155	-26.20413101	90.0	2.5	-150.0	1424.455959
156	166.169094	60.0	4.0	-150.0	1141.450665
157	-39.08392655	90.0	4.0	180.0	544.5739578
158	-50.88756761	61.0	1.0	180.0	1198.650564
159	126.7503977	90.0	2.0	180.0	382.7808363
160	50.72426682	75.0	2.0	60.0	957.6234018
161	121.5025573	90.0	22.0	180.0	451.939471

162	119.6950615	90.0	16.0	180.0	555.4873932
163	-70.15887366	58.0	10.0	180.0	842.9906736
164	-38.77273545	90.0	34.0	180.0	750.1661168
165	109.0983977	90.0	27.0	180.0	556.4521839
166	107.8265824	90.0	34.0	180.0	751.0052959
167	132.5664412	90.0	18.0	180.0	297.2277484
168	133.7954068	90.0	9.0	180.0	389.4844726
169	133.6890589	90.0	9.0	180.0	418.6002533
170	123.9291666	90.0	14.0	180.0	786.1407635
171	126.3629159	90.0	18.0	180.0	775.3124464
172	134.3923341	90.0	20.0	180.0	770.4324219
173	128.4342973	90.0	5.0	180.0	340.8997751
174	125.6662397	90.0	2.5	180.0	147.7212713
175	121.9282013	90.0	2.5	180.0	167.2703989
176	139.8740358	90.0	5.0	180.0	567.6202284
177	134.2110011	90.0	34.0	180.0	891.2256909
178	115.5150341	90.0	29.0	180.0	1278.981072
181	71.01763089	90.0	7.0	0.0	1276.136888
187	-47	90	4	180	3285
188	-35	90	10	180	1134
189	-67	90	4	180	1836

South box partial faults

Ratios of how much of fault is in the box in order of list below
[5/7,13/25,1/2,2/5,3/4,3/10,2/3]

10	143.3101458	90.0	1.0	180.0	1907.732537
30	-31.45025707	80.0	2.5	180.0	1182.228217
32	-40.06046446	90.0	34.0	180.0	371.5908331
41	-28.26264248	50.0	2.5	-90.0	497.3720676
93	-34.82908488	82.0	20.0	180.0	674.6529593
99	-49.22951965	90.0	3.5	180.0	1322.89065
131	136.0738421	15.0	1.5	90.0	743.7333501

Los Angeles box fault list

47	57.5799599	90.0	2.0	0.0	302.3648728
48	90.97338746	90.0	3.0	0.0	519.2524931
82	-48.64022845	90.0	0.7	180.0	741.9517328
83	-35.10899493	90.0	0.5	180.0	719.9929387
100	-115.5014465	74.0	0.5	30.0	322.7750225
101	-103.5286384	70.0	1.0	30.0	309.8676158
105	-59.4703495	55.0	0.5	90.0	513.4860698
106	-80.72085333	45.0	2.0	90.0	332.5567324
107	-71.36903256	53.0	2.0	90.0	1011.960387
116	-116.2164686	50.0	0.5	90.0	293.2582356
117	-102.9544062	45.0	5.0	90.0	308.8457378
135	-74.77190832	50.0	1.3	90.0	315.7264484
141	-102.0156306	79.0	1.5	60.0	357.2379105
147	-86.88902897	75.0	0.3	30.0	305.0807665
148	-107.1865129	75.0	1.0	30.0	267.3928918
154	-69.61224038	25.0	0.7	90.0	835.6808537
157	-39.08392655	90.0	4.0	180.0	544.5739578
189	-67	90	4	180	1836

Los Angeles box partial faults

Ratios of how much of fault is in the box in order of list below
[2/3,8/13,2/3,4/9,4/13,1/4,9/14,1/4,1/2,6/7,1/4,1/2,5/7,3/4,1/5,18/19,4/7,1/2,3/5,2/5,1/2,3/5,3/4,1/2,1/4]

77	97.42274035	90.0	3.0	0.0	391.8568763
78	81.0430746	49.0	1.0	90.0	1043.012394
80	-39.12921405	90.0	0.6	180.0	1459.194151
81	-46.7459093	90.0	0.9	180.0	1915.824787
84	-37.5802822	90.0	1.8	180.0	1624.325036
88	-30.01951978	90.0	0.6	180.0	1427.15399
102	-37.487553	90.0	3.0	180.0	1347.941142
108	-104.490274	60.0	1.0	30.0	501.7696116
112	135.4487212	90.0	6.0	180.0	725.7316865
119	111.2067365	35.0	1.5	90.0	546.4077678
132	114.3710172	23.0	0.5	90.0	730.0961398
134	-179.1153138	50.0	1.0	-90.0	173.0268
146	-95.58631598	45.0	3.0	60.0	1115.785685
149	-81.00101994	55.0	5.0	90.0	540.6694611
150	97.14864255	58.0	0.4	90.0	430.0512147
151	-41.18499123	88.0	1.0	180.0	980.5495407
152	-66.26707221	75.0	2.5	150.0	674.8205057
153	145.5857064	50.0	1.0	150.0	285.8834667
155	-26.20413101	90.0	2.5	-150.0	1424.455959
156	166.169094	60.0	4.0	-150.0	1141.450665
158	-50.88756761	61.0	1.0	180.0	1198.650564
161	121.5025573	90.0	22.0	180.0	451.939471
178	115.5150341	90.0	29.0	180.0	1278.981072
181	71.01763089	90.0	7.0	0.0	1276.136888
187	-47	90	4	180	3285

South of Los Angeles box fault list

28	119.5330218	90.0	5.0	180.0	325.8234224
79	96.56236988	41.0	0.5	90.0	677.9678743
85	-30.08623793	90.0	0.8	180.0	1158.807383
86	-38.60003052	90.0	0.6	180.0	761.8356905
87	-39.10629038	90.0	0.6	180.0	559.7724348
89	85.22576491	90.0	2.5	0.0	1147.810881
90	174.5662819	67.0	0.6	180.0	364.698984
91	-15.03776157	90.0	0.6	180.0	282.7409352
92	-140.3402293	90.0	1.0	0.0	330.5337807
94	130.0261945	90.0	4.0	180.0	455.8638615
95	133.0591279	90.0	4.0	180.0	448.4687641
96	132.7847548	90.0	4.0	180.0	681.5267123
97	-54.21481916	84.0	5.0	180.0	1426.064922
98	-54.72870569	82.0	4.0	180.0	517.2782765
113	146.5658988	90.0	3.0	180.0	1602.234945
114	136.892991	90.0	1.5	180.0	677.5214596
115	-22.34428898	90.0	1.5	180.0	538.0570886
159	126.7503977	90.0	2.0	180.0	382.7808363
162	119.6950615	90.0	16.0	180.0	555.4873932
163	-70.15887366	58.0	10.0	180.0	842.9906736
167	132.5664412	90.0	18.0	180.0	297.2277484
168	133.7954068	90.0	9.0	180.0	389.4844726
169	133.6890589	90.0	9.0	180.0	418.6002533

170	123.9291666	90.0	14.0	180.0	786.1407635
171	126.3629159	90.0	18.0	180.0	775.3124464
172	134.3923341	90.0	20.0	180.0	770.4324219
173	128.4342973	90.0	5.0	180.0	340.8997751
174	125.6662397	90.0	2.5	180.0	147.7212713
175	121.9282013	90.0	2.5	180.0	167.2703989
176	139.8740358	90.0	5.0	180.0	567.6202284
188	-35	90	10	180	1134

South of Los Angeles box partial faults

Ratios of how much of fault is in the box in order of list below
[1/3,5/13,1/3,4/9,9/13,3/4,3/4,1/5,5/14,1/2,3/4,1/19,3/7,1/2,2/5,1/5]

77	97.42274035	90.0	3.0	0.0	391.8568763
78	81.0430746	49.0	1.0	90.0	1043.012394
80	-39.12921405	90.0	0.6	180.0	1459.194151
81	-46.7459093	90.0	0.9	180.0	1915.824787
84	-37.5802822	90.0	1.8	180.0	1624.325036
88	-30.01951978	90.0	0.6	180.0	1427.15399
93	-34.82908488	82.0	20.0	180.0	674.6529593
99	-49.22951965	90.0	3.5	180.0	1322.89065
102	-37.487553	90.0	3.0	180.0	1347.941142
112	135.4487212	90.0	6.0	180.0	725.7316865
132	114.3710172	23.0	0.5	90.0	730.0961398
151	-41.18499123	88.0	1.0	180.0	980.5495407
152	-66.26707221	75.0	2.5	150.0	674.8205057
153	145.5857064	50.0	1.0	150.0	285.8834667
161	121.5025573	90.0	22.0	180.0	451.939471
187	-47	90	4	180	3285

REFERENCES CITED

CHAPTER II

Amelung, F., D.L. Galloway, J. Bell, H. Zebker, and R. Laczinak (1999), Sensing the ups and downs of Las Vegas: InSAR reveals structural control of land-subsidence and aquifer-system deformation, *Geology*, *27*, 483-486.

Anderson, M., J. Matti, and R. Jachens (2004), Structural model of the San Bernardino basin, California, from analysis of gravity, aeromagnetic, and seismicity data, *J. Geophys. Res.*, *109*, B04404, doi:10.1029/2003JB002544.

Bawden, G.W., W. Thatcher, R.S. Stein, K.W. Hudnut, G. Peltzer (2001), Tectonic contractions across Los Angeles after removal of groundwater pumping effects, *Nature*, *412*, 812-815.

Bell, J.W., F. Amelung, A. Ferretti, M. Bianchi, F. Novali (2008), Permanent scatterer InSAR reveals seasonal and long-term aquifer-system response to groundwater pumping and artificial recharge, *Water Resources Res., vol. 44*, W02407, doi:10.1029/2007WR006152.

Bennett, R.A., W. Rodi, R.E. Reilinger (1996), Global Positioning System constraints on fault slip rates in southern California and northern Baja, Mexico, *J. Geophys. Res.*, *101*(B10), doi:10.1029/1996JB02488.

Bennett, R.A., A.M. Friedrich, K.P. Furlong (2004), Codependent histories of the San Andreas and San Jacinto fault zones from inversion of fault displacement rates, *Geology*, *32*, 961-964.

Bilham, R., and G. King (1989), The morphology of strike-slip faults: examples from the San Andreas fault, California, *J. Geophys. Res.*, *94*(B8), doi:10.1029/198900545.

Blythe, A.E., M.A. House, J.A. Spotila (2002), Low-temperature thermochronology of the San Gabriel and San Bernardino Mountains, southern California: constraining structural evolution, *GSA Special Paper 365*, 231-250.

Bürgmann, R., P.A. Rosen, E.J. Fielding (2000), Synthetic aperture radar interferometry to measure Earth's surface topography and its deformation, *Annu. Rev. Earth Planet. Sci., vol. 28*, 169-209.

California Department of Water Resources (2004), Hydrologic region south coast: Upper Santa Ana Valley groundwater basin, Yucaipa subbasin, *California's Groundwater Bulletin 118*.

Carver, R.E. (1971), Model studies of differential compaction, in: *International Association of Scientific Hydrology – Union of Geodesy and Geophysics Publication*, *vol. 2*, *Is. 89*, 450-458.

Crowell, J.C. (1974), Origin of late Cenozoic basins in southern California, In*: Special Publication – Society of Economic Paleontologists and Mineralogists*, *vol. 22*, 190-204.

Dair, L., M.L. Cooke (2009), San Andreas fault geometry through the San Gorgonio Pass, California, *Geology*, *vol. 37*, 119-122, doi:10.1130/G25101A.1.

Danskin, W.R., and J.R. Freckleton (1992), Ground-water-flow modeling and optimization techniques applied to high ground-water problems in San Bernardino, California, *in* Selected Papers in the Hydrologic Sciences, 1988-92: *U.S. Geol. Surv. Water Suppl. Pap. 2340*, edited by Seymour Subitzky, 165-177.

Danskin, W.R., K.R. McPherson, and L.R. Woolfenden (2006), Hydrology, Description of Computer Models, and Evaluation of Selected Water-Management Alternatives in the San Bernardino Area, California, *U.S. Geol. Surv. Open File Rep. 05-1278*, 194 pp.

Dutcher, L.C., and A.A. Garrett (1963), Geologic and hydrologic features of the San Bernardino area, California-with special reference to underflow across the San Jacinto Fault, *U.S. Geol. Surv. Water Suppl. Pap. 1419*, 114 pp.

Feigl, K.L., D.C. Agnew, Y. Bock, D. Dong, A. Donnellan, B.H. Hager, T.A. Herring, D.D. Jackson, T.H. Jordan, R.W. King, S. Larsen, K.M. Larson, M.H. Murray, Z. Shen, F.H. Webb (1993), Space geodetic measurement of crustal deformation in central and southern California, 1984-1992, *J. Geophys. Res.*, *98*(B12), 21677-21712, 93JB02405.

Galloway, D.L., K.W Hudnut, S.E. Ingebritsen, S.P. Phillips, G. Peltzer, F. Rogez, and P.A. Rosen (1998), Detection of aquifer system compaction and land subsidence using interferometric synthetic aperture radar, Antelope Valle, Mojave Desert, California, *Water Resources Research*, *vol. 34*, 2573-2585.

Galloway, D.L., D.R. Jones, and S.E. Ingebritsen (1999), Land Subsidence in the United States, *U.S. Geol. Surv. Cir. 1182*, 177 pp.

Galloway, D.L., D.R. Jones, and S.E. Ingebritsen (2000), Measuring land subsidence from space: *U.S. Geol. Surv. Fact Sheet 051-00*, 4 pp.

Hall, W.H. (1888), Irrigation in (southern) California-the field, water supply, and works-organization and operation in San Diego, San Bernardino, and Los Angeles counties: Second part of the report of the State engineer of California on irrigation and the irrigation questions, Sacramento, California, State Printing Office, 672 pp.

Hamlin, S.N., K. Belitz, S. Kraja, and B. Dawson (2002), Ground-water quality in the Santa Ana Watershed, California: overview and data summary, *U.S. Geol. Surv. Water Res. Invest. Rep. 02-4243*, 137 pp.

Helm, D. C. (1978), Compaction and expansion of a confined aquifer system, in: *Proceedings - Hydraulics Division Specialty Conference*, *no. 26*: 189-196.

Hoffmann, J., and H.A. Zebker (2003), Prospecting for horizontal surface displacements in Antelope Valley, California, using satellite radar interferometry, *J. Geophys. Res.*, *108*(F1), 6011, doi:10.1029/2003JF000055.

Ireland, R.L. (1986), Land subsidence in the San Joaquin valley, California, as of 1983, *U.S. Geol. Surv. Water Res. Invest. Rep. 85-4196*, 55 pp.

Izbicki, J.A., W.R. Danskin, and G.O. Mendez (1998), Chemistry and isotopic composition of ground water along a section near the Newmark area, San Bernardino County, California, *U.S. Geol. Surv. Water Res. Invest. Rep. 97-4179*, 27 pp.

Kendrick, K.J., D.M. Morton, S.G. Wells, and R.W. Simpson (2002), Spatial and Temporal deformation along the northern San Jacinto fault, southern California: Implications for slip rates, *BSSA*, *vol. 92*, *no. 7*, 2782-2802.

Kümpel, H.J. (1991), Poroelasticity: parameters reviewed, *Geophys. J. Int.*, *105*, 783-799.

Langenheim, V.E., R.C. Jachens, J.C. Matti, E. Hauksson, D.M. Morton, and A. Christensen (2005), Geophysical evidence for wedging in the San Gorgonio Pass structural knot, southern San Andreas fault zone, southern California, *GSA Bull.*, *vol. 117*, *no. 11/12*, 1554-1572, doi:10.1130/B25760.1.

Lin, J., and R.S. Stein (2004), Stress triggering in thrust and subduction earthquakes, and stress interaction between the southern San Andreas and nearby thrust and strike-slip faults, *J. Geophys. Res.*, *109*, *B02303*, doi:10.1029/2003JB002607.

Lofgren, B. (1968), Analysis of stresses causing land subsidence, *U.S. Geol. Surv. Prof. Paper 600-B*, B219-B225.

Lu, Z., and W.R. Danskin (2001), InSAR analysis of natural recharge to define structure of a ground-water basin, San Bernardino, California, *Geophys. Res. Lett.*, *28*, 2661-2664.

Maupin, M.A., and Barber, N.L. (2005), Estimated withdrawals from principal aquifers in the United States, 2000, *U.S. Geol. Surv. Circular 1279*, 46pp.

McClay, K., and M. Bonora (2001), Analog models of restraining stopovers in strike-slip fault systems, *AAPG Bull.*, *vol. 85*, *no. 2*, 233-260

Meade, B.J., B.H. Hager (2005), Block models of crustal motion in southern California constrained by GPS measurements, *J. Geophys. Res.*, *110*(B03403), doi:10.1029/2004JB003209.

Mendez, G.O. W.R. Danskin, C.A. Burton (2001), Surface-water and round-water quality in the Yucaipa area, San Bernardino and Riverside counties, California, 1996-98, *U.S. Geol. Surv. Water Res. Invest. Rep. 00-4269*, 42 pp.

Miller, R.E. and J.A. Singer (1971), Subsidence in the Bunker Hill-San Timoteo area, southern California, *U.S. Geol. Surv. Open File Rep.*, 28 pp.

Moreland, J.A. (1972), Artificial recharge in the upper Santa Ana Valley, southern California, *U.S. Geol. Surv. Open File Rep.*, 51 pp.

Morton D.M., and F.K. Miller (2003), Preliminary geologic map and digital database of the San Bernardino 30' x 60' quadrangle, California, *U.S. Geol. Surv. Open File Rep. 03-293*, 190pp.

Planert, M., and Williams, J.S. (1995), Ground-water atlas of the United States – Segment 1, California, Nevada, *U.S. Geol. Surv. Hydro. Invest. Atlas, 730-B*, 28pp.

Poland, J.F. (1984), Mechanics of land subsidence due to fluid withdrawal, *Studies and reports in hydrogeology*, *vol. 40*, 37-54.

Poland, J.F. (1981), Subsidence in the United States groundwater withdrawal, *J. Irrigation and Drainage Div.*, *vol. 107*, *is. IR2,* 115-135.

Riley, F.S. (1969), Analysis of borehole extensometer data from central California, *Land Subsidence, v. 2: Internat. Assoc. Sci. Hydrology Pub. 89*, edited by Tison, L.J., 423-431.

Rosen, P.A, S. Hensley, G. Peltzer, M. Simons (2004), Updated repeat orbit interferometry package released, *EOS Trans. AGU*, 85, 35.

Schaefer, D.H., J.W. Warner (1975), Artificial recharge in the Santa Ana river area, *U.S. Geol. Surv. Water Res. Invest. Rep. 15-75*, 27 pp.

Schmidt, D.A., R. Bürgmann (2003), Time dependent land uplift and subsidence in the Santa Clara valley, California, from a large interferometric synthetic aperture radar data set, *J. Geophys. Res.*, *108*(B9), 2416, doi:10.1029/2002JB002267.

Sneed, M. (2001), Hydraulic and mechanical properties affecting ground-water flow and aquifer system compaction, San Joaquin Valley, California, *USGS Open File Rep. 01-35*, 32 pp.

Stephenson, W.J., J.K. Odum, R.A. Williams, and M.L. Anderson (2002), Delineation of faulting and basin geometry along a seismic reflection transect in urbanized San Bernardino valley, California, *BSSA*, *vol. 92*, *no. 6*, 2504-2520.

Teatini, P., L. Tosi, T. Strozzi, L. Carbognin, U. Wegmüller, F. Rizzetto (2005) Mapping regional land displacements in the Venice coastland by an integrated monitoring system, *Remote Sensing of Environment 98*, 403-413, doi:10.1016/j.rse.2005.08.002.

Teatini, P., M. Ferronato, G. Gambolati, M. Gonella (2006) Groundwater pumping and land subsidence in the Emilia-Romagna coastland, Italy: modeling the past occurrence and the future trend, *Water Resources Research*, *vol. 42*, W01406, doi:10.1029/2005WR004242.

Terzaghi, K. (1925), Principles of soil mechanics, IV – Settlement and consolidation of clay, *Engineering News - Record, 95(3)*, 874-878.

Toda, S., R.S. Stein, K. Richards-Dinger, and S. Bozkurt (2005), Forecasting the evolution of seismicity in southern California: Animations built on earthquake stress transfer, *J. Geophys. Res.*, *B05S16*, doi:10.1029/2004JB003415.

Uniform California Earthquake Rupture Forecast, Version 2 (UCERF2) (2008), 2007 Working Group on California Earthquake Probabilities (WGCEP) and the USGS National Seismic Hazard Mapping Program (NSHMP), *CGS Special Report 203*, *USGS Open File Rep. 2007-1437*, *SCEC Contribution 1138*, 96 pp. and Apps. A-P.

Van der Woerd, J., Y. Klinger, K. Sieh, P. Tapponnier, F.J. Ryerson, A. Mériaux (2006), Long-term slip rate of the southern San Andreas fault from ^{10}Be – ^{26}Al surface exposure dating of an offset alluvial fan, *J. Geophys. Res. 111*(B04407), doi:10/1029/2004JB003559.

Weldon, R.J., and K.E. Sieh (1985), Holocene rate of slip and tentative recurrence interval for large earthquakes on the San Andreas fault in Cajon Pass, southern California, *Geol. Soc. Am. Bull.*, *96*, 793-812.

Woolfenden, L.R. and, D. Kadhim (1997), Geohydrology and water chemistry in the Rialto-Colton basin, San Bernardino County, California, *U.S. Geol. Surv. Water Res. Invest. Rep. 97-4012*, 101 pp.

Zebker, H.A, P.A. Rosen, S. Hensley (1997), Atmospheric effects in interferometric synthetic aperture radar surface deformation and topographic maps, *J. Geophys. Res. 102*(B4), 7547-7563.

CHAPTER III

Anderson, M., J. Matti, and R. Jachens, 2004, Structural model of the San Bernardino basin, California, from analysis of gravity, aeromagnetic, and seismicity data, *J. Geophys. Res.*, *109*, B04404, doi:10.1029/2003JB002544.

Anderson, M.P., 1989, Hydrogeologic facies models to delineate large-scale spatial trends in glacial and glaciofluvial sediments, *GSA Bull*, Vol. 101, pp 501-511.

Appana, R., and M.O. Saar (2007), Determination of aquifer and fault permeabilities by studying the poroelastic response of rocks using InSAR in the Upper Coachella Valley area, CA, USA, *Eos Trans. AGU, 88*(52), Fall Meet. Suppl., Abstract H42B-08.

Artimo, A., J Mäkinen, R.C. Berg, C.C. Abert, V. Salonen, 2003, Three-dimensional geologic modeling and visualization of the Virttaankangas aquifer, southwestern Finland, *Hydrogeology J.* vol 11, pp 378-386, doi: 10.1007/s10040-003-0256-6.

Aydin A., and A. Nur, 1982, Evolution of pull-apart basins and their scale independence, *Tectonics*, Vol. 1, No. 1, pp 91-105.

Bawden, G.W., W. Thatcher, R.S. Stein, K.W. Hudnut, G. Peltzer (2001), Tectonic contractions across Los Angeles after removal of groundwater pumping effects, *Nature*, *412*, 812-815.

Bell, J.W., F. Amelung, A. Ferretti, M. Bianchi, F. Novali, 2008, Permanent scatterer InSAR reveals seasonal and long-term aquifer-system response to groundwater pumping and artificial recharge, *Water Resources Res.*, *vol. 44*, W02407, doi:10.1029/2007WR006152.

Bertran, P., and J. Texier, 1998, Facies and microfacies of slope deposits, *Catena*, vol 35, pp 99-121.

Bennett, R.A., A.M. Friedrich, K.P. Furlong, 2004, Codependent histories of the San Andreas and San Jacinto fault zones from inversion of fault displacement rates, *Geology*, *32*, 961-964.

Biehler, S., R.L. Kovach, and C.R. Allen, 1964, Geophysical framework of the northern end of Gulf of California structural province, *AAPG Memoir*, Vol. 3, pp 126-143.

Biehler, S., V.E. Langenheim, R.F. Sikora, R.H. Chapman, and L.A. Beyer, 1992, Complete Bouguer gravity anomaly map of the Santa Ana 1° by 2° Quadrangle, California, U.S. Geological Survey open-file report 92-279.

Blair, T.C. and W.L. Bilodeau, 1988, Development of tectonic cyclothems in rift, pull-apart, and foreland basins: Sedimentary response to episodic tectonism, *Geology*, v. 16, p. 517-520.

Blair, T.C. and J.G. McPherson, 1994, Alluvial fans and their natural distinction from rivers based on morphology, hydraulic processes, sedimentary processes, and facies assemblages, *Journal of Sedimentary Research*, v. 64, no. 3, p. 450-489.

Boggs, S., 1987, Principles of sedimentology and stratigraphy, 4th Edition, University of Oregon.

Bürgmann, R., P.A. Rosen, E.J. Fielding, 2000, Synthetic aperture radar interferometry to measure Earth's surface topography and its deformation, *Annu. Rev. Earth Planet. Sci., vol. 28*, 169-209.

Caine, J.S., S.A. Minor, 2011, Structural and geochemical characteristics of faulted sediments and inferences on the role of water in deformation, Rio Grande Rift, New Mexico, *GSA Bull.*, v. 121, no. 9/10, p. 1325-1340.

Carle, S.E., E.M. LaBolle, G.S. Weissmann, D. Van Brocklin, 1998, Conditional simulation of hydrofacies architecture: a transition probability/Markov approach. In: Fraser, G.S., Davis, J.M. (Eds.). Hydrogeologic Models of Sedimentary Aquifers, Concepts in Hydrogeology and Environmental Geology No. 1SEPM (Society for Sedimentary Geology) Special Publication, pp. 147 – 170.

Carr, D.D., A. Horowitz, S.V. Hrabar, K.F. Ridge, R. Rooney, W.T. Straw, W. Webb, P.E. Potter, 1966, Stratigraphic sections, bedding sequences, and random processes, *Science*, New Series, vol 154, no 3753, pp 1162-1164.

Carver, R.E., 1971, Model studies of differential compaction, in: *International Association of Scientific Hydrology – Union of Geodesy and Geophysics Publication, vol. 2, Is. 89*, 450-458.

Coachella Valley Water District, 2005, Engineer's report on water supply and replenishment assessment Upper Whitewater River subbasin area of benefit 2005-2006, 38 p.

Crowell, J.C., and A.G. Sylvester, 1980, Introduction to the San Andreas-Salton Trough juncture, in *Tectonics of the Juncture between the San Andreas Fault System and the Salton Trough, Southern California – A Guidebook*, edited by J.C. Crowell and A.G. Sylvester, Publ 1-13, University of California, Dept. of Geological Sciences, Santa Barbara.

Dibblee, T.W., edited by John A. Minch, 2008, Geologic map of the Palm Desert & Coachella 15 minute quadrangles, Riverside County, California, *Dibblee Geology Center Map #DF-373*, Santa Barbara Museum of Natural History.

Erskine, B.G., H.R. Wenk, 1985, Evidence for Late Cretaceous crustal thinning in the Santa Rosa mylonite zone, southern California, *Geology*, v.13, p274-277.

Fuis, G.S. and W.D. Mooney, 1990, Lithospheric structure and tectonics from seismic-refraction and other data, in *The San Andreas Fault System, California*, edited by Robert E. Wallace, U.S. Geological Survey Professional Paper 1515, pp 207-236.

Gonzalez, P.J., & J. Fernandez, 2011, Drought-driven fast transient aquifer compaction imaged using multi-temporal satellite radar interferometry, *Geology*, Vol. 39, No. 6, pp. 551-554, doi: 10.1130/G31900.1

Gourmelen, N., F. Amelung, F. Casu, M. Manzo, R. Lanari, 2007, Mining-related ground deformation in Crescent Valley, Nevada: Implications for sparse GPS networks, *Geophys. Res. Lett.*, vol. 34, L09309, doi:10.1029/2007GL029427.

Helm, D. C. (1978), Compaction and expansion of a confined aquifer system, in: *Proceedings - Hydraulics Division Specialty Conference*, *no. 26*: 189-196.

Hoffmann, J., and H.A. Zebker (2003), Prospecting for horizontal surface displacements in Antelope Valley, California, using satellite radar interferometry, *J. Geophys. Res.*, *108*(F1), 6011, doi:10.1029/2003JF000055.

Ikehara, M.E., S.K. Predmore, and D.J. Swope, 1997, Geodetic network to evaluate historical elevation changes and to monitor land subsidence in Lower Coachella Valley, California, 1996: U.S. Geological Survey Water-Resources Investigations Report 97-4237, scale 1:63,000, 1 sheet [folded in envelope].

Keller, E.A., M.S. Bonkowski, R.J. Korsch; R.J. Schlemon, 1982, Tectonic geomorphlogy of the San Andres fault zone in the southern Indio Hills, Coachella Valley, California, *GSA Bull.*, v. 93, p.46-56.

Langenheim, V.E., R.C. Jachens, J.C. Matti, E. Hauksson, D.M. Morton, and A. Christensen (2005), Geophysical evidence for wedging in the San Gorgonio Pass structural knot, southern San Andreas fault zone, southern California, *GSA Bull.*, *vol. 117*, *no. 11/12*, 1554-1572, doi:10.1130/B25760.1.

Langsholt, E., N. Kitterød, and L. Gottschalk, 1998, Development of three-dimensional hydrostratigraphic architecture of the unsaturated zone based on soft and hard data, *Ground Water*, vol. 36, no. 1, pp. 104-111.

Lu, Z., and W.R. Danskin, 2001, InSAR analysis of natural recharge to define structure of a ground-water basin, San Bernardino, California, *Geophys. Res. Lett.*, *28*, 2661-2664.

Matti, J.C., D.M. Morton, and B.F. Cox, 1992, The San Andreas fault system in the vicinity of the central Transverse Ranges province, southern California: U.S. Geological Survey Open-File Report 92-354, 40 p., scale 1:250,000.

Matti, J.C., and Morton, D.M., 1993, Paleogeographic evolution of the San Andreas fault in southern California: a reconstruction based on a new cross-fault correlation, in Powell, R.E., Weldon, R.J., and Matti, J.C., eds., The San Andreas fault system: displacement, palinspastic reconstruction, and geologic evolution: Geological Society of America Memoir 178, p. 107-159.

Mazzotti, S., A. Lambert, M. Van der Kooij, and A. Mainville, 2009, Impact of anthropogenic subsidence on relative sea-level rise in the Fraser River delta, *Geology*, Vol. 37, pp771-774, doi: 10.1130/G25640A.1.

Milana, J.P., 2010, The sieve lobe paradigm: Observations of active deposition, *Geology*, v. 38, no. 3, p.207-210, doi: 10.1130/G30504.1.

Neton, M.J., J. Dorsch, C.D. Olson, S.C. Young, 1994, Architecture and directional scales of heterogeneity in alluvial-fan aquifers, *J. of Sed. Res.*, vol B64, no 2, pp245-257, doi: 1073-1318/94/0B64-245.

Philibosian, B., T. Fumal, R. Weldon, 2011, San Andreas fault earthquake chronology and Lake Cahuilla History at Coachella, California, *BSSA*, v. 101, no. 1, p. 13-18, doi: 10.1785/0120100050.

Planert, M. and J.S. Williams, 1995, Groundwater Atlas of the United States – Segment 1, California, Nevada: U.S. Geological Survey Hydrologic Investigations Atlas 730-B, 28 p.

Poland, J.F., 1984, Mechanics of land subsidence due to fluid withdrawal, *Studies and reports in hydrogeology*, *vol. 40*, 37-54.

Ponce, D.A., Langenheim V.E., 1992, Isostatic residual gravity map of the Palm Springs 1:100,000 quadrangle, California: U.S. Geological Survey open-file report 92-702.

Reichard, E.G., J.K. Meadows, 1992, Evaluation of a ground-water flow and transport model in the Upper Coachella Valley, California: U.S. Geological Survey Water-Resources Investigations Report, 91-4142, 101 p.

Riley, F.S., 1969, Analysis of borehole extensometer data from central California, *Land Subsidence, v. 2: Internat. Assoc. Sci. Hydrology Pub. 89*, edited by Tison, L.J., 423-431.

Rogers, T.H., 1965, Geologic map of California: Santa Ana sheet: Calif. Div. Mines, scale 1:250000.

Rosen, P.A, S. Hensley, G. Peltzer, M. Simons (2004), Updated repeat orbit interferometry package released, *EOS Trans. AGU*, 85, 35.

Rymer, M.J., 2000, Triggered surface slips in the Coachella valley area associated with the 1992 Joshua Tree and Landers, California, earthquakes, *BSSA*, v. 90, no. 4, p. 832-848.

Scheibe, T.D., and D.L. Freyberg, 1995, Use of sedimentological information for geometric simulation of natural porous media structure, *Water Resources Res*., vol 31, no 12, pp 3259-3270, doi: 0043-1397/95/95WR-02570.

Schmidt, D.A., R. Bürgmann (2003), Time dependent land uplift and subsidence in the Santa Clara valley, California, from a large interferometric synthetic aperture radar data set, *J. Geophys. Res*., *108*(B9), 2416, doi:10.1029/2002JB002267.

Seeber, L., J.G. Armbruster, 1995, The San Andreas fault system through the Transverse Ranges as illuminated by earthquakes, *J. Geophys. Res. 100*(B5), p. 8285-8310.

Sims, S.J., 1961, Geology of part of the Santa Rosa Mountains, Riverside County, California, Thesis (Ph.D.)-Dept. of Geology, Stanford University.

Sneed, M., M.E. Ikehara, D.L. Galloway, and F. Amelung, 2001, Detection and measurement of land subsidence using global positioning system and interferometric synthetic aperture radar, Coachella Valley, California, 1996-98: U.S. Geological Survey Water-Resources Investigations Report 01-4193, 26 p.

Sneed, M., S.V. Stork, and M.E. Ikehara, 2002, Detection and measurement of land subsidence using global positioning system and interferometric synthetic aperture radar, Coachella Valley, California, 1998-2000: U.S. Geological Survey Water-Resources Investigations Report 02-4239, 29 p.

Sneed, M., J.T. Brandt, 2007, Detection and measurement of land subsidence using global positioning system and interferometric synthetic aperture radar, Coachella Valley, California, 1996-2005: U.S. Geological Survey Water-Resources Investigations Report 07-5251, 31 p.

Toda, S., R.S. Stein, V. Sevilgen, and J. Lin, 2011, Coulomb 3.3 graphic-rich deformation and stress-change software—user guide: U.S. Geological Survey Open-File Report 2011-1060, 63 p.

Tyley, S., 1974, Analog model study of the ground-water basin of the upper Coachella Valley, California, U.S. Geological Survey Water-Supply Paper 2027, 77 p.

Van Der Woerd, J., Y. Klinger, K. Sieh, P. Tapponnier, F.J Ryerson, and A. M´eriaux, 2006, Long-term slip rate of the southern San Andreas fault from ^{10}Be–^{26}Al surface exposure dating of an offset alluvial fan, *J. geophys. Res*., 111(B04407), doi:10/1029/2004JB003559.

Wentworth, C.M., R.A. Williams, R.A. Jachens, R.C. Graymer, and W.J. Stephenson, 2010, The Quaternary Silver Creek fault beneath the Santa Clara Valley, California, U.S. Geological Survey open-file report 2010-1010.

Wisely, B.A, 2005, Subsidence and differential surface movement in the upper Coachella Valley, California, as indicated by InSAR, in: *EOS*, Transactions, American Geophysical Union, December 2005, Vol. 86, Issue 52, Suppl.

Wisely, B.A., and D. Schmidt, 2010, Deciphering vertical deformation and poroelastic parameters in a tectonically active fault-bound aquifer using InSAR and well level data, San Bernardino basin, California, *Geophys. J. Int.*, doi: 10.1111/j.1365-246X.2010.04568.x.

Yule, D. and K. Sieh, 2003, Complexities of the San Andreas fault near San Gorgonio Pass: Implications for large earthquakes, *J. Geophys. Res. 108*(B11), doi: 10.1029/2001JB000451.

Zebker, H.A, P.A. Rosen, S. Hensley, 1997, Atmospheric effects in interferometric synthetic aperture radar surface deformation and topographic maps, *J. Geophys. Res. 102*(B4), 7547-7563.

CHAPTER IV

Aki, K. and P.G. Richards, 1980, Quantitative seismology, *Theory and Methods*, vol 1, Freeman and Co., New York, 557 p.

Bird, P., and Y.Y. Kagan, 2004, Plate-tectonic analysis of shallow seismicity: Apparent boundary width, beta, corner magnitude, coupled lithosphere thickness, and coupling in seven tectonic settings, *Bull. Seis. Soc. Amer.*, vol 94, no 6, pp 2380-2399, doi: 10.1785/0120030107.

Brown, R.D., Jr. and R.E. Wallace, 1968, Current and historic fault movement along the San Andreas fault between Paicines and Camp Dix, California, *Proceeding, Conference on Geologic Problems of the San Andreas Fault System*, W. R. Dickinson and A. Grantz, Editors, Stanford University Publ. Geol. Sci., 11, pp 22-39.

Burford, R.O., and P.W. Harsh, 1980, Slip on the San Andreas fault in central California from alignment array surveys, *Bull. Seis. Soc. Amer.*, vol 70, no 4, pp 1233-1261.

Burford, R.O., 1988, Retardations in fault creep rates before local moderate earthquakes along the San Andreas fault system, central California, *Paleogeography.*, vol 126, pp 499-529.

Chen, W.P., and P. Molnar, 1977, Seismic moments of major earthquakes and the average rate of slip in Central Asia, *Jour. Geophys. Res.*, vol 82, no 20, pp 2945-2969.

DeMets, C., R.G. Gordon, D.F. Argus, and S. Stein, 1994, Effect of recent revisions to the geomagnetic reversal time-scale on estimates of current plate motions: *Geophys. Res. Let.*, vol 21, pp 2191–2194, doi: 10.1029/94GL02118.

Freymueller, J.T., M.H. Murray, P. Segall, and D. Castillo, 1999, Kinematics of the Pacific–North America plate boundary zone, northern California, *J. Geophys. Res.*, vol 104, pp 7419–7441.

Galehouse, J.S., and J.J. Lienkaemper, 2003, Inferences drawn from two decades of alignment array measurements of creep on faults in the San Francisco Bay Region, *Bull. Seis. Soc. Amer.*, vol 93, pp 2415-2433.

Goulty, N.R., R.O. Burford, C.R. Allen, R. Gilman, C.E. Johnson, and R.P. Keller, 1978, Large creep events on the Imperial fault, California, *Bull. Seis. Soc. Am.*, vol 68, pp 517-521.

Humphreys, E.D., and R.J. Weldon, 1994, Deformation across the Western United States: A local determination of Pacific-North America transform deformation, *J. Geophys. Res.*, vol 99, pp 19975-20010.

King, C., R.D. Nason, and R.O. Burford, 1977, Coseismic steps recorded on creep meters along the San Andreas fault, *J. Geophys. Res.*, vol 82, pp 1655-1662.

Kostrov, B.V., 1974, Seismic moment and energy of earthquakes, and seismic flow of rock, *Izv. Acad. Sci. USSR Phys. Solid Earth I.*, pp 23-44.

Lienkaemper, J.J., J.S. Galehouse, and R.W. Simpson, 2001, Long-term monitoring of creep rate along the Hayward fault and evidence for a lasting creep response to the 1989 Loma Prieta earthquake, *Geophys. Res. Lett.* vol 28, pp 2265–2268.

Lienkaemper, J.J., G. Borchardt, and M. Lisowski, 1991, Historical creep rate and potential for seismic slip along the Hayward fault, California, *J. Geophys. Res.*, vol 96, pp 18261-18283.

Lisowski, M. and W.H. Prescott, 1981, Short-range distance measurements along the San Andreas fault system in central California, 1975 to 1979, *Bull. Seis. Soc. Amer.*, vol 71, no 5, pp 1607-1624.

Louie, J.N., Allen, C.R., Johnson, D.C., Haase, P.C., and S.N. Cohn, 1985, Fault slip in southern California, *Bull. Seis. Soc. Amer.*, vol 75, no 3, pp 811-833.

Molnar, P., 1983, Average regional strain due to slip on numerous faults of different orientations, *J. Geophys. Res.*, vol 88, no B8, pp 6430-6432.

Molnar, P., R.S. Anderson, and S.P. Anderson, 2007, Tectonics, fracturing of rock, and erosion, *J. Geophys. Res.*, vol 112, F03014, doi:10.1029/2005JF000433.

Molnar, P., 1979, Earthquake recurrence intervals and plate tectonics, *Bull. Seis. Soc. Amer.*, vol 69, no 1, pp 115-133.

Oppenheimer, D.H., W.H. Bakun, and A.G. Lindh, 1990, Slip partitioning on the Calaveras fault, California, and prospects for future earthquakes, *J. Geophys. Res.*, vol 95, pp 8483-8498.

Petersen M.D., W.A. Bryant, C.H. Cramer, T. Cao, M.S. Reichle, A.D. Frankel, J.J. Lienkaemper, P.A. McCrory, and D.P Schwartz, 1996, Probabilistic seismic hazard assessment for the state of California, *California Geological Survey Open-file Report 96-08*, *USGS Open-file Report 96-706*, 33 p.

Prescott, W.H., M. Lisowski, and S.C. Savage, 1981, Geodetic measurement of crustal deformation on the San Andreas, Hayward, and Calaveras faults near San Francisco, California, *J. Geophys. Res.*, vol 86, no B11, pp 10853-10869.

Prescott, W.H., and R.O. Burford, 1976, Slip on the Sargent fault, *Bull. Seis. Soc. Amer.*, vol 66 (3), pp 1013-1016.
Schulz, S.S., G.M. Mavko, R.O. Burford, and W.D. Stuart, 1982, Long-term fault creep observations in central California, *J. Geophys. Res.*, vol 87, no B8, pp 6977-6982.

Titus, S.J., C. DeMets, and B. Tikoff, 2005, New slip rate estimates for the creeping segment of the San Andreas fault, California, *Geology*, vol 33, pp 205-208.

Wallace, R.E., and E.F. Roth, 1967, Rates and patterns of progressive deformation, in The Parkfield-Cholame California Earthquakes of June-August 1966, *U. S. Geol. Surv. Prof. Paper 579*, pp 23-40.

Wdowinski, S., B. Smith-Konter, Y. Boch, and D. Sandwell, 2007, Diffuse interseismic deformation across the Pacific-North America Plate Boundary, *Geology*, vol 35, no 4, pp 311-314.

Wesson, R.L., 1988, Dynamics of fault creep, *J. Geophys. Res.*, vol 93, pp 8929-8951.

Wilmesher, J.F., and F.B. Baker, 1987, Catalog of alignment array measurements in central and southern California from 1983 through 1986, *U.S. Geol. Surv. Open-File Rep. 87–280*, 157 p.